SAPIENZA
UNIVERSITÀ DI ROMA

Phase-field fracture models for elastomers

Nico Stortini

March 19, 2024

Faculty of engineering
Department of Mechanical and Aerospace Engineering

Phd in Theoretical and applied mechanics, 36th cycle

Tutor
Jacopo Ciambella

Co-tutor
Giovanni Lancioni

A.Y. 2023-2024

Abstract

The primary objective of this work is to examine, present, and suggest phase-field damage models that are suitable for simulating the fracture behavior of soft materials, with a specific focus on rubbers. To achieve this, it is essential to comprehend the various ways in which fracture occurs in rubbers through different case studies, such as simple tension tests or tests with pre-etched specimens subjected to quasi-static loading conditions. Along with the specimen shape and testing mode, it is crucial to understand how the material's viscosity influences the rate and mode of fracture and the propagation of fracture. Next, this study will concentrate on three specific phenomena, aiming to replicate them numerically using the proposed models. To illustrate brittle fracture phenomena, the experiments detailed in Hocine et al. [2002], investigating the behavior of pre-incised specimens, will be replicated. The investigation into cohesive fracture phenomena will draw from the findings in Millereau et al. [2018], which explored double network elastomers and their pseudo ductility. Finally, the examination of dynamic fracture behavior will reference experiments from Corre et al. [2020], emphasizing the pivotal role of fracture propagation.

After analyzing the experimental data, it will be necessary to introduce finite elastic and viscoelastic models for soft materials, like rubber, hydrogels, biological tissues and others that are able to undergo significant deformations (even up to 700%) under low stresses. Additionally, phase-field models of damage will be incorporated. The existing literature on finite elasticity models will be explored, including well-known models summarized in Dal et al. [2021], as well as less known models such as the one proposed by Lopez-Pamies [2010], which will also be utilized in the proposed models. The utilization of these models will contribute to formulating a Maxwell rheological scheme, as outlined in Reese and Govindjee [1998], Holzapfel [1996], and Kumar and Lopez-Pamies [2016], in order to depict viscoelastic characteristics. Subsequently, a damage state variable will be introduced to create a viscoelastic phase field model. In these phase-field models, the material's characteristics, affecting its elastic parameters, are represented by fields of state variables. In the case of damage models, the state variable considered is damage, which progressively degrades the material parameters until failure. A literature review of damage models, including the works of Pham et al. [2011], Lancioni and Corinaldesi [2018], Wu [2017], and others, will also be conducted.

Following the introduction and literature review, an elastic rate independent model capable of reproducing both brittle (Hocine et al. [2002]) and pseudo-ductile (Millereau et al. [2018]) behaviors, by incorporating a cohesive damage model into the Ogden's (Ogden [2003]) finite elastic model will be proposed. By this way, an interpretation of failure phenomena at large damage displacements will be proposed. This model will be thoroughly explained from theoretical and numerical perspectives, elucidating the role of different constitutive parameters. In this scenario, three parameters within the degradation function (representing the impact of damage on the material's elastic moduli) will hold significant importance. These parameters will respectively define the fracture's onset, the progression during the initial post-elastic phase, and the material's behavior at the point of complete failure. Numerical simulations will be performed to replicate the actual behavior observed in experimental tests. The model's potential and limitations, particularly the absence of viscosity, will be analyzed and discussed.

To address the influence of viscosity on fracture propagation and failure modes, a second rate-dependent formulation will be proposed, utilizing a generalized Maxwell

rheological model similar to the works of Reese and Govindjee [1998] and Kumar and Lopez-Pamies [2016]. In this theory, a damage model representing brittle fracture will be considered. In this formulation, a parameter will be introduced to assess the energy dissipation resulting from the rate of damage and, thus, associated with crack propagation, as Loew et al. [2019], Levitas et al. [2010], Hakim and Karma [2009]. This parameter will serve as a characteristic time of the damage variable and it plays a crucial role in reproducing experiments of Corre et al. [2020]. This damage characteristic time will interact with the material characteristic time, which is the ratio between the viscous parameter and the stiffness. The complete model, along with the interpretation of constituent parameters, will be presented. Furthermore, considering the extreme scenarios of infinite and infinitesimal material characteristic times, pertaining to the damage characteristic time, as well as finite viscosity, will be investigated to understand their effects. The rate dependence will enable the study of loading rate influence on rupture and crack propagation in soft materials. The model will be properly calibrate to reproduce the behavior of Corre's material, to replicate crack propagation findings. Finite element modeling will be employed to examine the material's state around the fracture tip in terms of energies involved, dissipations, and stresses, observing the local response to crack formation.
Subsequently, these two models will be analyzed to highlight their strengths and weaknesses regarding their ability to reproduce experimental results and their numerical complexities. The conclusions will summarize the potential of the presented models, the applicability of phase-field damage models to finite viscoelasticity, and the limitations of the proposed approaches. Future developments will be suggested, considering the limitations discussed and taking into account existing models in the literature.

Contents

Chapter 1

Introduction

1.1 Background and motivations

The broader category of soft materials encompasses elastomers, hydrogels, biological tissues, and more. Within this context, rubber materials find applications in tires, vibration dampeners, and various components in industries such as valve membranes and elastomeric wave energy harvesting. Due to their diverse applications and unique characteristics, these materials have been extensively researched for the past 70 years. The current research work aligns with this context, aiming specifically to investigate and propose finite elastic and viscoelastic models capable of depicting their failure behavior using a phase-field approach to damage.

One distinctive characteristic of these materials is their remarkable capacity for significant deformation, also over 700%. Additionally, viscosity plays a crucial role in their overall behavior, particularly in fracture scenarios where large pre-existing strains result in substantial deformation rates during and after crack formation.

Moreover, the viscous dissipation indirectly influences the fracture yield condition, by its connection with the energetic part. While numerous elastic models effectively simulate rubber behavior under pseudo-static conditions, they struggle to capture rate-dependent phenomena. Notably, a comprehensive review of these elastic models for soft materials can be found in the review of Dal et al. [2021].

Conversely, modeling rate-dependent phenomena, which encompass temperature dependence, the Payne and Mullins effects, as well as hysteresis, poses greater challenges. While this study will offer insights into these effects, supported by empirical data, it will exclusively focus on hysteresis phenomena due to the assumption of a constant temperature and the negligible impact of Mullins and Payne effects in the crack propagation problem. Using these assumption, the prominent sources on viscoelastic models at large strain encompass the works of Holzapfel [1996], Reese and Govindjee [1998], and Kumar and Lopez-Pamies [2016].

Concerning the correlation between fracture problems and rate-dependent phenomena, existing models are scarce and often complex to apply and fit with experimental data. Some of the earlier models, such as those by Hakim and Karma [2009] from an anisotropic perspective and Levitas et al. [2010], are among the earliest contributions. More recent studies by Loew et al. [2019], Yin and Kaliske [2020], Dammaß et al. [2021] and Dammaß et al. [2023] have also explored this domain.

Understanding the viscoelastic and fracture behavior of a material significantly enhances its potential applications and product performance. Precise modeling of fracture behavior and the interaction between viscous properties and material failure streamlines

the design process, enabling the development of new applications under non-quasi-static conditions and with deformations approaching crack strains.

In addition to the rate dependent phenomena, many peculiar behaviors of these materials can be caught using a rate independent approach. In particular, in recent years, substantial efforts have been directed towards addressing a fundamental limitation of elastomers, namely, their inherent tendency to undergo brittle failure. Notably, by customizing the microscopic characteristics of elastomers, a novel category of materials known as double-network elastomers has emerged (Millereau et al. [2018]). These elastomers demonstrate a pseudo-ductile failure mode, which arises from the deliberate control of crack propagation within their internal structure. The modeling aspects related to this distinctive behavior represent a noteworthy area of investigation, and these will be one of the aspects investigated in this study.

The aforementioned aspects outlines a significant challenge in elastomer fracture models, particularly concerning the integration of fracture models with the viscous properties of rubber materials, specifically focusing on crack propagation. The process of crack propagation within pre-stretched elastomer samples, while interacting with high deformation ratios, poses a complex problem. Understanding how the crack evolves and behaves under these conditions, taking into account the rate-dependent aspects of fracture phenomena, represents an ongoing and intricate challenge in the field.

It's worth noting that these models can also be adapted for other soft materials, such as hydrogels and biological materials, extending their applicability beyond rubber-based materials.

1.2 Outlines

Given the previously outlined objectives, we distinguish experimental and modeling works from literature. In the initial phase (experimental part), the primary objective is to comprehensively examine and gain insights into the underlying phenomena related to the failure of rubber materials. In this context, following a comprehensive overview of the subject through sources such as Knauss [2015], Persson et al. [2005] and Yin et al. [2021], the subsequent emphasis will be placed on three following experiments:

- Hocine et al. [2002], shown in fig. 1.1, a double notched sample is subjected to a tensile test with different values of a. In this situation, the non regularity of the geometry is crucial to catch the experimental results. In this framework the more interesting part will be the caching of the role played by the notched and the high stretching regime.

- The experiment of Millereau et al. [2018], studies the behavior of the double network elastomers. In fig. 1.2, a tensile test of these particular rubbers can be observed. The peculiarity of this material is its pseudo ductility. This characteristic behavior is due to a particular damage pattern. In a tensile test, after the elastic branch, a localized damaged neck appears in a little region of the bar. This neck propagates during the test in a quasi constant stress regime, until the damaged zone is extended for all the bar. When the propagation is completed, the material exhibits a little hardening branch until the rupture.

- For what concerns the rate dependent phenomena, the crack propagation in a pre-stretched sample will be studied, by the experimental results of Corre et al. [2020].

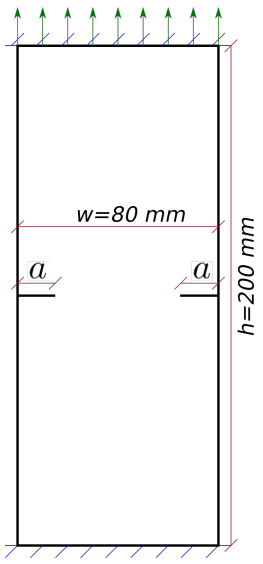

(a) Double notched sample

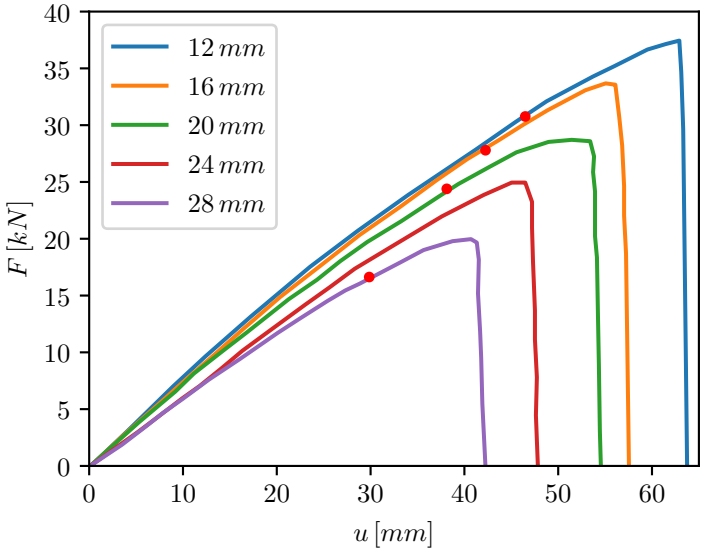

(b) results for different values of a (from $a = 12\,mm$ to $a = 28\,mm$)

Figure 1.1: Experimental set up 1.1a and results 1.1b of Hocine et al. [2002] for SBR rubber. In this case a double pre-notched sample is subjected to a tensile test with different values of a. The initiation of damage phenomena are highlighted by red points.

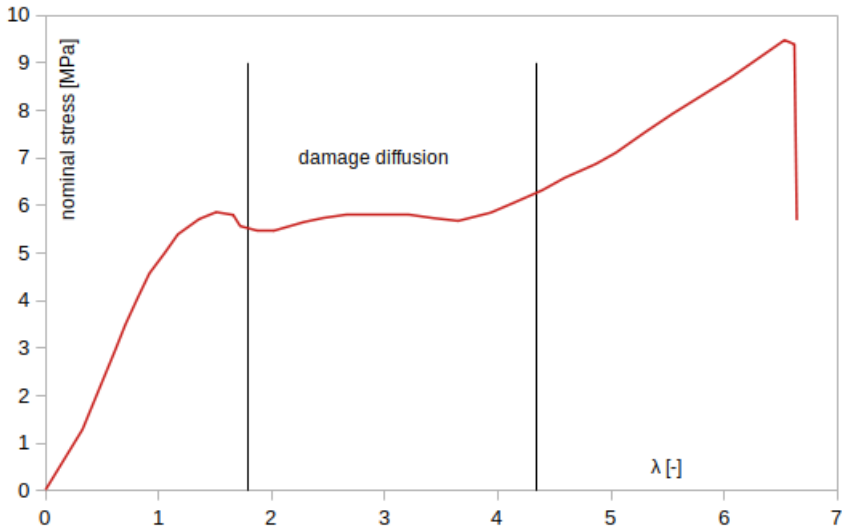

Figure 1.2: Double network elastomer's behavior in Millereau et al. [2018]. In this material, firstly a localized damage part can be observed and, during the constant stress part, it propagates over the bar.

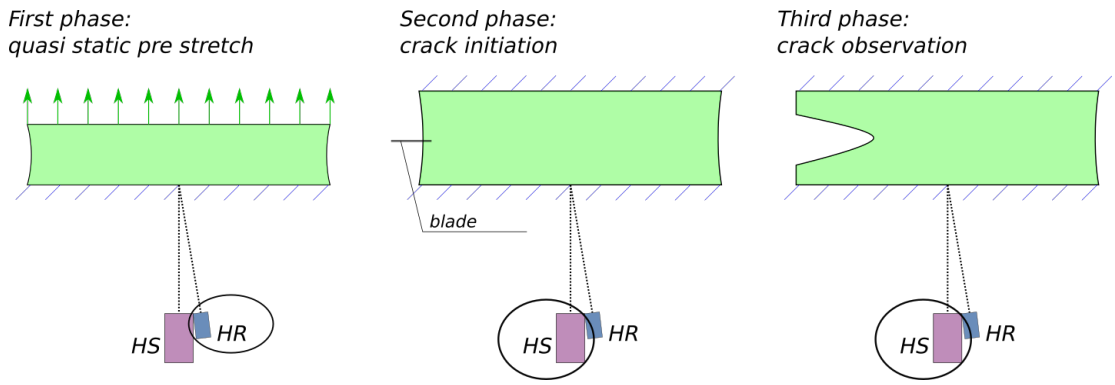

Figure 1.3: In this experiment of Corre et al. [2020], a rubber sample is pre-stretched and, after, a crack is made to observing the propagation.

> This experiment can be divided in three phases. In the first the sample is pre-stretched in pseudo-static conditions until a certain pre-stretch deformation. After this, in the second phase, a little cut is instantly made by a blade in the center of the stretched side. The last phase consists simply in the observation of the crack propagation along the bar. This experiment will be considered the main data set to study the interactions between the viscosity and the fracture behavior. These two aspects will be summarized in the present work, by the analysis of two distinct characteristic times, one linked to the viscosity of the material (the ratio between the viscous coefficient and the stiffness), and the other associated with the damage field. Notably, the relationship between these two time scales plays a pivotal role in determining the speed at which cracks propagate.

After a general study of fracture phenomenology, the focus of the study will shift to these three experiments, that will be simulated for their positive relationship between ease of modeling by finite element and relevance of the results.

The second portion of the outlined analysis pertains to the modeling aspects encompassing finite elasticity, finite viscoelasticity, and phase-field damage. In this work, the finite elastic models that will be used are the model in Ogden [2003], where the elastic energy density depends to the eigenvalue of the right Cauchy strain tensor ($\mathbf{C}$), and the model in Lopez-Pamies [2010], where it depends on the first invariant of $\mathbf{C}$. Both of these energy densities are appropriate for characterizing the diverse behaviors exhibited by soft materials. Specifically, Ogden's energy density tends to better fit with the experimental findings in pseudo-static loading conditions, albeit presenting challenges when coupled with viscous models compared to the Lopez-Pamiez energy density. Indeed, when using the Ogden's model to derive the stress tensor, the requirement to obtain the eigenvectors of $\mathbf{C}$ arises. This necessity, however, precludes the possibility of deriving the evolution equation for viscoelastic deformation in a closed and simple, form. Instead, in the Lopez-Pamiez model, it is possible to determine the stress tensor without the need for eigenvector calculations. As a result, the evolution equation for viscoelastic deformation can be assessed in a straightforward and analytical form.

For what concerns the viscous problem, it presents a more intricate challenge compared to the pseudo-static one. However, there are numerous contributions in the literature that can be explored to gain a deeper understanding of this issue. In particular, the foundational works that will serve as the cornerstone for the rate-dependent component of this research include Reese and Govindjee [1998], which introduces a viscoelastic model incorporating a Generalized Maxwell rheological model. Another important work

is Holzapfel [1996], where the volumetric contribution assumes a significant role in the modeling process. Additionally, Kumar and Lopez-Pamies [2016], extends the groundwork laid by Reese and Govindjee, both theoretically, by accommodating anisotropic conditions, and comprehensively, by incorporating nonlinear viscous modeling from theoretical, numerical, and experimental perspectives. While constructing the viscous part of the model in this study, Kumar's model will predominantly serve as the framework, while drawing supplementary insights from Reese and Govindjee [1998].

The last aspect that is considered consists in the modeling of fracture by following a phase-field approach. This kind of approach is commonly applied to the linear elasticity and its basis can be found in the work of Pham et al. [2011] or (for a more thermodynamics study) in Marigo [2006]. For an application to a real material, the work of Lancioni and Corinaldesi [2018] can be read. In this kind of model, the fracture/damage of the material is modeled as an internal scalar field that goes from zero (for the virgin material) to one (for the fully damaged material) named "damage" that can only increase. This internal variable is connected to the elastic parameters by the degradation function that is a decreasing function of the damage and it degrades the elastic moduli when the damage increase. Another significant component within these models includes the nominal energy release, which quantifies a localized energy release associated with fracture development. Additionally, there is a non-local energy term, which facilitates a seamless transition between the fractured region of the material and its intact part. In both the original contribution, the representation in Wu [2017] will be used, because it is an enough general treatment of the damage problem to include all the behaviors that we need (from brittle to pseudo-ductile or only brittle). For what concerns the pseudo-static application of the damage models, we can consider the work of Miehe and Schänzel [2014] as one of the first applications of the damage phase-field model to the finite elasticity. In this work, the experiments in Hocine et al. [2002] (see fig. 1.1) are simulated. Thus, our first aim will be to develop a model that are able to reproduce both the behavior in fig. 1.1 (brittle) and in fig. 1.2 (pseudo-ductile) by the coupling of the Ogden's and the phase field approaches.

After the development of a rate independent phase field damage model in the context of finite elasticity, the further development will become the study of the interactions between the fracture and the viscous propriety, through the analysis of the crack propagation. To achieve this goal, the experiment of Corre et al. [2020] (see fig. 1.3) will be the main point and the viscous models like Kumar and Lopez-Pamies [2016] will be coupled with the damage phase field models to reproduce that phenomenology.

1.3 Original Contribution

The main original contributions can be categorized into two main research endeavors: the first has been published in Ciambella et al. [2022] and is centered on quasi-static applications, while the second is currently ongoing and focuses on dynamic fracture in viscoelastic elastomers.

In the initial work, the objective is to accurately replicate the intricacies of crack phenomenology under pseudo-static conditions, accommodating a wide spectrum of behaviors from brittle to pseudo-ductile. Specifically, the study will encompass brittle behavior analysis, drawing insights from the experiments of Hocine et al. [2002], as also investigated in prior research by Miehe and Schänzel [2014], and Talamini et al. [2018]. This endeavor involves adapting the model to five distinct tensile tests, each featuring varying notch lengths, while also addressing irregularities that manifest in the vicinity

of these notches. Additionally, the investigation delves into pseudo-ductile phenomena, which are associated with the behavior of double network elastomers, as detailed in Millereau et al. [2018]. In this case, complexity arises from the post-elastic behavior exhibited by these materials. Specifically, a localized damage portion is observed initially, and during the constant stress phase, it propagates across the material until complete sample's damaging. After this phase a stress hardening phase is observed before the rupture.

In the second work, the focus will be the interaction between viscous effects and crack propagation. This study will be done by the analysis and the modeling of the experiment in Corre et al. [2020] (see fig. 1.3). In the formulation of a model able to reproduce this kind of experiment, in addition to the material's characteristic time τ_m (the ratio between the viscous coefficient and the stiffness), a damage characteristic time τ_d will be introduced using a dissipative viscous micro-stress to account the energy released by the material by the crack velocity. The interaction between these two characteristic times will be the first focus of this study and, after, the role played by other material's parameters or numerical choices will be analyzed. The formulation of this model will consists in the combination of a viscous model like Kumar and Lopez-Pamies [2016] or Reese and Govindjee [1998], with a brittle damage phase-field approach and, after this investigation, the model will be fitted with the experimental results.

1.4 Structure of the thesis

The structure of the thesis is the following:

- **Phenomenology and modeling of elastomers' behavior** This chapter will delve into the behavior of rubbers, initially exploring their viscoelastic properties through an analysis of the micro-mechanical structure, drawing insights from sources such as Baumard [2017], Persson et al. [2005], and other references. The aim is to illuminate the material's peculiarities as thoroughly as possible. Subsequently, the focus will shift to fracture analysis, investigating references like Persson et al. [2005] and Knauss [2015] to examine all contributing factors to material fracture.
  Following this phenomenological analysis, the study will progress to explore models present in the literature. Beginning with pseudo static elastic models, the review will encompass references such as Dal et al. [2021] and significant treatises in the field of viscoelasticity (Reese and Govindjee [1998], Holzapfel [1996], Kumar and Lopez-Pamies [2016]). Subsequent sections will introduce phase-field modeling, initially delving into damage modeling utilizing the Lancioni and Corinaldesi [2018] model, followed by the presentation of the Wu [2017] model.
  After introducing phase-field models for damage in linear elasticity, the exploration will advance to nonlinear elasticity (leveraging Miehe and Schänzel [2014] and Talamini et al. [2018]), preceding an introduction to the primary formulations in finite viscoelasticity and damage, drawing from sources such as Loew et al. [2019], Yin and Kaliske [2020], Dammaß et al. [2021] e Dammaß et al. [2023].

- **A cohesive phase-field model** The objective of this chapter is to introduce the model as presented in Ciambella et al. [2022]. The first section will provide a comprehensive overview, highlighting the model's adaptability as an exemplary illustration. It demonstrates a highly versatile formulation capable of simulating

both brittle and pseudo-ductile fracture behaviors.

- **Rate dependent phase-field model** This chapter will introduce a finite viscoelastic model coupled with a damage phase-field approach, with the goal of replicating crack propagation as observed in the experiment conducted by Corre et al. [2020]. Through this model, we will assess the impact of different material parameters on crack propagation, with particular attention to the material's characteristic time (τ_m) and the damage characteristic time (τ_d), as well as their interplay.

- **Conclusion** In this section, we will summarize the capabilities of the two formulations. Following that, we will underscore the constraints and limitations of these models. Starting from these limits, we will put forth suggestions for potential future advancements and developments.

1.5 Notation

For what concerns the notation, distinct conventions will be applied for matrices, vectors, and versors. Matrices will be represented by capital bold letters ($\mathbf{M}$), vectors typically denoted by lowercase letters and underlined ($\underline{u}$), and versors (unit modulus vectors) indicated by a hat over them ($\hat{n}$).

The scalar product, applicable to both vectors and tensors, will be denoted using a central dot, illustrated as follows:

$$\mathbf{M} \cdot \mathbf{N} = M_{ij} N_{ij} \qquad \underline{u} \cdot \underline{v} = u_i v_i, \tag{1.1}$$

where the components of vectors and matrices are identified by subscripts (for matrices first row, then column). In equations where there's a generic index, the summation symbol (e.g., $\sum_i$) is excluded unless explicitly stated, following the convention used in preceding equations.

For what concerns the derivation, the over dot indicates the time derivative ($\dot{\bullet} = \mathrm{d}\bullet/\mathrm{d}t$), while the former indicates the partial derivative with respect to the variable on which the function depends (e.g. $g'(d) = \partial g(d)/\partial d$), also when the variable is omitted for synthesis.

The row-column product of the tensors is represented without symbols ($\mathbf{MN}$) and the dyadic product between vectors gives a matrix as follows:

$$(\underline{u} \otimes \underline{v})_{ij} = u_i v_j, \qquad (\underline{u} \otimes \underline{v})(\underline{m} \otimes \underline{n}) = (\underline{v} \cdot \underline{m})(\underline{u} \otimes \underline{m}), \qquad (\underline{u} \otimes \underline{v})\underline{m} = (\underline{m} \cdot \underline{v})\underline{u}; \tag{1.2}$$

where the components, the matrix and the vector row-column products are respectively shown. Typically, this type of multiplication yields a tensor with an order equal to the sum of the orders of the individual factor tensors. For instance, the dyad of two vectors, each being first-order tensors, results in a second-order tensor. Meanwhile, a dyad formed by two second-order tensor (matrices) produces a fourth-order tensor.

Chapter 2

Phenomenology and modeling of elastomers' behavior

This chapter encompasses a literature review on elastomer behavior and the corresponding replicating models. It commences with an introduction to the phenomenology of elastomer deformation processes, encompassing micro-mechanical observations. Following the deformation phase, the review delves into the analysis of the phenomenology of the fracture processes. Subsequently, the focus moves to finite elastic and viscoelastic modeling, culminating in the introduction of phase-field models. These models will be utilized for simulating and studying the fracture behavior of elastomers.

2.1 A microscopic perspective on elasticity and viscoelasticity

Rubbery materials can undergo significant deformations, exceeding 700%, while experiencing relatively low levels of stress. The pseudo-static behavior of these materials has been extensively investigated, with a comprehensive review available in the work by Dal et al. [2021]. This review encompasses both statistical and phenomenological approaches. From a microscopic perspective, rubber materials consist of chains of monomers with freely rotating links. These chains are interconnected by weak chemical bonds with varying degrees of cross-linking. In a stress-free configuration, these chains adopt a curled-up arrangement, facilitated by the presence of these weak interconnections. However, when subjected to stretching from a nearly stress-free state, as also elucidated in the study by Baumard [2017], the probability (p) that the end of a random chain resides within a given volume (dv, with its origin at the opposite end) can be mathematically expressed using a Gaussian error function as follows

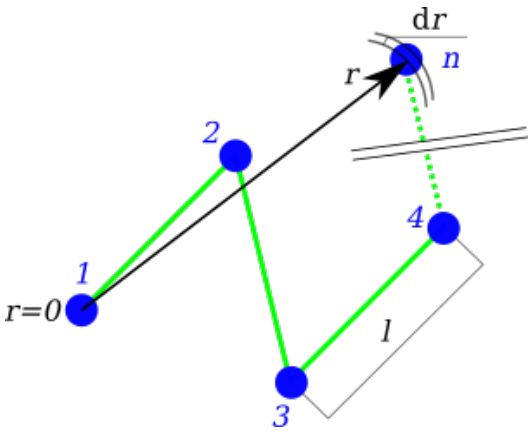

Figure 2.1: Micro mechanics framework of a single chain.

$$p(r)dv = \frac{c_1^3}{\pi^{3/2}} e^{-c_1^2 r^2} dv, \quad \text{s.t.} \quad P(r)dr = 4\frac{c_1^3}{\pi^{1/2}} r^2 e^{-c_1^2 r^2} dr \tag{2.1}$$

where r is the distance from the origin and $c_1^2 = 3/(2nl^2)$ is a parameter that depends only on the structure of the chain (n, the number of monomers and l the length of the single linkas in fig. 2.1). This equation also involves a change of coordinates to calculate the probability of finding the chain's end within a spherical shell of thickness dr at a distance r from the origin. It's crucial to highlight that equations (2.1) are applicable when the ratio $c_1 r = r/l \ll 1$, thus, when the end-to-end distance significantly differs from the fully extended length of the chain.
In such a scenario, the work ($\mathcal{W}$) for a reversible deformation can be expressed as the change in Helmholtz free energy. Due to the free rotation of the links, we can disregard the internal energy and focus solely on the entropy component of the energy, as it follows

$$\mathcal{W} = -\theta \Delta S \quad \text{where} \quad S = c_2 - k c_1^2 r^2, \tag{2.2}$$

where θ is the absolute temperature, S the entropy and, in the entropy definition, c_2 is an arbitrary constant and k is the Boltzmann constant. The transition from the microscale to the macroscale can be achieved by recognizing that the deformation of an individual chain mirrors the deformation of the entire network. Now, we can focus on the principal directions of deformation to determine the position vectors. For each principal direction (denoted as $i = 1, 2, 3$), the position vector can be expressed as $x_i = \lambda_i x_{0i}$ where 'x_{01}' is the initial position vector. In this context, both entropy and its change can be expressed as follows

$$S = c_2 - k c_1^2 (\lambda_i x_{0i})^2; \qquad \Delta S = -k c_1^2 (\lambda_i^2 - 3) x_{0i}^2. \tag{2.3}$$

Given the absence of a favored direction for the principal axes (indicating isotropic behavior), we can contemplate the average initial position as $\sum x_{0i}^2 = N_c \overline{r_{0i}^2}$ and it can be assumed as constant for the chains. Hence, during an isothermal transformation, the internal work performed by all the chains within a unit volume can be regarded as

$$\mathcal{W} = \frac{1}{2}\mu(\lambda_1^2 + \lambda_2^2 + \lambda_3^2 - 3) = \frac{1}{2}\mu(I_1 - 3), \tag{2.4}$$

where the constant μ includes all the constant coefficients in eqn. (2.3) and I_1 represents the first invariant of the right Cauchy strain tensor, as explained in sect. 2.4.1 and eqn. (2.15). Equation (2.4) is commonly referred to as the Neo-Hooke strain energy function. It's worth noting that this model is suitable for simulating rubber behavior primarily when deformations are relatively small compared to the maximum elongation, as depicted in fig. 2.2. Indeed, considering as example the probability function in Kuhn and Grün [1942]

$$\log p(r) = C_{NG} - n\frac{r}{nl}\mathcal{L}^{-1}\left(\frac{r}{nl}\right) + \log\left(\frac{\mathcal{L}^{-1}(r/(nl))}{\sinh[\mathcal{L}^{-1}(r/(nl))]}\right), \tag{2.5}$$

where $\mathcal{L}$ is the Lingevin function that tends linearly (with an angular coefficient of 3) to zero when the argument tends to zero (see Howard [2020] for more instances), we can observe that for $r/nl \to 0$, the last expression tends to the Gaussian distribution of eqn. (2.1). In this range, the strain energy is predominantly entropic, as also discussed in Puglisi and Saccomandi [2016], where the chains are not considered composed by hinged rods, but by hinged beams, obtaining a worm-like chain model, where the deformation of the links between the monomers gives an enthalpic contribution.

If the goal is to predict material behavior under higher levels of stretching, more complex probability functions (such as the inverse of the Langevin function, as seen in Treloar [1975]) and more intricate phenomenological models at the macro scale become

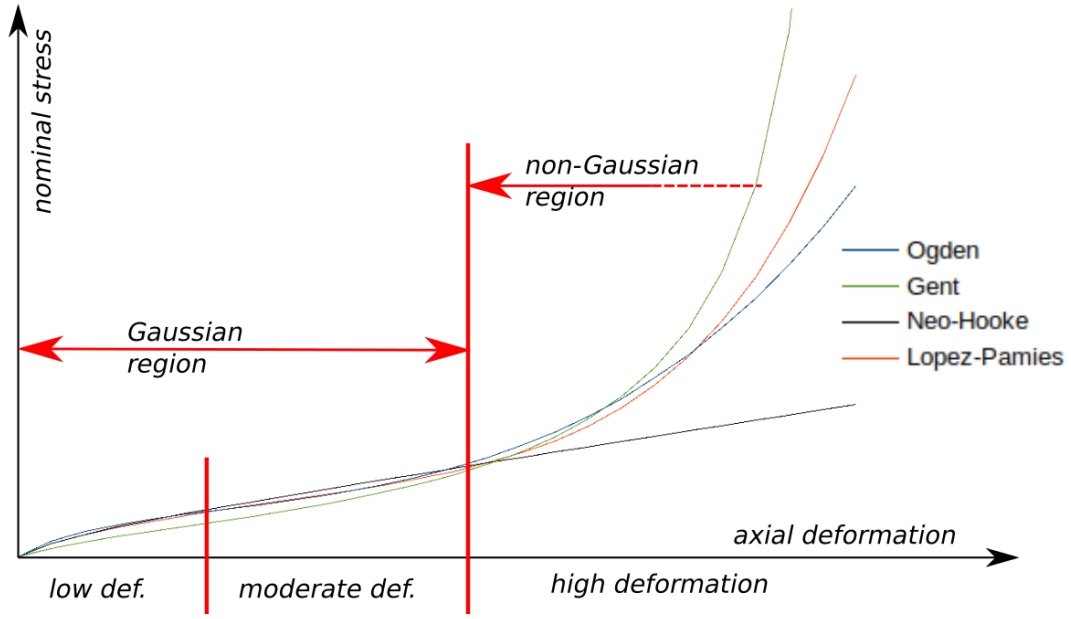

Figure 2.2: In this figure, the neo-Hooke model is qualitatively compared with other phenomenological models (Ogden [2003], Lopez-Pamies [2010] and Gent [1996]). Since this model is based on the micro mechanical treatment outlined in eqn. (2.1), it effectively accurately predicts rubber behavior within the region of low and moderate strains. However, for high strains, employing more intricate formulations becomes imperative. Furthermore, this graph includes a distinction of strain regimes as reported by Dal et al. [2021], where the low stretches refer to the concave part of the stress–stretch curve, moderate to the plateau region of the curve and high stretches to the stress hardening part. These models will be exposed in sect. 2.4.1.

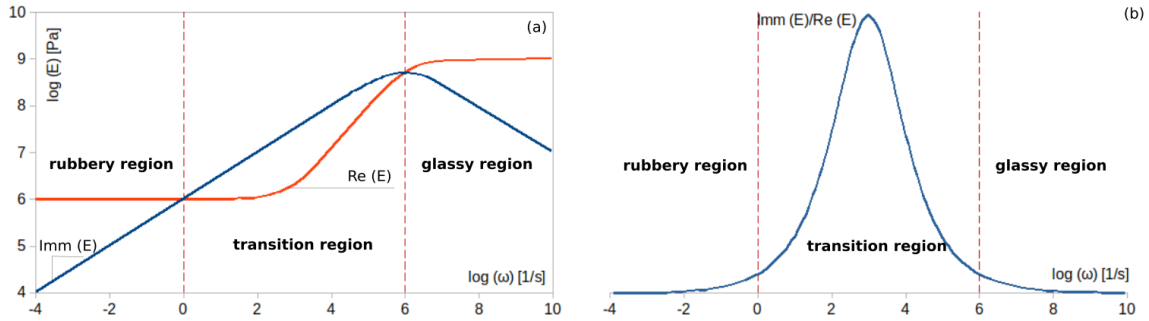

Figure 2.3: Viscoelastic modulus with the imaginary (loss) and real (storage) parts in fig. (a) and their ratio ($\tan\delta$) from Persson et al. [2005] over the frequency of the dynamic part of the deformation ω. Since $\tan\delta$ is often associated with viscous dissipation, it can be seen that the transition region has the maximum dissipation.

necessary.

For what concerns the viscoelastic behavior, as explained in Persson et al. [2005], from a micro structure point of view, this is due to the thermally activated switching of polymer segments between different configurations, facilitated by the stresses. If τ_m represents the characteristic switching time during which these phenomena occur (also known as *material characteristic time*), then, for a cycling load with frequency $\omega \gg \tau_m^{-1}$,

there is not time for thermally activated rearrangement of the polymer chain segments to occur, and the rubber response is that of a hard glassy material. On the other hand, when $\omega \ll \tau_m^{-1}$, thermally activated rearrangements of the chains occur adiabatically, resulting in a soft rubbery response. This behavior is evident in a cyclic test (e.g., with $\lambda = \lambda_{st} + \epsilon_{din}\sin(\omega t)$), in which the stiffness can be described as a complex modulus summing the contribution of the in-phase (elastic) and the out-of-phase (viscous) responses of the material. This modulus depends on the frequency of the load and on the temperature, in an indirect way, through τ_m as $E = E(\omega, \tau_m(T))$, such that

$$E = E' + iE'', \qquad \tan\delta = E''/E'; \tag{2.6}$$

where E' and E'' are the real and imaginary parts of E (also called storage and loss modulus), and $\tan\delta$ is the loss angle, providing an estimate of the damping in the material. Two limit loading conditions can be identified, where $\tau_m \gg 1/\omega$ or $\tau_m \ll 1/\omega$; in both cases, the imaginary part of the elastic modulus becomes $\mathrm{Im}(E) \to 0$, signifying that the material behavior becomes rate-independent. In the intermediate case, viscous effects become important. In this context, understanding the temperature dependence of τ_m is crucial. One possible relation is given by Williams et al. [1955], where the following relationship is derived

$$\tau_m = \tau_{m0}\, a_T, \qquad \text{where} \qquad a_T = \frac{C_1(T - T_g)}{C_2 + T - T_g}; \tag{2.7}$$

where T_g is the glass transition temperature and $C_1,\ C_2$ are two constants of the rubber. As shown in fig. 2.4, the temperature dependence of the loss modulus on the frequency can be completely absorbed by the a_T parameter in eqn. (2.7). In addition to the temperature effects, another dynamic effect that can be found in the rubber behavior is the Payne effect, shown in fig. 2.5 by the experiments of Ramier et al. [2007]. In a cyclic loading condition, the storage modulus decreases with the amplitude of the dynamic maximum strain of a cycling load. The loss factor presents a peak and, after, it decreases. This phenomenon can be found also in case of low strains and it is a non linear viscous effect. Another non linear elastic effect that can be found in these materials is the Mullins' effect. It is a phenomena where for a series of loading and unloading at the same maximum strain (also in pseudo-static load conditions), the maximum stress measured decreases with the number of cycles as shown in fig. 2.6. The intensity of this phenomenon normally decrease whit the number of the cycles, in fact it is relevant only for the firsts cycles and negligible for the others. An exhaustive review concerning this kind of behavior can be found in Diani et al. [2009]. The main physical interpretations of this phenomenon involve microstructural ruptures as well as microstructural changes in the interface between rubber-filler interface. These interpretations are mainly dedicated to filled rubbers and usually do not extend to not filled materials, but the Mullins effect is observed also in pure gums. Also for this reason, the various explanations suggested for the Mullins' effect show that there is still no general agreement on its origin.

A fundamental aspect of rubber response is hysteresis, which is manifested by the non-vanishing area between stress-strain curves in a cyclic experiment, as illustrated in fig. 2.7. The amount of energy dissipation is intricately connected to the rubber's composition and microscopic-scale phenomena that lead to energy dissipation, encompassing factors such as the friction between polymer chains and the degradation of the filler structure. This phenomenon has been explored in studies like Mark et al. [1994], where it is inferred that crosslinks reduce hysteresis as the elasticity of the rubber network increases. Additionally, in Lindley [1974], the investigation into the role played by fillers

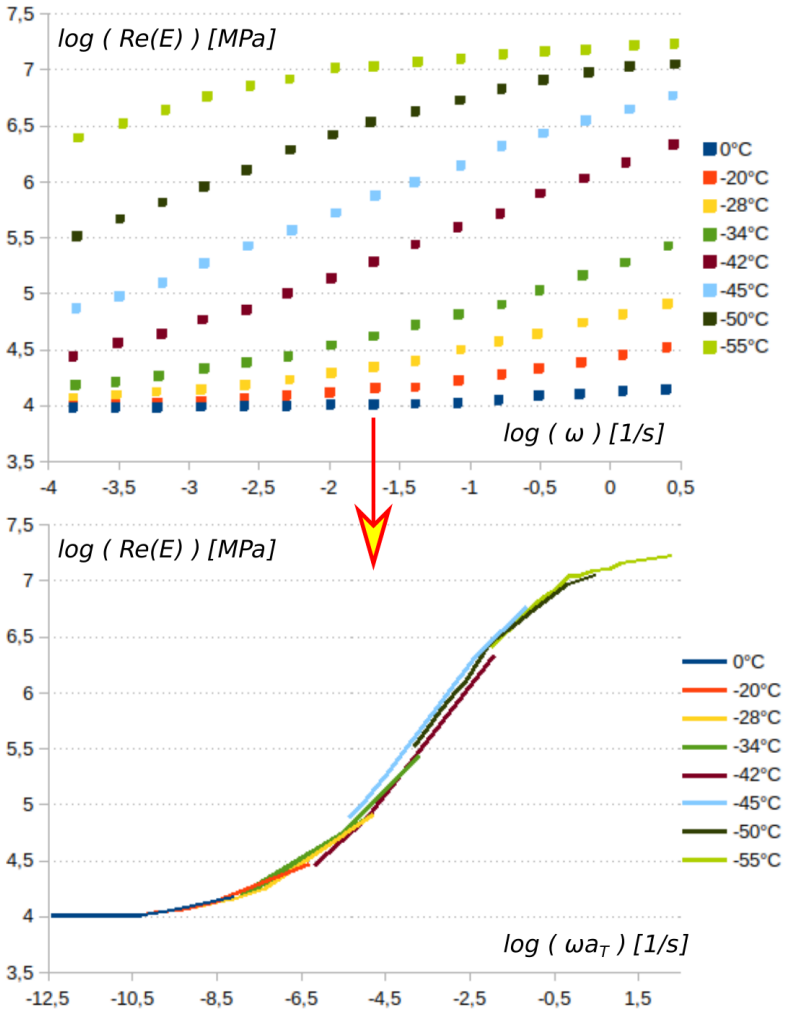

Figure 2.4: Effect of the temperature on the storage modulus (real part of the elastic modulus) from Gent and Walter [2006]. In this graphs the role played by a_T in eqn. (2.7) is shown. In particular, if ω is normalized with $\omega\, a_T$, the relation between the frequency and the storage modulus becomes temperature dependent only through a_T.

deduces that fillers contribute to increased energy loss. This phenomenon can be utilized to assess viscous dissipation during a viscous deformation process.
In the upcoming section, we will delve into the fracture propagation process, with a particular focus on the inelastic zone surrounding the fracture process area near its tip. Within this zone, viscous deformations significantly impact viscoelastic deformation, establishing parallels to the concept of hysteresis.

2.2 Phenomenology of fracture in elastomers

To understand the fracture behavior of a material, it is necessary to analyze its general behavior (as in the previous section), and then focus on the phenomena that occur around the fracture tip. In figs. 2.8 (Yin et al. [2021] and Persson et al. [2005]), both authors delineate two distinct regions surrounding the crack tip. In the nearer region, denoted as fracture process zone (FPZ) from Yin et al. [2021], the released energy is a consequence

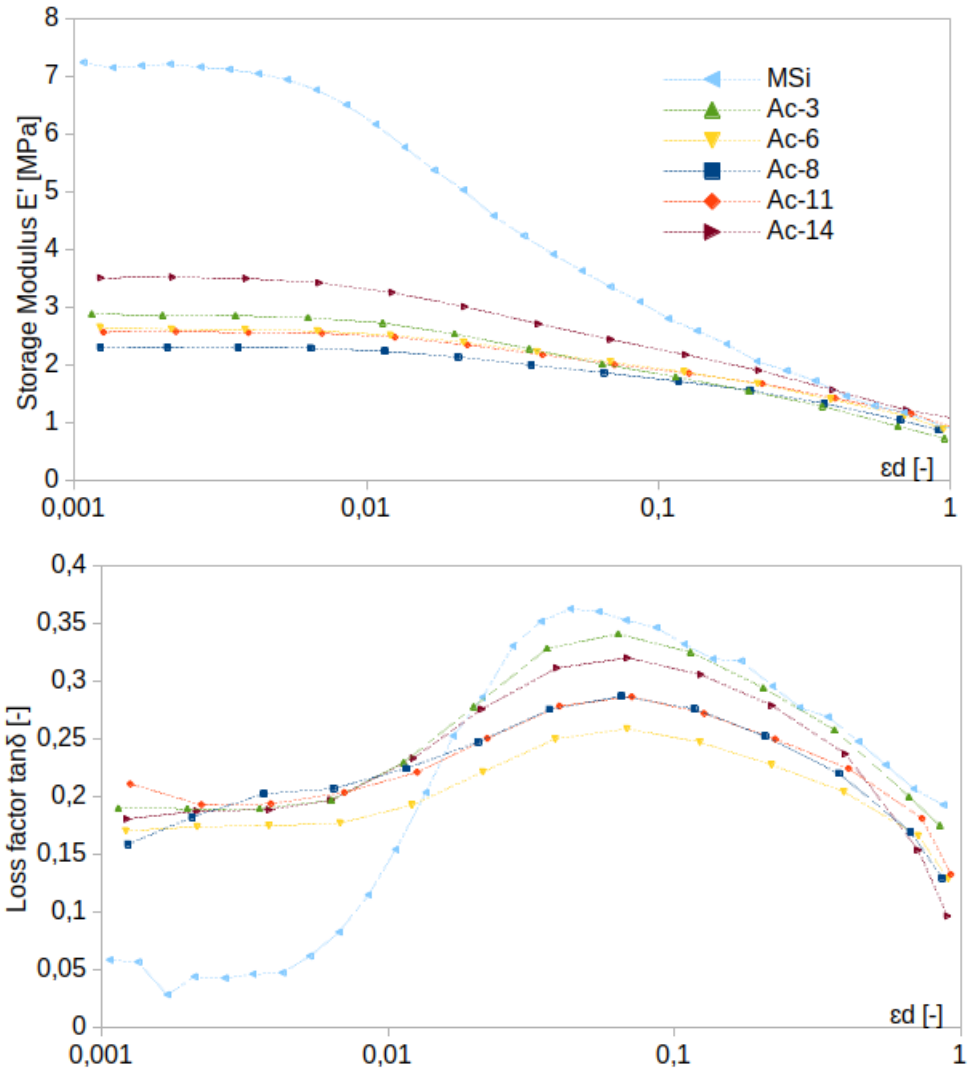

Figure 2.5: Example of Payne effect from Ramier et al. [2007] for SBR rubber with only silica filler (MPi) and different intensity of filler-matrix interface treatment (Ac-x). The storage modulus decreases with the amplitude of the dynamic maximum strain of a cycling load. The loss factor presents a peak and, after, it decreases.

of rupture phenomena (as cavitation and recrystallization in glassy micro-structure), whereas in the further region, energy is liberated due to viscoelastic deformations. In Persson et al. [2005], the total energy released per unit area during crack propagation is described as follows

$$G = G_0(1 + f(v, T)) \qquad \text{where} \qquad lim_{v \to 0} f(v, T) = 0, \tag{2.8}$$

where v is the crack tip velocity and G_0 represents the energy released for a quasi-static propagation. The energy released changes with the function $f(v, T)$, that is an increasing function of v and a decreasing function of the temperature as shown also in many works in literature. Furthermore, in Persson et al. [2005], the extent of the inelastic zone is correlated with both the peak frequency of the loss function (see fig. 2.3) and the velocity of crack propagation. A similar distinction is also addressed in Yin et al. [2021], where they divided the total work of fracture into the two contribution of essential

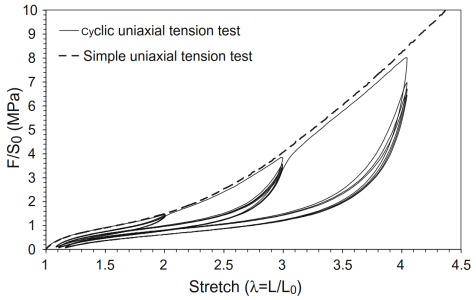

Figure 2.6: Example of Mullins' effect from the review Diani et al. [2009]

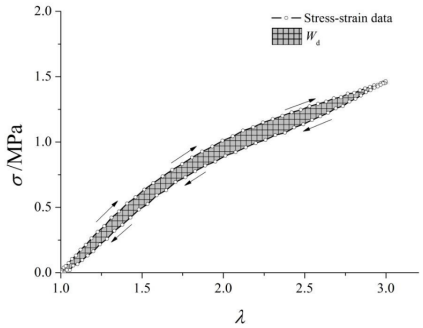

Figure 2.7: Viscous Hysteresis example from Baumard [2017] with the energy dissipated over the load-unload cycle.

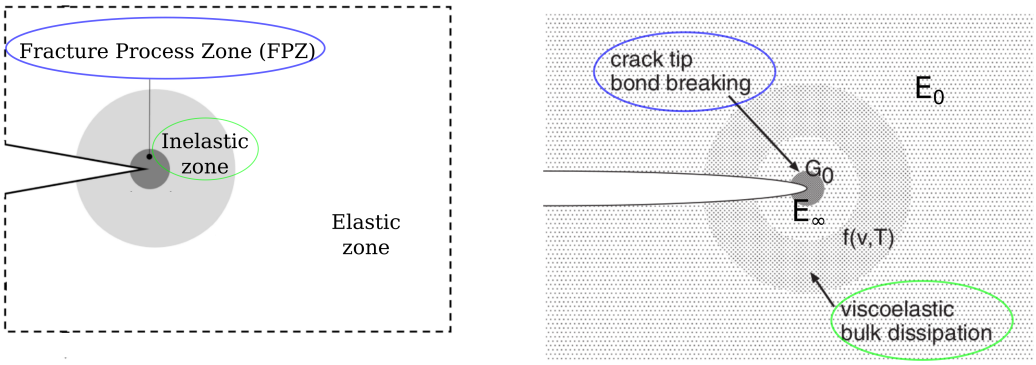

(a) crack tip in Yin et al. [2021]

(b) crack tip in Persson et al. [2005]

Figure 2.8: In this figure, both authors divide the energy dissipation at the crack tip into two distinct regions. The first region, depicted as the fracture process zone (dark grey), experiences dissipation primarily attributed to the fracture process and it can be assimilated to the cohesive zone of Knauss [2015]. In the inelastic zone, the predominant source of dissipation arises from viscous phenomena resulting from the significant deformations in the FPZ due to the crack propagation process.

work of fracture, expired by the FPZ and due to the fracture-related phenomena, and the non-essential fracture work expired by the inelastic zone and due to the viscoelastic dissipation. These considerations are done within the framework of fatigue analysis. Specifically, these two components of the work of fracture, are determined by testing double notched speciments, increasing the length of the incisions more and more, until the inelastic zones and, subsequently, the FPZs of the two tips overlap. The essential work is evaluated as the work required to break the specimens where the FPZs near to overlap, while the nonessential contribution as residual.

By analyzing the deformation state of the FPZ during the crack transition, it can be observed that an increase in deformations brings the deformation state into a high stretch regime (see stress hardening zone in fig. 2.2), leading to an increase in stiffness. A further rise in stiffness is attributed to the high strain rate condition (glassy region in fig. 2.3), wherein this increase predominantly affects the storage modulus. Concurrently, the loss modulus, which assesses effective viscous dissipation, tends to decrease. Dissipation at this stage will, therefore, primarily be attributed to the phenomena of rupture, as said before.

In contrast, beyond both the FPZ and the viscoelastic region, the stiffness resembles what seen in quasi-static loading conditions. This contrast in stiffness conditions is depicted in fig. 2.8b, with stiffness represented for simplicity by the Young modulus as in linear elasticity. This difference in deformation regimes also affects the parameter G as demonstrated in eqn. (2.8). This influence is mediated by the function $f(v,T)$ within the viscoelastic regime, serving to smooth the transition between E_0 and E_∞. In Persson et al. [2005], this relationship is employed to link energy release with the elastic modulus, akin to the crack criterion outlined by Griffith [1920], where the stress intensity factor (K) is expressed as follows

$$G = K^2/E \rightarrow \{\, G_0 = K^2/E_\infty\,;\; G_\infty = K^2/E_0 = G_0 E_\infty/E_0\,\}, \tag{2.9}$$

where G_0 is valid in the region close to the crack tip and G_∞ in the outer regions and E_∞ and E_0 are respectively the Young moduli of the FPZ and of the elastic zone (see fig.2.8b). It's worth emphasizing that the ratio E_∞/E_0 can also be on the order of 10^3. This significant difference in orders of magnitude highlights the crucial role of viscous dissipation phenomena in the energy dynamics during fracture propagation.
The intricate nature of material behavior necessitates a redefinition of energy dissipation (eqn. (2.8)), as outlined below

$$G(v,T) = G_0 \frac{s(v,T)}{s_0} \qquad \text{where} \qquad G_0 = G_0^* k(v,T),\; s_0 = s(0,T). \tag{2.10}$$

Where $s(v,T)$ represents the crack-tip radius for a crack propagating at velocity v and $k(v,T)$ accounts the variation of the stresses in the crack tip, that depends on the velocity of the deformation process.

The influence of the temperature and of the crack velocity into the energy released are summarized in figs. 2.10, where several rubber compounds give similar qualitative results. In particular it's clear that $G(v,T)$ is a increasing function of v and a decreasing function of T as expected.

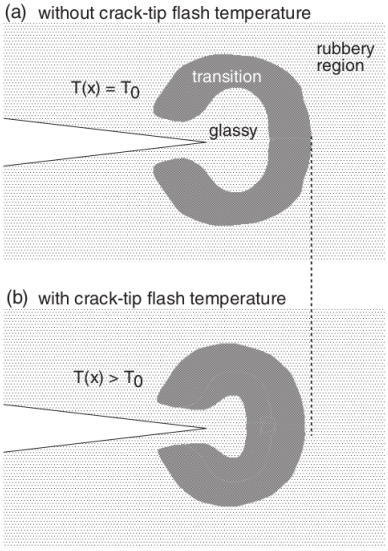

Figure 2.9: A qualitative picture of the effect of the flash temperature in Carbone and Persson [2005].

The temperature's impact can be notably pronounced in the immediate vicinity of the crack tip, where the energy liberated by the crack is converted into heat. In Carbone and Persson [2005] is shown that this phenomenon takes importance especially during high-velocity propagation. In this scenario, the flash temperature not only affects the elastic properties but also the crystalline microstructure of the rubber, as shown in fig. 2.9, where a slow crack propagation ((a), cold propagation regime) is compared with a fast propagation ((b), hot propagation regime). In the first case, the glassy region expands considerably, resulting in decreased viscoelastic dissipation, which primarily occurs within the transition region. Conversely, in the second case, the hot propagation reduces the size of the glassy region in favor of the transition region, which exhibits higher dissipation.

This glassy region appears in some kind of rubber (e.g. natural rubber) and it is due to the large strain regime, induced by the crack propagation. This crystallization

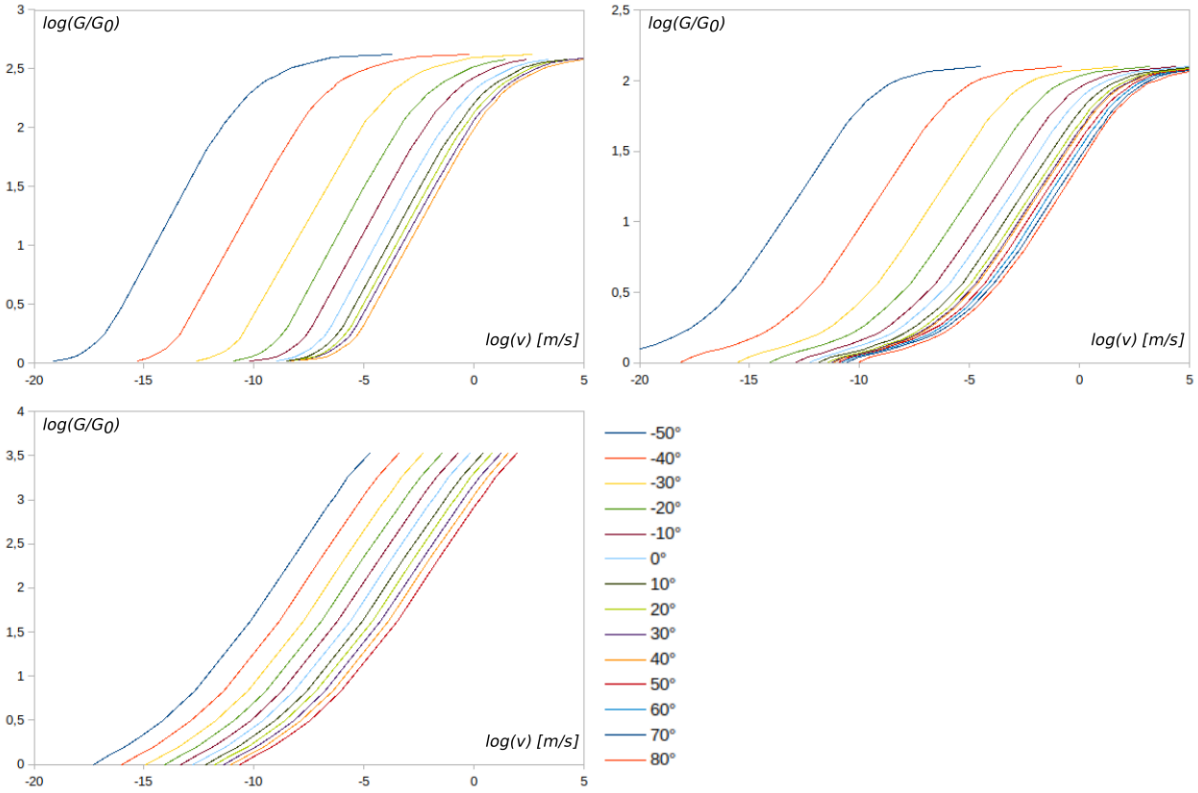

Figure 2.10: Influence of temperature and crack velocity into the dissipated energy for different rubbers from Persson et al. [2005]. In particular styrene–butadiene rubber without (up-left) and with carbon black filler (up-right), and for a pressure sensitive adhesive (PEHA-AA, on bottom).

enhances the rubber's wear resistance. Indeed, rubbers that do not undergo crystallization under extreme deformation, such as styrene-butadiene (SB), exhibit lower wear resistance compared to other materials.

This phenomenon is illustrated in fig. 2.12, which qualitatively depicts the bond-

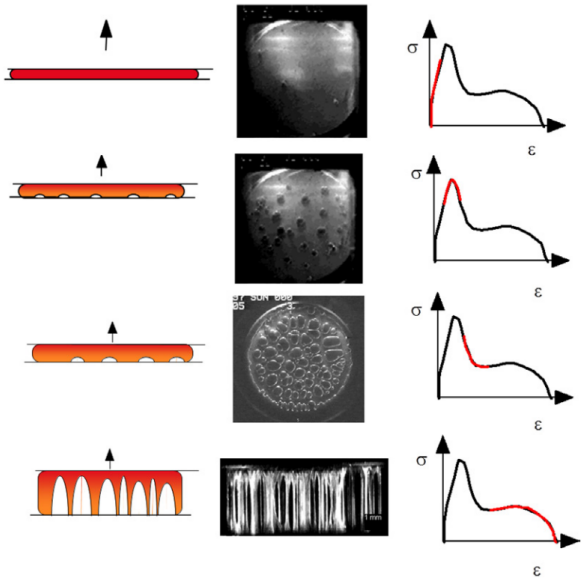

Figure 2.11: Cavitation phenomena become more conspicuous in instances of adhesive failure, as examined in Creton and Ciccotti [2016].

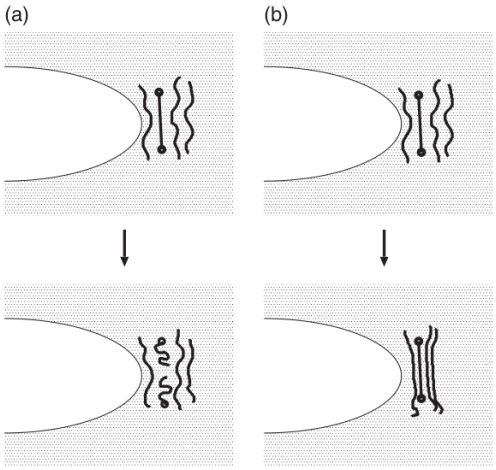

Figure 2.12: The bond-breaking process without(a) or with strain crystallization (Persson et al. [2005]).

breaking process in the presence of strain crystallization and in its absence. In this last case, due to the inhomogeneous characteristics of material, the various polymer chains at the crack tip will reach their breaking limits at different times. Indeed, in presence of strain crystallization, the chains near a fully stretched chain will adhere to it, reinforcing the weakest link. This leads to a significant increase in the average stress at the crack tip, which is crucial for initiating crack propagation. This rearrangement of macromolecules promotes the manifestation of cavitation, a phenomenon that holds exceptional importance, especially within adhesive applications, as extensively detailed in the work by Creton and Ciccotti [2016]. Cavitation, at its core, involves the formation of voids or empty spaces within the material. The presence of these voids is visually represented in fig. 2.11.

After this phenomenological analisys of the elastic, viscoelastic and fracture behavior, the focus moves on three experiments that are simulated during the formulation of the original models in chps. 3 and 4, where, using a phase field damage variable, these three experiments are studied.

2.3 Experiments

The experiments shown in this section concern two tensile tests are considered to describe the brittle behavior of rubber and the pseudo-ductile response of double-network elastomeric composites and the experimental set up and results of the experiments in Corre et al. [2020], where the dynamic of crack propagation in brittle elastomers is studied.

2.3.1 Tensile tests in double notches specimen (Hocine et al. [2002])

This first experiment is shown in Hocine et al. [2002] (see fig. 1.1) and it consists in a simple tensile test of a pre-etched sample. The experimental campaign was conducted using synthetic elastomers, specifically polybutadiene (PB) and styrene-butadiene rubber (SBR).

The elongation ratio (λ) was determined by measuring changes in the distance (l_0 in fig. 2.13) between two fine ink marks applied to the specimen's surface, to avoid errors arising from boundary effects. These elongation measurements were obtained through photographs taken during specimen loading. A camera connected to a thermal printer allowed for the instant recording of the deformed structure.

Fracture tests were carried out using the Double Edge Notch in Tension (DENT)

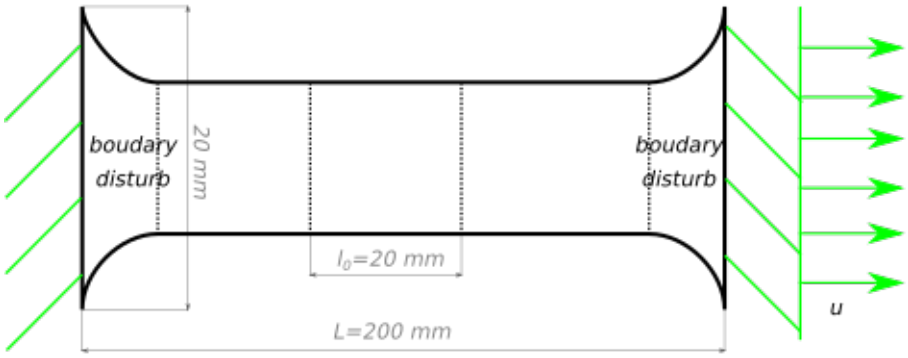

Figure 2.13: Tensile test specimen in Hocine et al. [2002].

geometry. Specimens, measuring 80 mm in width (w) and 200 mm in length (h), were created from a larger rubber sheet with a thickness of 3 mm for SBR and 4.5 mm for PB. Initial cracks were introduced using razor blades, with sizes ranging from 0 to 0.7, normalized by the ratio a/w (see 1.1). This paper presents also a dissipation analisys based on the J-integral, introduced by Rice [1968].

While these experiments may appear straightforward, they reveal intriguing phenomena due to the presence of highly irregular incisions and complex geometries at those locations, as shown by the circles in fig. 1.1, that denote the crack initiation points. For these reasons, this set of experiment has gained significant importance to the extent that it serves as a reference in works by Miehe and Schänzel [2014], where a phase field model of damage limited to brittle fracture is introduced, and in Talamini et al. [2018], where the elastic problem is approached from a more micro-mechanical perspective.

2.3.2 Tensile tests in double network elastomers (Millereau et al. [2018])

One of the most significant limitations associated with rubber materials is their propensity for brittle fracture behavior, which restricts their utility to strain levels considerably below their actual potential. In response to this challenge, extensive research has been conducted within the fields of chemical and materials engineering. One promising solution involves the utilization of multi-network elastomers, as explored in the study by Millereau et al. [2018]. A schematic representation of their fabrication process is illustrated in fig. 2.14. This process involves the integration of multiple networks at an intermediate pre-stretching value (λ_0) in the following manner: after the initial network is synthesized, it undergoes pre-deformation and is immersed in a solution containing a

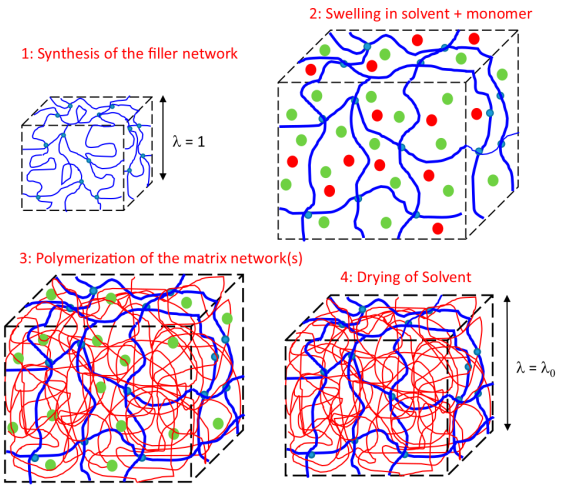

Figure 2.14: Integration of several networks at an intermediate pre-stretching (λ_0) occurs in the following manner: After the initial network is synthesized, it undergoes pre-deformation and is submerged in a solution containing a solvent and monomer, which subsequently polymerizes. Once the second elastomer has dried, the strains readjust, resulting in the attainment of a configuration with zero total stresses Millereau et al. [2018]).

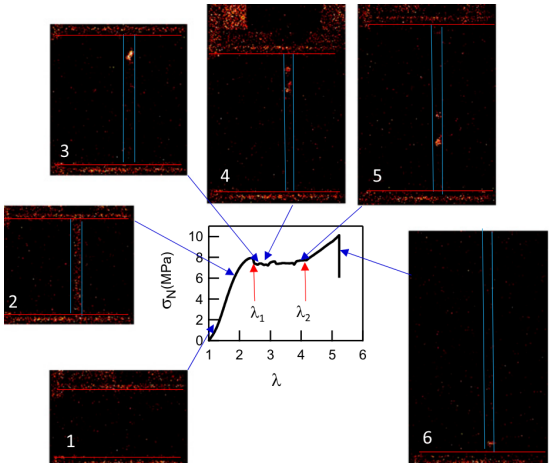

Figure 2.15: During a tension test on double network elastomers (Millereau et al. [2018]), the process of crack propagation unfolds (by the red mechano-luminescent signal). Following the initial elastic phase, a localized zone of damage emerges. As the test progresses, this damaged area spreads along the entire specimen with minimal alterations in stress levels. Subsequently, the material undergoes hardening until failure occurs.

solvent and monomer, which subsequently undergoes polymerization. Once the second elastomer has dried, the material's strains reconfigure, leading to the achievement of a state with zero total stresses. The mechanical characteristics of these materials exhibit a high degree of variability, contingent upon factors such as the composition of elastomer layers, their proportion, the presence of additional fillers and more. Notably, the material's pseudo-ductility in a simple tension test can vary, and fig. 2.15 provides a comprehensive illustration. Within this test, the process of crack propagation is evident through the red mechano-luminescent signal. After the initial elastic phase, a localized damage zone appears. As the test proceeds, this damaged area extends throughout the entire specimen with minimal changes in stress levels. Subsequently, the material undergoes a hardening process until it ultimately fails.In Millereau et al. [2018] , various other experiments involving different mixtures are documented. However, the experiment depicted in fig. 2.15 is selected for the model fitting in chp. 3 for two reasons. The first is the presence of the photographs of the damage evolution and the second one is the presence of both the damage onset phase (with the initial stress drop), the damage propagation phase (where the stress is constant) and the final stress hardening. For these reasons it is one of the most complex to reproduce.

Specifically, these advancements in technology underscore the necessity, from a modeling standpoint, for a comprehensive model capable of simulating brittle fracture phenomena (refer to fig. 1.1) even in scenarios involving significant geometric irregularities, and pseudo-ductile behavior, with the aim of accurately representing the behavior of double network elastomers.

2.3.3 Pure shear tests to determine crack tip speed in elastomeric membranes (Corre et al. [2020])

Following the establishment of the rate-independent model for pseudo-static simulations, the investigation into the failure of rubber materials will progress to a phase-field damage model that considers rate-dependent effects. This phase of the study will center on crack propagation, encompassing the interplay between viscoelasticity and fracture behavior. To achieve this goal, the experiment in Corre et al. [2020] (see fig. 1.3), made on a commercial polyurethane composed of toluene diisocyanate and polyether material, will be studied and reproduced. The experiments involve the use of "pure shear" specimens, commonly utilized for studying dynamic crack growth. These samples have the benefit of providing a means to derive an analytical expression for the energy release rate. Additionally, they offer a generous area characterized by a uniform strain field, enabling the continuous observation of crack growth in a steady state over a significant distance. These "pure shear" specimens are elongated and narrow pieces of material, with dimensions of $200 \times 40 \times 3$ mm^3. To prevent slippage during testing, they feature cylindrical bulges (diameter 15 mm) at the edges of their long sides, designed to fit into specialized grips. The "working area" of the specimens refers to the thin section between these bulges. The width-to-height ratio of the working area is 5, which satisfies pure shear conditions, meaning there is neither stretching nor compression in the width direction at the center of the specimen (Yeoh [2001]). The material itself is a commercial polyurethane composed of toluene diisocyanate and polyether. It is considered homogeneous, isotropic, and incompressible. The test procedure primarily involves the following three steps (see fig. 1.3 for a geometrical scheme of the experiment):

- Initially the specimen is stretched up to a specific value of λ_y. This stretch is executed at a very slow rate (20 mm/min) and is captured by a high-resolution, low-frequency camera (denoted as 'HR' in Figure 222). The camera offers a spatial resolution of approximately 0.04 mm per pixel and operates at a frame rate of 0.5 Hz.

- In the second phase, a crack is made in the center of the deformed specimen using a blade. This step is essentially instantaneous and is not rigorously documented.

- During the final phase, crack propagate, and its advancements are filmed by using a high-frequency camera (at 40000 Hz) with a relatively lower resolution (0.2 mm per pixel), denoted as 'HS' in fig. 1.3.

The article encompasses an examination of shear wave propagation attributed to the fracture's own propagation, alongside an analysis of energy components around the fracture tip using the J-integral method. This method highlights the negligible nature of the inertial energy component. Nonetheless, the most significant outcomes of Corre et al. [2020] for the present work, are visible in fig. 2.16, which displays the crack propagation velocity for various pre-stretch values throughout the evolution of the phenomena.

To describe such a behavior, it is required a model that can effectively integrate both viscoelastic and fracture components. The objective of the fourth chapter is to establish a model capable of capturing these characteristics and aligning with the experimental findings.

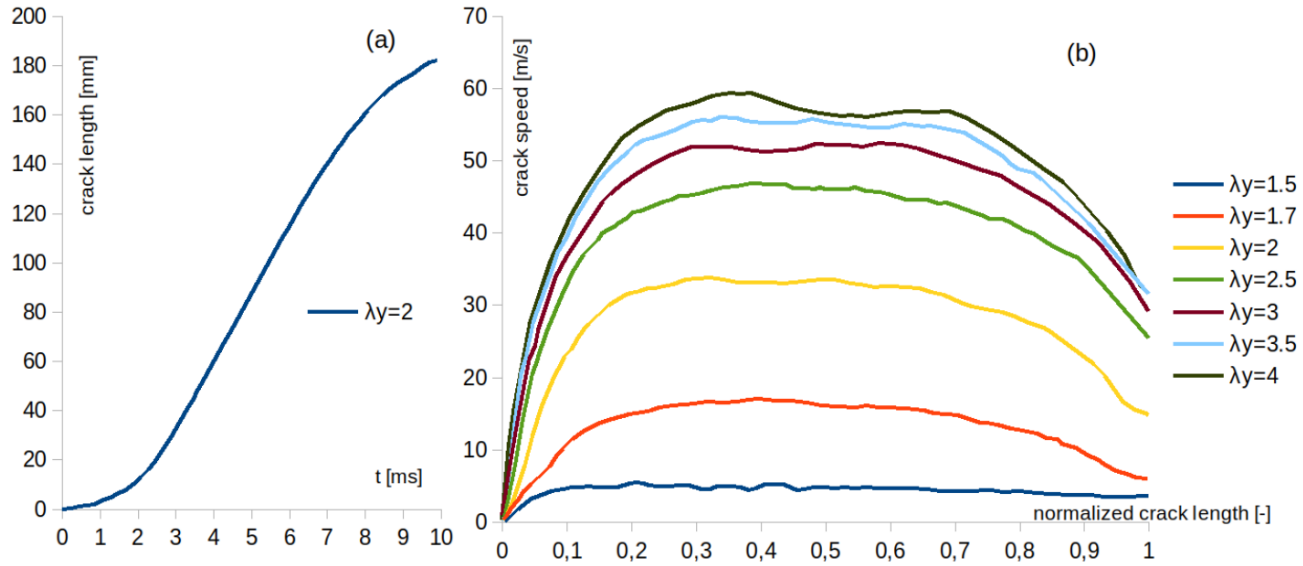

Figure 2.16: Results about crack propagation in Corre et al. [2020]. In particular in (a) the time evolution of crack length is shown for a pre-stretch of 2 and in (b) crack speed vs the crack length, normalized respect the total length of the sample, for different pre-stretches (λ_y).

2.4 Mechanics formulations

In this section, an overview of the models capable of describing the elastic and viscoelastic behavior of elastomers is presented. The overview begins with finite elasticity, including kinematic introduction, stress and energetic analysis, and the presentation of the main models in the literature. Following this examination, the focus shifts to viscoelastic formulations with thee main contribution to the formulation of a viscoelastic model (Reese and Govindjee [1998], Holzapfel [1996] and Kumar and Lopez-Pamies [2016]).

2.4.1 Finite elasticity

Kinematics

In the following, the kinematics ingredients of finite elasticity are presented. We consider a reference configuration (Ω_0) as the part of the three dimensional euclidean space occupied by the body under consideration at certain time instant $t = t_0$. In this configuration, the position vector is denoted by $\underline{X}$. The deformation function, denoted by $f(\underline{X})$, which maps points from the reference configuration to the current configuration Ω_t, will exhibit the following gradient

$$\mathbf{F} = \mathrm{Grad}(f(\underline{X})) = \frac{\partial f(\underline{X})}{\partial \underline{X}} = \frac{\partial \underline{x}}{\partial \underline{X}}; \qquad \mathbf{C} = \mathbf{F}^T\mathbf{F}; \qquad \mathbf{B} = \mathbf{F}\mathbf{F}^T, \tag{2.11}$$

where, by a slight abuse of notation, the points in the current configuration ($\underline{x}$) are treated as the map function ($f(\underline{X})$), while the right ($\mathbf{C}$) and left ($\mathbf{B}$) Cauchy-Green deformation tensors are defined in accordance with the polar decomposition theorem, as described in references such as Rubin [2020], Ogden [2003] or Gurtin [1982]. Drawing

from the same references, we can also refer to the following tensor definitions

$$\mathbf{L} = \text{grad}(\underline{\dot{x}}) = \frac{\partial \underline{\dot{x}}}{\partial \underline{x}} = \dot{\mathbf{F}}\mathbf{F}^{-1}; \quad \underbrace{\mathbf{D} = \text{sym}(\mathbf{L})}_{\text{stretch rate}}; \quad \underbrace{\mathbf{W} = \text{skw}(\mathbf{L})}_{\text{spin rate}}, \tag{2.12}$$

where, the time derivative of an element is indicated with a dot. In this equation, the gradient of velocity (with respect to the current configuration, distinct from eqn. (2.11)) is defined along with its symmetric and antisymmetric components. It's also useful to underline that only $\mathbf{D}$ represents the stretch rate, while $\mathbf{W}$ is only a rigid rotation velocity (spin rate).

Strain energy and stresses

Shifting our focus to the energy aspect of the problem, the strain energy density (ψ) can be expressed as a function of $\mathbf{C}$ according to frame invariance. In the case of an isotropic material, this dependency reduces to the invariants or eigenvalues of $\mathbf{C}$ alone, as it's done in eqn. (2.4). Stress tensors can be derived directly from strain energy density as it follows

$$\mathbf{P} = \frac{\partial \psi}{\partial \mathbf{F}}; \qquad \mathbf{S} = 2\frac{\partial \psi}{\partial \mathbf{C}}; \qquad \mathbf{T} = J^{-1}\mathbf{P}\mathbf{F}^T = J^{-1}\mathbf{F}\mathbf{S}\mathbf{F}^T, \tag{2.13}$$

where, $\mathbf{P}$ represents the first Piola-Kirchhoff stress tensor. When $\mathbf{P}$ is applied to a infinitesimal oriented surface of Ω_0 ($\mathrm{d}a_0\,\hat{n}_0$, where $\mathrm{d}a_0$ is the area extension and $\hat{n}_0$ is the normal area versor), it gives the surface forces vector in Ω_t ($\underline{t}_t = \mathbf{P}(\mathrm{d}a_0\,\hat{n}_0)$). Similarly, the second Piola stress tensor $\mathbf{S}$, can be applied to an infinitesimal oriented area in Ω_0 to obtain the surface forces vector in Ω_0 ($\underline{t}_0 = \mathbf{S}(\mathrm{d}a_0\,\hat{n}_0)$). In the same way, the Cauchy stress tensor $\mathbf{T}$ can be applied to an infinitesimal oriented area in Ω_t to obtain the surface forces vector in Ω_t ($\underline{t}_t = \mathbf{T}(\mathrm{d}a_t\,\hat{n}_t)$). Last term in eqn. (2.13) is $J = \det\mathbf{F}$. The third condition expressed in that equation, can be established by considering that vectors, such as stresses, can be transferred from the reference configuration ($\underline{t}_0$) to the current configuration ($\underline{t}_t$) through the application of $\mathbf{F}$ (with the inverse transformation achievable using $\mathbf{F}^{-1}$). In contrast, oriented area vectors undergo a transformation from the reference ($\mathrm{d}a_0\,\hat{n}_0$) to the current configuration ($\mathrm{d}a_t\,\hat{n}_t$) through the cofactor of $\mathbf{F}$, denoted as $J\mathbf{F}^{-T}$ (and the inverse transformation by $J^{-1}\mathbf{F}^T$). This perspective allows us to make the following assessments (where the extensions of the areas are omitted for brevity)

$$\mathbf{T}\hat{n}_t = \underline{t}_t, \text{ s. t. } \underbrace{J\mathbf{T}\mathbf{F}^{-T}}_{\mathbf{P}}\underbrace{J^{-1}\mathbf{F}^T\hat{n}_t}_{\hat{n}_0} = \underline{t}_t, \text{ s. t. } \underbrace{J\mathbf{F}^{-1}\mathbf{T}\mathbf{F}^{-T}}_{\mathbf{S}}\hat{n}_0 = \mathbf{F}^{-1}\underline{t}_t = \underline{t}_0\,. \tag{2.14}$$

The simpler way to define a strain energy density for an isotropic material is to establish a function that depends on the following orthogonal invariants of $\mathbf{C}$:

$$\begin{aligned} I_1 =& \text{tr}\mathbf{C} = \mathbf{F}\cdot\mathbf{F} = \lambda_1^2 + \lambda_2^2 + \lambda_3^2; \\ I_2 =& \frac{1}{2}(I_1^2 - \text{tr}(\mathbf{C}\mathbf{C})) = \lambda_2^2\lambda_3^2 + \lambda_1^2\lambda_2^2 + \lambda_1^2\lambda_3^2; \\ I_3 =& \det\mathbf{C} = J^2 = \lambda_1^2\lambda_2^2\lambda_3^2, \end{aligned} \tag{2.15}$$

where λ_i, with $i = 1;\ 2;\ 3$ are the eigenvalue of $\mathbf{F}$. Due to the significantly higher shear deformability compared to volumetric one, it is common practice to separate these two contributions, often disregarding the material's volumetric deformability. In such cases, one can express it as follows

$$\psi(I_1, I_2, J) = \psi^D(I_1, I_2) + \psi^V(J), \tag{2.16}$$

where ψ^D is the distorsional part of the strain energy density and ψ^V the volumetric. By this way, following eqn. (2.13), the first Piola-Kirchhoff stress tensor can be rewrite as

$$\mathbf{P} = \frac{\partial \psi^D}{\partial I_1}\frac{\partial I_1}{\partial \mathbf{F}} + \frac{\partial \psi^D}{\partial I_2}\frac{\partial I_2}{\partial \mathbf{F}} + \frac{\partial \psi^V}{\partial J}\frac{\partial J}{\partial \mathbf{F}} = r_1\mathbf{F} + r_2(I_1\mathbf{F} - \mathbf{F}\mathbf{C}) + pJ\mathbf{F}^{-T}, \tag{2.17}$$

where the stiffness coefficients $r_1 = \partial\psi/\partial I_1$, $r_2 = \partial\psi/\partial I_2$ and the hydrostatic pressure $p = \partial\psi/\partial J$. By the same procedure, also the second Piola stress tensor can be evaluated as

$$\mathbf{S} = r_1\mathbf{I} + r_2(I_1\mathbf{I} - \mathbf{C}) + pJ\mathbf{C}^{-1}. \tag{2.18}$$

Using eqns. (2.17) and (2.18), the third eqn. of (2.13) can be checked and it can be used to evaluate the Cauchy stress tensor as

$$\mathbf{T} = r_1 J^{-1}\mathbf{B} + r_2 J^{-1}(I_1\mathbf{B} - \mathbf{B}^2) + p\mathbf{I}. \tag{2.19}$$

From this concise introduction, it is evident that the selection of ψ dictates constitutive relation of the model. The subsequent section introduces a selection of the most frequently encountered finite elasticity models based also in the results presented in the review of Dal et al. [2021]. In this context, only the distorsional part ψ^D of the energy will be discussed.

Finite elastic models

The models presented in this study are phenomenological. Such models rely on mathematical expressions based on invariants or principal stretches for the free energy function, effectively matching stress-strain curves and other experimental observations. Although these models are restricted to describing the material's macroscopic behavior, as demonstrated in eqn. (2.4), they are typically derived from observations in statistical mechanics, as material behavior originates from its micro-mechanical structure.
One of the initial and most straightforward models is the neo-Hooke model, as shown in eqn. (2.4), which has been discussed previously. In this model, the parameters are set as $r_1 = \mu/2$ and $r_2 = 0$. As we further explore models that link the elastic energy density to the invariants of the right Cauchy-Green deformation tensor $\mathbf{C}$, one of the early proposals is presented in Rivlin [1948] (also called Mooney-Rivlin model). In this model, the energy is expressed as a function of the first two invariants, as follows

$$\psi^D = r_1(I_1 - 3) + r_2(I_2 - 3), \tag{2.20}$$

with constant r_1; r_2. In a simple shear test, as depicted in fig. 2.17, we use the deformation gradient tensor $\mathbf{F} = \mathbf{I} + k\hat{e}_1 \otimes \hat{e}_2$ where k represents the amount of shear, and $\hat{e}_i$ with $i = 1,\ 2,\ 3$ denote the canonical base components of $\mathbb{R}^3$. Employing eqn. (2.17) and considering the surface with $\hat{e}_2$ as the normal versor, the shear stress in the $\hat{e}_1$ direction is found to be a linear function of k, with r_2 representing the stiffness. Consequently, many models, such as those in Isihara et al. [1951] and Biderman [1958], which also take into account the invariant I_2, incorporate it linearly in the expression

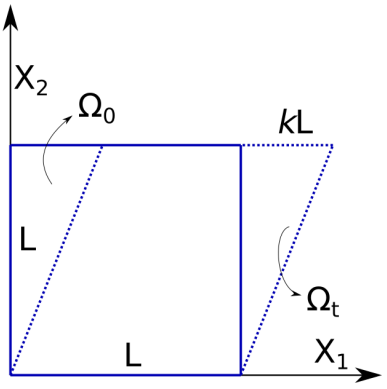

Figure 2.17: 2D Simple shear test.

for the elastic energy density

$$\psi^D = C_{10}(I_1 - 3) + C_{20}(I_1 - 3)^2 + C_{01}(I_2 - 3)^2 \qquad \text{Isihara et al. [1951]} \tag{2.21}$$

$$\psi^D = C_{10}(I_1 - 3) + C_{20}(I_1 - 3)^2 + C_{30}(I_1 - 3)^3 + C_{01}(I_2 - 3)^2 \qquad \text{Biderman [1958]} \tag{2.22}$$

This phenomenon is significant in a simple shear test but can be disregarded in other types of experiments. Furthermore, the neo-Hooke and Mooney-Rivlin models exhibit limitations at high levels of stretch.

Another approach for invariant-based phenomenological models involves formulating the strain energy density solely as a function of I_1. An intriguing model in this regard is the one proposed by Gent [1996], which incorporates the concept of chain extensibility limit (J_m). This model effectively simulates the material's behavior under high-stretch loading conditions through the following expression

$$\psi^D = \frac{\mu}{2} J_m \ln(1 - \frac{I_1 - 3}{J_m}), \qquad \text{s. t.} \qquad r_1 = \frac{\mu}{2} \frac{J_m}{J_m - (I_1 - 3)}. \tag{2.23}$$

It's clear that, for $I_1 - 3 \to 0$, indicating low levels of deformation, the stiffness $r_1 \to \mu/2$ as observed in the neo-Hooke model. However, as $I_1 - 3 \to J_m^-$, $r_1 \to \infty$ capturing the increasing stresses. This property allows the model to effectively simulate the material's behavior even under high levels of deformation. This approach for achieving asymptotic behavior at high deformations is also employed in other models, such as Gent and Thomas [1958], where the logarithm is applied to I_2, and in Pucci and Saccomandi [2002], where it is applied to both the invariants. However, this behavior can be also approximated with a polynomial function of I_1 as in Yeoh [1990]. One of the more general way to express the strain energy density as a polynomial function of I_1, is the Lopez-Pamies [2010] as it follows

$$\psi^D = \frac{3^{1-\alpha_i}}{2\alpha_i} \mu_i (I_1^{\alpha_i} - 3^{\alpha_i}). \tag{2.24}$$

These models prove to be highly versatile in capturing the characteristics of various materials, as evident in the comparisons between this model and Gent [1996] model in figs. 2.18 and 2.19. Notably, while the performance of both models is quite similar in the experiments presented in fig. 2.18, in fig. 2.19, the Lopez-Pamies [2010] model exhibits significantly superior performance (see fig. 2.19). This model is inspired by the model in Ogden [2003], where a model based on principal deformations is presented. While this method enhances its versatility in capturing the behavior of diverse materials, formulating the strain energy density in terms of principal stretches introduces greater complexity in both theoretical and numerical treatment. Indeed, while the eqns. in (2.17), (2.18), and (2.19) are adequate for calculating the stress tensors in the case of $\psi(I_1, I_2, J)$, when dealing with $\psi(\lambda_i)$, the determination of the first Piola tensor can be achieved through the following expression

$$\mathbf{P} = t_i \, \underline{b}_i \otimes \underline{c}_i, \qquad \text{with} \qquad t_i = \frac{\partial \psi}{\partial \lambda_i}, \tag{2.25}$$

where $\underline{c}_i$ and $\underline{b}_i$ are respectively the eigenvectors of $\mathbf{C}$ and $\mathbf{B}$, related to the eigenvalue λ_i. This expression of $\mathbf{P}$ implies the resolution of a eigenvalue problem and the determination

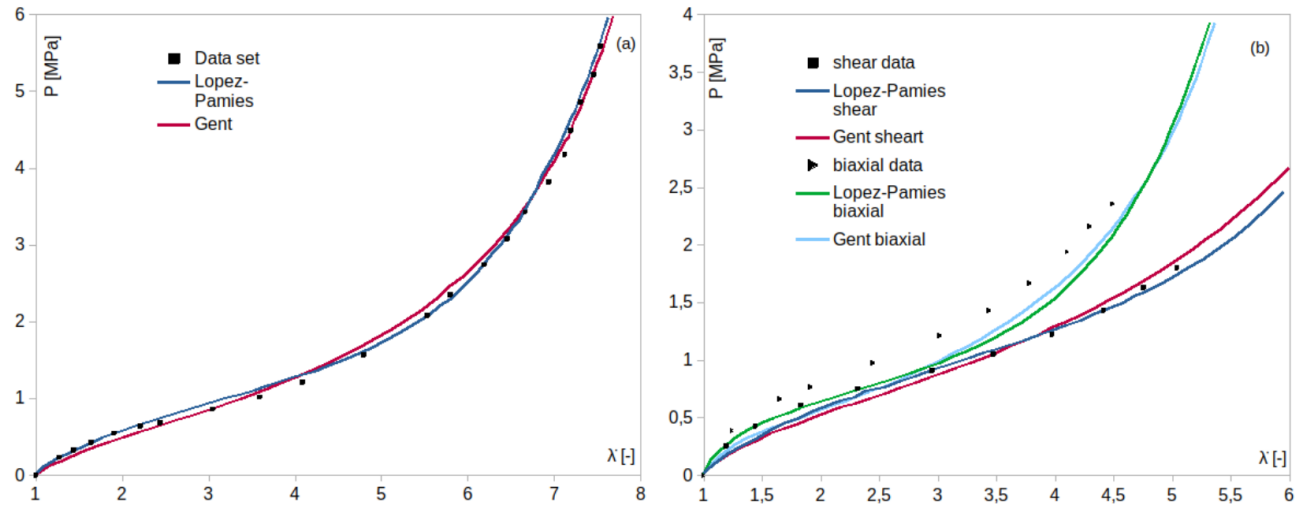

Figure 2.18: Lopez-Pamies [2010] and Gent [1996] models adapted to a vulcanized rubber behavior from the experiments of Treloar [1944]. In particular, uniaxial tension (a) and biaxial tension and pure shear (b) tests.

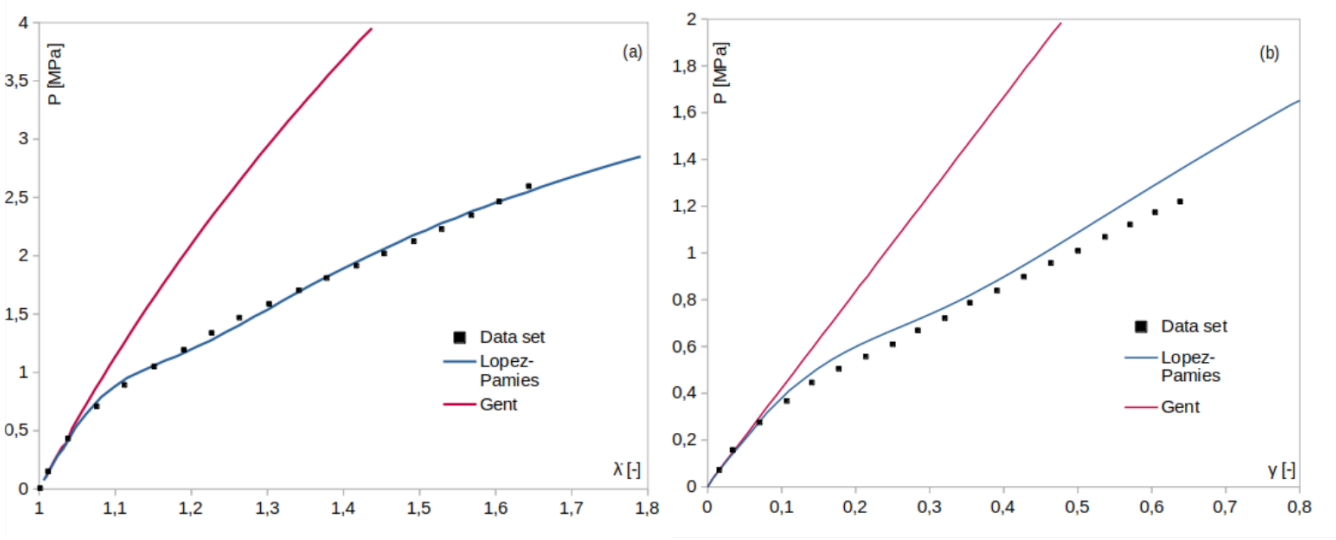

Figure 2.19: Lopez-Pamies [2010] and Gent [1996] models adapted to a commercial rubber behavior from Michelin in the experiments of Lahellec et al. [2004]. In particular, uniaxial tension (a) and simple shear (b) tests.

of the eigenvectors, thus the complexity of the problem increase significantly. In recent years, numerous models based on principal strains have been put forth, and a comprehensive review of this topic can be found in Dal et al. [2021]. In the model presented in chp. 3, the model in Ogden [2003] will be emploied (refer to fig. 2.20) to develop a rate-independent damage phase field model. In this model, the following form of strain energy density is proposed

$$\psi^D = \frac{\mu_i}{\alpha_i}(\lambda_1^{\alpha_i} + \lambda_2^{\alpha_i} + \lambda_3^{\alpha_i} - 3). \tag{2.26}$$

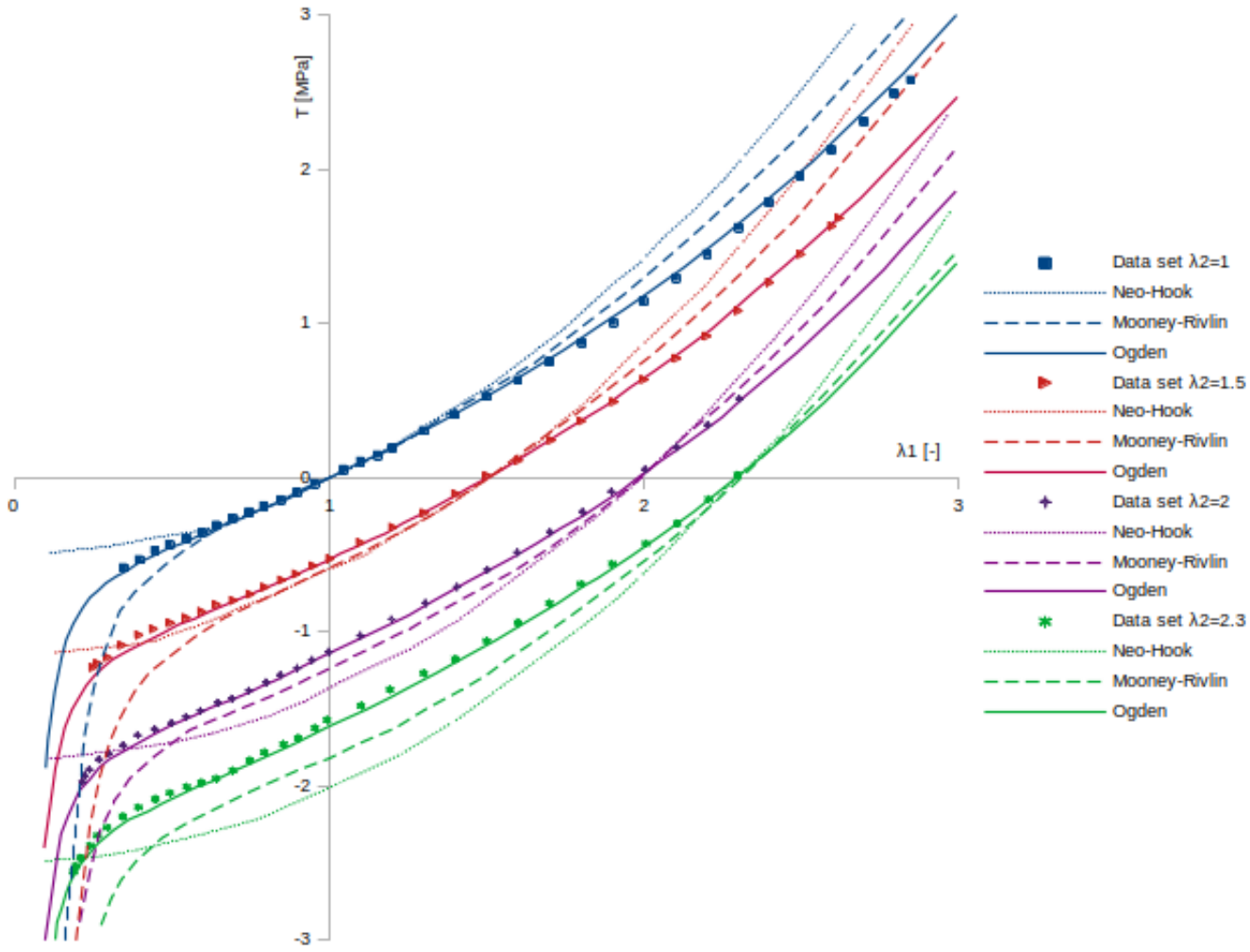

Figure 2.20: Experimental findings involve the assessment of vulcanized rubber in a uniaxial elongation test, where one principal direction experiences imposed deformation while the other remains unchanged. The x-axis represents strain in the principal direction, and the y-axis depicts the difference between the stresses in the two directions. The applied deformations are $\lambda_2 = 1$ (blue), $\lambda_2 = 1.5$ (red), $\lambda_2 = 2$ (violet), $\lambda_2 = 2.3$ (green). In dot lines the Neo-Hooke fit, in dash line the Mooney [1940] fit and in continuous line the Ogden [2003] fit.

Incompressibility constraint The impact of volumetric deformability on rubber tends to be insignificant when compared to shear deformability. To prevent computational issues related to locking and for the sake of convenience, it's common practice to enforce the condition $J = 1$ upfront and treat the pressure p as a Lagrangian multiplier, to be established through equilibrium equations outlined in Ogden [2003]. Under this approach, particularly when employing the strain energy formulation dependent on invariants, the resulting expression is as follows

$$\psi = \frac{\mu_i}{\alpha_i}(\lambda_1^{\alpha_i} + \lambda_2^{\alpha_i} + \lambda_3^{\alpha_i} - 3) - p(J-1). \tag{2.27}$$

Using this approach, the first Piola stress tensor becomes

$$\mathbf{P} = \frac{\partial \psi^D}{\partial \lambda_i} \hat{b}_i \otimes \hat{c}_i + pJ\mathbf{F}^{-T}, \tag{2.28}$$

where the summation symbol is omitted. The Cauchy stress tensor (considering $\mathbf{F} = \lambda_i \hat{b}_i \otimes \hat{c}_i$) becomes

$$\mathbf{T} = \frac{1}{J} \lambda_i \frac{\partial \psi^D}{\partial \lambda_i} \hat{b}_i \otimes \hat{b}_i + p\mathbf{I}, \tag{2.29}$$

from which the coaxiality of $\mathbf{B}$ and $\mathbf{T}$ is also evident. Referring back to the earlier discussion, the determination of hydrostatic pressure necessitates solving equilibrium equations and considering boundary conditions. Hypothesis of *2D plane stress* or *Uniaxial tension* allow to determine explicitly the reactive pressure p. These hypothesis are described in the following:

2D plane stress: This strain state pertains to a body where one of the three axes (typically the third) is considerably smaller compared to the other two, resulting in a strain state described as follows

$$\mathbf{F} = \lambda_1 \hat{e}_1 \otimes \hat{e}_1 + \lambda_2 \hat{e}_2 \otimes \hat{e}_2 + (\lambda_1 \lambda_2)^{-1} \hat{e}_3 \otimes \hat{e}_3, \tag{2.30}$$

where the versors $\hat{e}_i$ are the components of the canonical base of the three dimensional euclidean space. In this stress state, when the surface with normal $\hat{e}_3$ is considered unloaded, the component of Cauchy stress tensor $\mathbf{T}_{33} = 0$, leading to the determination of the hydrostatic pressure as

$$p = -\frac{\lambda_i}{J} \left[\frac{\partial \psi^D}{\partial \lambda_i} \hat{b}_i \otimes \hat{b}_i \right] \cdot (\hat{e}_3 \otimes \hat{e}_3) = -\frac{\lambda_3}{J} \frac{\partial \psi^D}{\partial \lambda_3} \tag{2.31}$$

that, for the model in Ogden [2003] and recalling $J = 1$, it becomes

$$p = -\mu_i \lambda_3^{\alpha_i} = -\mu_i (\lambda_1 \lambda_2)^{-\alpha_i}, \tag{2.32}$$

thus, from eqn. (2.31)

$$\mathbf{T} = \lambda_i \frac{\partial \psi^D}{\partial \lambda_i} \hat{b}_i \otimes \hat{b}_i - \lambda_3 \frac{\partial \psi^D}{\partial \lambda_3} \mathbf{I}, \tag{2.33}$$

Where $\mathbf{I}$ is the second order identity tensor. Considering now the strain energy density as

$$\psi(\lambda_1, \lambda_2, \lambda_3) = \psi(\lambda_1, \lambda_2, (\lambda_1 \lambda_2)^{-1}) = \hat{\psi}^D(\lambda_1, \lambda_2) + \hat{\psi}^V((\lambda_1, \lambda_2)^{-1}) = \hat{\psi}(\lambda_1, \lambda_2), \tag{2.34}$$

the evaluation of the in-plane submatrix $\overline{\mathbf{P}}$ and $\overline{\mathbf{T}}$ (where the third row and column of $\mathbf{P}$ and $\mathbf{T}$ are omitted) become

$$\begin{aligned} \overline{\mathbf{P}} =& \frac{\partial \hat{\psi}^D}{\partial \lambda_1} \hat{b}_1 \otimes \hat{c}_1 + \frac{\partial \hat{\psi}^D}{\partial \lambda_2} \hat{b}_2 \otimes \hat{c}_2 + \frac{\partial \hat{\psi}^V}{\partial ((\lambda_1 \lambda_2)^{-1})} \frac{\partial ((\lambda_1 \lambda_2)^{-1})}{\partial (\lambda_1 \lambda_2)} \frac{\partial (\lambda_1 \lambda_2)}{\partial \overline{\mathbf{F}}} \\ =& \underbrace{\frac{\partial \hat{\psi}^D}{\partial \lambda_1} \hat{b}_1 \otimes \hat{c}_1 + \frac{\partial \hat{\psi}^D}{\partial \lambda_2} \hat{b}_2 \otimes \hat{c}_2}_{\partial \psi^D / \partial \overline{\mathbf{F}}} + \underbrace{(-\frac{\partial \hat{\psi}^V}{\partial ((\lambda_1 \lambda_2)^{-1})})(\lambda_1 \lambda_2)^{-1}}_{p} \overline{\mathbf{F}}^{-T} \end{aligned} \tag{2.35}$$

$$\overline{\mathbf{T}} = \lambda_1 \frac{\partial \hat{\psi}^D}{\partial \lambda_1} \hat{b}_1 \otimes \hat{b}_1 + \lambda_2 \frac{\partial \hat{\psi}^D}{\partial \lambda_2} \hat{b}_2 \otimes \hat{b}_2 + \frac{\partial \hat{\psi}(\lambda_3)}{\partial \lambda_3} \lambda_3 \mathbf{I} = \frac{\partial \hat{\psi}(\lambda_1, \lambda_2)}{\partial \overline{\mathbf{F}}} \overline{\mathbf{F}}^T,$$

where the overline notation on matrices indicates the in-plane submatrix obtained by excluding the third row and column. The determinant of $\overline{\mathbf{F}}$ is denoted as $\det\overline{\mathbf{F}} = \lambda_3 = (\lambda_1\lambda_2)^{-1} = \overline{J}$, and this substitution is applied multiple times. Employing this approach yields results consistent with those obtained in three dimensions, effectively allowing the projection of the 3D problem onto a 2D plane. A similar process can be implemented for $\psi^D(I_1, I_2)$ or under uniaxial tensile loading conditions, as outlined in the subsequent paragraph.

Uniaxial stress condition This load condition considers a body where one of the three length (normally $\hat{e}_1$ is so higher than the others two. In this case $\mathbf{F} = \lambda\hat{e}_1 \otimes \hat{e}_1 + (\lambda_1)^{-1/2}(\hat{e}_2 \otimes \hat{e}_2 + \hat{e}_3 \otimes \hat{e}_3)$, where the axial deformation is renamed $\lambda_1 = \lambda$, and the stress components $\mathbf{T}_{33} = \mathbf{T}_{22} = 0$. From which

$$p = \lambda^{-1/2}\frac{\partial\psi^D(\lambda_1, \lambda_2, \lambda_3)}{\partial\lambda_2}, \tag{2.36}$$

where λ_2 and λ_3 can be substitute with $\lambda^{-1/2}$. According to the previous rewriting of the strain energy density, the first components of the stress tensors can be evaluated as

$$\begin{aligned} P =& \frac{\partial\hat{\psi}^D}{\partial\lambda} + \frac{\partial 2\hat{\psi}^V}{\partial(\lambda^{-1/2})}\frac{\partial\lambda^{-1/2}}{\partial\lambda} = \frac{\partial\hat{\psi}^D}{\partial\lambda} - \frac{\partial 2\hat{\psi}^V}{\partial(\lambda^{-1/2})}\lambda^{-3/2} \\ T =& \lambda\frac{\partial\hat{\psi}^D}{\partial\lambda} - \frac{\partial 2\hat{\psi}^V}{\partial(\lambda^{-1/2})}\lambda^{-1/2} = \frac{\partial\hat{\psi}(\lambda)}{\partial\lambda}\lambda, \end{aligned} \tag{2.37}$$

whit the same conclusion of the previous paragraph.

2.4.2 Finite viscoelasticity

Kinematics

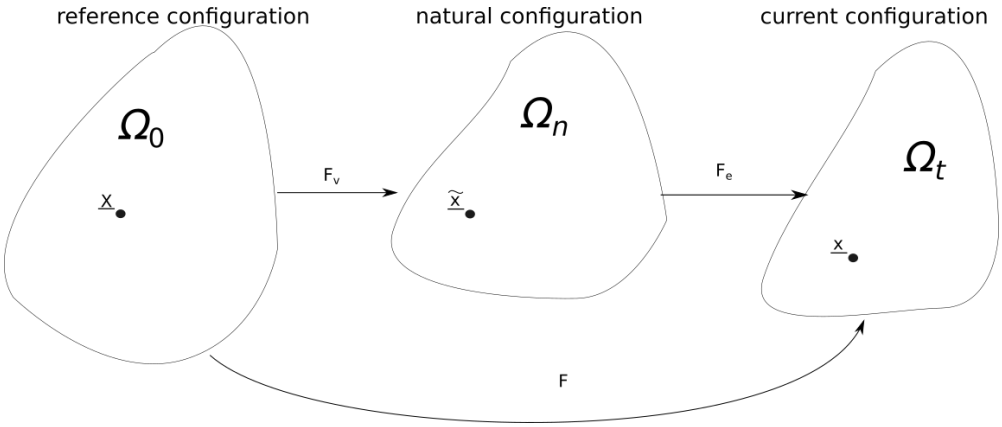

Figure 2.21: Decomposition of total deformation ($\mathbf{F}$) in viscous ($\mathbf{F}_v$) and elastic ($\mathbf{F}_e$) deformation. This decomposition, used by Lee [1964] in the context of elastoplasticity, was used in Sidoroff [1974] for the non linear viscoelasticity.

In this study, the multiplicative strain decomposition in fig. 2.21 (also employed in Reese and Govindjee [1998], Holzapfel [1996], Kumar and Lopez-Pamies [2016], Sidoroff [1974] and others), is utilized. This decomposition postulates the existence of an intermediate body configuration known as the 'natural configuration' (Ω_n), which represents

the state of the body deformed only by the viscous component of deformation ($\mathbf{F}_v$). The overall deformation is subsequently described as the combination of the viscous and elastic deformations ($\mathbf{F}_e$), expressed as $\mathbf{F} = \mathbf{F}_e\mathbf{F}_v$. The definition of this intermediate configuration changes the kinematic of the problem and, in order to consider as internal variable the displacement $\underline{u} = \underline{X} - \underline{x}$ and the viscous deformation $\mathbf{F}_v$, the elastic part of deformation can be write as

$$\mathbf{F} = \mathbf{F}_e\mathbf{F}_v, \quad \text{s.t.} \quad \mathbf{F}_e = \mathbf{F}\mathbf{F}_v^{-1}. \tag{2.38}$$

In addition, the right and the left Cauchy strain tensors become

$$\mathbf{C} = \mathbf{F}_v^T\mathbf{C}_e\mathbf{F}_v, \text{ s.t. } \mathbf{C}_e = \mathbf{F}_v^{-T}\mathbf{C}\mathbf{F}_v^{-1}; \qquad \mathbf{B}_e = (\mathbf{F}\mathbf{F}_v^{-1})(\mathbf{F}_v^{-T}\mathbf{F}^T) = \mathbf{F}\mathbf{C}_v^{-1}\mathbf{F}^T. \tag{2.39}$$

Following the same idea, the velocity gradients becomes

$$\mathbf{L} = \dot{\mathbf{F}}_e\mathbf{F}_e^{-1} + \mathbf{F}_e\dot{\mathbf{F}}_v\mathbf{F}_v^{-1}\mathbf{F}_e^{-1} = \mathbf{L}_e + \mathbf{F}_e\mathbf{L}_v\mathbf{F}_e^{-1}, \text{ s.t. } \mathbf{L}_e = \mathbf{L} - \mathbf{F}\mathbf{F}_v^{-1}\mathbf{L}_v\mathbf{F}_v\mathbf{F}^{-1}. \tag{2.40}$$

For what concerns the symmetric part of the velocity gradient, the first observation that can be don is

$$\dot{\mathbf{C}} = \dot{\mathbf{F}}^T\mathbf{F} + \mathbf{F}^T\dot{\mathbf{F}} = \mathbf{F}^T(\mathbf{F}^{-T}\dot{\mathbf{F}}^T + \dot{\mathbf{F}}\mathbf{F}^{-1})\mathbf{F} = 2\mathbf{F}^T\mathbf{D}\mathbf{F}, \tag{2.41}$$

and, by the same way

$$\dot{\mathbf{C}}_v = 2\mathbf{F}_v^T\mathbf{D}_v\mathbf{F}_v. \tag{2.42}$$

For what concerns $\dot{\mathbf{C}}_e$, using eqn. (2.39) and $\mathbf{0} = \dot{\overline{\mathbf{F}_v\mathbf{F}_v^{-1}}}$ such that $\dot{\overline{\mathbf{F}_v^{-1}}} = -\mathbf{F}_v^{-1}\mathbf{L}_v$, it can be write as

$$\begin{aligned}\dot{\mathbf{C}}_e &= -\mathbf{L}_v^T\mathbf{F}_v^{-T}\mathbf{C}\mathbf{F}_v^{-1} - \mathbf{F}_v^{-T}\mathbf{C}\mathbf{F}_v^{-1}\mathbf{L}_v + \mathbf{F}_v^{-T}(2\mathbf{F}^T\mathbf{D}\mathbf{F})\mathbf{F}_v^{-1} \\ &= 2\mathbf{F}_e^T\mathbf{D}\mathbf{F}_e - 2\text{sym}(\mathbf{C}_e\mathbf{L}_v) \\ &= \mathbf{F}_v^{-T}\dot{\mathbf{C}}\mathbf{F}_v^{-1} - 2\text{sym}(\mathbf{F}_v^{-T}\mathbf{C}\mathbf{F}_v^{-1}\mathbf{L}_v),\end{aligned} \tag{2.43}$$

and, to evaluate $\mathbf{D}_e$, both eqns. (2.43) and (2.40) can be used to derive

$$\mathbf{D}_e = \mathbf{D} - \text{sym}(\mathbf{F}_e\mathbf{L}_v\mathbf{F}_e^{-1}) = \mathbf{D} - \text{sym}(\mathbf{F}\mathbf{F}_v^{-1}\mathbf{L}_v\mathbf{F}_v\mathbf{F}^{-1}). \tag{2.44}$$

Following this kinematic overview, based on fig. 2.21, the subsequent sections will provide an introduction to viscoelastic models found in literature. The discussion will commence with an exploration of the linear viscoelastic model described in Reese and Govindjee [1998]. Subsequently, we will delve into the model presented by Holzapfel [1996], which includes a specific analysis of volumetric deformation. Finally, the presentation will conclude with a discussion of the model outlined in Kumar and Lopez-Pamies [2016], which offers a generalized extension of the linear model proposed by Reese and Govindjee [1998].

Viscoelastic model

In this model, the generalization of the Maxwell rheological model in fig. 2.22 is applied to the decomposition in 2.21. In this model, an "equilibrium spring" (associated with the total deformation $\mathbf{F}$) is connected in parallel with a "non-equilibrium" system. This system consists of a "non-equilibrium" spring (associated with the elastic deformation $\mathbf{F}_e$) in series with a dash-pot (related to the velocity of viscous deformation $\mathbf{L}_v$). In the work presented by Reese and Govindjee [1998], the presence of numerous "non-equilibrium"

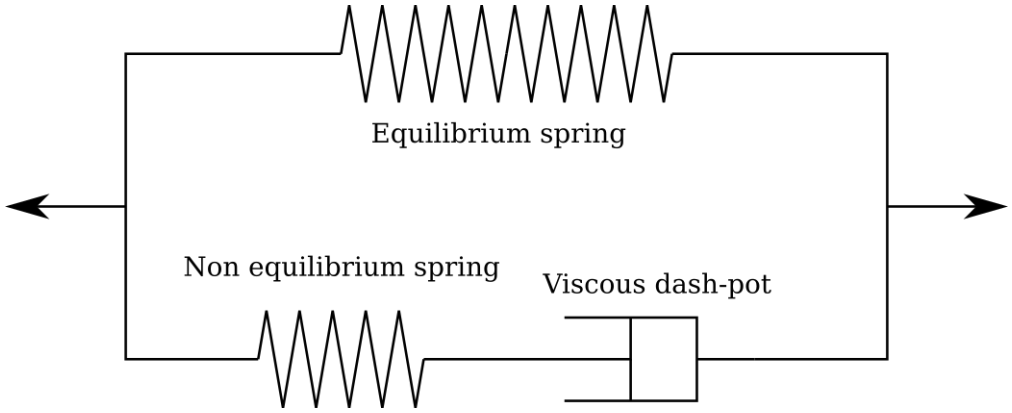

Figure 2.22: Maxwell rheological model used in Reese and Govindjee [1998] and Kumar and Lopez-Pamies [2016].In this model, an "equilibrium spring" (associated with the total deformation $\mathbf{F}$ in fig. 2.21) is connected in parallel with a "non-equilibrium" system. This system consists of a "non-equilibrium" spring (associated with the elastic deformation $\mathbf{F}_e$) in series with a dash-pot (related to the velocity of viscous deformation $\mathbf{L}_v$).

systems are examined. However, for the sake of simplicity, we will focus on just one system in this context. Within this system, the constitutive relationships associated with the dash-pots are treated as linear. The total elastic strain energy density can be expressed as follows

$$\psi(\mathbf{C}, \mathbf{F}_v) = \psi_{eq}(\mathbf{C}) + \psi_{neq}(\mathbf{C}_e(\mathbf{C}, \mathbf{F}_v)) = \psi_{eq}(\mathbf{C}) + \psi_{neq}(\mathbf{F}_v^{-T}\mathbf{C}\mathbf{F}_v^{-1}), \tag{2.45}$$

where, we make use of eqn. (2.39). By employing the expressions for $\dot{\mathbf{C}}_e$ in eqn. (2.43) and taking advantage of the symmetry of the second Piola stress tensor, we can evaluate the rate of strain energy density as follows

$$\dot{\psi} = (\frac{\partial \psi_{eq}}{\partial \mathbf{C}} + \mathbf{F}_v^{-1}\frac{\partial \psi_{neq}}{\partial \mathbf{C}_e}\mathbf{F}_v^{-T}) \cdot \dot{\mathbf{C}} - 2\frac{\partial \psi_{neq}}{\partial \mathbf{C}_e} \cdot \mathbf{C}_e\mathbf{L}_v, \tag{2.46}$$

where, for the sake of brevity, the explicit mention of the dependencies of the energy terms are omitted. Using this form of $\dot{\psi}$, the Clasius-Duhem inequality can be evaluated as

$$0 \leq \frac{1}{2}\mathbf{S} \cdot \dot{\mathbf{C}} - \dot{\psi} = (\frac{1}{2}\mathbf{S} - \frac{\partial \psi_{eq}}{\partial \mathbf{C}} - \mathbf{F}_v^{-1}\frac{\partial \psi_{neq}}{\partial \mathbf{C}_e}\mathbf{F}_v^{-T}) \cdot \dot{\mathbf{C}} + 2\mathbf{C}_e\frac{\partial \psi_{neq}}{\partial \mathbf{C}_e} \cdot \mathbf{L}_v. \tag{2.47}$$

From the last equation, the second Piola stress tensor is determined as follows

$$\mathbf{S} = 2\frac{\partial \psi_{eq}}{\partial \mathbf{C}} + 2\mathbf{F}_v^{-1}\frac{\partial \psi_{neq}}{\partial \mathbf{C}_e}\mathbf{F}_v^{-T} = \mathbf{S}_{eq} + \mathbf{F}_v^{-1}\hat{\mathbf{S}}_{neq}\mathbf{F}_v^{-T} = \mathbf{S}_{eq} + \mathbf{S}_{neq}, \tag{2.48}$$

where $\hat{\mathbf{S}}_{neq}$ serves as a connector between the surface normal and stress vectors within the domain Ω_n functioning as a second Piola stress tensor. When we apply $\mathbf{F}_v^{-T}$ to the normal vectors and $\mathbf{F}_v^{-1}$ to the stress vectors, they are transformed to the reference configuration vectors. The second part of eqn. (2.47) gives

$$\hat{\mathbf{S}}_{neq} \cdot \mathbf{F}_e^T\mathbf{F}_e\mathbf{L}_v = \mathbf{F}_e\hat{\mathbf{S}}_{neq}\mathbf{F}_e^T \cdot \mathbf{F}_e\mathbf{L}_v(\mathbf{F}_e^T\mathbf{F}_e^{-T})\mathbf{F}_e^{-1} = J_e\mathbf{T}_{neq}\mathbf{B}_e^{-1} \cdot \mathbf{F}_e\mathbf{L}_v\mathbf{F}_e^T \geq 0, \tag{2.49}$$

where $\mathbf{T}_{neq} = \mathbf{F}_e\hat{\mathbf{S}}_{neq}\mathbf{F}_e^T$ is used. In order to agree with last inequality, the following form of the non equilibrium Cauchy stress tensor $\mathbf{T}_{neq}$ is defined

$$\mathbb{V}^{-1}[\mathbf{T}_{neq}] = \frac{1}{2}\mathbf{F}_e\mathbf{L}_v\mathbf{F}_e^{-1}, \tag{2.50}$$

where $\mathbb{V}$ is a linear fourth order tensor that can be expressed as follows

$$\mathbb{V}^{-1} = \frac{1}{2\eta_D}(\mathbb{I} - \frac{1}{3}\mathbf{I}\otimes\mathbf{I}) + \frac{1}{9\eta_V}\mathbf{I}\otimes\mathbf{I} = \frac{1}{2\eta_D}\mathbb{D} + \frac{1}{3\eta_V}\mathbb{J}, \tag{2.51}$$

where $\mathbb{J}$ is a fourth order tensor that gives the spherical part of a second order tensor, $\mathbb{I}$ is the identity fourth order tensor and, thus, $\mathbb{D} = \mathbb{I} - \mathbb{J}$ gives the deviatoric part of a second order tensor. For these reasons, $\eta_D;\ \eta_V \geq 0$ are the viscous coefficients related to the deviatoric and the spherical part of the stresses. By this definition, eqn. (2.50) can be rewritten as

$$\mathbf{F}_e\mathbf{L}_v\mathbf{F}_e^{-1} = \frac{1}{\eta_D}\mathbb{D}[\mathbf{T}_{neq}] + \frac{2}{3\eta_V}\mathbb{J}[\mathbf{T}_{neq}]. \tag{2.52}$$

The inversion of this relation can be done as

$$\mathbf{T}_{neq} = \eta_D\mathbb{D}[\mathbf{F}_e\mathbf{L}_v\mathbf{F}_e^{-1}] + \frac{3\eta_V}{2}\mathbb{J}[\mathbf{F}_e\mathbf{L}_v\mathbf{F}_e^{-1}] = \eta_D[\mathbf{F}_e\mathbf{L}_v\mathbf{F}_e^{-1} - \frac{1}{3}\mathbf{D}_v\cdot\mathbf{I}] + \frac{\eta_V}{2}\mathbf{D}_v\cdot\mathbf{I}. \tag{2.53}$$

Further insights can be gleaned by focusing on linearized scenarios. The initial linearization revolves around the assumption that $\mathbf{B}_e \approx \mathbf{I}$. This condition means that the non-equilibrium spring in fig. 2.22 is near the zero stresses condition and it implies $\mathbf{C} \approx \mathbf{C}_v$. This implies that the non-equilibrium spring in fig. (2.22) is close to a state of zero stresses, indicating that $\mathbf{C} \approx \mathbf{C}_v$ that means that the total deformation is predominantly absorbed by the dash-pot, or in simpler terms, the non-equilibrium system is discharging. Consequently, these conditions correspond to cases of slow deformation, as elaborated in sect. (2.1). The smallness of the elastic deformation allows to approximate the non equilibrium spring behavior as neo-Hooke (eqn. (2.4)) as shown in Fig. 2.2 for low strain regime, through which (for an incompressible material)

$$\mathbf{T}_{neq} = 2\mathbf{F}_e\frac{\partial[(\mu_e/2)(\mathbf{C}_e\cdot\mathbf{I}-3)]}{\partial\mathbf{C}_e}\mathbf{F}_e^T + p_{neq}\mathbf{I} = \mu_e\mathbf{B}_e + p_{neq}\mathbf{I}, \tag{2.54}$$

where $J_e^{-1}\mathbf{F}_e\hat{\mathbf{S}}_{neq}\mathbf{F}_e^T = \mathbf{T}_{neq}$ is used. In an incompressible material $\mathbf{F}_e\mathbf{L}_v\mathbf{F}_e^{-1}\cdot\mathbf{I} = \mathbf{L}_v\cdot\mathbf{I} = 0$ from which $\mathrm{dev}\mathbf{L}_v = \mathbf{L}_v$, thus eqn. (2.52) becomes

$$\mathbf{F}_e\mathbf{L}_v\mathbf{F}_e^{-1} = \mathrm{dev}\mathbf{T}_{neq} = \frac{1}{\eta_D}\mu_e(\mathbf{B}_e - \frac{1}{3}(\mathbf{F}_e\mathbf{F}_e^T\cdot\mathbf{I})\,\mathbf{I}),\ \text{from which}\quad \mathbf{L}_v = \frac{\mu_e}{\eta_D}(\mathbf{C}_e - \frac{1}{3}(\mathbf{C}_e\cdot\mathbf{I})\,\mathbf{I}) \tag{2.55}$$

that, for the symmetry of $\mathbf{C}_e$ and eqn. (2.41), becomes

$$\mathbf{D}_v = \frac{\mu_e}{\eta_D}(\mathbf{C}_e - \frac{1}{3}(\mathbf{C}_e\cdot\mathbf{I})\,\mathbf{I})\ \text{from which}\quad \dot{\mathbf{C}}_v = \frac{\mu_e}{\eta_D}(\mathbf{C} - \frac{1}{3}(\mathbf{C}_e\cdot\mathbf{I})\mathbf{C}_v). \tag{2.56}$$

For an incompressible material in small deformation, the incompressibility constraint can be allied also with $\mathbf{C}_e\cdot\mathbf{I} = 3$, thus, in such instances, the evolution equation for the viscous deformation can be reformulated from equation (2.50) as follows

$$\dot{\mathbf{C}}_v = \frac{1}{\tau_m}(\mathbf{C} - \mathbf{C}_v), \tag{2.57}$$

where $\tau_m = \eta_D/\mu_e$ is the characteristic time of the material. This parameter is the ratio between the viscosity and the stiffness (it can be related to the shear η_D/μ_e or the volumetric η_V/K_e stiffness) of the material. The product between this time and the deformation ratio can be used to determine if the deformation condition are slow, medium or fast. Another linearization can be done from eqn. (2.57) by considering

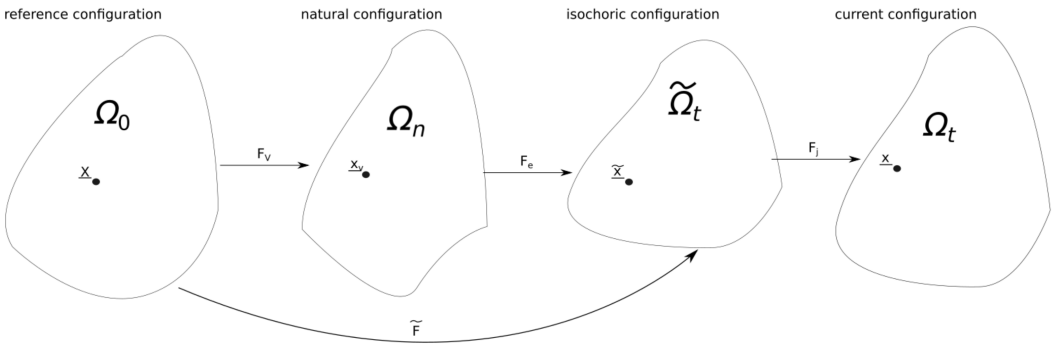

Figure 2.23: Decomposition of total deformation in Holzapfel [1996]. In contrast to the decomposition method presented in Reese and Govindjee [1998] (see fig 2.21), in this case, an extra intermediate configuration, referred to as the isochore, is introduced. The treatment of volumetric deformation occurs at the final stage of the viscoelastic transformation represented by $\tilde{\mathbf{F}}$.

infinitesimal also the total deformations. In this case, by $\mathbf{C} = \mathbf{I} + 2\text{sym}\nabla u + o(||\nabla u||^2) = \mathbf{I} + 2\mathbf{E}$ (and the same for $\mathbf{C}_v$), eqn. (2.57) can be rewritten as

$$\dot{\mathbf{E}}_v = \frac{1}{\tau_m}(\mathbf{E} - \mathbf{E}_v), \tag{2.58}$$

that represents the solution of the infinitesimal model of 2.22. The results of a comparison between the finite viscoelastic formulation of eqn. (2.50), and its linearized counterpart in eqn. (2.57) is shown in Reese and Govindjee [1998] (in the third figure) where the results of four cyclical shear test are presented. This comparison involved varying shear deformation values, with a fixed load frequency of $\omega = 0.3\,s^{-1}$ and a characteristic time of $\tau_m = 17.5\,s$. The results of these simulations, as reported in Reese and Govindjee [1998], indicate that the linearized equation remains valid only for infinitesimal deformations. All these simulations have been conducted with the omission of the volumetric component of deformation. Consequently, in the upcoming section, we will introduce the model proposed by Holzapfel [1996], which places specific emphasis on the volumetric deformation.

The volumetric deformation

The volumetric stiffness of rubber is often much higher than shear modulus. As a result, many models tend to disregard volumetric deformation. In the work presented by Holzapfel [1996], they separate this volumetric deformation from the isochoric deformation using a further spherical deformation step (see fig. 2.23) with the aim to avoid, during the numerical evaluation locking phenomena and to consider only the ishocoric deformation in the viscoelastic contribution. This step transforms the reference configuration into the isochoric configuration, and then it continues with the processes of viscous deformation and elastic deformation in the following manner

$$\mathbf{F} = \mathbf{F}_j\tilde{\mathbf{F}}; \qquad \text{where} \qquad \mathbf{F}_j = J^{1/3}\mathbf{I}; \;\; \tilde{\mathbf{F}} = \mathbf{F}_e\mathbf{F}_v = J^{-1/3}\mathbf{F}. \tag{2.59}$$

By this way $\det\mathbf{F}_j = J$ and $\det\tilde{\mathbf{F}} = 1$ and the deformation is split in the volumetric deformation ($\mathbf{F}_j$) and the isochoric deformation ($\tilde{\mathbf{F}}$) that follows the viscoelastic decomposition of fig. 2.21. In this context, the energy density in eqn. (2.45), can be rewritten

as

$$\psi(J, \tilde{\mathbf{C}}, \mathbf{F}_v) = \psi^V(J) + \psi_{eq}(\tilde{\mathbf{C}}) + \psi_{neq}(\mathbf{F}_v^{-T}\tilde{\mathbf{C}}\mathbf{F}_v^{-1}), \tag{2.60}$$

where $\psi^D = \psi_{eq} + \psi_{neq}$ and eqn. (2.39) is used. By this definition of the energy density, the second Piola stress tensor can be split as

$$\mathbf{S} = \mathbf{S}_V + \mathbf{S}_{eq} + \mathbf{S}_{neq}, \tag{2.61}$$

where, using (2.13), the single components can be evaluated as

$$\begin{aligned}
\mathbf{S}_V =& 2\frac{\partial \psi^V}{\partial J}\frac{\partial (J^2)^{1/2}}{\partial J^2}\frac{\partial J^2}{\partial \mathbf{C}} = pJ\mathbf{C}^{-1} \\
\mathbf{S}_{eq} =& 2\frac{\partial \psi_{eq}}{\partial \mathbf{C}} = \frac{\partial \tilde{\mathbf{C}}}{\partial \mathbf{C}}^T [2\frac{\partial \psi_{eq}}{\partial \tilde{\mathbf{C}}}] = J^{-2/3}\mathbb{P}[\tilde{\mathbf{S}}_{eq}] = J^{-2/3}(\tilde{\mathbf{S}}_{eq} - (1/3)(\tilde{\mathbf{S}}_{eq} \cdot \mathbf{C})\mathbf{C}^{-1}) \\
\mathbf{S}_{neq} =& 2\frac{\partial \psi_{neq}}{\partial \mathbf{C}} = \frac{\partial \tilde{\mathbf{C}}}{\partial \mathbf{C}}^T [2\frac{\partial \psi_{neq}}{\partial \tilde{\mathbf{C}}}] = \frac{\partial \tilde{\mathbf{C}}}{\partial \mathbf{C}}^T [2\mathbf{F}_v^{-1}\frac{\partial \psi_{neq}}{\partial \mathbf{C}_e}\mathbf{F}_v^{-T}] = J^{-2/3}\mathbb{P}[\tilde{\mathbf{S}}_{neq}],
\end{aligned} \tag{2.62}$$

where the fourth order tensor $\mathbb{P} = \mathbb{I} - (1/3)\mathbf{C}^{-1} \otimes \mathbf{C}$ is a projection tensor where $\mathbf{C}$ operating as a metric tensor. Indeed, by means of this operator, the stress tensors defined on the isochoric configuration ($\tilde{\mathbf{S}}_{eq}$, $\tilde{\mathbf{S}}_{neq}$) are mapped into the current configuration ($\mathbf{S}_{eq}$, $\mathbf{S}_{neq}$). The evolution problem is solved in Holzapfel [1996] with respect to the non equilibrium second Piola stress tensor following the constitutive equation in eqn. (2.50), the definition of material characteristic time (τ_m) and a procedure as in the previous chapter, by the following reformulation

$$\left\{ \begin{array}{c} \dot{\mathbf{S}}_{neq} + \frac{1}{\tau_m}\mathbf{S}_{neq} = \frac{\mathrm{d}}{\mathrm{d}t}\left(J^{-2/3}\mathbb{P}\left[2\frac{\partial \psi_{neq}}{\partial \tilde{\mathbf{C}}}\right]\right) \\ \mathbf{S}_{neq}|_{t=t_0} = \mathbf{S}^0_{neq} \end{array} \right. . \tag{2.63}$$

This evolution problem can be solved by

$$\mathbf{S}_{neq} = \mathbf{S}^0_{neq}\, e^{-\Delta t/\tau_m} \int_{t_0}^{t} \beta\, e^{-(t-s)/\tau_m} \frac{\mathrm{d}}{\mathrm{d}t}\left(J^{-2/3}\mathbb{P}\left[2\frac{\partial \psi_{eq}}{\partial \tilde{\mathbf{C}}}\right]\right) \mathrm{d}s, \tag{2.64}$$

where the non equilibrium energy is considered as a fraction of the equilibrium energy as $\psi_{neq} = \beta\psi_{eq}$. This modeling approach provides the flexibility to treat volumetric deformation independently, uncoupled from the viscoelastic properties of the material. This separation is effective in addressing numerical challenges like locking. However, it's important to acknowledge that this approach substantially amplifies the complexity of both numerical implementation and theoretical comprehension. Therefore, it is prudent to use this modeling technique selectively, applying it in situations where the evaluation of volumetric alterations is necessary, even when those alterations are minor. In the present context, there are various approaches available for disregarding volumetric deformation.

A generalized viscoelastic model

In the work presented by Kumar and Lopez-Pamies [2016], a viscoelastic model is introduced, which incorporates the strain rate as an internal variable and embeds it within a viscous dissipative potential. The model's most significant developments relevant to the present work primarily consist of two key aspects. Firstly, it extends and generalizes the model outlined in Reese and Govindjee [1998]. Secondly, it introduces an interesting

approach to solving the evolution equation for the viscous variable. The viscous constitutive relationship is employed with regard to the first Piola-Kirchhoff or Cauchy stress tensors as follows

$$\mathbf{P}_{neq}\mathbf{F}^T = J\mathbf{T}_{neq} = \mathbb{A}(\mathbf{F},\mathbf{F}_e)[\mathbf{F}_e\mathbf{L}_v\mathbf{F}_e^{-1}], \tag{2.65}$$

where the relation with eqn. (2.50) is clear. In the context of this paper, the model proposed by Reese and Govindjee [1998], is initially expanded to encompass not isotropic non equilibrium springs scenarios by means of the following generalization of the matrix $\mathbb{A}$

$$\begin{aligned}\mathbb{A}_{ijkl}(\mathbf{F},\mathbf{F}_e) =& 2\eta_K(I_1,I_2,\mathbf{C}_e,\mathbf{B}_v)\mathbb{K}_{ijkl}+\\ &+2\nu_K(I_1,I_2,\mathbf{C}_e,\mathbf{B}_v)(\mathbf{F}_e^{-1})_{mi}(\mathbf{F}_e)_{jn}\mathbb{K}_{mnpq}(\mathbf{F}_e^{-1})_{pk}(\mathbf{F}_e)_{lq}+\\ &+\theta_K(I_1,I_2,\mathbf{C}_e,\mathbf{B}_v)\mathbb{K}_{ijmn}(\mathbf{F}_e)_{mp}(\mathbf{F}_e)_{lp}(\mathbf{F}_e^{-1})_{qn}(\mathbf{F}_e^{-1})_{qk}+3\eta_J\mathbb{J}_{ijkl},\end{aligned} \tag{2.66}$$

where the subscripts select the tensors' components, the summation symbols (Σ) are omitted and $\mathbb{K}=\mathbb{S}-\mathbb{J}$ with $\mathbb{S}[\mathbf{M}]=\text{sym}(\mathbf{M})$. By this definition of $\mathbb{A}$, many viscoelastic models (as Le Tallec et al. [1993], Bergström and Boyce [1998], Reese and Govindjee [1998] and others) can be included. The application of the model introduced in Kumar and Lopez-Pamies [2016] involves utilizing a version of matrix $\mathbb{A}$ akin to the one in Reese and Govindjee [1998]. However, in this application, the viscosity parameters are not constant and the volumetric deformation is considered negligible. Notably, the proposed viscosity is found to be a function that increases with the applied deformation (through $I_{1v}=tr(\mathbf{C}_v)$ and decreases with the viscous deformation rate (through J_2^{neq}), as follows

$$\begin{aligned}\mathbb{A}_{ijkl}(\mathbf{F},\mathbf{F}_e) =& \eta_K(I_{v1},J_2^{neq}(I_{e1},I_{e2}))(\mathbb{K}_{ijkl}+\mathbb{K}_{ijmn}(\mathbf{F}_e)_{mp}(\mathbf{F}_e)_{lp}(\mathbf{F}_e^{-1})_{qn}(\mathbf{F}_e^{-1})_{qk})+3\eta_J\mathbb{J}_{ijkl}\\ \mathbb{A} =& \frac{\eta_K}{2}\mathbb{K}(\mathbf{I}+\mathbf{B}_e\mathbb{T}\mathbf{B}_e^{-1})+3\eta_J\mathbb{J},\end{aligned} \tag{2.67}$$

where $\mathbb{T}[\mathbf{M}]=\mathbf{M}^T$. In this definition, $\eta_J\to\infty$ to simulate the incompressibility constraint, while

$$\eta_K=\eta_\infty+\frac{\eta_0-\eta_\infty+K_1(I_{v1}^{\beta_1}-3^{\beta_1})}{1+(K_2J_2^{neq})^{\beta_2}},\ \text{where } J_2^{neq}=\frac{1}{2}||\text{dev}(\mathbf{T}_{neq})||^2=(\frac{I_{e1}^2}{3}-I_{e2})r_{neq}. \tag{2.68}$$

In the last equation, I_{1v} accounts the amount of viscous deformation, while J_2^{neq} accounts the viscous deformation ratio through the deviatoric part of the non equilibrium stress. The viscosity η_0 represents the "initial" viscosity for $I_{v1}=3$ and $J_2^{neq}=0$, while η_∞ is the viscosity for infinitely fast viscous deformation, thus for $J_2^{neq}\to\infty$. The other parameters that appear in the equation for η_K are all not negative parameters. For the evaluation of J_2^{neq}, the assumption that ψ_{neq} depends only on the invariant $I_{1e}=\text{tr}(\mathbf{C}_e=\mathbf{C}\cdot\mathbf{C}_v^{-1})$ has been made and $r_{neq}(I_{1e})=2\partial\psi_{neq}(I_{1e})/\partial I_{1e}$. Last assumption allows to evaluate the evolution equation of $\dot{\mathbf{C}}_v$ by the micro force balance in eqn. (2.65), through the following procedure:

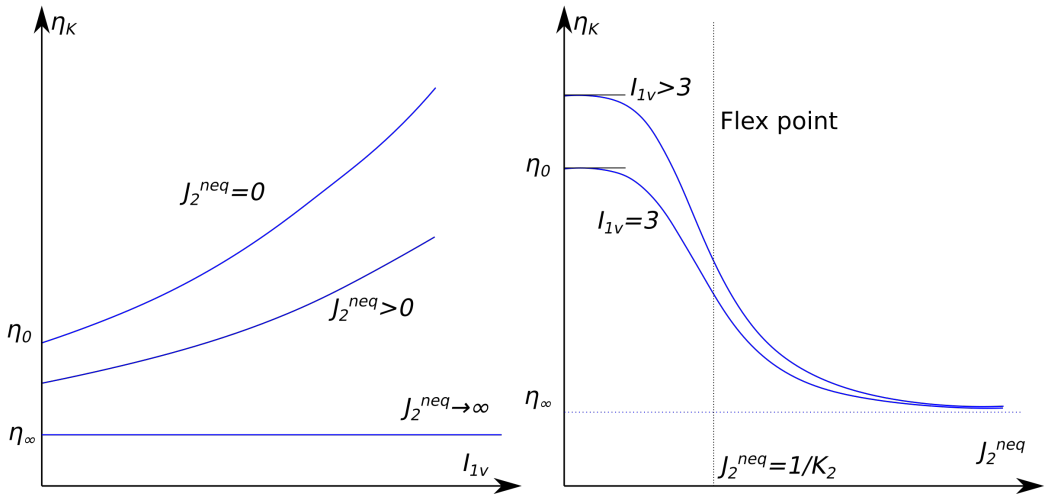

Figure 2.24: A qualitative description of how the parameters in equation (2.68) influence the viscosity η_K. In particular for an infinitely fast deformation process, $\eta_K \to \eta_\infty$ for any I_{1v}, while the dependence on J_2^{neq} presents a flex point in $J_2^{neq} = K_2^{-1}$ and it initiate with a maximum in $J_2^{neq} = 0$ and an horizontal asisthot in $J_2^{neq} \to \infty$.

- right side:

$$\begin{aligned}
\mathrm{dev}\mathbb{A}[\mathbf{F}_e\mathbf{L}_v\mathbf{F}_e^{-1}] &= \mathrm{dev}(\eta_K\mathbb{K}[\mathbf{F}_e\mathbf{L}_v\mathbf{F}_e^{-1} + \mathbf{F}_e\mathbf{F}_e^T(\mathbf{F}_e^{-T}\mathbf{F}_e^{-1}\mathbf{F}_e\mathbf{L}_v\mathbf{F}_e^{-1})^T]) \\
&= \mathrm{dev}(\frac{\eta_K}{2}\mathbb{K}[\mathbf{F}_e\mathbf{L}_v\mathbf{F}_e^{-1} + \mathbf{F}_e\mathbf{L}_v^T\mathbf{F}_e^{-1}]) \\
&= \frac{\eta_K}{4}[\mathbf{F}_e\mathbf{L}_v\mathbf{F}_e^{-1} + \mathbf{F}_e\mathbf{L}_v^T\mathbf{F}_e^{-1} + \mathbf{F}_e^{-T}\mathbf{L}_v^T\mathbf{F}_e^T + \mathbf{F}_e^{-T}\mathbf{L}_v\mathbf{F}_e^T] \\
&= \frac{\eta_K}{2}[\mathbf{F}_e\mathbf{D}_v\mathbf{F}_e^{-1} + \mathbf{F}_e^{-T}\mathbf{D}_v\mathbf{F}_e^T] \\
&= \frac{\eta_K}{2}[\mathbf{F}\mathbf{C}_v^{-1}\dot{\mathbf{C}}_v\mathbf{F}^{-1} + \mathbf{F}^{-T}\dot{\mathbf{C}}_v\mathbf{C}_v^{-1}\mathbf{F}^T] \\
&= \eta_K\mathrm{sym}(\mathbf{F}\mathbf{C}_v^{-1}\dot{\mathbf{C}}_v\mathbf{F}^{-1});
\end{aligned} \tag{2.69}$$

  where in the application of $\mathbb{K}$ (third line), the incompressibility constrain is used as $\mathbf{F}_e\mathbf{L}_v\mathbf{F}_e^{-1} \cdot \mathbf{I} = \mathbf{L}_v \cdot \mathbf{I} = 0$. in the fourt row, the definition of $\mathbf{D}$ in eqn. (2.12) is used and in last line eqns. (2.38) and (2.42) are used;

- left side

$$\begin{aligned}
\mathrm{dev}(\mathbf{P}_{neq}\mathbf{F}^T) =& \mathrm{dev}(\frac{\partial\psi_{neq}(I_{e1})}{\partial I_{e1}}\frac{\partial(\mathbf{F}\cdot\mathbf{F}\mathbf{C}_v^{-1})}{\partial\mathbf{F}}\mathbf{F}^T) \\
=& r_{neq}\mathrm{dev}(\mathbf{F}\mathbf{C}_v^{-1}\mathbf{F}^T) \\
=& r_{neq}(\mathbf{F}\mathbf{C}_v^{-1}\mathbf{F}^T - \frac{1}{3}I_{e1}\mathbf{I}) \\
=& r_{neq}\mathbf{F}\mathbf{C}_v^{-1}(\mathbf{C} - \frac{1}{3}I_{e1}\mathbf{C}_v)\mathbf{F}^{-1};
\end{aligned} \tag{2.70}$$

  where the fact that ψ_{neq} depends only on $I_{e1} = \mathbf{C}_e \cdot \mathbf{I} = \mathbf{F}_v^{-T}\mathbf{C}\mathbf{F}_v^{-1} \cdot \mathbf{I} = \mathbf{C} \cdot \mathbf{C}_v^{-1} = \mathbf{F} \cdot \mathbf{F}\mathbf{C}_v^{-1}$ is used in the first row and, in the last one, the left multiplication for $\mathbf{F}\mathbf{C}_v^{-1}\mathbf{C}_v\mathbf{F}^{-1} = \mathbf{I}$ and the right multiplication for $\mathbf{F}\mathbf{F}^{-1} = \mathbf{I}$ is done.

applying last procedure to eqn. (2.69) and considering $\mathbf{C}_e$ and $\mathbf{D}_v$ as coaxial tensors, the left and the right side of eqn. (2.65) can be recomposed as follows

$$\dot{\mathbf{C}} = \frac{r_{neq}}{\eta_K}(\mathbf{C} - \frac{1}{3}I_{e1}\mathbf{C}_v) = \mathbf{G}(t, \mathbf{C}_v), \tag{2.71}$$

that is defined also as a function of the time t and of the viscous deformation $\mathbf{C}_v$. Note that eqn. (2.71) is the same of eqn. (2.56), with $\mu_e = r_{neq}(I_{1e})$.

In Kumar and Lopez-Pamies [2016], the evolution problem in eqn. (2.71) is solved using the following fifth order Runge Kutta (see Lawson [1966]) routine

$$\mathbf{C}_v|_{t+\Delta t} = \mathbf{C}_v|_t + \frac{\Delta t}{90}(7\mathbf{K}_1 + 32\mathbf{K}_3 + 12\mathbf{K}_4 + 32\mathbf{K}_5 + 7\mathbf{K}_6) \tag{2.72}$$

where the viscous deformation (and the other variable, the displacement $\underline{u}|_t$) at time t ($\mathbf{C}_v|_t$) is considered known and, the $\mathbf{K}_i$ tensors are

$$\begin{aligned}
\mathbf{K}_1 =& \mathbf{G}(t, \mathbf{C}_v|_t) \\
\mathbf{K}_2 =& \mathbf{G}(t + \frac{\Delta t}{2}, \mathbf{C}_v|_t + \frac{\Delta t}{2}\mathbf{K}_1) \\
\mathbf{K}_3 =& \mathbf{G}(t + \frac{\Delta t}{4}, \mathbf{C}_v|_t + \frac{\Delta t}{16}(3\mathbf{K}_1 + \mathbf{K}_2)) \\
\mathbf{K}_4 =& \mathbf{G}(t + \frac{\Delta t}{2}, \mathbf{C}_v|_t + \frac{\Delta t}{2}\mathbf{K}_3) \\
\mathbf{K}_5 =& \mathbf{G}(t + \frac{3\Delta t}{4}, \mathbf{C}_v|_t + \frac{3\Delta t}{16}(-\mathbf{K}_2 + 2\mathbf{K}_3 + 3\mathbf{K}_4) \\
\mathbf{K}_6 =& \mathbf{G}(t + \Delta t, \mathbf{C}_v|_t + \frac{\Delta t}{7}(\mathbf{K}_1 + 4\mathbf{K}_2 + 6\mathbf{K}_3 - 12\mathbf{K}_4 + 8\mathbf{K}_5)).
\end{aligned} \tag{2.73}$$

Using this evolution equation, we can address the viscous problem. The solution involves solving the equilibrium problem either in the reference configuration (div$\mathbf{P}+\underline{b}_0 = \underline{0}$ where $\underline{b}_0$ represents the body forces in the reference configuration) or in the current configuration (div$\mathbf{T} + \underline{b}_t = \underline{0}$). This process entails a step-by-step double minimization problem for the two internal variables ($\underline{u}$ and $\mathbf{C}_v$). This viscous constitutive equation is integrated with the finite elastic model presented in Lopez-Pamies [2010] (see eqn. (2.24)). This combination is utilized to calibrate the resulting viscoelastic model, aligning it with numerous experimental outcomes, as in fig. 2.25, where the experimental data from Bergström and Boyce [1998], particularly concerning Nitrile rubber under uniaxial compression loading/unloading at constant stretch rates, is interpreted by this model.

The model offers a relative straightforward modeling and solution approach, with its single limitation being the dependence of ψ_{neq} solely on I_{e1} which, although it simplifies the treatment, may not be general enough to fit the behavior of some materials. Consequently, it will be coupled with phase-field damage in the model proposed in chp. 4 to describe crack propagation phenomena.

2.5 Phase-field damage models

2.5.1 Internal variables and domain of reversibility

Damage phase-field model incorporates internal variables and a reversibility domain. A model is considered to have internal variables when, with a given set of internal variables

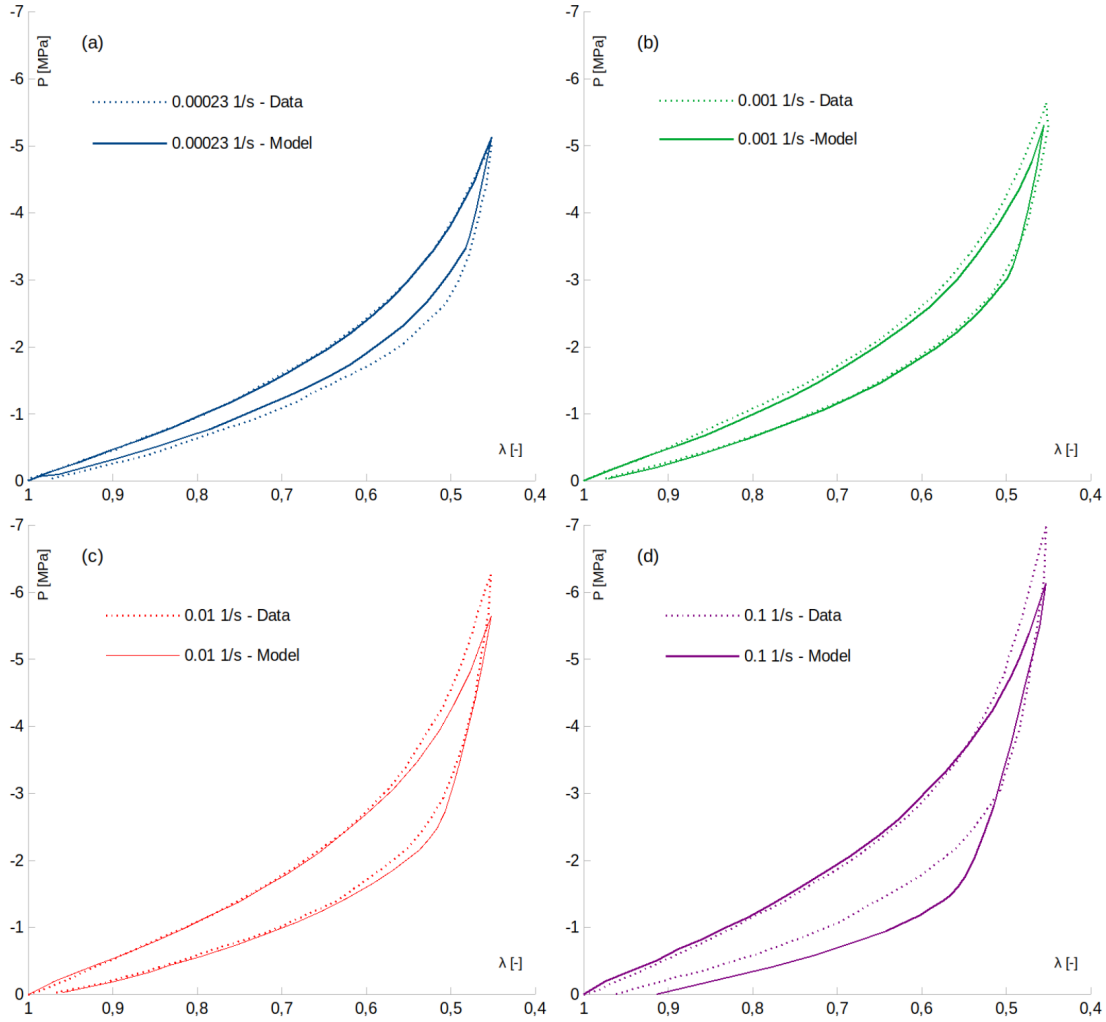

Figure 2.25: Experimental data from Bergström and Boyce [1998], concerning Nitrile rubber under uniaxial compression loading/unloading cycles at constant stretch rates, is interpreted by the described model in Kumar and Lopez-Pamies [2016].

$\underline{a}$, the temporal evolution of the stress tensor can be reformulated solely in terms of the evolution of deformations and internal variables, as follows

$$\hat{\mathbf{S}}(t) = \tilde{\mathbf{S}}(\mathbf{C}(t), \underline{a}(t)). \tag{2.74}$$

The reversibility domain ($\mathcal{R}(t)$), is a subset of deformations wherein the internal variables remain unchanged if the deformation process (π) remains within this defined domain. By leveraging the principle of work non-negativity within a deformation cycle (refer to Ilyushin [1961]) and its equivalence to the non-negativity of the dissipation rate (see Drucker [1952]), we can establish the ensuing fundamental inequality of variational calculus for any deformation process

$$-\frac{\partial \psi}{\partial \underline{a}}(\mathbf{C}, \underline{a}) \cdot \dot{\underline{a}} \geq -\frac{\partial \psi}{\partial \underline{a}}(\mathbf{C}^*, \underline{a}) \cdot \dot{\underline{a}} \qquad \forall \mathbf{C}^* \in \mathcal{R}(t). \tag{2.75}$$

This inequality implies that, when the material state is about to leave its reversibility domain, the actual release of energy ($\mathcal{D}(\mathbf{C},\underline{a},\underline{\dot{a}}) = -(\partial\psi(\mathbf{C},\underline{a})/\partial\underline{a})\cdot\underline{\dot{a}}$), is greater or equal to any other possible energy release due to other deformation in the reversibility domain. Eqn. (2.75) can be proved by considering the deformation cycle in fig. 2.26, where the cycle $\pi = \pi_1 \circ \pi_\epsilon \circ \pi_2$, with an infinitesimal part (π_ϵ) out of the initial reversibility domain $\mathcal{R}(t_0)$ (in blue) is shown. The evaluation of the work performed in this cycle can be determined by employing the characteristics of hyperelastic materials in the following way

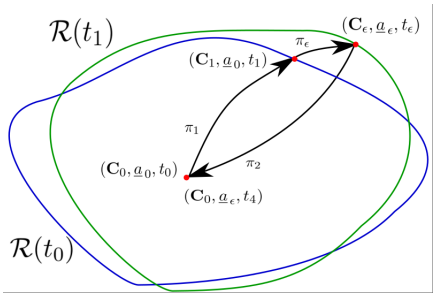

Figure 2.26: Deformation cycle $\pi = \pi_1 \circ \pi_\epsilon \circ \pi_3$, with π_ϵ out of the initial reversibility domain $\mathcal{R}(t_0)$.

$$\mathcal{W}(\pi) = \overbrace{\psi(\mathbf{C}_1,\underline{a}_0) - \psi(\mathbf{C}_0,\underline{a}_0)}^{\mathcal{W}(\pi_1)} + \mathcal{W}(\pi_\epsilon) + \overbrace{\psi(\mathbf{C}_0,\underline{a}_\epsilon) - \psi(\mathbf{C}_\epsilon,\underline{a}_\epsilon)}^{\mathcal{W}(\pi_2)} \geq 0, \tag{2.76}$$

that can be rewritten as

$$\mathcal{W}(\pi) = -[-\psi(\mathbf{C}_1,\underline{a}_0) + \psi(\mathbf{C}_\epsilon,\underline{a}_\epsilon)] + \int_{t_1}^{t_\epsilon} \frac{1}{2}\mathbf{S}\cdot\dot{\mathbf{C}}\,\mathrm{d}t + \psi(\mathbf{C}_0,\underline{a}_\epsilon) - \psi(\mathbf{C}_0,\underline{a}_0) \geq 0. \tag{2.77}$$

Dividing by $\mathrm{d}t = t_\epsilon - t_1$ and applying the limit $\mathrm{d}t \to 0$, the equation becomes

$$\mathcal{W}(\pi) = -\frac{\partial\psi}{\partial\mathbf{C}}(\mathbf{C}_1,\underline{a}_0)\cdot\dot{\mathbf{C}} - \frac{\partial\psi}{\partial\underline{a}_0}(\mathbf{C}_1,\underline{a}_0)\cdot\underline{\dot{a}} + \frac{1}{2}\mathbf{S}(t_1)\cdot\dot{\mathbf{C}} + \frac{\partial\psi}{\partial\underline{a}_0}(\mathbf{C}_0,\underline{a}_0)\cdot\underline{\dot{a}} \geq 0. \tag{2.78}$$

Considering that the first term is the opposite of the third term, the resulting expression indicates that for any deformation state into the reversibility domain (as $\mathbf{C}_0$), , the dissipation assessed under the current deformation (in proximity to the reversibility domain, $\mathbf{C}_1$), is greater, as said in eqn. (2.75). Using the fundamental inequality, the following support function can be defined

$$s_f(\underline{a},\underline{b}) = \sup_{\mathbf{C}\in\mathcal{R}(t)} \frac{\partial\psi}{\partial\underline{a}}(\mathbf{C},\underline{a})\cdot\underline{b} = \overline{\underline{w}}(\underline{a})\cdot\underline{b}, \tag{2.79}$$

where $\overline{\underline{w}}(\underline{a})$ is defined to maximize $s_f(\underline{a},\underline{b})$. Notably, this function depends not on the deformation itself but solely on other internal variables ($\underline{a}$) and the velocity parameter $\underline{b}$. This definition allows a redefinition of the reversibility domain

$$\mathcal{R}(t) = \{\mathbf{C} \mid -\frac{\partial\psi}{\partial\underline{a}}(\mathbf{C},\underline{a})\cdot\underline{\dot{a}} \leq s_f(\underline{a},\underline{\dot{a}})\ \}. \tag{2.80}$$

Using this redefined $\mathcal{R}(t)$ and the fundamental inequality in equation (2.75), the dissipation can respectively be considered at same time as $\mathcal{D}(\mathbf{C},\underline{a},\underline{\dot{a}}) \leq s_f(\underline{a},\underline{\dot{a}})$ and $\mathcal{D}(\mathbf{C},\underline{a},\underline{\dot{a}}) \geq s_f(\underline{a},\underline{\dot{a}})$. This means that the dissipation rate can only be equal to $s_f(\underline{a},\underline{\dot{a}})$, that does not depends on the deformation $\mathbf{C}$. This condition allows

$$\Delta = \int_{t_0}^{t} \mathcal{D}\,\mathrm{d}t = \int_{t_0}^{t} s_f(\underline{a},\underline{\dot{a}})\,\mathrm{d}t = \int_{t_0}^{t} \overline{\underline{w}}(\underline{a})\cdot\frac{\mathrm{d}\underline{a}}{\mathrm{d}t}\mathrm{d}t = \int_{\underline{a}_0}^{\underline{a}} \overline{\underline{w}}(\underline{a})\cdot\mathrm{d}\underline{a} = w(\underline{a}) - w(\underline{a}_0), \tag{2.81}$$

where, the dissipation potential $w(\underline{a}) \mid \partial w/\partial\underline{a} = \overline{\underline{w}}(\underline{a})$ is implicitly defined. If it's possible to define $w(\underline{a}$, this formulation allows for the assignment of the dissipation potential (with

$w(\underline{a}_0) = 0$ for simplicity) as a constitutive assumption, leading to the definition of the internal energy density as follows

$$\phi = \psi(\mathbf{C}, \underline{a}) + w(\underline{a}). \tag{2.82}$$

Upon the addition of external works and boundary conditions, this formulation enables the problem's solution via minimization over the body.

This approach enables the incorporation of specific material characteristics impacting its elastic response as phase-fields variables defined over the examined body. The evaluation of these fields can be done, as for the displacement field, via minimization of the total energy. Some examples of these formulation are plasticity as discussed in Miehe et al. [2016], Lancioni and Yalçinkaya [2019] and other references, damage as explored in Pham et al. [2011], Lancioni and Corinaldesi [2018], Wu [2017] and related works, or other distinct phenomena. The subsequent sections will introduce and elaborate on the modeling of material damage using the internal variable named "damage" (d).

2.5.2 Introduction of phase field damage models

The fundamental principles underlying this damage phase-field formulation were presented in Francfort and Marigo [1998], where the fracture problem was formulated as a free-discontinuity minimum problem. The variational formulation of fracture was approximated in Bourdin et al. [2000] by a regularized problem that operates on a functional defined on continuous fields, with fracture replaced by the so-called *phase-field* variable. Acting like a damage variable, the phase-field assumes values between 0 and 1, with 0 for sound material and 1 for the fractured material, with the irreversibility constrain ($\dot{d} \geq 0$), and its evolution describes the coalescence and propagation of cracks Bourdin et al. [2008a], Miehe et al. [2010b], Pham et al. [2011]. As the phase-field increases, the stiffness of the material reduces, vanishing when the damage variable reaches 1. A non-local term, proportional to the gradient of the phase-field, is incorporated into the internal energy functional and it plays the role of localization limiter by penalizing abrupt damage variations Miehe and Schänzel [2014], and by promoting smooth transitions from 0 to 1 in regions of finite width. The gradient contribution automatically introduces an internal length, that in the present formulation is a constitutive parameter, to be calibrated through experimental data Marigo et al. [2016]. Numerous models serve as introductions to this modeling approach (e.g., Pham et al. [2011] or Lancioni and Corinaldesi [2018]).

Understanding the uniqueness of this model is best achieved through the analysis of the 1D tensile test. Here, the body is depicted by its longitudinal position (represented by the scalar value $x \in [0; L]$), and the variables are the longitudinal displacement u and the damage d. The external forces are neglected and the boundary conditions for the displacement are $u(0) = 0$ and $u(L) = \overline{u}_t = \overline{\varepsilon}_t L$. The internal energy density (refer to eqn. (2.82)) is

$$\phi(u, d) = \underbrace{\frac{1}{2} E(d)(u')^2}_{\text{elastic energy}} + \overbrace{w(d)}^{\text{local dissipation}} + \underbrace{\frac{1}{2} A(d')^2}_{\text{non local term}}, \tag{2.83}$$

where $E(d)$ is the Young modulus, that depends on the damage state variable as a strictly decreasing function and A is the constant coefficient of the non local term. The equilibrium conditions can be deducted using the stability criterion, that consists in

the requirement of the non negativity of the first variation of the total internal energy ($\Phi(u,d) = \int_0^L \phi(u,d)\mathrm{d}x$), made in the direction of an arbitrary perturbation $[\hat{u}, \hat{d}]$. This procedure, after the integration by parts of the elastic energy and of the non local term, gives

$$\begin{aligned} \partial\Phi(u,d)[\hat{u},\hat{d}] = \int_0^L -\sigma'(x)\hat{u} \,+\, (\frac{1}{2}E'(d)(u')^2 + w'(d) - Ad'')\hat{d}\,\mathrm{d}x + \\ + (\sigma(x)\hat{u})|_0^L \,+\, (Ad'\hat{d})|_0^L \,\geq 0, \end{aligned} \tag{2.84}$$

where the first equilibrium condition is that the longitudinal stress ($\sigma(x) = E(d)u'$) is constant over the bar for the arbitrariness of the perturbation (from witch $\sigma' = \mathrm{d}\sigma/\mathrm{d}x = 0$ for any $x \in [0; L]$). The second condition gives the equation of the yield condition as follows

$$Y = \frac{1}{2}E'(d)(u')^2 + w'(d) - Ad'' \geq 0, \tag{2.85}$$

that, if it is satisfied as an equality, allows the damage evolution ($\dot{d} > 0$), otherwise $\dot{d} = 0$. This condition arises from applying the energy balance, resulting in $Y\dot{d} = 0$, indicating that either Y or $\dot{d}$ must be equal zero. The yield function (Y) can be rewritten also as

$$Y = -\frac{1}{2}C'(d)\sigma^2 + w'(d) - Ad'', \tag{2.86}$$

where $C(d) = 1/E(d)$, thus $C'(d) = -E'(d)/E^2(d)$ and $\sigma^2 = E^2(d)(u')^2$.

The second line of equation (2.84) allows for the imposition of boundary conditions. While boundary conditions for displacements are specified at $x = 0; L$, two different conditions can be assigned to the damage. Dirichlet conditions (also known as *hard* b.c.; $d(0) = d(L) = 0$) or Neumann conditions (also known as *soft* b.c.; $d'(0) = d'(L) = 0$) can be selected. However, in subsequent parts of this thesis, only Dirichlet b.c. will be considered, since they reproduce the conditions usually found in experiments.

Key insights into damage models can be derived from the subsequent equations governing the evolution of equilibrium conditions

$$(\sigma + \Delta t\dot{\sigma})' = 0; \quad \dot{d} \geq 0; \quad (Y + \Delta t\dot{Y}) \geq 0; \quad (Y + \Delta t\dot{Y})\dot{d} = 0, \tag{2.87}$$

where Δt is an infinitesimal increment of the time. These equations can be considered as the first order Taylor series development, but a more rigorous derivation can be found in Lancioni and Corinaldesi [2018]. Using now $\dot{\sigma}' = 0$, the mean value of $\dot{\sigma}$ can be considered equal to its value over the bar, thus

$$\dot{\sigma} = \frac{1}{L}\int_0^L \dot{\sigma}\mathrm{d}x = \frac{1}{L}\int_0^L (E'u'\dot{d}) + (E\dot{u}')\mathrm{d}x = E'u'\bar{\dot{d}} + E\,\bar{\dot{\varepsilon}}, \text{ s.t. } \dot{u}'(x) = \frac{E'u'}{E}(\bar{\dot{d}} - \dot{d}) + \dot{\bar{\varepsilon}}, \tag{2.88}$$

where $\bar{\dot{d}} = (1/L)\int_0^L \dot{d}\mathrm{d}x$, and where an evolution equation of the deformation rate $\dot{u}'(x)$ is obtained. Substituting this equation in the evolution form of the yield condition (derived from eqn. (2.85)), the following differential problem is obtained

$$AC'(0)\dot{d}'' - j(0)\dot{d} = -(C'(0))^2\sigma\dot{\sigma}, \tag{2.89}$$

where

$$j(d) = w''(d)C'(d) + w'(d)C''(d), \tag{2.90}$$

that depends only on the local damage dissipation and the effect of the damage into the stiffness. For this reason, these two function (that are assigned as constitutive assumption) will define completely the behavior of the studied material. Indeed the solution of

the differential equation (2.89), depends on the $\text{sgn}(j(0))$ and on the ratio between L and the following internal lengths

$$\ell_i = 2\pi\sqrt{\frac{AC'(0)}{\text{abs}\,(j(0))}}; \qquad \ell_c = 2\frac{C'^2(0)w'(0)}{C(0)\text{abs}\,(j(0))}\ell_i. \tag{2.91}$$

Using last definition, eqn. (2.89) and the third relation of $\dot{\sigma}$ in eqn. (2.88), the evolution regime after the crack initiation can be determine as follows:

- $j(0) > 0$. This condition is characterized by a stress hardening ($\dot{\sigma}$) and diffuse damage regime and the solutions for $\dot{d}(x)$ and $\dot{\sigma}$ are:

$$\dot{d}(x) = \frac{C'^2}{j}\sigma\dot{\sigma}k(x), \text{ where } k(x) = 1 - \frac{\cosh[\pi(L-2x)/\ell_i]}{\cosh(\pi L/\ell_i)}; \quad \dot{\sigma} = \frac{E}{1+(\overline{k}\ell_c/\ell_i)}\overline{\dot{\varepsilon}}. \tag{2.92}$$

- $j(0) = 0$ implies a quadratic form of $\dot{d}$ and a stress hardening regime:

$$\dot{d}(x) = \frac{3E}{6AC' + E^2Cw'L^3}\sigma x(L-x); \qquad \dot{\sigma} = \frac{6EA}{6A + E^2CC'w'L^3}\overline{\dot{\varepsilon}}. \tag{2.93}$$

- for $j < 0$, the regime of the solution depends on the ratio L/ℓ_i. Indeed if $l \leq \ell_i$, the solution is a trigonometric function of x and it remains non negative, but if $L > \ell_i$, the simple trigonometric solution of eqn. (2.89) gives region of the bar where $\dot{d} < 0$ and it disagree with the irreversibility condition. For this reason the solution will be localized. For these reasons, the shape of the solution is:

  - for $L \leq \ell_i$, the solution will be as in eqns. (2.92), but with:

$$k(x) = 1 - \frac{\cos[\pi(L-2x)/\ell_i]}{\cos(\pi L/\ell_i)}; \qquad \text{with } \overline{k}(x) = \frac{1}{L}\int_0^L k(x) = 1 - \frac{\ell_i}{L\pi}\tan(\pi L/\ell_i). \tag{2.94}$$

    Now, if if $L < \ell_i/2$, the stress regime remains in stress hardening and if $L > \ell_i/2$ in stress softening.

  - for $L > \ell_i$, the full size solution doesn't agree with the irreversibility condition, thus the solution will be as in eqns. (2.92), but a damage localization as follows

$$k(x) = \begin{cases} 1 - \cos(2\pi x/\ell_i) & \text{if } x \in [0;\ell_i] \\ 0 & \text{if } x > \ell_i \end{cases}; \qquad \text{with } \overline{k} = \ell_i/L, \tag{2.95}$$

    and it gives a stress softening regime with a localization of the fracture.

This analysis serves as an introduction to understanding the predictive capabilities and the operation of phase-field damage models and the effects of the different coefficients and functions, such as internal lengths or local dissipation, on the damage mechanism. The main focus of this section, as highlighted in the preceding bulleted list, pertains to solution of the evolution problem of $\dot{d}$, $\dot{\sigma}$, which will also be used in the formulation of the rate-independent model discussed in chp. 3. However, for a thorough formulation of the examined model, refer to Lancioni and Corinaldesi [2018]. The next section introduces a model general model for cohesive fracture.

2.5.3 A unified gradient damage model for linear elasticity (Wu [2017])

This section will introduce a general damage model that includes many model as special cases (refer to Li et al. [2016], Simo and Ju [1987] and others) and specifically capable of simulating different cohesive fracture mechanism. In Wu [2017], one of the more general description of these models in case of infinitesimal deformation is shown and, in this section, it will be presented. In this paper, the dissipation potential is written starting from the regularization of the crack surface (as in Miehe et al. [2010a]) by

$$A_d = \int_\Omega \gamma(d, \nabla d)\mathrm{d}\Omega \approx \int_\Omega \delta_s \mathrm{d}\Omega = A_s, \tag{2.96}$$

where, the Dirac delta (δ_s) is regularized by the crack surface density $\gamma(d, \nabla d)$, that can be written as

$$\gamma(d, \nabla d) = \frac{1}{c_0}(\frac{1}{b}\eta(d) + b\nabla d \cdot \nabla d), \qquad \text{with} \qquad c_0 = 4\int_0^1 \sqrt{\eta(d)}\mathrm{d}d. \tag{2.97}$$

where the geometric function $\eta(d)$ describes the uniform progression of the crack phase-field; b stands for an internal length scale that measures the size of the localization band; $c_0 > 0$ is a scaling parameter ensuring the approximation in eqn. (2.97). In order to agree with this approximation, the conditions $\eta(0) = 0$ and $\eta(1) = 1$ have also to be satisfy. For this reason, the following form of $\eta(d)$ is proposed in Wu [2017]

$$\eta(d) = \sum_{i=1}^{n} \xi_i d^i, \qquad \text{with} \qquad \sum_{i=1}^{n} \xi_i = 1. \tag{2.98}$$

The elastic energy density is multiplied by a function $g(d)$, called *degradation function*, decreasing with d, which accounts for the deterioration of the elastic proprieties where the damage evolves. These characteristics can be summarized as

$$\psi(\mathrm{sym}\nabla \underline{u}, d) = g(d)\,\psi_{el}(\mathrm{sym}\nabla \underline{u}); \qquad g(1) = 0; \;\; g(0) = 1; \;\; g'(d) < 0, \tag{2.99}$$

where $g'(d) = \partial g(d)/\partial d$. The solution of the problem can be found by the bounded minimization of the total energy, minus the external forces' energy as it follows

$$o\Phi(\underline{u}, d) = \int_\Omega \psi(\mathrm{sym}\nabla \underline{u}, d) + G_c\gamma(d, \nabla d)\mathrm{d}\Omega - \int_\Omega \underline{b} \cdot \underline{u}\mathrm{d}\Omega - \int_{\partial\Omega_2} \underline{s} \cdot \underline{u}\mathrm{d}\partial\Omega_2 \;, \tag{2.100}$$

where $\partial\Omega_2$ is the part of the boundary of the body Ω where the stresses are assigned and $\underline{b}$, $\underline{s}$ are the body and the surface external forces. The formulation of such as model, can be summarized as the definition of the uniform progression of the crack function ($\alpha(d)$) and the degradation function $g(d)$.

The more general way to define the degradation function, that includes the major part of the definition in literature, is the following

$$g(d) = \frac{1}{1 + \phi(d)} = \frac{(1-d)^p}{(1-d)^p + Q(d)}, \tag{2.101}$$

where $\phi(d) = Q(d)/(1-d)^p$, the exponent p is a positive number and $Q(d) > 0$ is a continuous function. Using $Q(d) = 1 - (1-d)^p$, and $p = 1;\ 2$ (thus $g(d) = (1-d)^p$), many damage models can be included (as Simo and Ju [1987], Bourdin et al. [2008b] and others), while using $Q(d) = (1+\rho_0)^q - (1-d)^q$ (that implies $g(d) = (1-d)^p/(1+\rho_0 d)^q$

), models as Lorentz and Godard [2011] are included. In the context of Wu [2017], the following polynomial function is chosen

$$Q(d) = \sum_{i=1}^{n}[(\prod_{j=1}^{i} a_j)d^i], \tag{2.102}$$

where the parameters a_i are determines following the material's behavior. Last constitutive assumption concerns the elastic strain energy density, which, in cases of infinitesimal deformation, is regarded as a quadratic form of the symmetric part of the displacement gradient

$$\psi_{el}(\text{sym}\nabla\underline{u}) = \frac{1}{2}\mathbb{C}_0[\text{sym}\nabla\underline{u}]\cdot\text{sym}\nabla\underline{u} \qquad \text{and} \qquad \mathbf{T} = g(d)\mathbf{T}_0 = g(d)\mathbb{C}_0[\text{sym}\nabla\underline{u}], \tag{2.103}$$

where also the stress tensor ($\mathbf{T}$) equation is shown.

Equilibrium

The equlibrium conditions can be determined by the minimization of the total energy in eqn. (2.100), using the stability criterion as follows

$$\begin{aligned}\partial\Phi(\underline{u},d)[\hat{\underline{u}},\hat{d}] = &-\int_\Omega(\text{div}\mathbf{T}+\underline{b})\cdot\hat{\underline{u}}\text{d}\Omega + \int_{\partial\Omega_2}(\mathbf{T}\hat{n}-\underline{s})\cdot\hat{\underline{u}}\text{d}\partial\Omega_2 + \\ &+\int_\Omega(g'(d)\psi_{el}(\text{sym}\nabla\underline{u}) + \frac{G_c}{c_0\,b}(\alpha'(d)-2b^2\Delta d)\cdot\hat{d}\text{d}\Omega + \\ &+2\int_{\partial\Omega}\frac{G_c}{c_0\,b}(\nabla d\cdot\hat{n})\hat{d}\text{d}\partial\Omega \geq 0,\end{aligned} \tag{2.104}$$

where $[\hat{\underline{u}},\hat{d}]$ represents the admissible perturbation set for the internal variable $(\underline{u},d)$. The first variation evaluation of equation (2.100) involves the application of the divergence theorem to the terms $\int_\Omega g(d)\mathbb{C}_0[\nabla\underline{u}]\cdot\nabla\hat{\underline{u}}\text{d}\Omega$ and $\int_\Omega 2(G_c/c_0\,b)b^2\nabla d\cdot\nabla\hat{d}\text{d}\Omega$. In the third line, $\partial\Omega$ denotes the boundary of Ω, comprising $\partial\Omega_1$ where displacements are assigned, and $\partial\Omega_2$, which is a direct sum. The first line of the above equation, gives the following equilibrium equations for the displacement

$$\text{div}\mathbf{T}+\underline{b}=0 \ \text{ in } \ \Omega, \ \text{ with b.c.: } \ \mathbf{T}\hat{n}=\underline{s} \ \text{ in } \ \partial\Omega_2 \ \text{ and } \ \underline{u}=\underline{u}_0 \ \text{ in } \ \partial\Omega_1. \tag{2.105}$$

The second line of eqn. (2.104), gives the following yield condition:

$$Y(\nabla\underline{u},d) = g'(d)\psi_{el}(\text{sym}\nabla\underline{u}) + \frac{G_c}{c_0\,b}(\eta'(d)-2b^2\Delta d)\geq 0, \tag{2.106}$$

that, considering $g'(d)\leq 0$, for a fixed $\overline{d}$, $Y(\text{sym}\nabla\underline{u},\overline{d})$ is a decreasing function of $\text{sym}\nabla\underline{u}$. In all damage models, this condition suggests that as deformation increases from an undeformed state, the elastic energy increases. This increment is then diminished by multiplication with $g'(d)<0$ in $Y(\text{sym}\nabla\underline{u},d)$ until the point where the positive component $(\eta'(d))$ of $Y(\text{sym}\nabla\underline{u},d)=0$ is attained, leading to material damage initiation. In this context, the sole contribution to the dissipation rate arises from the damage dissipation, as stated by in equation (2.82). This can be evaluated through both the damage dissipation density potential or the function in Drucker [1952] definition as follows

$$\frac{G_c}{c_0\,b}\dot{\gamma}(d,\nabla d) = \mathcal{D}_d = \mathbf{T}\cdot\text{sym}\nabla\dot{\underline{u}} - \dot{\psi}(\text{sym}\nabla\dot{\underline{u}},d). \tag{2.107}$$

After the divergence theorem application to the left side of this equation, it gives:

$$Y(\text{sym}\nabla\underline{u}, d)\dot{d} = 0, \tag{2.108}$$

that means that one of the two terms (Y or $\dot{d}$) must be equal to zero. From a physical point of view, this condition implies that the damage can change only when the yield condition in eqn. (2.106) is satisfy as equality. Last equation with eqn. (2.106) and the irreversibility condition ($\dot{d} \geq 0$) are also known as Kuhun-Tucker condition.

In the third line of eqn. (2.104), two potential boundary condition for the damage can be inferred. The first scenario suggests the Neumann b.c. that meas $\nabla d \cdot \hat{n} = 0$ in $\partial\Omega$ and the second scenario is the Dirichlet boundary condition, where $d = 0$ in $\partial\Omega$. In all of the next analysis, the Dirichlet boundary condition will be considered.

The characteristics of this model will be detailed in the next section, specifically focusing on a 1D tensile test. This study will be done following the constitutive assumption in Wu [2017] about $\eta(d)$ and $g(d)$ as follows

$$\eta(d) = \xi d + (1-\xi)d^2; \qquad Q(d) = a_1 d + a_1 a_2 d^2 + a_1 a_2 a_3 d^3, \tag{2.109}$$

where respectively with $\xi = 1$ and $\xi = 0$ the AT-1 and AT-2 models described in Ambrosio and Tortorelli [1990] can be included.

1D tensile test

We consider the 1D tensile problem schematized in fig. 2.27. Here, the position vector (x) and displacement vector ($u(x)$) are scalar quantities. In this context, neglecting surfaces and body forces, the equilibrium conditions of eqn. (2.105) becomes:

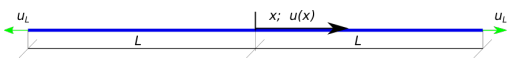

Figure 2.27: 1D tensile test scheme. The boundary displacement (u_L) is applied to $x = L$ and $x = -L$ equal. The center of the sample is considered as the origin of the position scalar x.

$$\frac{\mathrm{d}\sigma}{\mathrm{d}x} = \sigma' = 0; \quad u(-L) = u(L) = u_L, \tag{2.110}$$

where σ is the longitudinal stress over the bar and it assumes the following form:

$$\sigma = g(d)E_0 u'. \tag{2.111}$$

Using last equation, and considering that (by eqn. (2.110)) σ is constant over the bar, the deformation $u'(x)$ can be rewritten ad function of $d(x)$ as it follows

$$u' = \frac{\sigma}{E_0} g^{-1}(d) = \frac{\sigma}{E_0}(1 + \phi(d)), \tag{2.112}$$

where the function $\phi(d)$ is defined in eq. (2.101). Using now the symmetry of the problem (see fig. 2.27), the deformation can be integrated between $x = 0$ and $x = L$ as it follows

$$u_L = \frac{\sigma}{E_0}L + \frac{\sigma}{E_0}\int_0^L \phi(d)\mathrm{d}x = \frac{\sigma}{E_0}L + \frac{\sigma}{E_0}\int_0^{l_f/2} \phi(d)\mathrm{d}x = u_e + w_d, \tag{2.113}$$

where the localization of the damage in a internal length (l_f) is considered and the damage displacement jump (w_d) is defined. The specification of the yield function in eqn. (2.106) involves in

$$Y(u', d) = \frac{g'(d)}{2g^2(d)E_0}\sigma^2 + \frac{G_c}{c_0\, b}(\eta'(d) - 2bd'') = \frac{-\phi'(d)}{2E_0}\sigma^2 + \frac{G_c}{c_0\, b}(\eta'(d) - 2b^2 d''), \tag{2.114}$$

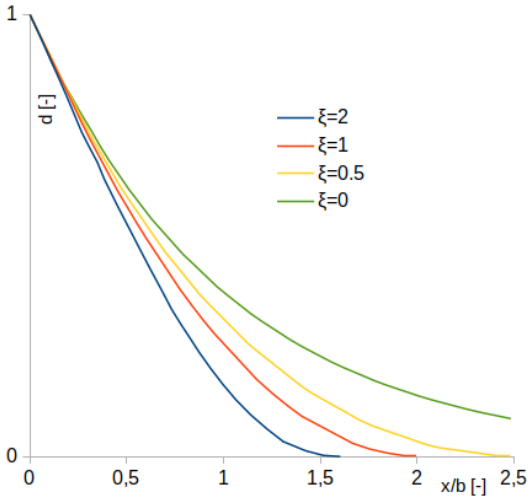

Figure 2.28: Damage profile along the dimensionless position (x/b) for different values of ξ from Wu [2017].

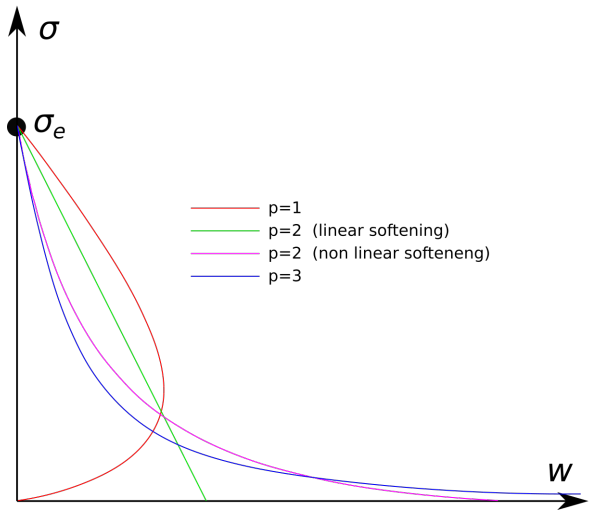

Figure 2.29: cohesive curve for different p from Wu [2017].

where $g'(d) = -g^2(d)\phi'(d)$ is used. The crack onset will be given by the equality in (2.106) with $d = 0$; $\Delta d = 0$ as follows

$$\phi'(0)\sigma_e^2 = \frac{2E_0G_c}{c_0\, b}\eta(0),\ \text{s. t.}\ \sigma_e = \sqrt{\frac{2E_0G_c\xi}{c_0\, b\, a_1}} \rightarrow a_1 = \frac{2E_0G_c}{c_0\, b\sigma_e^2}, \tag{2.115}$$

where also a parameter of $Q(d)$ (a_1) is determined and σ_e is the elastic limit of the stress. Considering now the following equation

$$\overline{Y} = \sigma^2\phi(d) - \frac{2E_0G_c}{c_0\, b}(\eta(d) - b^2(d')^2), \tag{2.116}$$

by its derivation with respect to x, the yield condition (multiplied for $-2E_0$) can be found. For this reason, during the damage evolution, $\overline{Y} = 0$ will be verified. Now, focusing on the point $x = 0$, which is where the damage reaches its maximum value $(d = d_m)$, the non-local term can be deemed negligible due to the symmetry of the problem $(d' = 0)$. From these considerations, the following expression for σ can be derived

$$\sigma(d_m) = \sigma_e\sqrt{\frac{a_1}{\xi}\frac{\eta(d_m)}{\phi(d_m)}}. \tag{2.117}$$

From eqn. (2.116), an expression for d' can be derived as follows:

$$|d'| = \frac{1}{b}\sqrt{\eta(d) - \frac{\sigma^2}{\sigma_e^2}\frac{\xi}{a_1}\phi(d)} = \frac{1}{b}\sqrt{\eta(d) - \frac{\eta(d_m)}{\phi(d_m)}\phi(d)}, \tag{2.118}$$

where eqn. (2.117) is used. This expression can be applied in eqn. (2.113) to explicitly establish an equation for $w_d(d_m)$. These expressions, along with eqn. (2.117), allows the plotting of the cohesive curve, as illustrated in fig. 2.29. This plot illustrates the relationship between the damage-induced displacement jump and the stress presented. Such a curve holds crucial significance in the forthcoming finite elastic model detailed in chapter 3. In the model by Wu [2017], the initial slope of this curve is utilized to

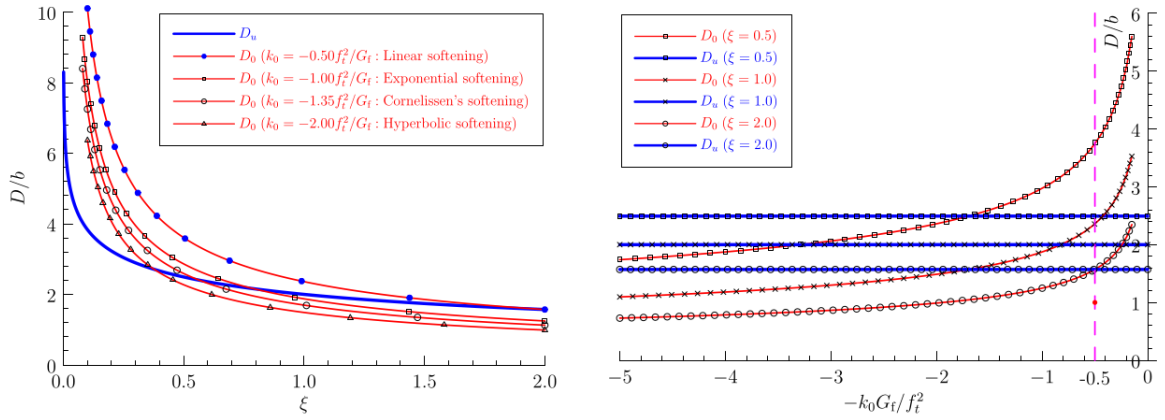

(a) Various parameter $0 \leq \xi \leq 2$

(b) Various initial slope $k_0 < 0$

Figure 2.30: Influence of ξ (a) and of the initial slope of the cohesive curve (k_o) on the half bandwidths of the damage at the crack initiation (D_o) and at the failure ($D_u = l_f/2$) of the sample from Wu [2017].

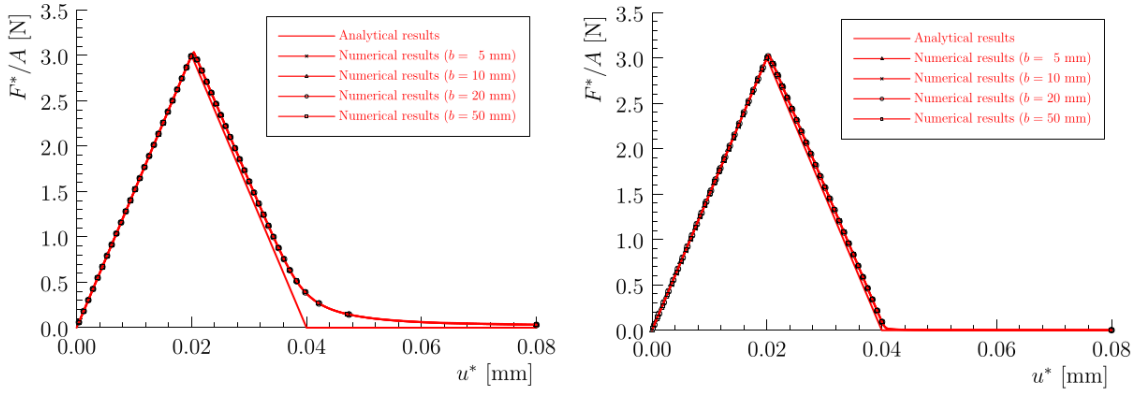

(a) $b/h_{mesh} = 5$

(b) $b/h_{mesh} = 200$

Figure 2.31: Influence of the mesh size h_{mesh} on the precision of the results. In particular the numerical results (also for different values of b) of a 2D uniaxial tensile test are related with the analytical results from Wu [2017].

determine a_2, while a_3 can be determined using $w_d(1)$.

Another significant insight drawn from these equations pertains to the damage profile, allowing for observation of damage localization (refer to fig. 2.28). The localization of damage bands during crack progression heavily relies on the uniform advancement of the crack phase-field (thus, on ξ) and the initial slope of the cohesive curve (k_o) depicted in fig. 2.29. These relationships are depicted in fig. 2.30, highlighting that the extent of localized damage is inversely related to ξ. Furthermore, this length primarily depends on k_o solely during the initial phase of crack evolution. Indeed, applying eqn. (2.118) in the last instant of the crack (when $d_m = 1$ and $\sigma = 0$), the following expression (for $x > 0$) can be deduced

$$\frac{\mathrm{d}d}{\mathrm{d}x} = -\frac{1}{b}\sqrt{\eta(d)}, \quad \text{s. t.} \quad -b\int_{d_m=1}^{0} \frac{1}{\sqrt{\eta(d)}}\mathrm{d}d = \int_0^{D_u} \mathrm{d}x, \quad \text{s. t.} \quad b = \frac{D_u}{\int_0^1 \eta^{-1/2}(d)\mathrm{d}d}; \tag{2.119}$$

where D_u can be measured in the broken sample and the only other parameter that affect the ratio D_u/b is ξ.

One of the final noteworthy features of this model (and, generally, of damage phase-field models) involves the correlation between the maximum mesh size (h_{mesh}), providing numerically accurate results, and the internal length b. This linear relationship is depicted in fig. 2.31, where he fact that changing b, maintaining constant b/h_{mesh} doesn't affect the results, but the variation of b/h_{mesh} moves numerical results away from the analytical.

In the work by Wu [2017], the model described above is extensively compared with various other damage models, proving its high adaptability and generality. Therefore, it serves as a foundational framework for developing a phase-field damage model applicable to finite elasticity. This model will be extended to accommodate both brittle (as in sect. 2.3.1) and pseudo-ductile (as in sect. 2.3.2) rupture types.

2.5.4 Phase field damage model in finite elasticity

One of the first application of the damage phase-field model in finite elasticity can be seen in Miehe and Schänzel [2014]. Here, a damage phase-field model with $\xi = 0$ is merged with a compressible micro mechanical based finite elastic model. The aim is to replicate crack formation in a penny-shaped tension test, involving a simple shear sample ($L = 2mm$ and $H = 0.4mm$) with a horizontal notch parallel to the longer side in the middle of the sample. The sample is stretched in the direction of the shorter side, allowing observation of damage evolution within the horizontal notch. Additionally, these simulations predict the experiments summarized in sect. 2.3.1 and presented in Hocine et al. [2002]. The assumption of $\xi = 0$ implies that the linear term in $\eta(d)$ disappears and, thus its derivative becomes a linear function of the damage such that $\eta'(d = 0) = 0$, while the degradation function is $g(d) = (1 - d)^2$. For this reason, the only one possible deformation that allows $d = 0$ is $\mathbf{C} = \mathbf{I}$. However, in the supposed elastic phase of the material, damage is expected to be minimal, while the rupture phase becomes sudden owing to damage and deformation becoming localized.

The shift from infinitesimal to finite elasticity presents several challenges. These diffi-

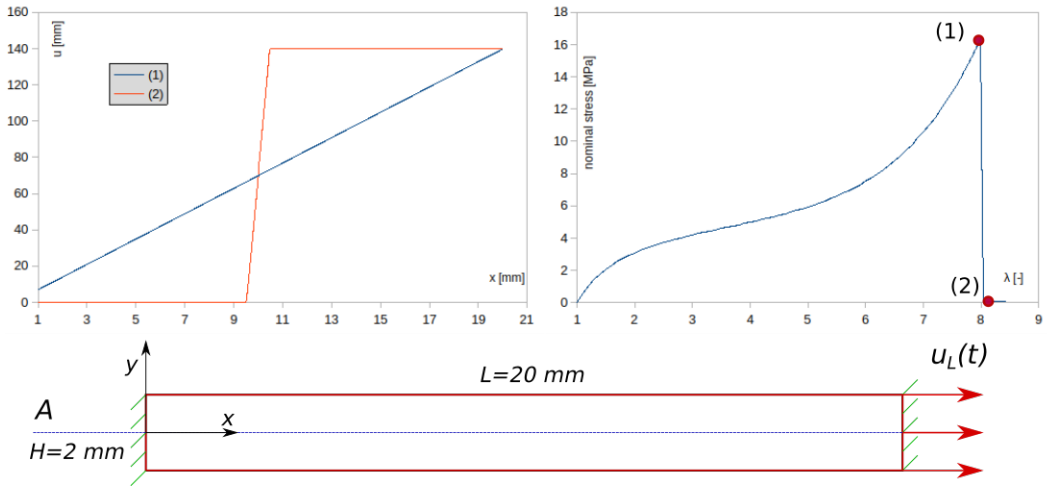

Figure 2.32: 2D tensile test simulation with Lopez-Pamies [2010] model and damage phase-field variable. On bottom the simulation set up, on right the engineer stress-strain curve and on left the x component of the displacement over x axis in the middle of the sample for the two time instant before and after the crack.

culties begin with the nonlinear nature of the models, discussed in chapters 2.4, which necessitate more intricate elastic problem-solving step by step algorithms like Newton-Raphson, more complex than the linear methods used in preceding chapters. These procedures present convergence problems when the solutions of two close instants are very different, as happens in the case of brittle fracture during a tensile test (as shown in fig. 2.32). Also if this phenomenology is welcomed to reproduce the brittle materials' behavior, it makes the incremental resolutions of the elastic problem unstable. For this reason, given the following energy functional

$$\Phi(\underline{u}, d) = \int_{\Omega_0} \underbrace{(1-d)^2}_{g(d)} \psi_{el}(\nabla \underline{u}) + \frac{G_c}{c_0\, b}(\underbrace{d^2}_{\alpha(d)} + b^2(\nabla d)^2) \mathrm{d}\Omega_0, \tag{2.120}$$

a viscous regularization is added in the yield condition as it follows

$$Y(\nabla \underline{u}, d) = g'(d)\psi_{el}(\nabla \underline{u}) + 2\frac{G_c}{c_0\, b}(d - b^2 \Delta d) + \kappa \dot{d} \geq 0, \tag{2.121}$$

where κ is a damage viscosity that regularize the damage growth. The significance of

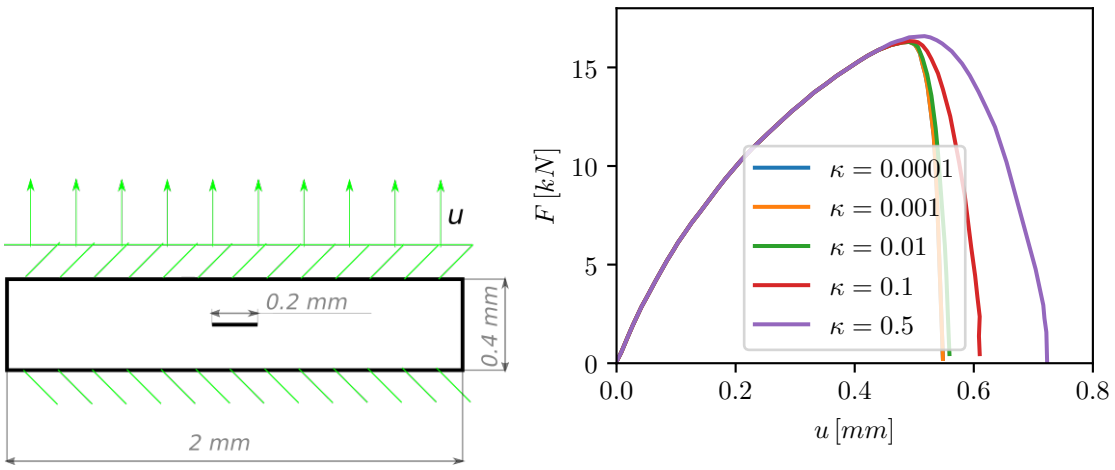

(a) Sample and test set up.

(b) Influence of viscous regularization.

Figure 2.33: Tension test using a penny-shaped geometry incorporates the impact of viscous damage regularization. Specifically, it's evident that the regularization's effect on the solution diminishes as κ approaches zero, indeed the simulation results for $\kappa = 0.0001$ and $\kappa = 0.001$ are not distinguishable. However, it remains significant during the phase characterized by extensive damage growth.

this regularization is depicted in fig. 2.33, illustrating its substantial impact during the phase marked by extensive damage growth. As the rate-dependent model evolves, a key question emerges: is this viscosity merely a form of regularization, or does it represent an inherent material property? This question is analyzed in the fourth chapter, using the rate dependent model. The numerical results presented in this chapter underscore the significant influence of this term, leading to the definition of the damage characteristic time $\tau_d = (\kappa\, c_0\, b)/G_c$. This parameter assesses the characteristic time of the micro-scale damage-related deformation phenomena e.g. strain crystallization (see fig. 2.12) or cavitation (see fig. 2.11), occurring in the fracture process zone (see fig. 2.8), which cannot be evaluated by $\mathbf{F}_v$, as it measures the macro-scale deformations.

In fig. 2.34, the model in Miehe and Schänzel [2014] and the model in Talamini

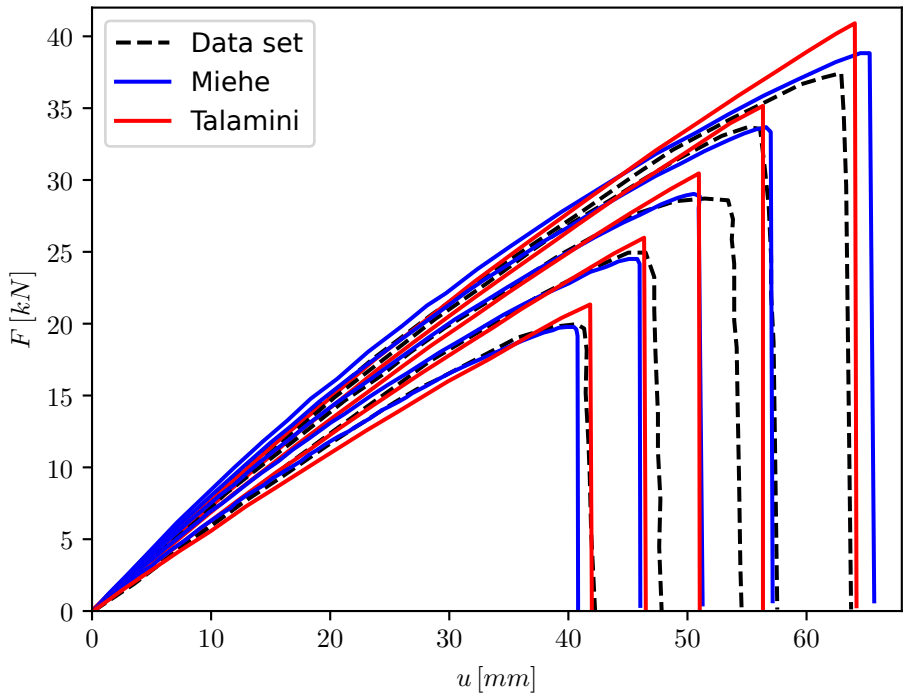

Figure 2.34: Numerical results of model in Miehe and Schänzel [2014] (blue) and Talamini et al. [2018] (red) for the experiments of Hocine et al. [2002] (dot line).

et al. [2018] are fitted to the experiments of Hocine et al. [2002]. In particular the model of Talamini et al. [2018] consists in a micro-mechanical based approach, that derived the elastic strain energy density, the damage dissipation and the other components of the internal energy, from the structure and the interaction of rubber macro-molecules (see sect. 2.1). The main difference between this two models are:

- the inclusion of an effective bond stretch in Talamini et al. [2018], an additional internal variable, which governs the deformation of the individual link within the longer macro-molecule,
- the interpretation of the gradient term in $\gamma(d, \nabla d)$ as an energy-related factor (Miehe and Schänzel [2014]) rather than a contribution to dissipation (Talamini et al. [2018]),
- the assumption, micro-mechanical based, of $\xi = 1 \rightarrow \eta(d) = d$ done in Talamini et al. [2018], that, with $g(d) = (1-d)^2$, implies a brittle fracture behavior.

Specifically, when observing the propagation of a damage front (e.g., in double-network elastomers as described in Millereau et al. [2018], see sec. 2.3.2), the area of maximum damage will extend from a localized point to encompass the entire bar. Throughout this progression, the undamaged section and the region with maximal damage will exhibit $\nabla d = 0$, whereas in the transitional region, $\nabla d \neq 0$. As this region is in motion, it appears more appropriate to regard the gradient term as energetic, although this remains a topic of ongoing debate. For what concerns the assumption of $\xi = 1 \rightarrow \eta(d) = d$, it results in a brittle fracture model and consequently a less gradual rupture of the sample. This distinct behavior is evident in the comparison shown in fig. 2.34, where the stress drop is consistently smoother for the model presented in Miehe and Schänzel [2014] compared

to that in Talamini et al. [2018].

Building upon these two investigations, the upcoming chapter will introduce a rate-independent model. This model will incorporate a damage geometric function capable of ensuring both a fully elastic phase for the material and a gradual fracture, employing $\xi = 2 \rightarrow \eta(d) = 2d - d^2$. Additionally, it will integrate a suitable degradation function aimed at capturing the different post-fracture behavior of materials as observed in Millereau et al. [2018] and Hocine et al. [2002] by a proper calibration of the model parameters.

2.5.5 Phase field damage model in finite viscoelasticity

Numerous theories have included rate dependent contribution into the formulation. The approach proposed in Farrahi et al. [2020], in the context of linear elasticity, includes a kinematic coefficient as in Miehe and Schänzel [2014]), that allows an explicit evaluation of the damage growth rate, as done in eqn. (4.15). The existence of a damage evolution equation allows the overrun of the eventual elastic stress limit, when the loading rate was high enough to exceed the damage rate. By managing and regulating this rate, a consequential implication emerges: the definition of fracture stress remains pertinent predominantly within quasi-static contexts. This circumstance allows for its validity, especially in the proximity of the fracture tip.

Furthermore, in the work of Hakim and Karma [2009], introducing a dependence in the non local energetic term on the direction of the crack surface, the crack propagation is studied in a linear elastic and anisotropic context. This incorporation introduces a pivotal control mechanism governing the direction of fracture propagation.

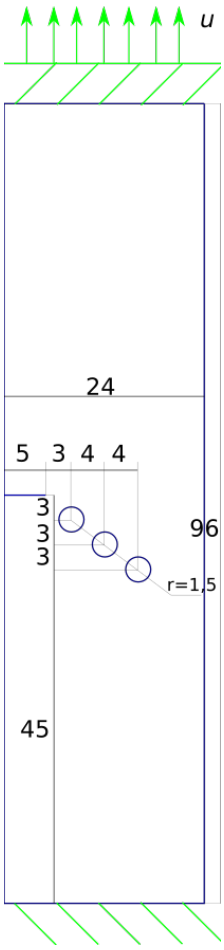

Figure 2.35: Experimental set up for numerical simulation in Yin and Kaliske [2020].

Phase-field damage models have only recently been introduced within a finite viscoelastic models, and one of the earliest examples in the literature is that in Loew et al. [2019], where the behavior of EPDM rubber is reproduced. This work combines the generalized Maxwell rheological model, utilizing the volumetric deformation decomposition method from Holzapfel [1996] (see sect. 2.4.2 and fig. 2.22), with a damage phase-field model as in Miehe et al. [2010b]. Specifically, it employs functions $g(d) = (1-d)^2$ and $\eta(d) = d^2$ and as elastic strain energy density, the model detailed in Yeoh [1993] is chosen, with $\psi_{el} = C_i(I_1 - 3)^i$. In this context, the damage viscosity, introduced in eq. 2.121 by Miehe and Schänzel [2014] is treated as a material's parameter and the solution for the viscous stresses is evaluated as in Holzapfel [1996] by eqn. (2.64). This model's primary drawbacks stem from its initial assumption, $\psi_{neq} = \beta\psi_{eq}$, which restricts the range of energy forms available (as opposed to the model in Kumar and Lopez-Pamies [2016], exposed in sect. 2.4.2, where it isn't necessary). Additionally, it doesn't account the characteristic time of damage as a crucial determinant parameter that governs the fracture propagation rates. Indeed, this parameter goes to limit the speed of damage formation, not allowing properly brittle failure mechanisms, unless a temporal discretization is chosen in which

damage formation is not caught. Moreover, this parameter has also numerical implications that will be shown in the analysis in 4.3.2. Despite these limitations, its significance remains noteworthy as one of the pioneering models of its type. In addition to the model formulation, the article proposes a method for the parameter fitting through various tests like uniaxial tensile, single-edge notch tensile (SENT), and double-edge notch tensile (DENT), all made at different deformation rates, to catch the peculiarity of the rate dependent material's behavior.

In the work of Yin and Kaliske [2020], a model similar to that in Loew et al. [2019] is introduced, featuring an extensive thermodynamic formulation, following Holzapfel [1996], and simulations employing intricate test configurations, exemplified by the scenario depicted in Fig. 2.35, among other tear test setups (in plane and out plane tear test). This model employs a neo-Hooke strain energy density for both the equilibrium and non equilibrium springs, with the following form of volumetric strain energy density

$$\psi^{vol} = K(J - \log(J) - 1), \tag{2.122}$$

where K is the bulk modulus, treated as in Holzapfel [1996] (see sec. 2.4.2). It explores also the application of the subsequent degradation function

$$g(d) = 1 - \sin\left(\frac{d\pi}{2}\right). \tag{2.123}$$

The simulation outcomes demonstrate a strong alignment of the model with the material's behavior, while the article emphasizes the correlation between the material's failure point and the strain rate. While the utilization of the neo-Hooke strain energy density might appear restrictive, the incorporation of various test configurations and model fittings (including those in Loew et al. [2019], the experiments in Hocine et al. [2002] and the in-plane and out plane shear fracture set up) renders the study highly intriguing.

Further compelling insights into the utilization of phase-field variables for finite viscoelasticity are presented in Dammaß et al. [2021] and Dammaß et al. [2023]. These studies delve into not only the mechanical characteristics of EPDM rubber (through experiments detailed in Loew et al. [2019]) but also explore the mechanical behavior of HTPB, a binder employed in solid rocket motor propellants, where the SENT speciment is used to calibrate the parameters and the DENT speciment for the model validation and the analysis. In Dammaß et al. [2023], the energy release rate is considered as dependent on the deformation rate ($G_c = G_c(\mathbf{D})$) to control the dependence of the fracture onset on the strain rate

Across these studies employ the form $\eta(d) = d^2$ (AT-2 in Ambrosio and Tortorelli [1990]), that precludes a purely elastic phase. They also do not consider the viscous term of the damage with its characteristic time, which would help to analyze fracture propagation over time and its development on the various experimental set up. These inquiries will be addressed in the fourth chapter of this thesis, through the development of a viscoelastic phase-field damage model. This numerical study aims to scrutinize the interaction between this characteristic times with the material's characteristic time.

Chapter 3

A cohesive phase field model

The forthcoming chapter introduces a rate-independent model able to replicate material behavior under two distinct conditions: pseudo-static loading (where, at low deformation ratios, the dash-pot in fig.2.22 remains fully relaxed and the non-equilibrium spring remains unloaded) and high strain rates. Under high strain rates, the dash-pot in fig.2.22 lacks the time to relax and it becomes a rigid link. This transformation causes the two springs to function in parallel without any viscous effect. This model is proposed in Ciambella et al. [2022], published in the special issue "The Ogden model of rubber mechanics: Fifty years of impact on nonlinear elasticity".

The proposed model combines the elastic strain energy of Ogden [2003] for the incompressible materials (see eqn. (2.27) or fig. 2.20), with the damage phase field model of Wu [2017], summarized in sect. 2.5.3. The distorsional part of the strain energy density of Ogden [2003], can be seen as a set of n non linear elastic springs as follows

$$\psi_{el}^{D}(\underline{u}) = [\sum_{i}(\frac{\mu_i}{\alpha_i}\sum_{j=1}^{3}(\lambda_j^{\alpha_i} - 1))] = \tilde{\psi}_i(\lambda_1, \lambda_2, \lambda_3), \tag{3.1}$$

where the dependence on the displacement field ($\underline{u}$) of the eigenvalues of $\mathbf{F} = \mathbf{I} + \nabla\underline{u}$, ($\lambda_i(\underline{u})$) is omitted for synthesis and $\tilde{\psi}_j$ means the single spring that compose the system of non linear spring included by the Ogden's formulation. To catch the versatility of this split, that adherent to the so-called Valanis–Landel split in Valanis [2022], it offers the opportunity to simulate the material's behavior across various strain ranges as depicted in fig. 2.2. For instance, in the context of a tensile test, incorporating a spring with an exponent $\alpha_i \in (0; 2]$ and a shear modulus comparable to the mean stress of the test allows replication of behavior in low and moderate strain ranges. However, to model high strains, introducing a spring with a significantly higher exponent and considerably lower shear modulus becomes adequate. While the latter spring's impact remains minimal during Gaussian regimes, it introduces a hardening effect in the high strain regime. An instance illustrating the application of this model is presented in fig. 3.1, demonstrating the modeling of the material examined in the experiments conducted by Corre et al. [2020] (commercial polyurethane), using two $\tilde{\psi}_j$, as outlined earlier. These remarkable properties are exploited to formulate a theory for the cohesive failure of elastomeric materials at large strain. The inclusion of the damage into the hyperelastic energy in eqn. (3.1) is formulated in according to the proposal in Wu [2017] and described in sec. 2.5.3, that is a formulation capable of describing brittle and quasi-brittle failure modes. In particular, for the cohesive phenomena, the damage propagation along the bar is simulated.

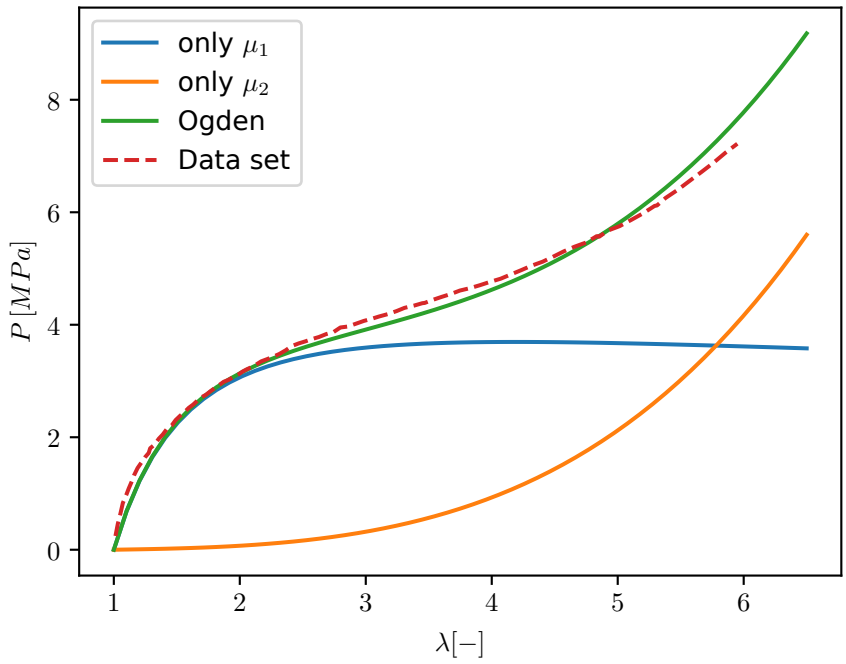

Figure 3.1: Adaptation of the Ogden [2003] model to the material studied in the Corre et al. [2020] experiments by the use of two springs in parallel with $\alpha_1,\ \mu_1 = 0.7,\ 7.3$ and $\alpha_2,\ \mu_2 = 4.7,\ 0.0055$. This engineer stress-strain curve is obtained by a 1D tensile test simulation.

From this point, the chapter reports the formulation and the results of Ciambella et al. [2022].

3.1 Model formulation

The aim of this section is the formulation of the nonlinear damage phase-field elastic model in a three-dimensional plane stress settings, before carrying out in Sec. 3.2 a sensitivity analysis by considering the response of a bar under traction with the assumption analyzed a the end of sec. 2.4.1. The approach adopted to equilibrium is based on a unilateral minimality principle under the condition of irreversibility of the damage field. The same approach has been widely adopted in plasticity Marigo [1989], Del Piero et al. [2007], Lancioni [2015], plasticity with damage Alessi et al. [2014], Lancioni and Alessi [2020] and cohesive damage Wu [2017, 2018].

Throughout the paper we will assume that all fields are sufficiently smooth so that all the calculations can be performed. For a precise definition of the functional spaces needed the reader is referred to Mielke and Roubíček [2015].

3.1.1 State variables

We identify a body with a region Ω_0 of the three-dimensional Euclidean space $\mathcal{E}$, that occupies at some time instant $t = 0$, which we denote as the *reference configuration*. The external boundary $\partial\Omega_0$ is divided into a subset $\partial\Omega_{0\,1}$ in which displacement is applied, and a complementary boundary $\partial\Omega_{0\,2}$ in which surface forces are present. The deformation of the body is the bijective orientation-preserving map $P : \Omega_0 \times [0, t] \to \mathcal{E}$ which assigns

at each point $\underline{X} \in \Omega_0$ a point $\underline{x} = P(\underline{X}, t)$ in the deformed configuration; accordingly we set $\Omega_t = P(\Omega_0, t)$ as the deformed configuration of the body.

At each material point $\underline{X}$, the state of the continuum is identified by the displacement field $\underline{u}(\underline{X}, t)$ and by the damage scalar phase-field variable $d(\underline{X}, t)$. In this formulation, d is a Lagrangean parameter defined on the reference configuration Ω_0. We further denote by $\mathscr{U}$ the space of kinematically admissible displacement field

$$\underline{u}(\underline{X}, t) \in \mathscr{U} := \{\underline{u} : \underline{u}(\underline{X}, t) = \underline{u}^* \ \ \forall \underline{X} \in \partial\Omega_0^u\}, \tag{3.2}$$

and with $\mathscr{D}$ the set of the admissible damage field

$$d(\underline{X}, t) \in \mathscr{D} := \{d : d(\underline{X}, t) \in [0, 1]\}.$$

We denote the deformation gradient by $\mathbf{F} = \mathbf{I} + \nabla\underline{u}$, where ∇ is the gradient operator defined with respect to the reference coordinates $\underline{X}$.

The variations $\tilde{\underline{u}}$ and $\tilde{d}$ will be used in the application of the minimality principle to derive the governing equations of the problem. These have to satisfy homogeneous boundary conditions, and as such belong to the following sets

$$\tilde{\underline{u}}(\underline{X}, t) \in \widetilde{\mathscr{U}} := \{\tilde{\underline{u}}(\underline{X}, t) = \underline{0} \ \ \forall \underline{X} \in \partial\Omega_{0\,1}\}, \tag{3.3}$$

$$\tilde{d}(\underline{X}, t) \in \widetilde{\mathscr{D}} := \{\tilde{d} : \tilde{d}(\underline{X}, t) \geq 0 \ \text{ for almost all } \ \underline{X} \in \Omega_0\}, \tag{3.4}$$

the latter being the convex cone of positive damage rate. As it will be apparent in the following sections, in the present formulation the damage variable can only increase (no–healing).

For the sake of conciseness the explicit dependence on the position $\underline{X}$ and time t will be omitted from all variables, except when needed.

3.1.2 Energy functional

The behavior of the continuum is characterized at each material point $\underline{X}$ and at each time instant t by two state variables $\{\underline{u}, d\}$ in $\mathscr{U} \times \mathscr{D}$, and by a state function φ, which gives the energy density at each material point; φ depends on the local strain $\mathbf{F}(\underline{X})$, on the value of the damage variable $d(\underline{X})$ and on the local value of damage gradient $\nabla d(\underline{X})$, with the following functional form

$$\varphi(\nabla\underline{u}, d, \nabla d) = \overbrace{\psi(\mathbf{I} + \nabla\underline{u}, d)}^{\text{Elastic energy}} + \overbrace{\frac{G_c}{c_0\, b}\eta(d) + b\,\frac{G_c}{c_0}|\nabla d|^2}^{\text{Fracture energy}}, \tag{3.5}$$

composed by three terms:

- $\psi(\mathbf{I} + \nabla\underline{u}, d)$ is the *elastic energy* in the damage state d;
- $G_c\eta(d)/(c_0\, b)$ can be interpreted as the *fracture dissipation potential* during a homogeneous damage process with $\nabla d = 0$;
- $b\, G_c|\nabla d|^2/c_0$ is the *nonlocal* term which limits the possibility of damage localization in an infinitesimal region of the body (see for instance Pham et al. [2011]); such a term introduces an intrinsic length scale which controls the size of the damage localization zone.

The second and third terms in Eq. (3.5) constitute the *non-local fracture energy density*, in which the constitutive parameter G_c is the *critical elastic energy release rate*, b represents an internal length that regularizes the sharp crack and $c_0 := 4\int_0^1 \sqrt{\eta(d)}\,\mathrm{d}d$ is a scaling parameter in according with the previous sec. 2.5.3.

We further assume that the elastic strain energy density ψ can be multiplicative decomposed as

$$\psi(\mathbf{I} + \nabla\underline{u}, d) = g(d)\ \psi_{el}(\mathbf{I} + \nabla\underline{u})\,, \tag{3.6}$$

in which $\psi_{el}(\mathbf{I} + \nabla\underline{u})$ is the elastic energy density of the neat material, and $g(d)$ is the *degradation function* describing the degradation of the stored energy with evolving damage. The bulk strain energy density ψ_{el} is a continuous isotropic function such that $\psi_{el}(\cdot)$ is frame indifferent. Such a requirement, as mentioned in sec. 2.4, implies that, for any given deformation $\mathbf{F}$, one has $\psi_{el}(\mathbf{Q}^T\mathbf{F}\mathbf{Q}) = \psi_{el}(\mathbf{F})$ (isotropic response) and $\psi_{el}(\mathbf{Q}^T\mathbf{F}) = \psi_{el}(\mathbf{F})$ (frame indifference) for every rotation matrix $\mathbf{Q}$.

The energetic degradation function $g(d)$ plays an important role in determining the properties of the material during the onset of the fracture and in the post-elastic regime as explained in secs. 2.5.2 and 2.5.3.[1] Motivated by the analysis presented in Wu [2017], the following form for the degradation function g is considered

$$g(d) := \frac{(1-d)^2}{(1-d)^2 + a_1\ \underbrace{d(1 + a_2\,d + a_2 a_3\,d^2)}_{Q(d)}}, \tag{3.7}$$

where a_1, a_2 and a_3 are constitutive parameters, whose calibration allows the description of different fracture modes from brittle to pseudo-ductile as shown in Sec. 3.2 with uniaxial numerical tests. The chosen form of g heavily affect the softening behavior once crack is initiated. Specifically, the function $Q(d)$ can be interpreted as a Taylor expansion of a certain function of d around $d = 0$ (integer material). This explains why, as discussed in sect. 3.2.5, the different parameters a_i influence the material's behavior after the damage initiation based on their respective index i. Indeed, a_1 solely determines the onset of fracture, a_2 affects the slope of the cohesive curve at the onset, and a_3 reflects the material's behavior upon complete fracture. For this reason, as the complexity of the material's behavior post-fracture onset increases, additional parameters (a_4, a_5, etc.) could be included to improve the correspondence between the simulations and the material's response, whereas in the case of brittle materials, parameter a_3 becomes superfluous.

The dissipated energy density plays a significant role in the evolution of the damage as well. As said in sec. 2.5.4, $\xi = 1$ will be assumed and the following quadratic expression of η is obtained:

$$\eta(d) = 2\,d - d^2, \tag{3.8}$$

in a way that $\eta(0) = 0$ and $\eta(1) = 1$. With this assumption, the scaling parameter c_0 becomes $c_0 = 4\int_0^1 \sqrt{2d - d^2}\,\mathrm{d}d = \pi$. It's important to point out that different choices of ξ can be made for the function $\eta(d)$, as exposed in sect. 2.5.3.

With the definition eqn. (3.5) of the state variable φ, we are in the position of defining the total energy stored in the material during the deformation process. For each admissible pair $(\underline{u}, d) \in \mathscr{U} \times \mathscr{D}$, the total energy of the continuum is

$$\mathcal{I}(\underline{u}, d) = \int_{\Omega_0} \varphi(\nabla\underline{u}, d, \nabla d)\mathrm{d}\Omega_0 - \int_{\Omega_0} \underline{b}_0 \cdot \underline{u}\mathrm{d}\Omega_0 - \int_{\partial\Omega_{0\,2}} \underline{s}_0 \cdot \underline{u}\mathrm{d}\partial\Omega_{0\,2}, \tag{3.9}$$

[1] In the numerical examples carried out in Sec. 3.3 a small positive value of the degradation function is assumed when the material is fully broken. This is a standard technique to guarantee that the numerical problem remains well-posed for broken specimen.

$\underline{b}_0$ and $\underline{s}_0$ being the forces per unit of reference volume and area respectively, the latter applied on the part of the boundary $\partial\Omega_{0\,2}$. These latter terms represent (minus) the work expended by the external forces.

3.1.3 Governing equations

The derivation of the governing equations of the problem, including the damage evolution, is carried out following the classical variational approach to fracture mechanics (as in sec. 2.5.2, see for instance Pham et al. [2011] or Marigo et al. [2016]) which consists of:

1. the *damage irreversibility* condition $\dot{d}(\underline{X}, t) \geq 0$ and $d(\underline{X}, 0) = 0$,
2. a *stability criterion*, which is indeed a necessary condition for the unilateral minimality condition on the functional eqn. (3.9),
3. the *energy balance principle*, that states that the total energy at time t is equal to the work of the external forces up to time t.

A posteriori it is shown that, under the imposed constitutive assumptions, the *dissipation inequality*, that is the second principle of thermodynamics, is also satisfied, as shown in sec. 2.5.

Stability condition. Starting from an undamaged state at $t = 0$, we say that the process evolves through stable equilibrium configurations if and only if at each time instant the system attains a local minimum of the total energy (3.9). This leads us on introducing the following *stability condition*:

$$\begin{aligned} &\text{For each } t > 0\ , \{\underline{u}, d\} \in \mathscr{U} \times \mathscr{D} \text{ is stable iff} \\ &\forall \{\tilde{\underline{u}}, \tilde{d}\} \in \widetilde{\mathscr{U}} \times \widetilde{\mathscr{D}}, \exists \bar{h} > 0 :\ \forall h \in [0, \bar{h}], \quad \mathcal{I}(\underline{u}, d) \leq \mathcal{I}(\underline{u} + h\tilde{\underline{u}}, d + h\tilde{d}), \end{aligned} \tag{3.10}$$

with the initial condition $d(\underline{X}, 0) = 0$.

The variational inequality in eqn. (3.10) is satisfied if the Gâteaux derivative of the functional $\mathcal{I}$ at $\{\underline{u}, d\}$ is positive for each set of test functions, in particular $\tilde{d}$ being in the convex cone defined by $\widetilde{\mathscr{D}}$. Formally we write

$$\partial\mathcal{I}(\underline{u}, d)[\tilde{\underline{u}}, \tilde{d}] \geq 0, \qquad \forall \{\tilde{\underline{u}}, \tilde{d}\} \in \widetilde{\mathscr{U}} \times \widetilde{\mathscr{D}}, \tag{3.11}$$

with

$$\partial\mathcal{I}(\underline{u}, d)[\tilde{\underline{u}}, \tilde{d}] = \int_{\Omega_0} \mathbf{P} \cdot \nabla\tilde{\underline{u}} - \Sigma\,\tilde{d} + \underline{q} \cdot \nabla\tilde{d}\mathrm{d}\Omega_0 - \int_{\Omega_0} \underline{b}_0 \cdot \tilde{\underline{u}} + \int_{\Omega_{0\,2}} \underline{s}_0 \cdot \tilde{\underline{u}}\mathrm{d}\partial\Omega_{0\,2}, \tag{3.12}$$

where the dual quantities $\mathbf{P}$, Σ and $\underline{q}$ are obtained from the energy density (3.5) as

$$\mathbf{P} = \frac{\partial\psi}{\partial\mathbf{F}} = g(d)\sum_{i=1}^{2} \frac{\partial\psi_{el}}{\partial\lambda_i}\hat{b}_i \otimes \hat{c}_i \qquad \text{(Piola stress tensor)} \tag{3.13}$$

$$\Sigma = -\frac{\partial\varphi}{\partial d} = -g'\psi_{el} - \frac{G_c}{\pi b}\,\eta' \qquad \text{(Energy release rate density)} \tag{3.14}$$

$$\underline{q} = \frac{\partial\varphi}{\partial\nabla d} = \frac{2G_c b}{\pi}\nabla d \qquad \text{(Damage flux vector)} \tag{3.15}$$

where the Piola stress $\mathbf{P}$ being given whit the *Plane stress state* as described at the end of sec. 2.4.1 with the strain energy density in terms of the principal stretches λ_1, λ_2.

Upon substitution of eqns. (3.13)-(3.14)-(3.15) into eqn. (3.12) and integration by parts, the variational inequality in eqn. (3.11) gives

$$\int_{\Omega_0} \big(\mathrm{Div}\mathbf{P} + \underline{b}_0\big) \cdot \underline{\tilde{u}} \mathrm{d}\Omega_0 + \int_{\partial\Omega_{0\,2}} \big(\underline{s}_0 - \mathbf{P}\hat{n}_0\big) \cdot \underline{\tilde{u}} \mathrm{d}\Omega_0 = 0, \tag{3.16}$$

$$-\int_{\Omega_0} \big(\mathrm{Div}\underline{q} + \Sigma\big)\, \tilde{d} \mathrm{d}\Omega_0 + \int_{\partial\Omega_0} \big(\underline{q} \cdot \hat{n}_0\big)\, \tilde{d} \mathrm{d}\partial\Omega_0 \geq 0, \tag{3.17}$$

where latter is evaluated as inequality since $\tilde{d}$ belongs to the convex cone $\widetilde{\mathscr{D}}$.

By the classical localization argument, we obtain from eqn. (3.16) the standard macroscopic balance equation with boundary conditions

$$\begin{aligned} &\mathrm{Div}\mathbf{P} + \underline{b}_0 = \underline{0}, \quad \text{on } \Omega_0, \\ &\mathbf{P}\hat{n}_0 = \underline{s}_0, \qquad\quad \text{on } \partial\Omega_{0\,2}, \end{aligned} \tag{3.18}$$

and from eqn. (3.17) the damage threshold condition

$$\begin{aligned} &\mathrm{Div}\underline{q} + \Sigma \leq 0, \quad \text{on } \Omega_0, \\ &\underline{q} \cdot \hat{n}_0 \geq 0, \qquad\quad \text{on } \partial\Omega_0, \end{aligned} \tag{3.19}$$

with the corresponding flux condition on the boundary.

On using the definition of the energy release rate eqn. (3.14) and of the damage flux vector eqn. (3.15), we can rewrite the damage threshold condition eqn. $(3.19)_1$ as

$$Y(\nabla\underline{u}, d, \Delta d) := g'(d)\psi_{el}(\mathbf{I} + \nabla\underline{u}) + \frac{G_c}{\pi}\big(\frac{1}{b}\eta'(d) - 2\,b\,\Delta d\big) \geq 0, \tag{3.20}$$

where we have defined the so-called *damage yield function* Y. In the interior region where damage has yet to occur one has $g'(0)\psi_{el}(\mathbf{I} + \nabla\underline{u}) < \frac{G_c}{\pi b}\eta'(0)$ and since $g'(d) < 0$ the elastic energy density ψ_{el} is bounded.

We should remark once more that the damage threshold condition eqn. (3.20) is indeed a necessary condition for the state $\{\underline{u}, d\}$ to be stable. Indeed if eqn. (3.20) is satisfied everywhere in the domain as a strict inequality, then the derivative eqn. (3.11) is strictly positive, and $\{\underline{u}, d\}$ is a stable state; on the other hand, if there are points in which the damage yield function is zero, then the stability of the state is given by the second derivative of the functional $\mathcal{I}$. This latter case will be discussed in Sec. 3.2 for the one-dimensional problem of a bar under traction.

Energy balance. On assuming that the evolution is smooth in time, the energy balance principle requires that the rate of the internal energy equals the working of external forces at each time instant, that is

$$\frac{d}{dt}\int_{\Omega_0} \varphi(\nabla\underline{u}, d, \nabla d) d\Omega_0 = \int_{\Omega_0} \underline{b}_0 \cdot \dot{\underline{u}} \mathrm{d}\Omega_0 + \int_{\partial\Omega_{0\,2}} \underline{s}_0 \cdot \dot{\underline{u}} \mathrm{d}\partial\Omega_{0\,2}, \tag{3.21}$$

which, upon using the macroscopic balance eqn. (3.18), gives

$$\int_{\Omega_0} -\big(\mathrm{Div}\underline{q} + \Sigma\big)\, \dot{d} \mathrm{d}\Omega_0 + \int_{\partial\Omega_0} \big(\underline{q} \cdot \hat{n}_0\big)\, \dot{d} \mathrm{d}\partial\Omega_0 = 0. \tag{3.22}$$

Since each integrand is non negative by the balance equation (3.19), and the damage irreversibility condition requires that $\dot{d} \geq 0$, the above energy balance equation is satisfied

if its integrands vanish. These requests give the Kuhn-Tucker conditions for the threshold function eqn. (3.20):

$$\begin{cases} Y(\nabla \underline{u}, d, \Delta d) = 0, & \text{if } \dot{d} > 0, \\ Y(\nabla \underline{u}, d, \Delta d) > 0, & \text{if } \dot{d} = 0, \end{cases} \tag{3.23}$$

supplemented by Neumann-type boundary condition $\nabla d \cdot \hat{n}_0 = 0$ on $\partial\Omega_0$.

Remark 1 (Evolution problem). The evolution problem arising from stability condition and energy balance is usually solved numerically in an incremental form. The problem is discretized in time, and at each time step the rates $\{\dot{\underline{u}}, \dot{d}\}$ are computed through a staggered minimization scheme obtained by alternating the minimization between $\dot{\underline{u}}$ and $\dot{d}$, keeping the other variable constant. This numerical procedure is indeed a standard approach to solve variational problems like the present one (see for instance Farrell and Maurini [2017]).

Remark 2 (Energy dissipation). The second principle of thermodynamics requires that, for each admissible state $\{\underline{u}, d\}$, the external working be equal to or larger than the rate of the free energy, i.e.,

$$\delta = \int_{\Omega_0} \underline{b}_0 \cdot \dot{\underline{u}} \mathrm{d}\Omega_0 + \int_{\Omega_0 2} \underline{s}_0 \cdot \dot{\underline{u}} - \frac{\mathrm{d}}{\mathrm{d}t} \int_{\Omega_0} \mathcal{F} \mathrm{d}\Omega_0 \geq 0, \tag{3.24}$$

where $\mathcal{F} = \mathcal{F}(\nabla \underline{u}, d, \nabla d)$ is the free energy density. On using the energy balance equation (3.21) and the definitions in eqns. (3.5) and (3.13)-(3.15), the dissipation inequality (3.24) is satisfied if

$$\left(\mathbf{P} - \frac{\partial \mathcal{F}}{\partial \mathbf{F}}\right) \cdot \nabla \dot{\underline{u}} - \left(\Sigma + \frac{\partial \mathcal{F}}{\partial d}\right) \dot{d} + \left(\underline{q} - \frac{\partial \mathcal{F}}{\partial \nabla d}\right) \cdot \nabla \dot{d} \geq 0. \tag{3.25}$$

If we assume that $\mathbf{P}$ and $\underline{q}$ are energetic

$$\mathbf{P} = \frac{\partial \mathcal{F}}{\partial \mathbf{F}}, \qquad \underline{q} = \frac{\partial \mathcal{F}}{\partial \nabla d}, \tag{3.26}$$

and that Σ is made of elastic and dissipative terms

$$\Sigma = \Sigma_{\text{el}} + \Sigma_{\text{diss}}, \quad \text{with} \quad \Sigma_{\text{el}} = -\frac{\partial \mathcal{F}}{\partial d} \quad \text{and} \quad \Sigma_{\text{diss}} = -\frac{G_c}{\pi b} \eta', \tag{3.27}$$

inequality eqn. (3.25) reduces to

$$\frac{G_c}{\pi b} \eta' \dot{d} \geq 0, \tag{3.28}$$

that is satisfied since $\eta' = 2(1 - d) \geq 0$ from the definition in Eqn. (3.8). By comparing eqns. (3.26) and (3.27) with eqns. (3.13)-(3.15), we obtain the expression of the free-energy density

$$\mathcal{F}(\underline{u}, d, \nabla d) = \psi(\mathbf{I} + \nabla \underline{u}, d) + \frac{1}{\pi} G_c \, b |\nabla d|^2. \tag{3.29}$$

Here, by following the approach in Talamini et al. [2018], we have assumed that the damage non-local energy is stored. However, its thermodynamic nature is still debated. In Miehe and Schänzel [2014], Marigo et al. [2016], Wu [2018], it is assumed that is a dissipative term. This assumption is motivated by the fact that the sum of the second and third term in eqn. (3.5) tends to the fracture energy when the internal length b goes to zero.

Remark 3 (Internal length). The internal length b in eqn. (3.5) can be related to the damage bandwidth l_f at complete fracture, that is the support of the damage function when $\max\{d\} = 1$, by solving the equilibrium problem of a fractured bar with a passing-through transversal crack. In this case, strains vanish because the bar is broken into two parts, and the strain energy density ϕ nullifies. Thus the balance equation $(3.23)_1$ reduces to $2\,b\,\Delta d - \frac{1}{b}\eta'(d) = 0$. On integrating it over a line orthogonal to the crack surface (see Pham et al. [2011] or Wu [2017] for details on the calculation), it gives

$$b = \frac{l_f}{2\int_0^1 \frac{1}{\sqrt{\eta(d)}}\mathrm{d}d}\,,$$

that, by assuming the quadratic expression of $\eta(d)$ in (3.8), reduces to

$$b = \frac{l_f}{\pi}. \tag{3.30}$$

3.1.4 Recap of all modelling equations

By following the classical approach to variational fracture mechanics enunciated in the three principles (1)., (2). and (3). of Sec. 3.1.3 we have arrived at the following equations governing the macroscopic balance

$$\boxed{\begin{array}{lll}\text{Macroscopic balance:} & \mathrm{Div}\mathbf{P} + \underline{b}_0 = \underline{0} & \text{on } \Omega_0 \\ & \mathbf{P}\hat{n}_0 = \underline{s}_0 & \text{on } \partial\Omega_0\end{array}} \tag{3.31}$$

together with Kuhn-Tucker conditions for the damage evolution problem

$$\boxed{\begin{array}{ll}\text{Damage irreversibility:} & \dot{d}(\underline{X},t) \geq 0 \\ \text{Damage threshold:} & Y(\nabla\underline{u}, d, \Delta d) \geq 0 \\ \text{Energy balance:} & Y(\nabla\underline{u}, d, \Delta d)\dot{d} = 0\end{array}} \tag{3.32}$$

with initial condition $d(\underline{X}, 0) = 0$. The Piola stress tensor $\mathbf{P}$ and the damage threshold function Y are

$$\begin{aligned}\mathbf{P} &= g(d)\sum_{i=1}^{2}\frac{\partial\hat{\psi}}{\partial\lambda_i}\hat{b}_i\otimes\hat{c}_i\,,\\ Y &= g'(d)\psi_{el} + G_c\big(\frac{1}{l_f}\eta' - \frac{2}{\pi^2}\,l_f\,\Delta d\big),,\end{aligned} \tag{3.33}$$

with $\hat{b}_i$ and $\hat{c}_i$ eigenvectors of the left and right Cauchy–Green strain tensors (see sec. 2.4, and

$$\begin{aligned}\psi_{el} &= \frac{\mu_n}{\alpha_n}(\lambda_1^{\alpha_n} + \lambda_2^{\alpha_n} + (\lambda_1\lambda_2)^{-\alpha_n} - 3)\,,\\ g(d) &= \frac{(1-d)^2}{(1-d)^2 + a_1\,d(1 + a_2\,d + a_2a_3\,d^2)}\,,\\ \eta &= 2\,d - d^2\,.\end{aligned} \tag{3.34}$$

The constitutive parameters included into the formulation are the elastic moduli μ_n and exponents α_n of the strain energy density ψ_{el}, the fracture energy release rate G_c, the internal length l_f, and the polynomial coefficients a_1, a_2 and a_3 of the degradation function g. In the next Sect. 3.2.5, strategies to calibrate the constitutive parameters are discussed.

3.2 1D tension test

In order to fully exploit the capabilities of the proposed model, the uniaxial problem of a bar under tension is going to be studied in this section. Such a simplified example will allows us to solve the governing equations in semi-analytical form, and assess thoroughly the role of the different constitutive coefficients that appears in the model.

3.2.1 Problem definition

We consider a bar of length L and cross-section area A_0. The reference configuration is described through a triad of orthonormal vector $\{\hat{e}_1, \hat{e}_2, \hat{e}_3\}$, with $\hat{e}_1$ being the main axis of the bar and $\hat{e}_3$ and $\hat{e}_2$ the thickness direction, i.e.,

$$\Omega_0 = \{\underline{X} : \underline{X} = x_1\,\hat{e}_1 + x_2\,\hat{e}_2 + x_3\,\hat{e}_3,\ x_1 \in (0,\ell), \big(x_2, x_3\big) \in A_0\}.$$

The equilibrium problem can be solved as in sect. 2.4.1 for the *Uniaxial stress condition*, where the following form of deformation gradient is considered:

$$\mathbf{F}(x_1) = \lambda(x_1)\,\hat{e}_1 \otimes \hat{e}_1 + \frac{1}{\sqrt{\lambda(x_1)}}\,\big(\hat{e}_2 \otimes \hat{e}_2 + \hat{e}_3 \otimes \hat{e}_3\big), \tag{3.35}$$

such that the principal stretches are $\lambda_1 = \lambda(x_1)$, $\lambda_2 = \lambda_3 = (\lambda(x_1))^{-1/2}$, $J = 1$, and all fields depend only on the longitudinal coordinate x_1, which, from now on, we call x without the risk of confusion.

The displacement of the bar axis is $u(x)$, and the longitudinal stretch $\lambda(x)$ can be computed from the latter *via*

$$\lambda(x) = 1 + u'(x)\,, \tag{3.36}$$

with the boundary conditions

$$u(0) = 0, \quad u(L) = \varepsilon L, \tag{3.37}$$

with $\varepsilon \geq 0$ a control parameter, that represents the dimensionless displacement applied at the right end side of the bar.

We assume the damage field to be constant within the bar cross-section, so that it depends only on the abscissa x, i.e., $d = d(x)$ and satisfies homogeneous boundary conditions at both ends, i.e.,

$$d(0) = d(L) = 0, \tag{3.38}$$

meaning that no crack can appear at the extremities. Indeed, cracks near the clamping are avoided in the experiments by using dog-bone shaped specimen.

In this 1D-setting, the energy density of the bar takes the following form

$$\varphi(\lambda, d, d') = g(d)\phi_{el}(\lambda) + G_c\big(\frac{1}{l_f}\eta(d) + \frac{l_f}{\pi^2}\,d'^{\,2}\big)\,, \tag{3.39}$$

where we have indicated by ϕ_{el} assumes the form shown in sect. 2.4.1 for the *Uniaxial stress condition* as a function of the only variable λ.

The only non zero component of the Piola stress is the one directed along the bar main axis, i.e., $P = \mathbf{P}\,\hat{e}_1 \cdot \hat{e}_1$, with

$$P = g(d)\,\psi'_{el}(\lambda), \tag{3.40}$$

that, by applying the definition of the Ogden's strain energy density, gives

$$P = g(d)\sum_{n=1}^{N}\frac{\mu_n}{\lambda}\big(\lambda^{\alpha_n} - \lambda^{-\frac{\alpha_n}{2}}\big).$$

The macroscopic balance equation (3.18) can be rewritten as

$$P'(x) = 0, \tag{3.41}$$

meaning that the stress is constant along the bar. The reduced damage threshold condition eqn. $(3.32)_2$ with the deformation eqn. (3.35) yields the following form of the one-dimensional threshold function

$$Y(\lambda, d, d'') = g'(d)\psi_{el} + G_c\big(\frac{1}{\ell_f}\eta'(d) - \frac{2\ell_f}{\pi^2}\,d''\big) \geq 0. \tag{3.42}$$

3.2.2 Incremental Evolution

Following the analysis in Lancioni and Yalçinkaya [2019], we now solve the incremental evolution problem for both displacement and damage variables starting from a known solution $\{u, d\}$ achieved at a certain time instant t. In doing so, we assume a uniform discretization of the time axis, we call Δt the time step, and we expand both displacement and damage fields at the first order in Δt:

$$u(x, t+\Delta t) = u(x,t) + \Delta t\,\dot{u}(x,t), \quad d(x,t+\Delta t) = d(x,t) + \Delta t\,\dot{d}(x,t), \tag{3.43}$$

such that

$$\dot{u}(0,t) = 0, \quad \dot{u}(L,t) = \dot{\varepsilon}L, \quad \dot{d}(0,t) = 0, \quad \dot{d}(L,t) = 0. \tag{3.44}$$

with $\dot{\varepsilon}$ the rate of the applied displacement at the right end of the bar.

At each time instant the solution of the incremental problem requires the evaluation of the unknown rates $\{\dot{u}, \dot{d}\}$ obtained by imposing the stability condition in eqn. (3.11) and the energy balance condition in eqn. (3.23) for the solution $\{u + \tau\dot{u}, d + \tau\dot{d}\}$.

The total energy functional in eqn. (3.9), with null volume forces, is expanded at the second order as

$$\mathcal{I}(u+\Delta t\dot{u}, d+\Delta t\dot{d}) \simeq \mathcal{I}(u,d) + \Delta t\,\dot{\mathcal{I}}(u,d,\dot{u},\dot{d}) + \frac{1}{2}\Delta t^2\,\ddot{\mathcal{I}}(u,d,\dot{u},\dot{d}) = \mathcal{I}(u,d) + \Delta t\,\mathcal{J}(\dot{u},\dot{d}), \tag{3.45}$$

in which we have defined the following functional of the displacement and damage rates

$$\begin{aligned}\mathcal{J}(\dot{u},\dot{d}) = A_0\int_0^L \big[g(d)\psi'_{el}\dot{u}' + (g'(d)\psi_{el} + \frac{G_c}{l_f}\eta')\dot{d} + \frac{2}{\pi^2}G_c l_f d'\dot{d}'\big]\,\mathrm{d}x \\ + \frac{1}{2}\,\Delta t A_0\int_0^L \big[\omega\psi''_{el}\dot{u}'^2 + (g''(d)\psi_{el} + \frac{G_c}{l_f}\eta'')\dot{d}^2 + 2g'(d)\psi'_{el}\dot{u}'\dot{d} + \frac{2}{\pi^2}G_c l_f \dot{d}'^2\big]\,\mathrm{d}x.\end{aligned} \tag{3.46}$$

Stability and energy balance, expressed by relations (3.11) and (3.21) in the three-dimensional formulation of Sec. 3.1, are rewritten in the following form

$$\begin{aligned}&\partial\mathcal{J}(\dot{u},\dot{d})[\tilde{\dot{u}},\tilde{\dot{d}}] \geq 0, \text{ for any } \{\tilde{\dot{u}},\tilde{\dot{d}}\} \text{ such that } \tilde{\dot{u}} = \tilde{\dot{d}} = 0 \text{ at } x = 0,\, L, \text{ and } \tilde{\dot{d}} \geq 0, \\ &\frac{d}{d\Delta t}\mathcal{I}(u+\Delta t\dot{u}, d+\Delta t\dot{d}) = \frac{d}{d\Delta t}\Big(\Delta t\,\mathcal{J}(\dot{u},\dot{d})\Big) = 0.\end{aligned} \tag{3.47}$$

By performing calculations analogous to those followed in Sect. 3.1.3 to deduce the governing equations (3.18) and (3.19) from the stability condition in eqn. (3.11), and the evolution relations in eqns.(3.23) from the energy balance in eqn. (3.21), we obtain the following macroscopic evolution equation

$$P' + \Delta t \dot{P}' = \frac{d}{dx}(\,\psi'_{el}) + \Delta t \frac{d}{dx}(g\,\psi''_{el}\dot{u}' + g'\psi'_{el}\dot{d}\,) = 0, \tag{3.48}$$

together with the set of Kuhn-Tucker conditions that govern the evolution of the damage field

$$\dot{d} \geq 0, \quad Y + \Delta t \dot{Y} \geq 0, \quad (Y + \Delta t \dot{Y})\,\dot{d} = 0, \tag{3.49}$$

with $\dot{Y}$ computed from (3.42) as

$$\dot{Y} = g'\psi'_{el}\dot{\lambda} + \Big(\frac{G_c}{\ell_f}\eta'' + \omega''\psi_{el}\Big)\dot{d} - \frac{2}{\pi^2}G_c\ell_f\dot{d}''\,. \tag{3.50}$$

These conditions state that, at each point, the damage can increase only if the yield function $f + \Delta t\dot{Y}$ is equal to zero.

3.2.3 Damage onset

At the beginning of the loading process the damage is zero, and the bar is stretched elastically. The balance equation (3.41) shows that the stress and the corresponding deformation are homogeneous along the bar. In this initial phase the damage yield condition in eqn. (3.42) is not satisfied, i.e., $Y > 0$.

The elastic stage terminates when damage appears, meaning that $Y = 0$ somewhere along the bar. The stretch $\lambda_{\rm o}$ corresponding to the damage onset is evaluated from eqn. 3.42 as

$$\psi_{el}(\lambda_{\rm o}) = -\frac{G_c}{l_f}\frac{\eta'(0)}{g'(0)}. \tag{3.51}$$

At this time instant, say $t_{\rm o}$, one can solve the incremental evolution problem of Sec. 3.2.2 by assuming the following form of the series expansion in eqn. (3.43)

$$u(x, t_{\rm o} + \Delta t) = \varepsilon(t_{\rm o})x + \Delta t\,\dot{u}_{\rm o}(x), \qquad d(x, t_{\rm o} + \Delta t) = \Delta t\,\dot{d}_{\rm o}(x), \tag{3.52}$$

since the stretch at the onset is homogeneous, $\lambda_{\rm o} = 1 + \varepsilon(t_{\rm o})$, and the damage is null, $d(x,\, t_{\rm o}) = 0$; in addition, $\dot{u}_{\rm o}$ and $\dot{d}_{\rm o}$ satisfy the boundary conditions of eqn. (3.44). At the step $t_{\rm o} + \Delta t$, the stretch becomes $\lambda(x, t_{\rm o} + \Delta t) = 1 + \varepsilon_{\rm o} + \Delta t\,\dot{\lambda}_{\rm o}(x)$, such that $\dot{\lambda}_{\rm o}(x) = \dot{u}'_{\rm o}(x)$, which is a function of x due to the varying damage profile. A subscript "o" is used to indicate, here and henceforth, that the corresponding variable is evaluated at time $t_{\rm o}$.

The incremental stress in the bar is approximated at the first order in Δt from the definition of the one-dimensional Piola stress (3.40)

$$P = g(\Delta t\dot{d}_{\rm o})\;\psi'_{el}(\lambda_{\rm o} + \Delta t\dot{\lambda}_{\rm o}) \simeq P_{\rm o} + \Delta t\,\dot{P}_{\rm o}, \tag{3.53}$$

with

$$P_{\rm o} = \psi'_{el\,{\rm o}}, \quad \text{and} \quad \dot{P}_{\rm o} = g_{\rm o}\,\psi'_{el\,{\rm o}}\,\dot{d}_{\rm o} + \psi''_{el\,{\rm o}}\,\dot{\lambda}_{\rm o}. \tag{3.54}$$

Since the zero order stress $P_{\rm o}$ is constant along the bar, the macroscopic balance in eqn. (3.48) yields $(\dot{P}_{\rm o})' = 0$, meaning that also $\dot{P}_{\rm o}$ is homogeneous. The damage threshold

condition $Y = 0$ is verified both at $t = t_\mathrm{o}$ and $t = t_\mathrm{o} + \Delta t$, thus the incremental threshold in eqn. (3.49) is zero at both zero-th and first orders; the latter gives

$$\frac{2}{\pi^2} G_c \, l_f \; \dot{d}_\mathrm{o}{}''(x) - \big(g_\mathrm{o}'' \psi_{el\,\mathrm{o}} + \frac{G_c}{l_f} \eta_\mathrm{o}''\big) \dot{d}_\mathrm{o}(x) = \psi'_{el\,\mathrm{o}} \, \dot{\lambda}_\mathrm{o}(x) \tag{3.55}$$

which is, indeed, a second order differential equation for the damage rates $\{\dot{\lambda}_\mathrm{o}, \dot{d}_\mathrm{o}\}$. The rhs of eqn. (3.55) can be transformed by using the definition of $\dot{P}_\mathrm{o}$ in eqn. (3.54); after some manipulations we arrive at a differential equation in terms of the variable $\dot{d}_\mathrm{o}$:

$$\frac{2}{\pi^2} G_c \, \ell_f \; \dot{d}_\mathrm{o}''(x) - j \, \dot{d}_\mathrm{o}(x) = \frac{g'_\mathrm{o} \psi'_{el\,\mathrm{o}}}{\psi''_{el\,\mathrm{o}}} \dot{P}_\mathrm{o}, \qquad \text{with} \quad j = g_\mathrm{o}'' \psi_{el\,\mathrm{o}} - \frac{g_\mathrm{o}'^2 \psi'^2_{el\,\mathrm{o}}}{\psi''_{el\,\mathrm{o}}} + \frac{G_c}{\ell_f} \eta_\mathrm{o}''. \tag{3.56}$$

where the rhs is now independent of x. If we introduce the internal lengths

$$\ell_i = 2\sqrt{\frac{2 G_c \, l_f}{|j|}}, \quad \ell_s = \frac{g_\mathrm{o}'^2 \psi'^2_{el\,\mathrm{o}}}{\psi''_{el\,\mathrm{o}} |j|} \, \ell_i, \tag{3.57}$$

Eqn. (3.56) can be rewritten in the following form

$$\dot{d}_\mathrm{o}{}''(x) - \mathrm{sign}(j) \Big(\frac{2\pi}{\ell_i}\Big)^2 \dot{d}_\mathrm{o}(x) = \Big(\frac{2\pi}{\ell_i}\Big)^2 \sqrt{\frac{\ell_s}{\ell_i}} \frac{\dot{P}_\mathrm{o}}{\sqrt{\psi''_{el\,\mathrm{o}} |j|}}, \tag{3.58}$$

which is a second order differential equation in the variable x of the unknown rate $\dot{d}_\mathrm{o}$ to be solved with the boundary conditions $\dot{d}_\mathrm{o}(0) = 0$ and $\dot{d}_\mathrm{o}(L) = 0$. A similar equation was already studied in Lancioni and Corinaldesi [2018] for a small strain model (see equation (31) in Lancioni and Corinaldesi [2018]). The solution strategy exploited there can be equally applied to the large strain analysis carried out in this work. In particular, the following steps allows us to calculate the unknown rates $\{\dot{u}_\mathrm{o}, \dot{d}_\mathrm{o}\}$: (i) first $\dot{d}_\mathrm{o}$ is determined in terms of $\dot{P}_\mathrm{o}$ by solving eqn. (3.58); thereafter (ii) $\dot{P}_\mathrm{o}$ is determined by evaluating the mean value, i.e., $< \cdot >= \frac{1}{L} \int_0^L \cdot \mathrm{d}x$, of both the sides of Eqn. 3.54_2, that gives

$$\dot{P}_\mathrm{o} = g'_\mathrm{o} \, \psi'_{el\,\mathrm{o}} < \dot{d}_\mathrm{o} > + \psi''_{el\,\mathrm{o}} \, \dot{\varepsilon}_o, \tag{3.59}$$

where we made use of the fact that $\dot{P}_\mathrm{o}$ is constant along the bar and $< \dot{\lambda}_\mathrm{o} >= \dot{\varepsilon}_\mathrm{o}$ by the boundary condition i eqn. (3.44); finally, (iii) u is determined by integration of 3.54_2 expressed in terms of $\dot{\lambda}_\mathrm{o} = \dot{u}'_\mathrm{o}$. Different solutions are found depending on the sign of j and on the ratio between length L and the internal lengths ℓ_i and ℓ_s (as in sect. 2.5.2). Their analytical expressions are itemized in the following.

a. For $j \geq 0$, the solution obtained by applying the procedure (i), (ii) and (iii) is

$$\dot{d}_\mathrm{o}(x) = -\frac{g'_\mathrm{o} \psi'_{el\,\mathrm{o}}}{j(1 + < k > \ell_s/\ell_i)} \dot{\varepsilon}_\mathrm{o} \, g(x), \quad \text{and} \quad \dot{P}_\mathrm{o} = \frac{\phi''}{1 + < k > \ell_s/\ell_i} \dot{\varepsilon}_\mathrm{o}, \tag{3.60}$$

with

$$k(x) = 1 - \frac{\cosh\big(\pi(L - 2x)/\ell_i\big)}{\cosh(\pi L/\ell_i)}, \quad \text{and} \quad < k >= 1 - \frac{\ell_i}{\pi L} \tanh\big(\frac{\pi L}{\ell_i}\big). \tag{3.61}$$

Damage evolution is *full-size* in a regime of *stress-hardening*.

b. For $j < 0$ and $\ell_i \geq L$, the solution is

$$\dot{d}_{\rm o}(x) = -\frac{g'\phi'}{j(1- <k> \ell_s/\ell_i)}\dot{\varepsilon}_{\rm o} k(x), \quad \text{and} \quad \dot{P}_{\rm o} = \frac{g\psi''_{el\,{\rm o}}}{1- <k> \ell_s/\ell_i}\dot{\varepsilon}_{\rm o} \tag{3.62}$$

with

$$k(x) = 1 - \frac{\cos\left(\pi(L-2x)/\ell_i\right)}{\cos(\pi L/\ell_i)}, \quad \text{and} \quad <k> = 1 - \frac{\ell_i}{\pi L}\tan\left(\frac{\pi L}{\ell_i}\right). \tag{3.63}$$

Solution $\dot{d}_{\rm o}$ is *full-size* and two evolution regimes are obtained:

b.1. if $\ell_i > 2L$, the regime is *stress-hardening*, since $<k> < 0$;

b.2. if $L < \ell_i \leq 2\ell$, the regime is *stress-softening*, being $<k> > 0$. In this case, the condition

$$<k> \geq \ell_i/\ell_s \tag{3.64}$$

must be satisfied to have $\dot{d}_{\rm o} \geq 0$ everywhere.

c. For $j < 0$ and $\ell_i < L$, the solution has the expression 3.62, with

$$k(x) = \begin{cases} 1 - \cos(2\pi x/\ell_i), \text{ if } 0 < x < \ell_i, \\ 0, \text{ if } x \geq \ell_i, \end{cases} \quad \text{and} \quad <k> = \ell_i/\ell. \tag{3.65}$$

and so is localized in a portion of length ℓ_i (*localized solution*), and the evolution regime is *stress-softening*. Even in this case, the inequality

$$L \leq \ell_s \tag{3.66}$$

has to be fulfilled to have $\dot{d}_{\rm o} \geq 0$.

It can be proved that inequalities (3.64) and (3.66) are necessary conditions for stability of the evolution problem (see Lancioni and Corinaldesi [2018]); indeed they guarantee non-negativeness of the second variation of the functional in eqn. (3.46). If stability conditions are not satisfied, the bar fails catastrophically at the time instant $t_{\rm o}$, experiencing brittle fracture.

According to the sign of j, and, in case of $j < 0$, to the ratios L/ℓ_i and L/ℓ_s, different solutions are found. A schematic representation of the different regimes is given in Fig. 3.2. It is possible to distinguish *full-size* and *localized* fracture initiations, depending on whether the support of $\dot{d}_{\rm o}$ is the entire bar or a sub-region of length $\ell_i < L$. Moreover, the evolution regime can be *stress-hardening* if $\dot{P}_{\rm o} > 0$, or *stress-softening* if $\dot{P}_{\rm o} < 0$. As shown in Fig. 3.2, for $j < 0$, four different regions are found in the plane $(L/\ell_i, \ell/\ell_s)$, each characterized by a different damage evolution.

In case of localized solution (region c.), the bar must be longer than ℓ_i to have damage localization in a sub-region of length ℓ_i, and smaller than ℓ_s to avoid brittle failure. These requirements express the size sensitivity of the model: as the size of the bar increases, the response moves from pseudo-ductile to brittle. If we suppose damage localization at $t_{\rm o}$, the slope $k_{\rm o}$ of the curve $S = S(\varepsilon)$ is obtained from Eq. $(3.62)_2$

$$k_{\rm o} = \left.\frac{dP}{d\varepsilon}\right|_{t_{\rm o}} = \frac{\dot{P}_{\rm o}}{\dot{\varepsilon}_{\rm o}} = \frac{g_{\rm o}\psi''_{el\,{\rm o}}}{1 - \ell_s/L}, \tag{3.67}$$

that has a negative value and decreases as L increases; in particular $k_{\rm o} \to -\infty$ for $L \to \ell_s$.

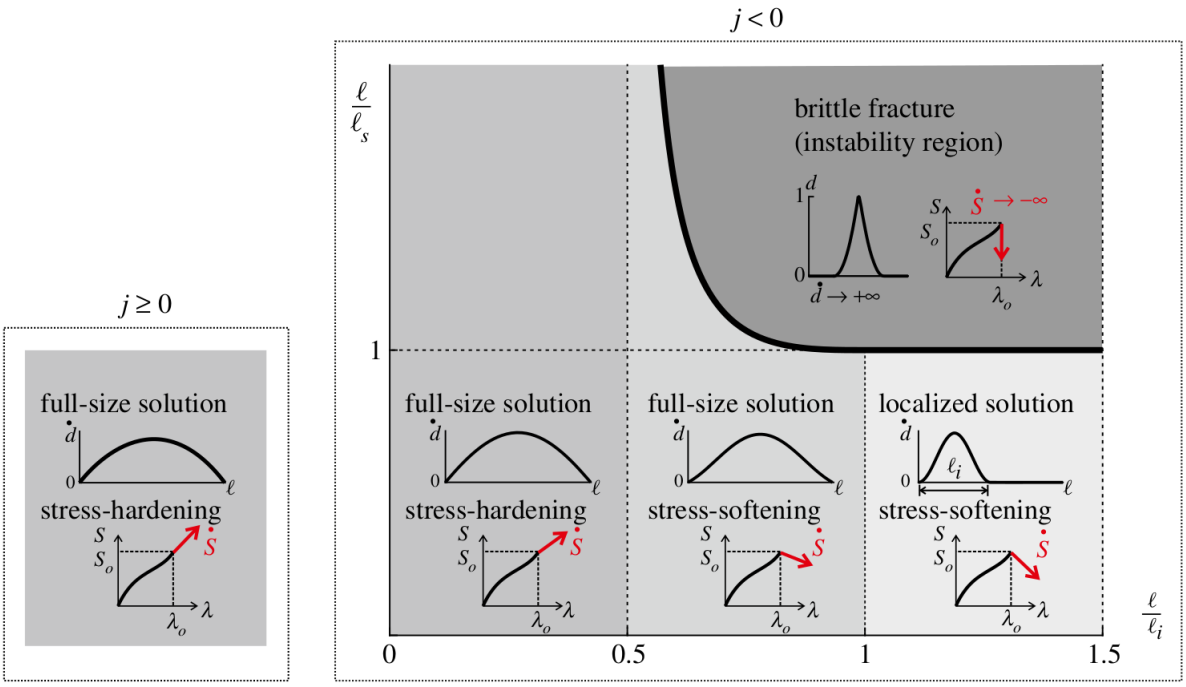

Figure 3.2: Different damage evolution regimes obtained from Eq. 3.58 for $j \geq 0$ (left) and $j < 0$ (right).

On integrating eqn. (3.59) over $(0, L)$ and rearranging the terms, we obtain the displacement rate at the end-section

$$\dot{u}_{\mathrm{o}}(L) = L\dot{\varepsilon}_{\mathrm{o}} = \dot{v}_{\mathrm{o}} + \dot{w}_{\mathrm{o}} \quad \text{with } \dot{v}_{\mathrm{o}} = L\frac{\dot{P}_{\mathrm{o}}}{\psi''_{el\,\mathrm{o}}}, \quad \text{and } \dot{w}_{\mathrm{o}} = -\frac{g'_{\mathrm{o}}\psi'_{el\,\mathrm{o}}}{\psi''_{el\,\mathrm{o}}}\int_0^L \dot{d}_{\mathrm{o}}\mathrm{d}x, \tag{3.68}$$

which is the sum of two contributions: $\dot{v}_{\mathrm{o}}$ is the displacement rate due to elastic stretching, and $\dot{w}_{\mathrm{o}}$ is the displacement rate induced by the fracture opening. In case of localized $\dot{d}_{\mathrm{o}}$ (case c., with $\ell_i \leq \ell \leq \ell_s$), the fracture opening rate is

$$\dot{w}_{\mathrm{o}} = \frac{\ell_s}{1 - \ell_s/\ell}\dot{\varepsilon}_{\mathrm{o}}. \tag{3.69}$$

Let $w = w(t)$ be the displacement accounting for fracture opening in a fracture evolution process. Using $(3.62)_2$ and (3.69), we can evaluate the derivative of S with respect to w at fracture initiation as

$$\hat{k}_{\mathrm{o}} = \left.\frac{dS}{dw}\right|_{t_{\mathrm{o}}} = \frac{\dot{S}_{\mathrm{o}}}{\dot{w}_{\mathrm{o}}} = -\frac{\psi''_{el\,\mathrm{o}}}{\ell_s}. \tag{3.70}$$

The coefficient $\hat{k}_{\mathrm{o}}$ represents the initial slope of the so-called *cohesive curve* $S = S(w)$, which describes the specific failure mode of the material. Since the cohesive law $S = S(w)$ is an intrinsic property of the material, $\hat{k}_{\mathrm{o}}$ does not depend on the length ℓ, differently from eqn. 3.67.

3.2.4 Cohesive fracture

In this section we define a strategy to estimate the cohesive curve $P = P(w)$, that characterizes the fracture opening process. The function $P(w)$ is usually assigned a-priori in standard formulations of cohesive fracture mechanics Nonato Da Silva et al.

[2019], Da Silva et al. [2020]), whereas in the proposed variational approach is obtained from the peculiar form of the fracture energy.

We suppose that, at a certain time instant of the evolution process, damage is localized in a sub-region $(0, 2x^*)$, with $x^* < L/2$ the half-bandwidth length, and that it has attained the maximum value d^* at $x = x^*$. The proposed procedure allows us to determine the length x^*, the stress S, the functions d and λ, the fracture opening w, as well as the corresponding strain ε in terms of d^* by integrating the balance equations (3.41) and (3.42).

We suppose that, at each material point, the stretch λ is the superposition of an elastic λ_e and fracture λ_f stretches

$$\lambda = \lambda_\mathrm{f}\,\lambda_\mathrm{e}, \tag{3.71}$$

where λ_e would be the homogeneous stretch obtained from P if d were zero; as such, it can be evaluated from the constitutive equation of the undamaged material by

$$\psi_{el}'(\lambda_\mathrm{e}) = P. \tag{3.72}$$

The fracture opening w, that is the displacement at $x = \ell$ produced by the damage occurrence is

$$w = \int_0^{\lambda_\mathrm{e} L} \big(\lambda_\mathrm{f}(x_e) - 1\big)\mathrm{d}x_e = \int_0^L (\lambda - \lambda_\mathrm{e})\,\mathrm{d}x = (1+\varepsilon)L - L\lambda_\mathrm{e}. \tag{3.73}$$

Within the damage region $(0, 2x^*)$, the damage threshold condition in eqn. (3.42) is evaluated as an equality and

$$g'\psi_{el} + G_c\left(\frac{1}{l_f}\eta' - \frac{2l_f}{\pi^2}d''\right) = 0, \tag{3.74}$$

On multiplying all terms by d' and on integrating over $(0, x)$, with $x \le x^*$, previous equation gives

$$G_c\left(\frac{1}{l_f}\eta - \frac{2l_f}{\pi^2}d'^2\right) + \int_0^x \frac{\mathrm{d}g}{\mathrm{d}\hat{x}}\psi_{el}\,\mathrm{d}\hat{x} = 0. \tag{3.75}$$

where the latter term is rewritten by integration by parts as

$$\int_0^x \frac{\mathrm{d}g}{\mathrm{d}\hat{x}}\psi_{el}\,\mathrm{d}\hat{x} = g\psi_{el} - \psi_{el}(\lambda_\mathrm{e}) - \int_0^x g\psi_{el}'\frac{\mathrm{d}\lambda}{\mathrm{d}\hat{x}}\,\mathrm{d}\hat{x} = g\psi_{el} - \psi_{el}(\lambda_\mathrm{e}) - (\lambda - \lambda_\mathrm{e})P, \tag{3.76}$$

since $P = g\psi_{el}'$ is constant along the bar. Equation (3.75) becomes

$$G_c\left(\frac{1}{l_f}\eta - \frac{2l_f}{\pi^2}d'^2\right) + g\psi_{el} - \psi_{el}(\lambda_\mathrm{e}) - (\lambda - \lambda_\mathrm{e})P = 0. \tag{3.77}$$

At $x = x^*$, where the maximum damage is attained, $d'(x^*) = 0$ and previous equation further simplifies into

$$\frac{G_c}{l_f}\eta(d^*) + g(d^*)\psi_{el}(\lambda^*) - \psi_{el}(\lambda_\mathrm{e}) - (\lambda^* - \lambda_\mathrm{e})P^* = 0, \tag{3.78}$$

where quantities evaluated at $x = x^*$ are labelled by an asterisk. In eqn. (3.78), the stretches λ^* and λ_e are worked out by inversion of the constitutive equations

$$g(d^*)\psi_{el}'(\lambda^*) - P^* = 0, \quad \psi_{el}'(\lambda_\mathrm{e}) - P^* = 0. \tag{3.79}$$

For any assigned value of $d^* \in [0,1]$, the triplet $\{\lambda^*, \lambda_e, S^*\}$ solves the set of equations (3.78) and (3.79). Once P^* is determined, the profiles of d and λ at points $x \in [0, x^*]$ can be evaluated from eqn. (3.77), here rewritten in the following form

$$d' = \frac{1}{l_f} h(d, d^*), \quad \text{with} \quad h(d, d^*) := \pi \sqrt{\frac{l_f}{G_c} \left[g(d)\psi_{el}(\lambda) - \psi_{el}(\lambda_e) - f^*(\lambda - \lambda_e) \right] + \eta}, \tag{3.80}$$

where λ is the solution of the equation

$$g(d)\psi'_{el}(\lambda) - P^* = 0. \tag{3.81}$$

Upon inversion of Eq. 3.80, one obtains the expression of x in terms of the damage profile and of the maximum damage d^*,

$$x(d, d^*) = \int_0^d \frac{l_f}{h(\hat{d}, d^*)} \, \mathrm{d}\hat{d}, \tag{3.82}$$

and the stretch λ at x is the solution of eqn. (3.81). The half-bandwidth length is obtained from the above relation by assigning $d = d^*$

$$x^* = \int_0^{d^*} \frac{l_f}{h(\hat{d}, d^*)} \, \mathrm{d}\hat{d}, \tag{3.83}$$

and the fracture opening w is determined from eqn. (3.73), once λ, λ_e and x^* are known. Upon inversion of the equation, also the assigned stretch can be computed

$$\varepsilon = \lambda_e + \frac{w}{L} - 1. \tag{3.84}$$

To conclude, the above procedure can be implemented numerically through the following steps:

i. Assign the value d^* of the maximum damage.

ii. Solve equations (3.78) and (3.79) to determine P^*, λ^* and λ_e.

iii. Discretize the damage range $[0, d^*]$, and, for any d_i of the discretized set, determine the position x_i from (3.82). The discrete profile of $d = d(x)$ is given by the pairs (x_i, d_i).

iv. Determine λ_i at point x_i from (3.81). The discrete profile of $\lambda = \lambda(x)$ is drawn by points (x_i, λ_i). At points $x > 2x^*$ the stretch is equal to λ_e.

v. Determine w from (3.73).

Previous algorithm allows the cohesive curve $P = P(w)$ to be evaluated at discrete points, by iterating the scheme for different $d^* \in [0,1]$. The damage evolution determined through this procedure is based on the balance equations (3.41) and (3.42). It is pointed out that the numerical simulations of Sec. 3.3 are indeed obtained by solving the full evolution problem of Sec. 3.2.2 by finite elements. Although the approaches are different, the estimate of the cohesive curve obtained through steps $(i) - (v)$ gave accurate enough results to catch the qualitative behaviour of the model. As such, the proposed numerical scheme represents an useful tool to explore the variety of damage mechanisms. In the next section, these results are used to assess the effects of the different constitutive parameters on the damage evolution modes. Criteria for parameters calibration will be also discussed.

3.2.5 Physical interpretation of the cohesive parameters

The constitutive coefficients a_1, a_2 and a_3 that appear in the energy degradation function $g(d)$, as defined in eqn. (3.7), are put in relation to specific properties of cohesive fracture evolution, to give them a clear physical meanings and to allow their robust evaluation from the experimental data. In the following calculations, the elastic coefficients μ_n and α_n, the fracture energy release rate G_c, and the internal length l_f are supposed to be known.

The coefficients a_1, a_2 in eqn. (3.7) can be tailored from the model response at the damage onset. At this time instant $\lambda_\mathrm{f} = 1$, $\lambda_\mathrm{e} = \lambda_\mathrm{o}$ and the stress P_o is known. Since $d_\mathrm{o} = 0$, the functions g and η at t_o are

$$\begin{aligned}&\eta(0) = 0, \quad g(0) = 1, \quad \eta'(0) = 2, \quad g'(0) = -a_1,\\ &\eta''(0) = -2, \quad g''(0) = 2a_1(a_1 - a_2 - 2).\end{aligned}$$

Therefore, one has:

1. a_1 is determined by the limit elastic stretch λ_o through relation 3.51, which, once inverted, gives
$$a_1 = 2\frac{G_c}{\psi_{el\,\mathrm{o}}\, l_f}. \tag{3.85}$$

2. a_2, that appears in $g''(0)$, is made dependent on the slope $\hat{k}_\mathrm{o}$ of the cohesive curve of eqn. 3.70 at the damage onset, i.e.,
$$\hat{k}_\mathrm{o} = -\frac{\psi''^2_{el\,\mathrm{o}}}{2a_1^2 P_\mathrm{o}^2}\sqrt{\frac{|j|^3}{2\,G_c\, l_f}}, \quad \text{with} \quad j = 2a_1(a_1 - a_2 - 2)\psi_{el\,\mathrm{o}} - \frac{a_1^2 P_\mathrm{o}^2}{\psi''_{el\,\mathrm{o}}} - \frac{2G_c}{l_f}, \tag{3.86}$$
where j is negative, as the formula is evaluated for the localized damage case (case c. in Sec. 3.2.3). From eqn. (3.86), a_2 has the following expression
$$a_2 = \frac{1}{2a_1\psi_{el\,\mathrm{o}}}\left[\left(-\frac{2a_1^2 P_\mathrm{o}^2}{\psi''^2_{el\,\mathrm{o}}}\sqrt{2G_c\, l_f}\hat{k}_\mathrm{o}\right)^{2/3} + 2a_1(a_1 - 2)\psi_{el\,\mathrm{o}} - \frac{a_1^2 P_\mathrm{o}^2}{\psi''_{el\,\mathrm{o}}} + \frac{2G_c}{l_f}\right]. \tag{3.87}$$

3. a_3 multiplies the third-order term in the polynomial (3.7), thus it mainly influences states with a large damage. In Wu [2017], indeed, a_3 was related to the displacement jump $\tilde{w}$ at complete fracture of the specimen through the formula
$$a_3 = \frac{1}{a_2}\left[\frac{1}{2}\left(\frac{\tilde{w}P_\mathrm{o}}{2G_c}\right)^2 - (1 + a_2)\right]. \tag{3.88}$$
Since this relation was derived within the context of linear elasticity, it cannot be straightforwardly extended to the finite strain case. Accordingly, it is just used to obtain an estimate of the parameter a_3. For damage occurring at small strains, formula (3.88) provides the exact value to assign to a_3 in order for the fracture jump to be $\tilde{w}$. On the contrary, for damage onset at large strains it gives only an approximate value. Further insights can indeed be gained by the drawing of the cohesive curve, as discussed in the following.

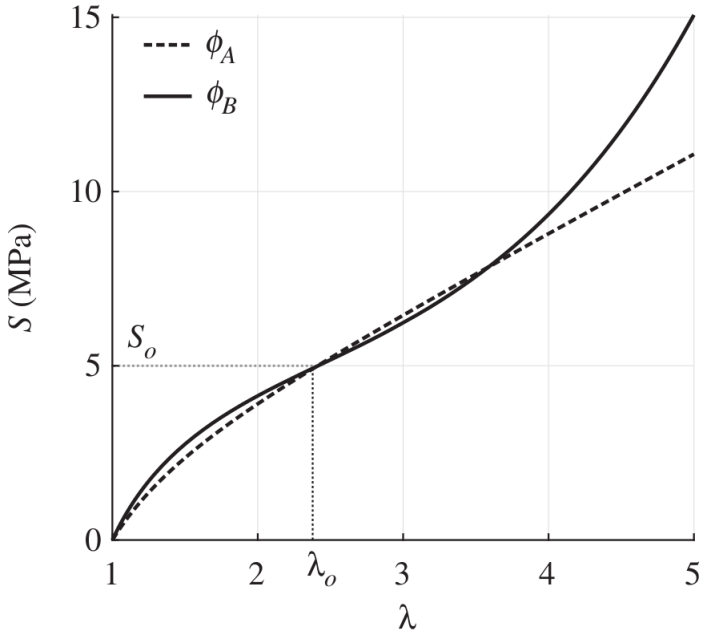

Figure 3.3: First Piola stress S versus (elastic) stretch λ for the two strain energies $\phi_{_A}$ and $\phi_{_B}$.

To better highlight the role of the different cohesive parameters we now consider two different forms of the Ogden elastic strain energy density with different elastic parameters: one with $N = 1$ in the series 3.34_3 and $\mu_1 = 2.2$ MPa, $\alpha_1 = 2$, that we call quadratic energy $\phi_{_A}$, the other with $N = 2$ and $\{\mu_1, \mu_2\} = \{4.8, 0.01\}$ Mpa and $\{\alpha_1, \alpha_2\} = \{1.2, 5.1\}$, say $\phi_{_B}$. As shown in Fig. 3.3, such a choice of the elastic coefficients represents two plausible elastic response of a rubbery material, the former has a linear Piola stress at large stretches, whereas the latter shows the stress hardening at large stretches typical of elastomers.

The cohesive curves $P = P(w)$ corresponding to these elastic energies are shown in Figs. 3.4 for $l_f = 5$ mm and different values of the parameters G_c, $\hat{k}_{\rm o}$ and a_3. For a given G_c, the values of $\hat{k}_{\rm o}$ and $\tilde{w}$ are assigned by supposing that the cohesive law is linear with the fracture opening $P = -\frac{P_{\rm o}^2}{2G_c} w + P_{\rm o}$, an expression which is the simplest triangular cohesive curve. Accordingly, $\hat{k}_{\rm o} = -\frac{P_{\rm o}^2}{2G_c}$ and $\tilde{w} = \frac{2G_c}{P_{\rm o}}$. The coefficients a_1, a_2 and a_3 are derived from eqns. (3.85), (3.87) and (3.88). For low values of G_c, the cohesive curves recover the linear law when the energy density $\phi_{_A}$ is used, whereas they deviate from linearity as G_c is increased. When the two terms energy density $\phi_{_B}$ is considered, linearity is lost, as shown by the dashed curves of Fig. 3.4a. In this case, the curves initially decrease with lower slope, attaining larger values of stress. Then, they exhibit snap-back branches that are more pronounced for increasing values of G_c. The initial raising of the curve and the presence of a snap-back tail, indicated with a star in the figure, depends on the specific shape of $\phi_{_B}$, that has a convex branch where stiffness grows as stretches increase (see Fig. 3.3). This determines the fracture properties of the material. Indeed the softening process of fracture requires a larger stress for crack opening in the initial stage, and, when the snap-back branch is encountered, it stops due to the complete rupture of the specimen. As a consequence the recovery in the elastic stiffness for large stretches induces an increased stiffness in the initial phase of crack opening and a brittle response in the final stage of the fracture evolution.

A way to reduce the snap-back tails in the cohesive curves is to increase the initial slope $\hat{k}_o$. This is shown in Fig. 3.4(b), where cohesive curves for different values of $\hat{k}_o$ are plotted by keeping the fracture toughness $G_c = 60$ MPa mm and $a_3 = -0.6851$ constant.

It is noted that also the parameter a_3 influences the softening process, as shown in Fig. 3.4(c,d). By scrutinizing the curves of Fig. 3.4(c), one can notice that a decrease of $a_3 < 0$ has two distinct effects: (i) the negative slope of the curve is increased in its initial part, and (ii.) the displacement w at the snap-back is increased, with the final stage of brittle failure being reduced. The curves in Fig. 3.4(d) are drawn for a fixed value of $\hat{k}_o$ which is ten times larger than that of curves of Fig. 3.4(c). In this case, the coefficient a_3 influences the final part of the cohesive curves: large negative values of a_3 raise the curve tail, reducing the snap-back up to its complete disappearance. It turns out that the final catastrophic fracture is replaced by a recovery of stiffness that allows the material to further bear stresses.

As a result, coefficients a_1 and a_2 can be assigned through formulas (3.85) and (3.87), which relate them to the limit elastic stretch λ_o and to the initial slope of the cohesive curve $\hat{k}_o$, respectively. The calibration of a_3 is more troublesome. The estimate in Eq. (3.88) gives an initial value of the paramter, yet the choice of a more appropriate value can be obtained only after having numerically examined the cohesive curves, as those in Figs. 3.4(c,d). The qualitative behaviour observed for increasing value of a_3 is a stretching of the cohesive curve with the consequent reduction or even removal of the final brittle fracture.

We finally remark that the model proposed in Wu [2017] is indeed size-independent as shown in Wu and Nguyen [2018]. However, in the proposed extension to finite elasticity, this independence is only partially maintained: the fracture activation stress P_o and the initial slope $\hat{k}_o$ of the cohesive curve still do not dependent on l_f, but the shape of the softening cohesive curve $P = P(w)$ does. As a result, the convergence of the model to the cohesive fracture is lost, meaning that the model should be interpreted as a damage model in which the internal length is a constitutive parameter representing the length of the transition zone (process zone). Such a parameter may be directly calibrated through ad-hoc experiments as the one reported in Yin et al. [2021].

3.3 Numerical Examples

The variational model in eqns. (3.31)-(3.32) was implemented in the finite element open-source framework FEniCS®Logg et al. [2012].

The displacement and damage fields were projected over a piecewise affine finite element space (Lagrange elements) by using the same mesh domain. As the energy functional $\mathcal{I}$ defined in eqn. (3.9) for the general formulation and in eqn. (3.45) for the simple tension incremental problem is separately convex in each variable, an alternate minimization algorithm in the variables $\underline{u}$ and d was implemented. At a given time step, the solution of the iterative evolution of Sect. 3.2.2 was achieved iterating on the following subproblems until convergence:

1. The minimization of $\mathcal{I}$ with respect to $\underline{u}$ at fixed d is an unconstrained optimization problem solved as a nonlinear elastic problem with the prescribed boundary conditions through the Newton-Raphson method;

2. The minimization of $\mathcal{I}$ with respect to d at fixed $\underline{u}$ is a unilateral constrained optimization problem, which was solved through TAO (Tool-kit for Advanced Optimization).

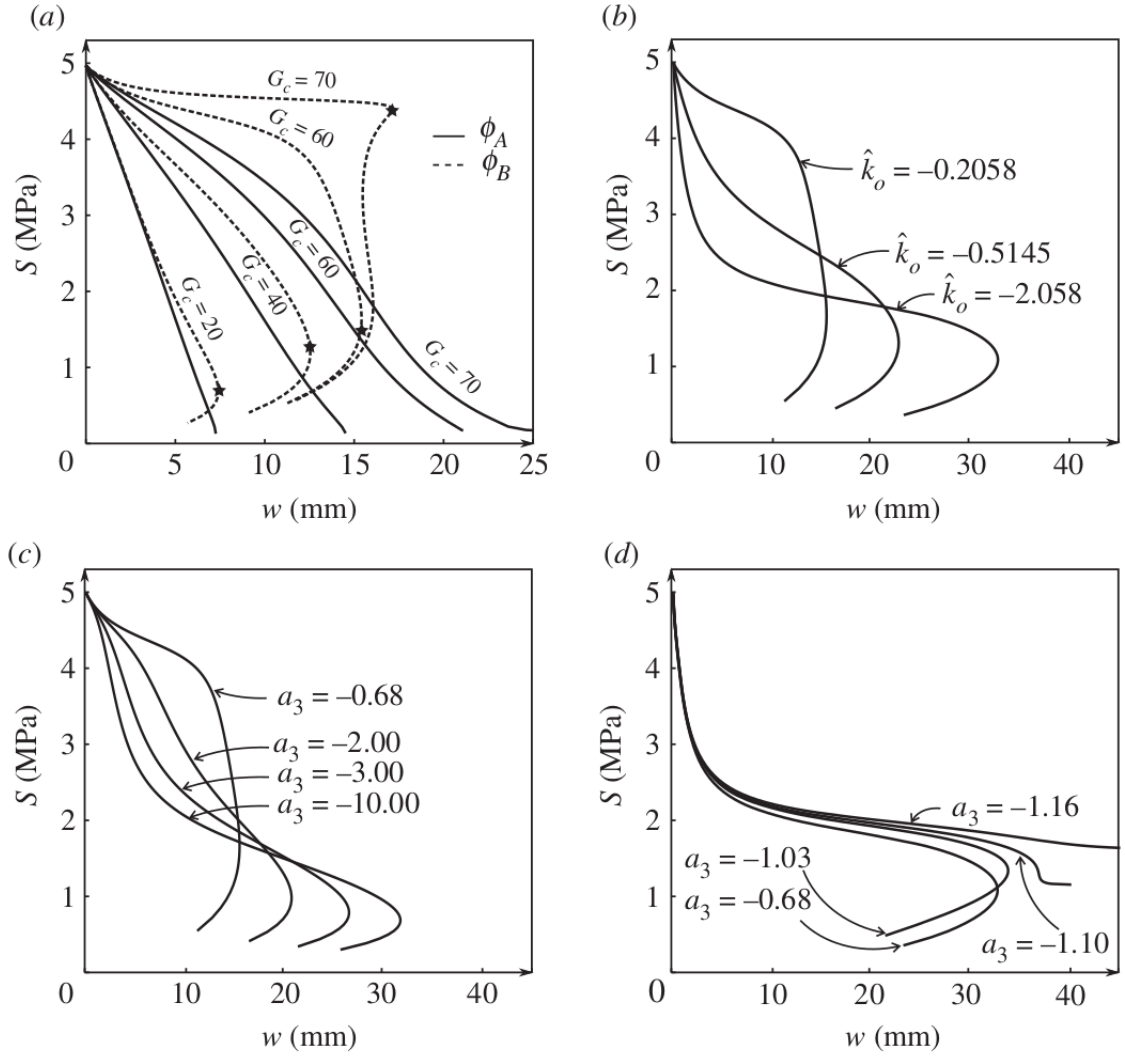

Figure 3.4: Cohesive curves for: (a) different values of the parameter G_c in case of energy densities ϕ_A (solid-line) and ϕ_B (dashed-line);(b) different $\hat{k}_o$ and fixed $G_c = 60$ MPa and $a_3 = -0.6851$; (b,c) different a_3 and fixed $G_c = 60$ MPa and $\hat{k}_o = -0.2058$ MPa/mm in (b) and $\hat{k}_o = -2.0580$ MPa/mm in (c).

Further details on the numerical implementation can be found in Farrell and Maurini [2017]. Simulations on both 1D or 2D geometries were carried out, although the results shown in the paper refer to the latter.

Two numerical examples are discussed in the following. As a first benchmark problem, we consider a rectangular test specimen subjected to tensile loadings. This example has twofold purpose: assessing the sensitivity of the model with respect to the different constitutive parameters and demonstrating the ability of the proposed modelling framework of capturing the large-strain behaviour of double network elastomers Millereau et al. [2018], (see sect. 2.3.2). Afterwards, we use a double edge notched specimen in tension to validate the model prediction up to the specimen rupture with respect to the experiments on conventional elastomers reported in Hocine et al. [2002] (see sect. 2.3.1).

The rectangular specimen used to carry out the sensitivity analysis is shown in Fig. 3.5 together with boundary conditions and details of the mesh. This latter was made up of 12.000 Lagrange triangular elements. The height of the specimen was kept fixed

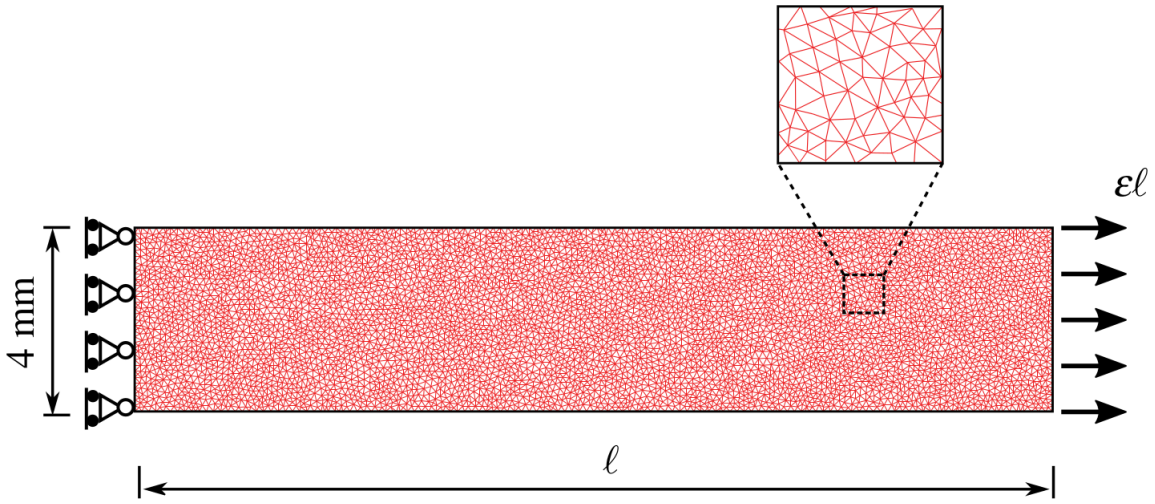

Figure 3.5: Geometry of the rectangular specimen with details of the mesh made of about 12.000 Lagrange triangular elements. The height of the specimen was kept fixed in all numerical tests, whereas different lengths $\ell = \{6, 13, 20\}$ mm were considered.

Table 3.1: Constitutive parameters used in the numerical examples.

Elastic		
	ϕ_A: $\mu_1 = 2.2$ MPa	$\alpha_1 = 2$
	ϕ_B: $\{\mu_1, \mu_2\} = \{4.8, 0.01\}$ MPa	$\{\alpha_1, \alpha_2\} = \{1.2, 5.1\}$
Fracture		
	$l_f = 5$ mm, $G_c = 60$ MPa mm, $\lambda_o = 2.4$, $\hat{k}_o = -0.21$ MPa/mm	
	ϕ_A: $a_3 = -0.57$, ϕ_B: $a_3 = -0.68$	

at 4 mm, whereas three different lengths were considered $L = \{6, 13, 20\}$ mm. In all simulations two different sets of elastic parameters were used to assess the effects of the particular form of the Ogden energy on the fracture properties of the material, that correspond to the energies ϕ_A and ϕ_B in Fig. 3.3; the other constitutive parameters are the ones in Tab. 3.1 except where stated. We point out that the coefficients a_1, a_2 and a_3 were obtained from G_c, $\hat{k}_o$ and $\tilde{w}$ by using the formulas 3.85, 3.87 and 3.88.

The Piola stress P in terms of overall strain ε as well as the damage profiles along the mean axis of the bar are plotted in Figs. 3.6 and 3.7 for the two energy densities ϕ_A and ϕ_B and different values of the energy release rate G_c.

By increasing values of G_c, the maximum strain attained at rupture grows with a larger region in which a pseudo-ductile response is achieved. With the energy ϕ_A, the response with $G_c = 20$ MPa mm (green curve in Fig. 3.6) shows a sudden drop in the stress caused by an abrupt damage growth at the end of the elastic stage, that almost immediately reaches values close to 1 as shown by the green damage profiles in the figure. The resulting overall behaviour is brittle. For larger values of G_c, the drop in the stress is smoothed out with cohesive-like softening curves; in terms of damage this behaviour is produced by the phase field variable progressively growing and enlarging.

For the elastic coefficients in the energy ϕ_B, brittle and cohesive responses are obtained for $G_c = 20$ and 40 MPa mm, respectively. For $G_c = 60$ MPa mm, the specimen exhibits a pseudo-ductile behaviour in which two response stages are clearly observed:

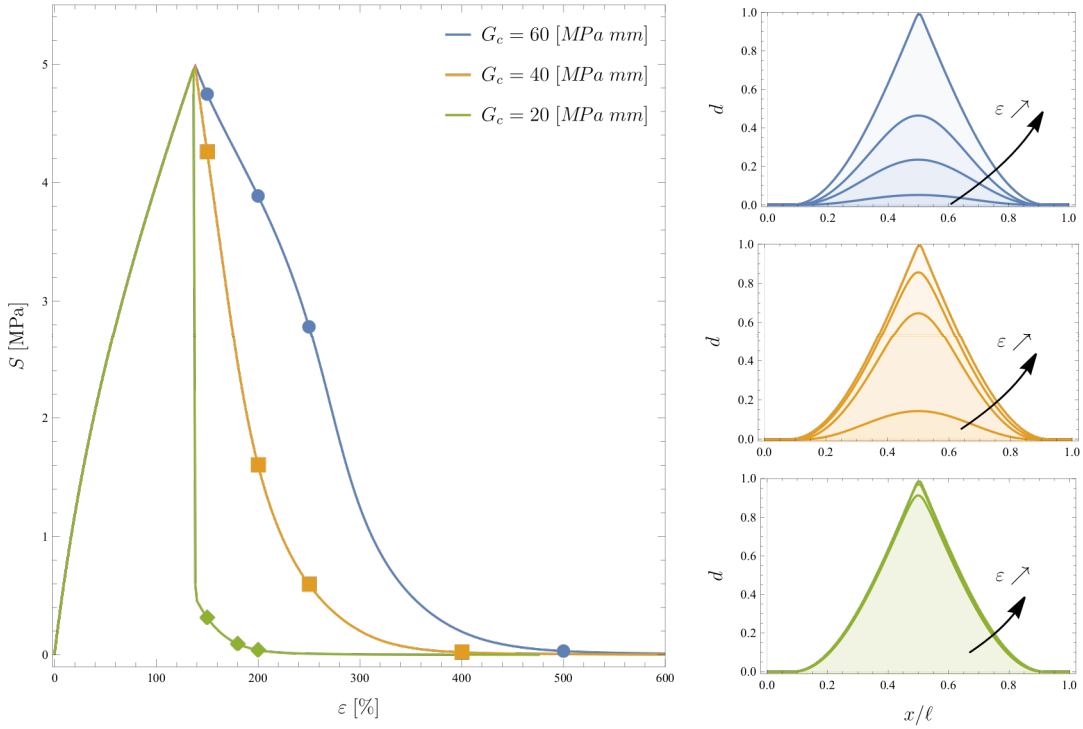

Figure 3.6: Influence of the energy release rate G_c in the case of elastic energy ϕ_A. Piola stress S versus overall strain ε for $G_c = \{20, 40, 60\}$ MPa mm. The insets show the damage profiles d evaluated on the mean axis of the bar at the different stretch levels indicated by dots on each curve.

a softening branch with a low slope, followed by a sudden drop in the stress. As the damage profiles show, in the first stage of moderate softening, the damage grows slowly whilst expanding trough the bar. At the end of this phase, the damage has covered the entire domain and has reached its maximum value of 0.3. Thereafter damage immediately increases producing the rupture of the specimen with the resulting stress rapidly decreasing to zero.

Since the gradient term in the fracture energy make the model size dependent, the effect of specimen length is analysed in Fig. 3.8 for $L = \{6, 13, 20\}$ mm. The results indicates that when L is comparable with the internal length $l_f = 5$ mm the response is cohesive, whereas sufficiently long bars displays a brittle or quasi-brittle failure for both the energies ϕ_A (Fig. 3.8a) and ϕ_B (Fig. 3.8b).

In Fig. 3.9, the dependency of the material response on the slope of the cohesive curve $\hat{k}_o$ is also investigated. This constitutive parameter is directly related through Eq. (3.87) to a_2. As the results show, $\hat{k}_o$ controls the stress decrease at the damage onset, and regulates the softening branch with moderate slope, that is associated to a process of damage propagation over the whole domain. Large value of $\hat{k}_o$ may induce snap-back of the cohesive curve, with a subsequent discontinuous drop in the stress. Simulations start with values of $\hat{k}_o$ in Tab. 3.1 (blue curve in the figure), with a cohesive–like behaviour for both the energies ϕ_A (Fig. 3.9a) and ϕ_B (Fig. 3.9b).

Finally, the influence of coefficient a_3 is analysed in Fig. 3.10. The green curve corresponds to the value of $a_3 = -0.68$ in Fig. 3.9(b) (with $\hat{k}_o = -2$ MPa/mm), whereas the others are obtained by increasing a_3 by a factor of 2 and 4, respectively, such that

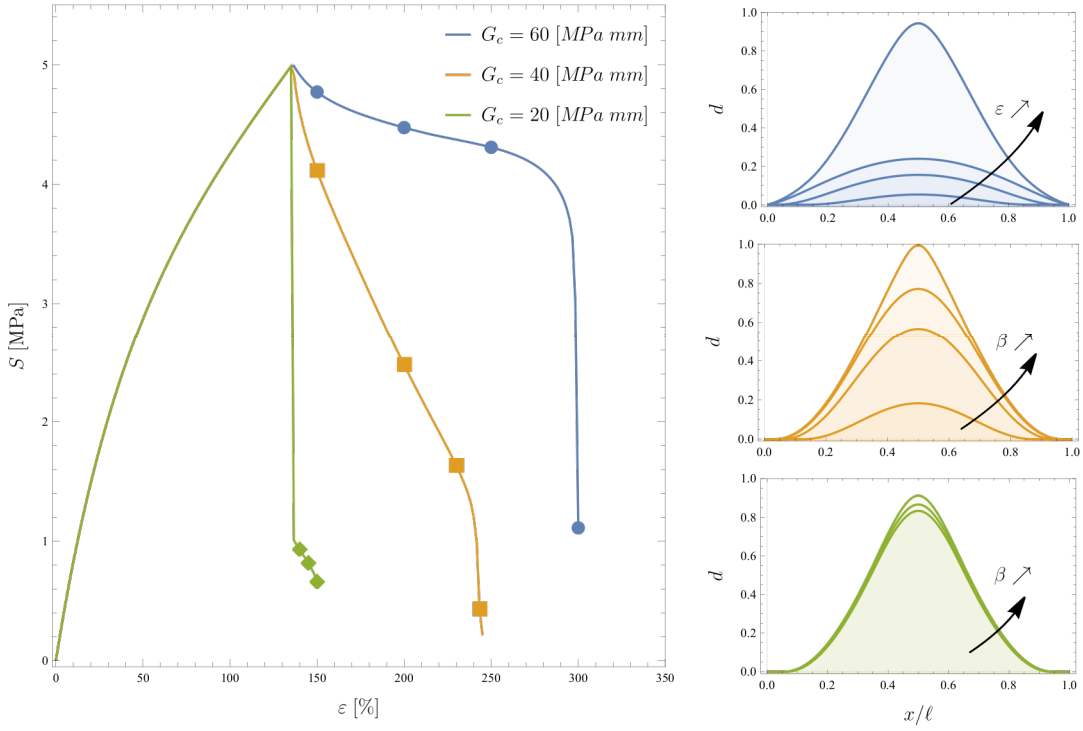

Figure 3.7: Influence of the energy release rate G_c in the case of elastic energy ϕ_B. Piola stress S versus overall strain ε for $G_c = \{20, 40, 60\}$ MPa mm. The insets show the damage profiles d evaluated on the mean axis of the bar at the different stretch levels indicated by dots on each curve.

$a_3 = \{-0.68, -1.36, -2.72\}$. As pointed out in Sec. 3.2.5, increasing values of a_3 lead to a recovery of the material stiffness, with a consequent transition from a softening (green curve) to a hardening responses (orange and blue curves). In all cases, it is seen a significant stress drop at the end of the elastic phase, that corresponds to the sudden occurrence of a localized damage in the central part of the specimen, with the phase field variable reaching 0.2. Thereafter different damage evolution regimes are seen: for the green curve ($a_3 = -0.68$) the damage increases sharply in the central part of the specimen until it reaches the value of 1 meaning that the specimen is completely broken; on the contrary, the orange and blue curves show a rather limited increase in the damage intensity, $d < 0.4$, yet the support of the phase field variable enlarges, up to the point where the damage occupies the entire bar. This type of evolution resembles a sort of "plastic-wave" that propagates inside the bar (damage-wave in this case) and has indeed been observed in double-network elastomers.

As a general remark for the model behaviour, in all simulations it was observed that the rate of damage growth is proportional to the slope of the softening branch. Furthermore, a broadening of the damage localization zone is observed when the softening branch is convex, whereas a concave softening branch produces damage localization is narrow regions.

Having shown the main features of the proposed model, we are now in the position of comparing the model prediction against the experimental data on double network elastomers. The experiments used to calibrate the model are the ones reported in Millereau et al. [2018] (see sect. 2.3.2, where a cross-linked elastomer was first swollen in monomer

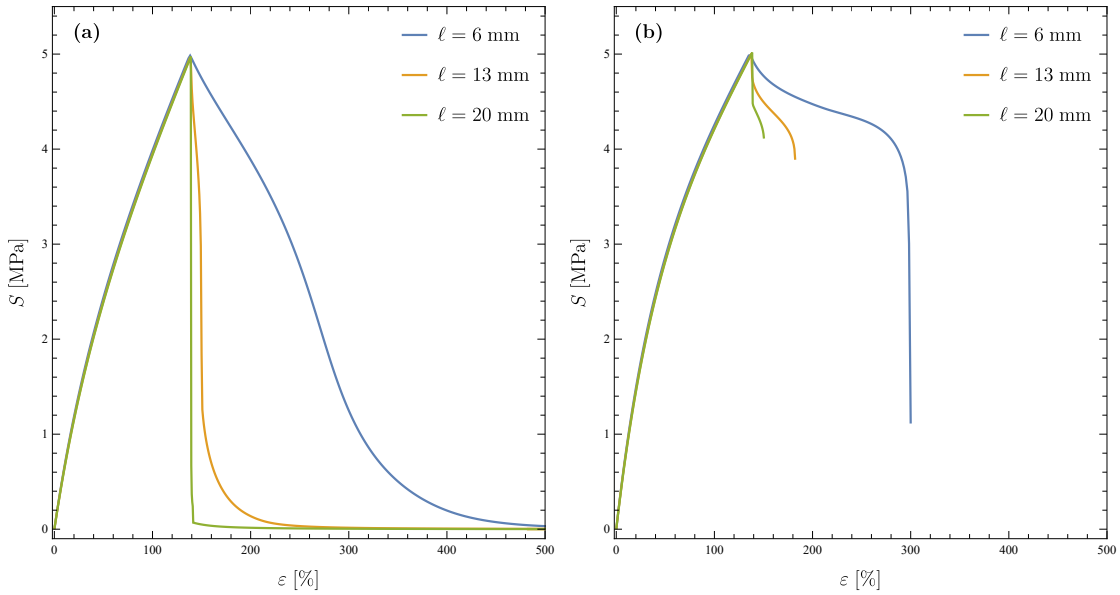

Figure 3.8: Size dependency of the model. Piola stress vs. strain curves for different bar lengths $\ell = \{6, 13, 20\}$ mm and elastic energies ϕ_A (a) and ϕ_B (b).

Table 3.2: Constitutive parameters used for the fitting of the experimental data in Fig. 3.11.

Elastic	
	$\{\mu_1, \mu_2\} = \{4.6, 0.012\}$ MPa $\quad \{\alpha_1, \alpha_2\} = \{1.2, 5.5\}$
Fracture	
	$l_f = 5$ mm, $\quad G_c = 100$ MPa mm, $\quad \lambda_\circ = 2.4$, $\quad \hat{k}_\circ = -0.37$ MPa/mm, $\quad a_3 = -4.73$

and subsequently polymerized to create the so-called double network. This novel class of elastomers displays unique mechanical features due to the combined use of a stretchy matrix with a stiff filler network, that make the compound fails in a controlled, pseudo-ductile way, at large strain.

These peculiarities are readily seen from the data in Fig. 3.11 where the Piola stress, P, is plotted against the normalized displacement at bar's end, ε. The initial part of the curve resembles the typical response of an elastomeric material with a pronounced nonlinear elastic behaviour. The elastic phase terminates at about $\varepsilon = 1.4$ where a sharp decrease in the stress appears. Microscopically this drop corresponds to the emergence of a very localized damage region. By continuing loading, the applied force remains constant and the stress-strain plot shows a plateau for a wide range of stretches. The formation of a neck and its propagation along the specimen is observed in this region. When necking has expanded all over the sample, at about $\varepsilon = 4.2$, the damage start increasing uniformly, yet the overall stiffness of the sample grows. This behaviour is a competition between the stress softening induced by the damage and the stiffening caused by the intact polymer chains being almost completely stretched. Such a peculiar behaviour for an elastomer was reported for the first time in Millereau et al. [2018].

Remarkably the proposed model is able to capture the main features seen in the experimental data as the fitting in Fig. 3.11 proves. The stress-strain plot displays

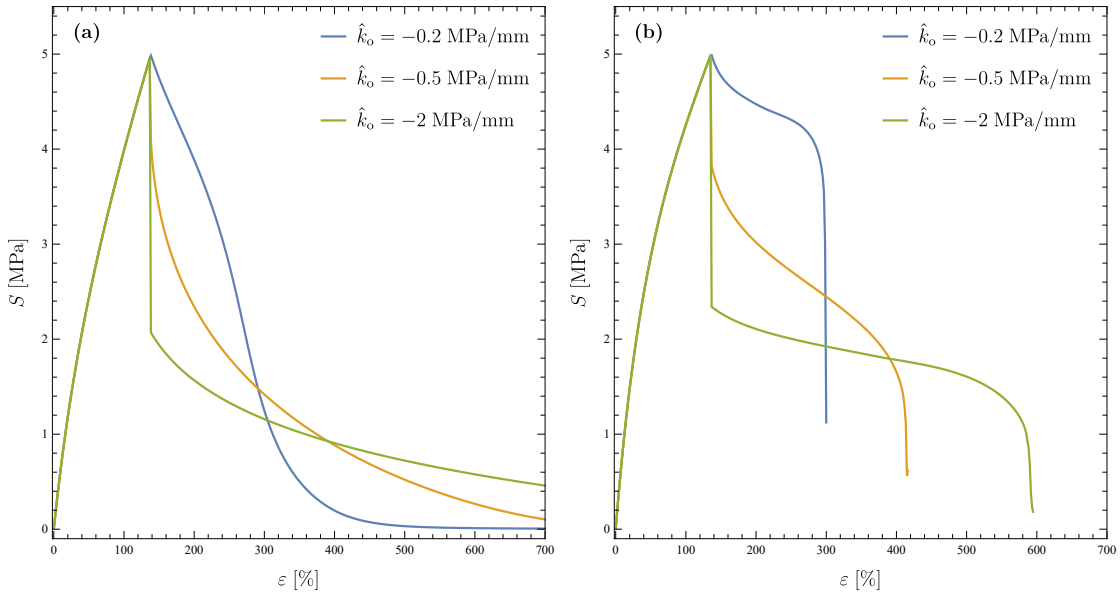

Figure 3.9: Influence of the cohesive parameters $\hat{k}_o$. Piola stress vs. strain for different values of the cohesive curve slope $\hat{k}_o = \{-0.2, -0.5, -2\}$ MPa/mm and elastic energies ϕ_A (a) and ϕ_B (b).

three different curves along with the experimental points represented by open orange circles: the continuous orange curve, is the output of the model and has all the main characteristics of the experimental response, including the initial nonlinear elastic regime, the stress peak with the subsequent stress plateau and the stiffness increase at large strain. The green and orange dashed curves are indeed the elastic stresses of each of the two terms in the Ogden model of eqn. (3.40) with the parameters $\{\mu_1, \alpha_1, \mu_2, \alpha_2\}$ in Tab. 3.2: at each material point, the elastic stress is the superposition of the response of two nonlinear springs, one with $\{\mu_1, \alpha_1\} = \{4.6 \text{ MPa}, 1.2\}$, that controls the response at low strains (dashed orange curve), and the other with $\{\mu_2, \alpha_2\} = \{0.012 \text{ MPa}, 5.5\}$ is activated at high strain and is responsible for the strain hardening seen in the experiments (dashed green curve). In this sense the model resembles the microscopical model proposed in De Tommasi et al. [2008] where a two-phase material model was considered. The insets in Fig. 3.11 shows the damage field obtained from the numerical simulations at different level of strains. At the position designated with (a) in Fig. 3.11, the sudden appearance of a localized damage produces the drop in the stress seen in the experiments, that corresponds to the occurrence of a necked region in the central part of the specimen, as shown in Fig. 3.12 (see Fig. S5 in Millereau et al. [2018]). The corresponding strain level $\varepsilon = 1.4$ is used to calibrate the value of the parameter λ_o. At increasing level of strains, the necking enlarges with constant maximum value up to the stretch at which it has filled the whole specimen (region (b) in the figure). Thereafter (region (c)) the damage value starts increasing and at $\varepsilon = 4.55$ was $d = 0.33$. The hardening behaviour is achieved in the model by taking the absolute value of a_3 to be large enough ($a_3 = -4.73$ in this case).

In order to highlight the capability of the model to describe also the unloading process, unloading curves at different strain levels are shown in Fig. 3.11. The unloading branches follows a path with lower tangent stiffnesses due to the occurrence of damage, but they follow a different path respect the data in Millereau et al. [2018]; as was also expected,

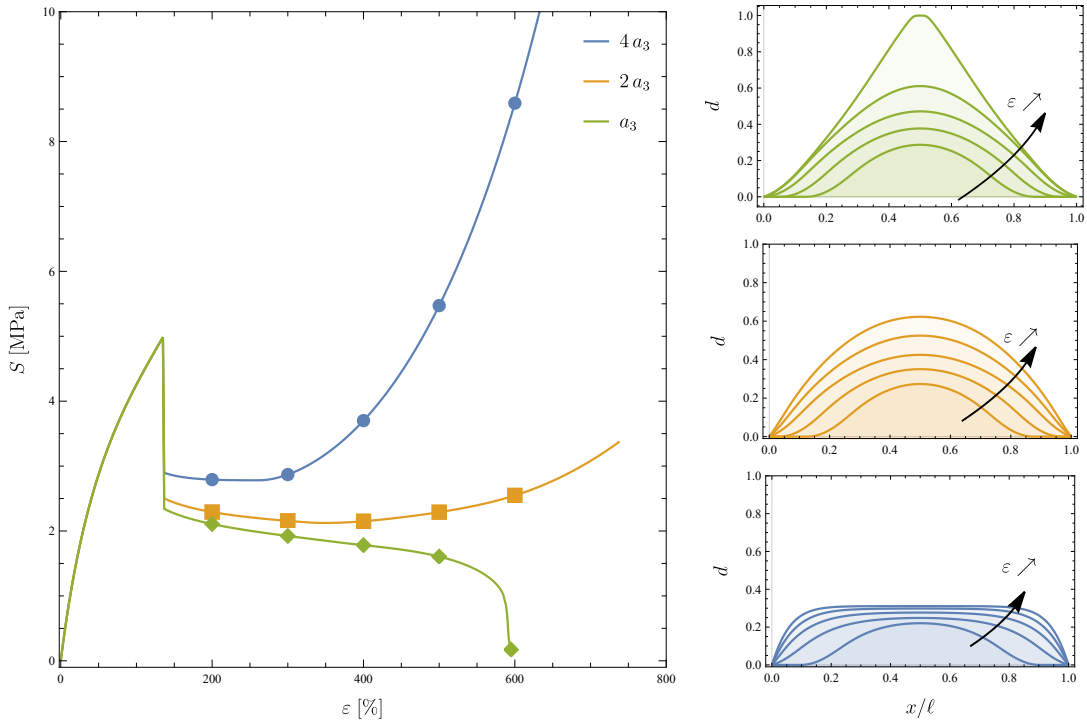

Figure 3.10: Influence of the fracture parameter a_3. Piola stress vs. strain for $a_3 = \{-0.68, -1.36, -2.72\}$ with the elastic parameters in ϕ_B. The insets show the damage profile at the different strain levels indicated by dots on the stress-strain curve.

no residual strains are observed at the complete unloading of the specimen. During the subsequent loading path, the curve perfectly follows the branch with lower stiffness up to the stress level at which damage starts increasing again. At a high strain levels, this additional reduction of stress is compensated by the elastic energy, that produces the stiffness increase seen at $\varepsilon > 300\%$, corresponding to the experimental situation of the elastomer network being completely unfolded. While this chapter successfully demonstrates the adaptability of the proposed formulation to the characteristics of double network elastomers, further enhancement of the model's alignment with the experimental data in fig. 3.11 can be improved by introducing an extra parameter to the degradation function (as elaborated in the description of the equation (3.7)) to reproduce the post-stress hardening failure. In addition, the unloading branches can be better fitted by improve the calibration of the elastic energy density.

The final numerical benchmark of the model corresponds to the deformation of a double notch tension specimen that is normally used to estimate the critical fracture energy (see for instance Loew et al. [2019], Miehe et al. [2010a]). The dimensions of the specimen, boundary conditions and mesh for this configuration are displayed in Fig. 3.13a and correspond to the experiments carried out in Hocine et al. [2002], with different lengths of the notch as shown in the insets (the same data was used as a benchmark problem in Miehe and Schänzel [2014], Talamini et al. [2018]). The constitutive parameters used in the simulation are those in Tab. 3.3 with the elastic energy ϕ_A and fracture parameters $a_1 = 1.03$, $a_2 = 32.13$ and $a_3 = -0.81$. These parameters are indeed coherent with those reported in Miehe and Schänzel [2014] to fit the same experimental data. Figure 3.13b shows the stress-strain curves that displays typical brittle response expected from

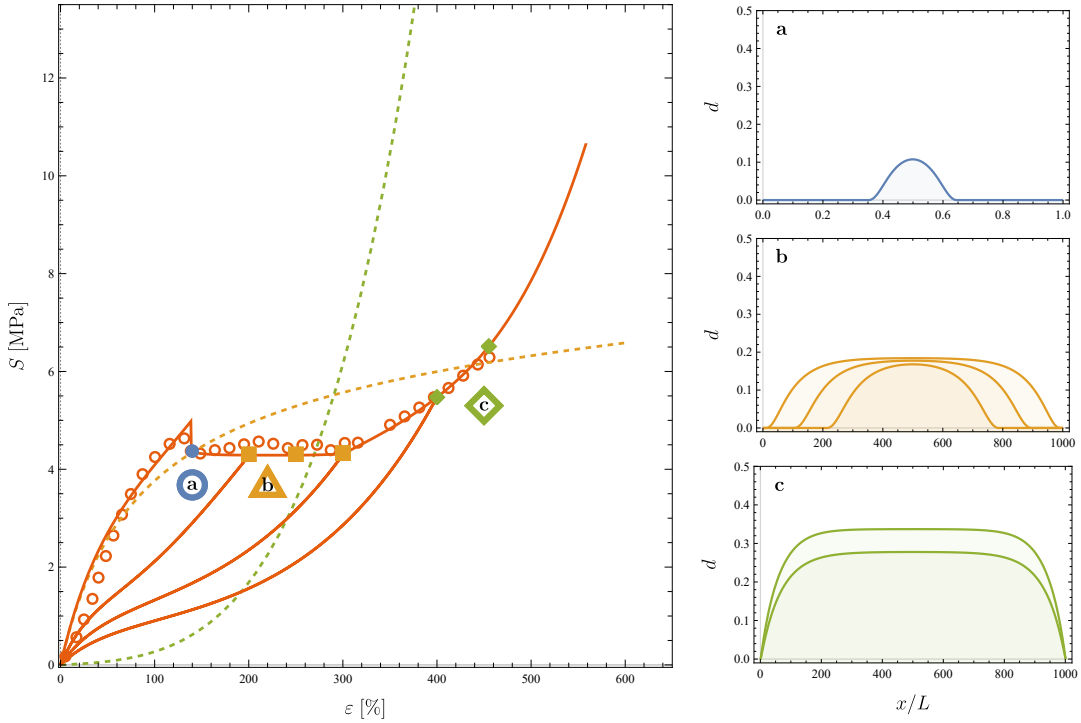

Figure 3.11: Piola stress S versus overall strain ε for a double network elastomers: open circles - experimental data from Millereau et al. [2018], orange continuous curve - model prediction, dashed curve - response of purely elastic model. The fitting is achieved with the model parameters in Tab. 3.2. The insets show the damage profile along the specimen middle axis at the strain levels (a), (b) and (c) indicated in the plot. Specifically, based on (b), it's observed that the transition region progresses along the bar in tandem with the nonlocal energy contribution. This proves the validity of regarding the nonlocal damage term as energy.

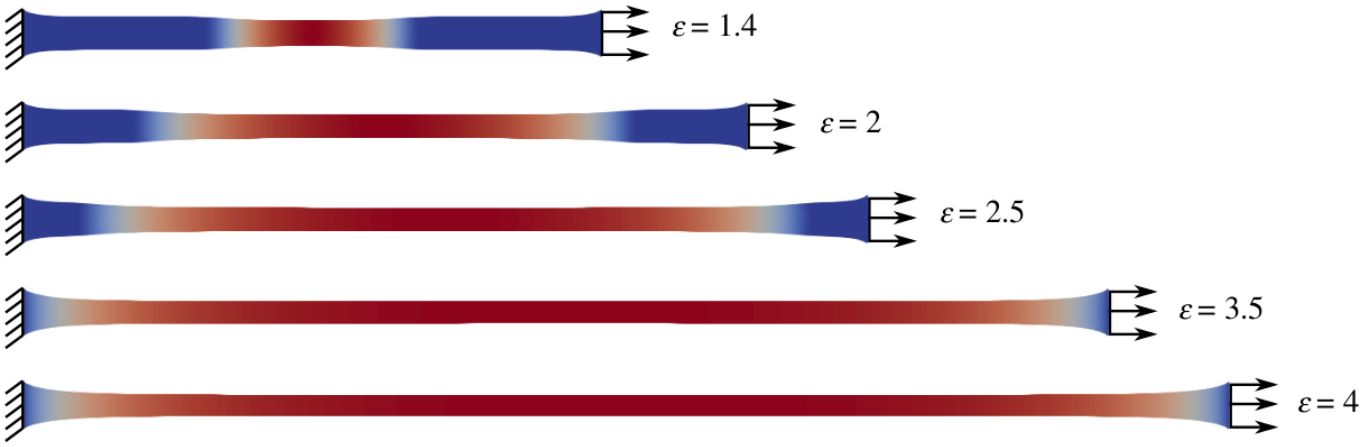

Figure 3.12: Deformed configuration of the rectangular specimen used for fitting the data in Fig. 3.11. The plateau in the stress-strain curves corresponds to the propagation of a necking region along the bar. The colormap represents the damage intensity, red being the damage with higher damage. Propagation of a damage wave in the central part of the specimen was observed in the experimental data in Millereau et al. [2018] (see Fig. S5 therein).

Table 3.3: Constitutive parameters used for the fitting of the experimental data in Fig. 3.13.

Elastic					
	$\mu_1 = 0.23$ MPa	$\alpha_1 = 2$			
Fracture					
	$\ell_f = 3.14$ mm,	$G_c = 3.15$ MPa mm,	$\lambda_\mathrm{o} = 4.4$,	$\hat{k}_\mathrm{o} = -9.53$ MPa/mm,	$a_3 = -0.81$

elastomers in this type of test. The numerical results show a very narrow cohesive region in which the damage rapidly propagates between the notches up to the point at which it occupies the entire width and immediately jumps to 1, leading to the catastrophic failure of the specimen.

The corresponding deformed configurations are shown in Fig. 3.14 at different levels of the overall strain. At $\bar{u} = 63.005$ mm the specimen is completely broken and, in fact, the material in the central part of the specimen is completely broken having reached a valued of d close to 1, with the lateral parts being almost unloaded.

3.4 Summary of rate independent model

In this work a phenomenological damage phase-field model for the cohesive failure of elastomers at large strain is presented and described in its main aspects. The elastic response of the model is described through an Ogden-like strain energy density, which has the advantage of accurately matching the quasi-static response of many materials up to significant strains. Fracture was incorporated by complementing the Ogden formulation with a phase-field variable, whose evolution was derived in a consistent thermodynamic framework by invoking the three principles of damage irreversibility, stability conditions and energy balance.

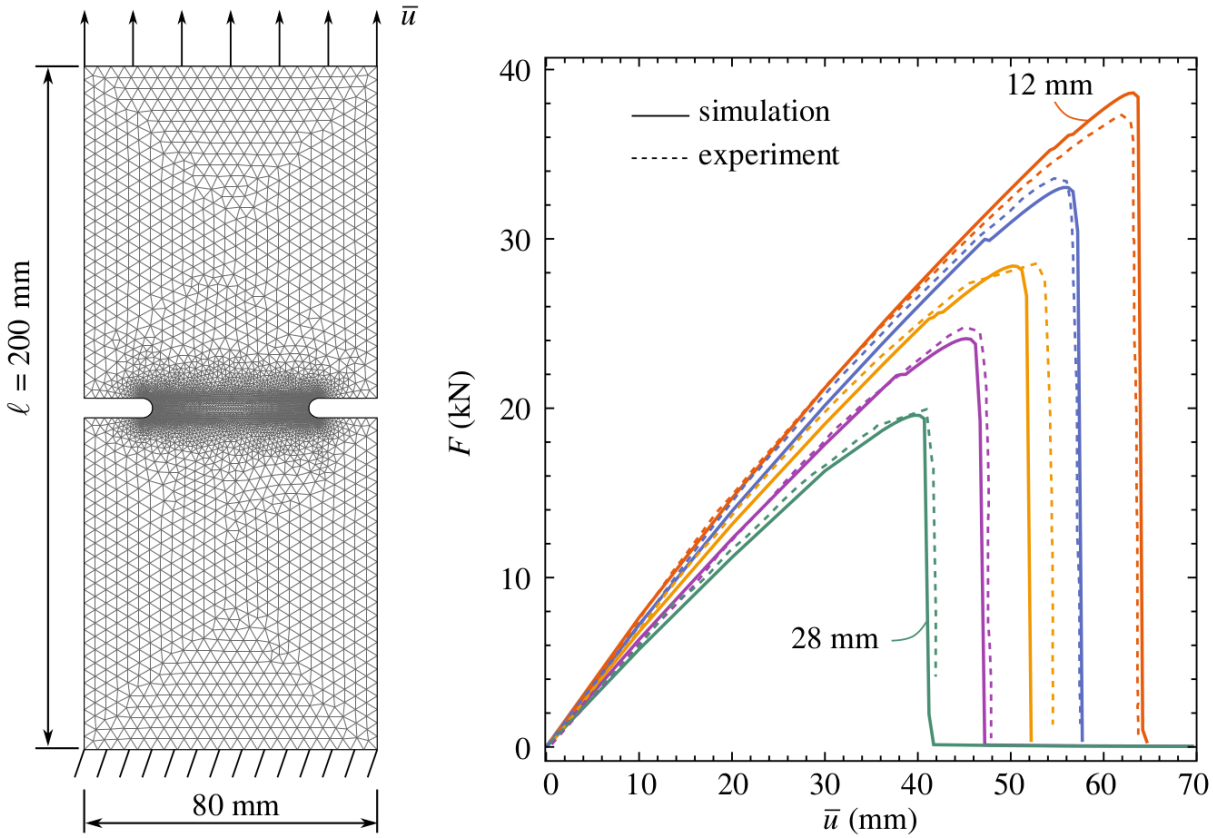

Figure 3.13: Geometry, mesh and boundary conditions of the double notch tensions specimen (left). Comparison of force-displacement curves with the constitutive parameters in Tab. 3.3 and different notch semi-lengths $\{12, 26, 20, 24, 28\}$ mm from Hocine et al. [2002].

The fracture energy was defined according to a recent proposal in Wu [2017] in terms of 5 constitutive parameters: the energy release rate G_c, the internal length l_f, that represents the size of the fracture process zone, and 3 coefficients a_1, a_2 and a_3 that defines the energetic degradation function responsible of the stiffness decrease induced by damage. Analytical and numerical results were used to establish the connection between shape of damage energy, degradation function and damage evolution modes. In particular, a_1 is related to the stretch at the damage onset in the one-dimensional test, a_2 depends on the slope of the cohesive curve, which is normally considered a material property, and, finally, a_3 influences the displacement jump at complete specimen fracture. This research could benefit from further analysis involving additional constituent parameters, such as ξ shaping $\eta(d)$, and exploring the experimental perspective regarding the roles of different internal lengths (l_f, ℓ_i, ℓ_c). By properly tuning these constitutive parameters, the model was capable of matching a variety of fracture modes including brittle and pseudo-ductile failures, whereas most of the phase field models at large strain currently available in the literature can only describe brittle fracture. The application to double-network elastomers as well as conventional rubber compounds were discussed in the paper with reference to the experiments in Hocine et al. [2002] and Millereau et al. [2018]. The model was able to accurately capture the main features of the fracture process, such as the necking propagation and hardening stage at large strains for dou-

ble network elastomers, and brittle failure modes for conventional rubber compounds. Anyway, the model is adaptable to numerous elastomeric materials and a wide array of experiments while upholding the requirement of rate independence.

Compared to other approach in the literature (such as Lavoie et al. [2019]), the phenomenological nature of the model does not implies any information on the material microstructure, and so it is suitable for a large class of materials including biological tissues.

The derivations were carried out by enforcing plane stress condition and perfect incompressibility of the matrix. However, experimental evidence shows that fracture may occur due to the coalescence of voids and the subsequent propagation of the defects, that may lead to a reduction of the apparent bulk modulus. Therefore, further development of the model include the possibility of degrading with the phase-field variable both volumetric and isochoric parts of the energy. In addition, since viscous effects may become significant during the propagation of fractures, the incorporation of viscoelastic effects appears of paramount importance to correctly describe the dynamic evolution of fracture in elastomeric compounds.

Ultimately, it becomes evident that the main constraint of the current model is its rate independence. Consequently, the forthcoming work in the following chapter will focus on formulating and studying a phase-field model of damage applied specifically to a viscoelastic model. The main viscoelastic models are introducted in sect. 2.1, and the more relevant combination of viscoelasticity and damage are cited in sect. 2.5.5.

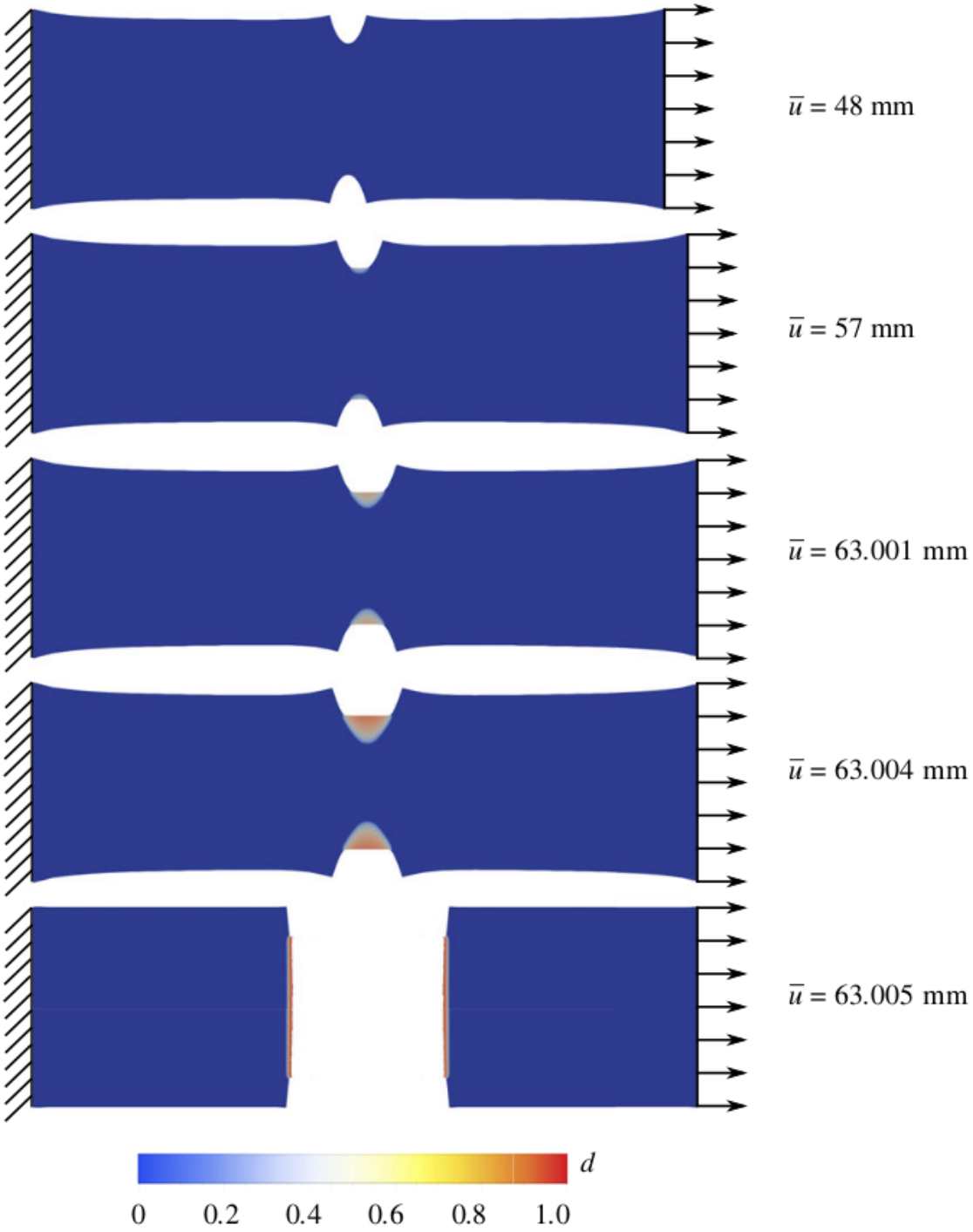

Figure 3.14: Deformed configuration of the double notch tension specimen used for the numerical experiment in Fig. 3.13 with notch semi-length 12 mm. The colormap represents the intensity of the damage field; at final step, regions where $d \geq 0.99$ were removed from the plot.

Chapter 4

A rate dependent damage phase field model

Within this chapter, the viscoelastic model discussed in Kumar and Lopez-Pamies [2016] (refer to sect. 2.4.2) will be augmented by incorporating a phase-field model addressing brittle damage as formulated in Pham et al. [2011] for brittle fracture ($\eta(d) = d$ of sect. 2.5.3). A related modeling approach has been briefly introduced in sect. 2.5.5.

The primary objective is to reproduce fracture propagation, as observed in the experiments by Corre et al. [2020] (see figs. 1.3 and 2.16). This chapter is divided into the introduction of the model from a thermodynamic viewpoint, the presentation of constitutive relations with related equilibrium equations (sect. 4.1), where also the numeric solution routine is presented and the specification of the model for the uniaxial tensile load conditions from a theoretical and numerical point of view (sect. 4.2). In addition, in sect. 4.3, the model is specialized to the plane stress state.

The main results are discussed in sect. 4.3, where the role of the different parameters on the crack propagation are studied. Starting from the results of Hakim and Karma [2009], who proved that the damage velocity is inversely proportional to the damage characteristic time (in this work named τ_d), the role of the material characteristic time τ_m (related to the material viscosity) is analyzed. From this point of view, the influence of the ratio τ_m/τ_d will be studied with their limit cases $\tau_m/\tau_d \to \infty$, i.e. (the characteristic time of the material is significantly larger than the damage characteristic time) or $\tau_m/\tau_d \to 0$. After this analysis, the influence of the numerical discretization is discussed in terms of Δt and the mesh size. The proposed analysis is propedeutic to reproduce the experimental results of Corre et al. [2020].

In the proposed approach the damage characteristic time τ_d is considered a material parameter as opposed to a merely numerical one,as it is sustained in the literature. The physical role of τ_d lies in accounting for the duration of all those phenomena that occur within the FPZ (see fig. 2.8 and sect. 2.2) at the micro-scale level, such as recrystallization, cavitation, or chain's rupture. These phenomena cannot be captured by the viscous deformation $\mathbf{F}_v$ alone, that rather represents a macroscopic parameter.

This decision is supported by the numerical findings in section 4.3.2, where the significance of τ_d in determining crack propagation speed outweigh that of all other parameters, including τ_m.

4.1 Model formulation

The model is developed within the framework of finite viscoelasticity, employing the multiplicative decomposition of the deformation gradient already introduced in sect. 2.1, with the notation in sects. 1.5, 2.1 and 2.4.1. We recall that the total deformation $\mathbf{F}$ is decomposed as $\mathbf{F} = \mathbf{F}_e\mathbf{F}_v$, where the $\mathbf{F}_e$ is the so-called elastic deformation and $\mathbf{F}_v$ is the viscous component of the deformation (see fig. 2.21). In this context, the following form of internal energy will be considered

$$\mathcal{E}_{int} = \overbrace{\int_{\Omega_0} \underbrace{g_{eq}(d)\psi_{eq}(\mathbf{C}) + g_{neq}(d)\psi_{neq}(\mathbf{F}_v^{-T}\mathbf{C}\mathbf{F}_v^{-1})}_{\text{Strain energy density}} + \underbrace{\frac{G_c}{c_0} b(\nabla d)^2}_{\text{Non local damage energy}} \, \mathrm{d}\Omega_0}^{\text{Free energy } (\Psi)} + \overbrace{\int_{\Omega_0} \frac{G_c}{c_0\, b}\eta(d)\mathrm{d}\Omega_0}^{\text{Dissipative damage energy}} \quad , \tag{4.1}$$

where ψ_{eq} is the equilibrium component of the elastic energy (given by the equilibrium spring in fig. 2.22) assumed dependent on the right Cauchy-Green strain tensor $\mathbf{C} = \mathbf{F}^T\mathbf{F}$ ($\mathbf{F} = \mathbf{I} + \mathrm{Grad}(\underline{u})$). ψ_{neq} is the non equilibrium component, given by the non equilibrium spring, dependent on the elastic right Cauchy strain tensor $\mathbf{C}_e = \mathbf{F}_v^{-T}\mathbf{C}\mathbf{F}_v^{-1}$. The third term in eqn. (4.1) is the regularization term for the damage variable. Both of the elastic energies are multiplied by a distinct degradation function which accounts for the reduction of the elastic parameters for the damaged material (g_{eq} and g_{neq}). This means that the effect of the damage into the two springs (see fig. 2.22) may be different. The last integral computes the local dissipation due to the damage phase-field state variable d, which was presented and analyzed in sect. 2.5.

4.1.1 Stability criterion

To deduce the equilibrium equations, a first order *stability criterion*, as in sect. 3.1.3, is invoked. Namely

$$\partial\mathcal{E}_{int}(\underline{u}, \mathbf{F}_v, d)[\hat{\underline{u}}, \hat{\mathbf{F}}_v, \hat{d}] - \partial\mathcal{E}_{ext}(\underline{u})[\hat{\underline{u}}] + \partial\mathcal{W}_{nc}(\dot{\mathbf{F}}_v, \dot{d})[\hat{\mathbf{F}}_v, \hat{d}] \geq 0 \qquad \forall[\hat{\underline{u}}, \hat{d}, \hat{\mathbf{F}}_v], \tag{4.2}$$

where $[\hat{\underline{u}}, \hat{\mathbf{F}}_v, \hat{d}]$ are the perturbations of the displacement, viscous deformation and damage field. $\partial\mathcal{E}_{int}$ and $\partial\mathcal{E}_{ext}$ are the first variations of internal and external energies and $\partial\mathcal{W}_{nc}$ is the internal virtual work of the viscous forces. This component of the stability criterion was absent in the rate-independent model of chp. 3 because, in that instance, the only dissipative term (due to damage) admitted a dissipative potential. Consequently, this potential could be incorporated into the internal energy. However, in this scenario, the two viscous dissipations (represented by $\dot{\mathbf{F}}_v$ and $\dot{d}$) do not allow a dissipative potential and hence the former alternative approach was used.

The equation for the first variation of the external energy is

$$\partial\mathcal{E}_{ext}(\underline{u})[\hat{\underline{u}}] = \int_{\Omega_0} \underline{b}_0 \cdot \hat{\underline{u}}\mathrm{d}\Omega_0 + \int_{\partial\Omega_{0\,2}} \underline{s}_0 \cdot \hat{\underline{u}}\mathrm{d}\partial\Omega_{0\,2}\,, \tag{4.3}$$

where $\underline{b}_0$ and $\underline{s}_0$ are the body and the surface forces and $\partial\Omega_{0\,2}$ is the part of the reference body boundary ($\partial\Omega_0$) where the forces are assigned. For what concerns the virtual work

of viscous forces, the equation is

$$\partial \mathcal{W}_{nc}(\dot{\mathbf{F}}_v, \dot{d})[\hat{\mathbf{F}}_v, \hat{d}] = \int_{\Omega_0} J_v \mathbf{T}_v \mathbf{F}_v^{-T} \cdot \hat{\mathbf{F}}_v + \frac{G_c}{c_0\, b} \tau_d \dot{d} \hat{d}\, \mathrm{d}\Omega_0\,, \tag{4.4}$$

where $\mathbf{T}_v = \mathbf{T}_v(\dot{\mathbf{F}}_v)$ is the viscous stress tensor (linked with the dash-pot in fig. 2.22) defined per unit of volume in the natural configuration and τ_d is the characteristic time for the damage state variable. After these definitions, the stability criterion in eqn. (4.2) can be evaluated, firstly with $[\hat{\underline{u}}, \hat{\mathbf{F}}_v, \hat{d}] = [\hat{\underline{u}}, \mathbf{0}, 0]$ to obtain the following macro force balance

$$\begin{aligned} \mathrm{Div}(\mathbf{P}) + \underline{b}_0 = \underline{0} \qquad & \text{in } \Omega_0 \\ \mathbf{P}\hat{n}_0 = \underline{s} \qquad & \text{in } \partial\Omega_{0\,2}, \\ \underline{u} = \underline{u}^* \qquad & \text{in } \partial\Omega_{0\,1} \end{aligned} \tag{4.5}$$

where $\mathbf{P}$ is the first Piola stress tensor (see eqn. (2.13)). The second Piola stress tensor is defined accordingly

$$\mathbf{S} = 2g_{eq}\frac{\partial \psi_{eq}}{\partial \mathbf{C}} + 2g_{neq}\mathbf{F}_v^{-1}\frac{\partial \psi_{neq}}{\partial \mathbf{C}_e}\mathbf{F}_v^{-T} = \mathbf{S}_{eq} + \mathbf{F}_v^{-1}\tilde{\mathbf{S}}_{neq}\mathbf{F}_v^{-T} = \mathbf{S}_{eq} + \mathbf{S}_{neq}, \tag{4.6}$$

where $\tilde{\mathbf{S}}_{neq} = 2\partial\psi_{neq}/\partial\mathbf{C}_e$ is the stress tensor in the natural configuration. An important observation is that, for fixed $\mathbf{F}_v$ and d, $\partial\mathcal{W}_{nc} = 0$, thus the problem in eqn. (4.5), can be solved in weak form as

$$\partial \mathcal{E}_{int}(\underline{u}, \mathbf{F}_v, d)[\hat{\underline{u}}, \mathbf{0}, 0] - \partial \mathcal{E}_{ext}(\underline{u})[\hat{\underline{u}}] = 0. \tag{4.7}$$

The next minimization step is the solution of eqn. (4.2) with $[\hat{\underline{u}}, \hat{\mathbf{F}}_v, \hat{d}] = [\underline{0}, \hat{\mathbf{F}}_v, 0]$ such that $\hat{\mathbf{C}}_e = -2\,\mathrm{sym}(\mathbf{C}_e\hat{\mathbf{F}}_v\mathbf{F}_v^{-1})$. Using this assumption, eqn. (4.2) yields

$$\int_{\Omega_0} -2g_{neq}\frac{\partial \psi_{neq}}{\partial \mathbf{C}_e} \cdot \mathbf{C}_e\hat{\mathbf{F}}_v\mathbf{F}_v^{-1} + J_v\mathbf{T}_v\mathbf{F}_v^{-T} \cdot \hat{\mathbf{F}}_v \mathrm{d}\Omega_0 \geq 0, \;\; \text{s. t. } \; J_v\mathbf{T}_v = g_{neq}\mathbf{C}_e\frac{\partial \psi_{neq}}{\partial \mathbf{C}_e} \tag{4.8}$$

which is equal to the one obtained in Reese and Govindjee [1998] (see sect. 2.1 therein). The minimization of eqn. (4.2) with respect to the damage variable (thus with $[\hat{\underline{u}}, \hat{\mathbf{F}}_v, \hat{d}] = [\underline{0}, \mathbf{0}, \hat{d}]$) gives

$$Y = g'_{eq}\psi_{eq} + g'_{neq}\psi_{neq} + \frac{G_c}{c_0\, b}(\eta' - 2b^2\Delta d + \tau_d\dot{d}) \geq 0, \tag{4.9}$$

that represents the yield condition for the damage variable.

4.1.2 Energy balance

The *energy balance* principle requires that

$$\dot{\mathcal{E}}_{int}(\underline{u}, \mathbf{F}_v, d) + \mathcal{P}_{nc}(\dot{\mathbf{F}}_v, \dot{d}) = \dot{\mathcal{E}}_{ext}(\underline{u}); \tag{4.10}$$

where

$$\mathcal{P}_{nc} = \int_{\Omega_0} J_v\mathbf{T}_v \cdot \mathbf{L}_v + \frac{G_c}{c_0\, b}\tau_d\dot{d}^2\, \mathrm{d}\Omega_0, \tag{4.11}$$

is the internal viscous power, whereas the internal power is

$$\begin{aligned} \dot{\mathcal{E}}_{int} = \int_{\Omega_0} g_{eq}\frac{\partial \psi_{eq}}{\partial \mathbf{C}} \cdot \dot{\mathbf{C}} + g_{neq}\frac{\partial \psi_{neq}}{\partial \mathbf{C}_e} \cdot \dot{\mathbf{C}}_e + (g'_{eq}\psi_{eq} + g'_{neq}\psi_{neq} + \frac{G_c}{c_0 b}(\eta' - 2b^2\Delta d))\dot{d}\mathrm{d}\Omega_0 + \\ + \int_{\partial\Omega_0} \frac{G_c}{c_0 b} b^2 \nabla d \cdot \hat{n}_0\, \dot{d}\mathrm{d}(\partial\Omega_0). \end{aligned} \tag{4.12}$$

By using the Macro and the Micro force balance eqns. (4.5) and (4.8) and the identity $\dot{\mathbf{C}}_e = \mathbf{F}_v^{-T}\dot{\mathbf{C}}\mathbf{F}_v^{-1} - 2\text{sym}(\mathbf{C}_e\mathbf{L}_v)$, eqn. (4.10) turns into

$$Y\dot{d} = 0. \tag{4.13}$$

This last condition, with eqn. (4.9) and the irreversibility condition for the damage ($\dot{d} \geq 0$), gives the Kuhn-Tucker conditions

$$Y\dot{d} = 0; \qquad Y \geq 0; \qquad \dot{d} \geq 0. \tag{4.14}$$

In this context, the evolution of the damage variable can be expressed (similar to Hakim and Karma [2009]) by introducing the Macaulay brackets as:

$$\dot{d} = \frac{1}{\tau_d} < \frac{-c_0\, b}{G_c}(g'_{eq}\psi_{eq} + g'_{neq}\psi_{neq}) - \eta' + 2b^2\Delta d >= \frac{1}{\tau_d} < f(\mathbf{C}, \mathbf{F}_v, d) >, \tag{4.15}$$

where $< \bullet >= \max\{0\,, \bullet\}$ such that:

$$\begin{cases} \dot{d} = \frac{1}{\tau_d} f(\mathbf{C}, \mathbf{F}_v, d) & \text{if } \; f(\mathbf{C}, \mathbf{F}_v, d) > 0 \\ \dot{d} = 0 & \text{if } \; f(\mathbf{C}, \mathbf{F}_v, d) < 0 \end{cases}. \tag{4.16}$$

This set of equations can be solved as a bounded incremental minimization problem by the backward Euler approximation of the damage rate by

$$\dot{d} \simeq \frac{d_t - d_{t-\Delta t}}{\Delta t}, \tag{4.17}$$

where the time dependence is reported as subscript and $d_{t-\Delta t}$ is considered to be known. In this case, the problem for the damage field becomes

$$\text{argmin}_{d\in[0,1]\, d\geq d_{t-\Delta t}}\{\mathcal{F}(d)\} \qquad \text{with } \; \mathcal{F}(d) = \mathcal{E}_{int}(\underline{\overline{u}}, \overline{\mathbf{F}}_v, d) + \frac{G_c}{c_0\, b}\int_{\Omega_0} \tau_d \frac{(d - d_{t-\Delta t})^2}{2\Delta t}\, \mathrm{d}\Omega_0. \tag{4.18}$$

Indeed the constrained minimization of $\mathcal{F}(d)$ with respect to d can be expresses in weak form by

$$\partial\mathcal{F}(d)[\hat{d}] = \partial\mathcal{E}_{int}(\underline{\overline{u}}, \overline{\mathbf{F}}_v, d)[\underline{0}, \mathbf{0}, \hat{d}] + \frac{G_c}{c_0\, b}\int_{\Omega_0} \tau_d \frac{d - d_{t-\Delta t}}{\Delta t}\hat{d}\, \mathrm{d}\Omega_0 \geq 0, \tag{4.19}$$

which, with the approximation in (4.17), gives eqn. (4.9).

4.1.3 Dissipation inequality

The non negativeness of the dissipation rate requires that

$$\mathcal{D} = \mathcal{E}_{ext} - \dot{\Psi} \geq 0, \tag{4.20}$$

which is normally referred as Clausius-Duhem inequality. By the substitution of the *energy balance* in eqn. (4.10), the dissipation inequality reduces to

$$J_v\mathbf{T}_v \cdot \mathbf{L}_v \geq 0, \qquad \frac{G_c}{c_0\, b}\tau_d\dot{d}^2 \geq 0, \tag{4.21}$$

where the former inequality requires a constitutive choice of $\mathbf{T}_v$, here assumed to be linear in $\mathbf{L}_v$, thus in $\mathbf{D}_v$, due to its symmetry, whereas the second inequality is automatically

satisfied due to the positiveness of the coefficients. These definitions imply an implicit constitutive assumption for the dual micro force of $\dot{d}$, defined as $\Sigma_v = [G_c/(c_0\, b)]\tau_d \dot{d}$.

In order to further exploit the implications of eqn. (4.20), it is important to observe that, for a fixed $\mathbf{F}_v$, the time derivative of ψ_{neq} is

$$\dot{\psi}_{neq} = \frac{\partial \psi_{neq}}{\partial \mathbf{C}_e} \cdot \dot{\mathbf{C}}_e = \frac{\partial \psi_{neq}}{\partial \mathbf{C}_e} \cdot (\mathbf{F}_v^{-T} \dot{\mathbf{C}} \mathbf{F}_v^{-1}) = \mathbf{F}_v^{-1} \frac{\partial \psi_{neq}}{\partial \mathbf{C}_e} \mathbf{F}_v^{-T} \cdot \dot{\mathbf{C}} = \frac{\partial \psi_{neq}}{\partial \mathbf{C}} \cdot \dot{\mathbf{C}}, \quad (4.22)$$

where, in the last passage, ψ_{neq} is derived with respect to $\mathbf{C}$ for fixed $\mathbf{F}_v$. From the last equations, two alternative, but equivalent definition of the non equilibrium part of the second Piola stress tensor are obtained

$$\mathbf{S}_{neq} = \mathbf{F}_v^{-1} \frac{\partial \psi_{neq}}{\partial \mathbf{C}_e} \mathbf{F}_v^{-T} = \frac{\partial \psi_{neq}}{\partial \mathbf{C}}. \quad (4.23)$$

For an isotropic material, it is required that the non equilibrium energy density depends only on the invariants of $\mathbf{C}_e$ namely

$$\psi_{neq} = \overline{\psi}_{neq}(I_{e1}, I_{e2}, J_e); \quad (4.24)$$

with

$$\begin{aligned} I_{1e} &= \mathbf{C}_e \cdot \mathbf{I} = \mathbf{F}_v^{-T} \mathbf{C} \mathbf{F}_v^{-1} = \mathbf{C} \cdot \mathbf{C}_v^{-1}; \\ I_{2e} &= \mathrm{cof}(\mathbf{C}_e) \cdot \mathbf{I} = \frac{1}{2}(I_{e1}^2 - \mathbf{C}_e \mathbf{C}_e \cdot \mathbf{I}) = \frac{1}{2}((\mathbf{C} \cdot \mathbf{C}_v^{-1})^2 - \mathbf{C}_v^{-1} \mathbf{C} \cdot \mathbf{C} \mathbf{C}_v^{-1}); \\ I_{3e} &= \det \mathbf{C}_e = J_e^2 = J^2 / J_v^2, \end{aligned} \quad (4.25)$$

where $J_e = \det \mathbf{F}_e$; $J = \det \mathbf{F}$, $J_v = \det \mathbf{F}_v$ and $\mathrm{cof}(\mathbf{C}_e) = J_e \mathbf{C}_e^{-T}$ is the cofactor of $\mathbf{C}_e$. As a consequence, $\mathbf{S}_{neq}$ assumes the following form

$$\mathbf{S}_{neq} = \frac{\partial \overline{\psi}_{neq}}{\partial \mathbf{C}} = \frac{\partial \overline{\psi}_{neq}}{\partial I_{e1}} \mathbf{C}_v^{-1} + \frac{\partial \overline{\psi}_{neq}}{\partial I_{e2}} (I_{e1} \mathbf{C}_v^{-1} - \mathbf{C}_v^{-1} \mathbf{C} \mathbf{C}_v^{-1}) + \frac{\partial \overline{\psi}_{neq}}{\partial J^2} (J^2 / J_v^2) \mathbf{C}^{-1}. \quad (4.26)$$

It is pointed out that eqns. (4.24)-(4.26) only depend on the viscous strain $\mathbf{C}_v$ rather on the entire deformation $\mathbf{F}_v$. This fact allows us to evaluate the viscous deformation $\mathbf{C}_v$ only, that is a symmetric tensor.

4.1.4 A specific form of strain energy density

Here, a most specific choice of constitutive equations is introduced. In particular isotropic and incompressible material will be considered, such that $J = J_v = J_e = 1$. For what concerns the elastic energy densities of the equilibrium and the non equilibrium springs, they are assumed in the following form (taken from Lopez-Pamies [2010])

$$\begin{aligned} \psi_{eq} = \psi_{eq}^D + \psi_{eq}^V &= \sum_i \frac{3^{1-\alpha_i}}{2\alpha_i} \mu_i (I_1^{\alpha_i} - 3^{\alpha_i}) - p_{eq}(J-1) \\ \psi_{neq} = \psi_{neq}^D + \psi_{neq}^V &= \sum_i \frac{3^{1-a_i}}{2a_i} m_i [I_{e1}^{a_i} - 3^{a_i}] - p_{neq}(J_e - 1) \end{aligned} \quad (4.27)$$

where volumetric and distorsional contributions are split in a way that p_{eq} and p_{neq} are the Lagrangian multipliers for the incompressibility constraints as already discussed at the end of sect. 2.4.1).

In addition, a brittle model is chosen for the damage variable as in Pham et al. [2011] (see sect. 2.5.2). The characteristic functions are

$$\eta(d) = d; \qquad c_0 = \frac{8}{3};\ b = \frac{l_f}{4}; \qquad g_{eq}(d) = g_{neq}(d) = g(d) = (1-d)^2. \tag{4.28}$$

By using last definitions, the yield condition in eqn. (4.9) assumes the expression

$$Y = \frac{3G_c}{2l_f}(1 - \frac{l_f^2}{8}\Delta d + \tau_d \dot{d}) - 2(1-d)(\psi_{eq} + \psi_{neq}) \geq 0. \tag{4.29}$$

The rate dependence is captured by the generalization of the Reese and Govindjee [1998] model, proposed by Kumar and Lopez-Pamies [2016]. For such a model, the micro force balance (as eqn. (4.8)) is

$$\mathbf{F}\mathbf{S}_{neq}\mathbf{F}^T = \mathbb{A}(\mathbf{F}_e, \mathbf{F}_v)[\mathbf{F}_e\mathbf{L}_v\mathbf{F}_e^{-1}], \tag{4.30}$$

where for isotropic material, the 4^{th} order tensor $\mathbb{A}$ has the following form

$$\begin{aligned} \mathbb{A} &= \eta_K \mathbb{K}(\mathbf{I} + \mathbf{B}_e \mathbb{T}\mathbf{B}_e^{-1}) + 3\eta_J \mathbb{J} \\ \mathbb{A}[\mathbf{A}] &= \eta_K \mathbb{K}(\mathbf{A} + \mathbf{B}_e\mathbf{A}^T\mathbf{B}_e^{-1}) + 3\eta_J \mathbb{J}[\mathbf{A}] \end{aligned} \tag{4.31}$$

with $\mathbb{J}[\mathbf{A}] = sph(\mathbf{A})$; $\mathbb{T}[\mathbf{A}] = \mathbf{A}^T$; $\mathbb{K}[\mathbf{A}] = dev(\mathbf{A})$. By (4.30) and the incompressibility constraint ($\mathbb{J}[\mathbf{F}_e\mathbf{L}_v\mathbf{F}_e^{-1}] = 0$), the following evolution equation for the viscous strain is obtained

$$\dot{\mathbf{C}}_v = \frac{r_{neq}}{\eta_K}(\mathbf{C} - \frac{1}{3}I_{e1}\mathbf{C}_v), \qquad \text{where} \qquad r_{neq} = 2\frac{\partial \psi_{neq}}{\partial I_{e1}} = \sum_i 3^{1-a_i} m_i I_{e1}^{1-a_i}. \tag{4.32}$$

as shown in sect. 2.4.2. In the next section, a numerical algorithm is developed to determine the solution of the problem.

4.1.5 Numerical implementation

The evolution equations are numerically solved by means of a FE by code which iterates the following steps, where a single variable field is determined, keeping the others fixed:

- Equation (4.5) (in the weak form (4.7)) is solved using a Newton-Raphson routine to determine the displacement field $\underline{u}$.
- Equation (4.18) (with constraints $d \leq 1$, $\dot{d} \geq 0$, and $d \geq 0$) is minimized using a constrained quadratic programming problem to determine the damage field d. This problem is solved using TAO (Tool-kit for Advanced Optimization).
- The evolution equation (4.32) for the viscous strain is solved using an explicit fifth-order Runge-Kutta scheme with an extended region of stability. This scheme has been described in detail in Lawson [1966] and Kumar and Lopez-Pamies [2016] and it is summarized here in sect. 2.4.2.

The problem will be tackled using the FEniCS® open-source framework for finite elements analysis (Logg and Wells [2010]). The approach involves a step-by-step time integration, with the variables $\underline{u}_t$, $\mathbf{C}_{v\,t}$, and d_t, i.e. the displacement, viscous deformation and damage field values at time instant t, respectively assumed to be known, and $\underline{u}_{t+\Delta t}$,

$\mathbf{C}_{v\,t+\Delta t}$, and $d_{t+\Delta t}$ being the unknown functions. The internal iterative scheme is conducted to evaluate $\underline{u}$ and $\mathbf{C}_v$, denoted by the superscript i during these iterations. The external iterative scheme will solve the problem for the couple $[\underline{u}; \mathbf{C}_v]$ and d, denoted by the superscript j in this case. This is carried out according to the following procedure at each time step:

- update boundary conditions
- Initialize: $i = 0$; $j = 0$ and $\{\underline{u}_i^j,\ \mathbf{C}_{v\,j}^i,\ d_j\} = \{\underline{u}_t, \mathbf{C}_{v\,t}, d_t\}$
- Start iterations for j (while $err_d < tol_d$):
  * Start iterations for i (while $err_v < tol_v$):
    → solve Eqn. (4.7) to find $\underline{u}_j^{i+1}$ with fixed $\mathbf{C}_{v\,j}^i$ and d_j
    → evaluate $\mathbf{C}_{v\,j}^{i+1}$ by Eq. (4.32) with Runge-Kutta scheme with $\underline{u}_j^{i+1}$ and d_j,
    → update $err_v = ||\mathbf{C}_{v\,j}^{i+1} - \mathbf{C}_{v\,j}^i||_\infty$
    → update $i = i + 1$
  * Solve eqn. (4.18) to find d_{j+1} with fixed $\underline{u}_j = \underline{u}_j^i$; $\mathbf{C}_{v\,j} = \mathbf{C}_{v\,j}^i$ with constraint $d_{j+1} \geq d_t$
  * update $err_d = ||d^{j+1} - d^j||_\infty$
  * update $j = j + 1$
- assign: $\underline{u}_{t+\Delta t} = \underline{u}_j$; $\mathbf{C}_{v\,t+\Delta t} = \mathbf{C}_{v\,j}$; $d_{t+\Delta t} = d_j$; $d_{min} = d_j$; $t = t + \Delta t$

In the last line d_{min} is also updated. This damage field is used to guarantee the irreversibility condition by the constrain $d \geq d_{min}$ for all of the subsequent time steps.

4.2 Uniaxial tensile test

We study the case of a 3D cylindrical body under a simple tension state in the direction $\hat{e}_1$ as in sects. 2.4.1 and 3.2. The problem reduces to 1D and the solution of the balance equation and evolution equation are sought in the form

$$\mathbf{F} = \lambda\, \hat{e}_1 \otimes \hat{e}_1 + \frac{1}{\lambda^{\frac{1}{2}}}(\hat{e}_2 \otimes \hat{e}_2 + \hat{e}_3 \otimes \hat{e}_3), \qquad \mathbf{C}_v = \lambda_v^2\, \hat{e}_1 \otimes \hat{e}_1 + \frac{1}{\lambda_v}(\hat{e}_2 \otimes \hat{e}_2 + \hat{e}_3 \otimes \hat{e}_3) \quad (4.33)$$

where the unknowns of the problem are assumed as dependent on the longitudinal coordinate, $X \in [0, L]$ only, in a way that

$$\begin{aligned} \lambda = \lambda(X) = 1 + u'(X) \qquad & \text{macroscopic stretch;} \\ \lambda_v = \lambda_v(X) \qquad & \text{viscous stretch;} \\ d = d(X) \qquad & \text{damage field;} \end{aligned} \quad (4.34)$$

$u(X)$ being the longitudinal displacement field (in the $\hat{e}_1$ direction). The dependence on X is omitted in the next part of the work for brevity.

By using eqn. (4.23) with the elastic energies in eqns. (4.27), one obtains the following expression of the stress $S = \mathbf{S} \cdot \hat{e}_1 \otimes \hat{e}_1$ and $P = \mathbf{P} \cdot \hat{e}_1 \otimes \hat{e}_1$,

$$\begin{aligned} S =& g\, r_{eq} - p_{eq}\lambda^{-2} + g\, r_{neq}\lambda_v^{-2} - p_{neq}\lambda_v\lambda^{-2} = g\, r_{eq}(1 - \lambda^{-3}) + g\, r_{neq}(\lambda_v^{-2} - \lambda_v\, \lambda^{-3})\,, \\ P =& g\, r_{eq} - p_{eq}\lambda^{-1} + g\, r_{neq}\lambda_v^{-2} - p_{neq}\lambda_v\lambda^{-1} = g\, r_{eq}(\lambda - \lambda^{-2}) + g\, r_{neq}(\lambda_v^{-2}\lambda - \lambda_v\, \lambda^{-2}) \end{aligned} \quad (4.35)$$

in which the unknown pressure is evaluated following the procedure in sects. 3.2 and 2.4.1, with

$$r_{eq} = 2\partial\psi_{eq}(I_1)/\partial I_1, \quad r_{neq} = 2\partial\psi_{neq}(I_{1e})/\partial I_{1e}. \tag{4.36}$$

In particular, the pressure is obtained by enforcing zero stress condition on the lateral directions

$$\mathbf{S}_\alpha \cdot \hat{e}_2 \otimes \hat{e}_2 = \mathbf{S}_\alpha \cdot \hat{e}_3 \otimes \hat{e}_3 = 0 \tag{4.37}$$

either for $\alpha = \{neq, eq\}$. This gives

$$p_{eq} = r_{eq}\,\lambda^{-1}, \qquad p_{neq} = r_{neq}\,\lambda^{-1}\lambda_v\,. \tag{4.38}$$

that is equivalent to use the following reduced forms of energies and stresses

$$\psi^{1D}(\lambda, \lambda_v, d) = g\psi^D_{eq}(I_1(\lambda)) + g\psi^D_{neq}(I_{1e}(\lambda, \lambda_v)); \qquad S = 2\frac{\partial\psi^{1D}}{\partial\lambda^2}, \tag{4.39}$$

where

$$I_1 = \mathbf{C}\cdot\mathbf{I} = \lambda^2 + 2\lambda^{-1}; \qquad I_{1e} = \mathbf{C}_e\cdot\mathbf{I} = \mathbf{C}\cdot\mathbf{C}_v^{-1} = \lambda^2\lambda_v^{-2} + 2\lambda^{-1}\lambda_v. \tag{4.40}$$

By eqn. (4.39) and neglecting the external forces, eqn. (4.5) becomes

$$\begin{aligned} \frac{\partial S}{\partial X} &= 0 \qquad \text{on } X \in [0; L] \\ u(X=0) &= u_0; \qquad u(X=L) = u_L, \end{aligned} \tag{4.41}$$

Where $X \in [0; L]$ is the coordinate of the point of Ω_0.
Upon substitution of ((4.33).2) into (4.32) the following evolution equation is obtained

$$\dot{\lambda}_v = \frac{r_{neq}}{3\,\eta_K}(\lambda^2\lambda_v^{-1} - \lambda^{-1}\lambda_v^2). \tag{4.42}$$

In a quasi static tensile test, the non equilibrium part of energy, can be neglected and, therefore by eqns. (4.13) and (4.39), the yield condition at fracture onset becomes

$$Y|_{d=0;\lambda=\lambda_f} = \frac{3G_c}{2l_f} - \psi^{1D}_{eq}(I_1(\lambda_f)) = 0; \tag{4.43}$$

and, thus:

$$G_c = \frac{4l_f\,\psi_f}{3}. \tag{4.44}$$

where $\psi_f = \psi^{1D}_{eq}(I_1(\lambda_f))$ and λ_f is the strain at the fracture onset. Another important parameter that can be measured in this test is the engineering stress of fracture under pseudo-static loading conditions, and it can be evaluated by eqn. (4.35) as

$$P_f = r_{eq}|_{\lambda=\lambda_f}(\lambda_f - \lambda_f^{-2}). \tag{4.45}$$

By replacing eqns. (4.7) (for the displacement), (4.19) (for the damage) and (4.32) (for the viscous strain) into eqns. (4.41), (4.29) (4.42), the numerical algorithm shown in the listing of sect. 4.1.5, can be implemented to evaluate the solution of the 1D problem., with the following damage evolution equation:

$$\dot{d} = \frac{1}{\tau_d} < \frac{2c_0\,b}{G_c}(1-d)(\psi_{eq} + \psi_{neq}) - 1 + 2b^2\,d'' > . \tag{4.46}$$

Equilibrium spring			
$\mu_1 = \quad 2.4\,MPa$	$\mu_2 = \quad 0.008\,MPa$	$\alpha_1 = \quad 0.5$	$\alpha_2 = \quad 2.7$
Non equilibrium spring			
$m_1 = \quad 1.2\,MPa$	$m_2 = \quad 0.004\,MPa$	$a_1 = \quad 0.5$	$a_2 = \quad 2.7$
Damage parameters			
$\lambda_c = \quad 7$	$l_f = \quad 1\,mm$	$G_f = \quad 40.652\,MPa/mm$	
Viscous parameters			
$\tau_d = \quad 0\,s$	$\eta_K = \quad 1\,MPa\,s$		

Table 4.1: Material parameters for the commercial polyurethane used in the experiments of Corre et al. [2020], used for the 1D simulations.

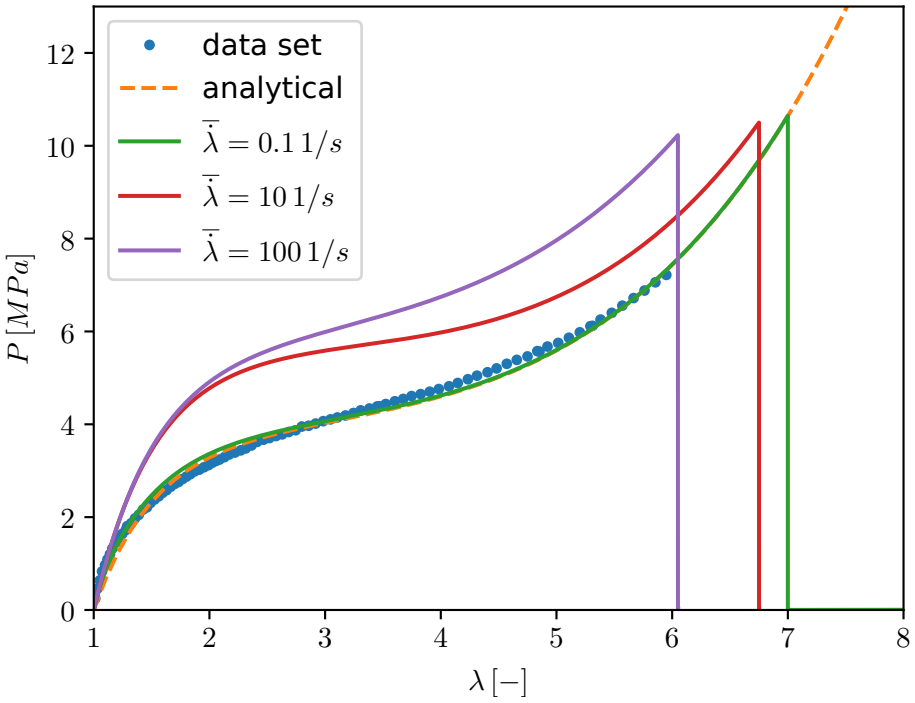

Figure 4.1: Engineering stress-strain curve depicts the uniaxial tensile test data from Kamasamudram et al. [2023], utilizing material properties from Corre et al. [2020] (listed in tab. 4.1). The curves depend on the average deformation rates ($\dot{\bar{\lambda}}$). The dashed line represents the analytical value of the equilibrium first Piola stress. The simulations are conducted on a sample measuring $L = 10\,mm$ in length, employing a mesh size of $h_{mesh} = L/5000$.

4.2.1 Numerical results

In this section, 1D simulations are performed to explore the impact of viscosity on fracture onset and examine the post-fracture behavior of the specimen.

Regarding the opening of the fracture, in fig. 4.1, it is seen (in agreement with Yin and Kaliske [2020]) that the deformation rate affects the fracture onset, phenomenon independently on τ_d. Indeed this effect can be explained by examining the yield condition (4.9) and noting that, in a quasi static experiment, $\psi_{neq} \to 0$ and, thus, it does not contributes to the fracture creation. By increasing the deformation rate, ψ_{neq} comes into play and the yield condition is achieved at a smaller strain. The data from Kamasamudram et al. [2023], specifically the uniaxial and quasi-static tensile data of the commercial polyurethane studied also in Corre et al. [2020], is used to obtain the material parameters listed in tab. 4.1. Using these parameters, the analytical engineering stress-strain curve is generated via eqn. (4.35) (dashes curve in fig. 4.1), excluding the non-equilibrium component. The response curve with $\dot{\bar{\lambda}} = 0.1\,1/s$, that is the lowest deformation rate, is accurately matched by the analytical (dashed) curve with $1/\tau_m \approx 1.2\,1/s$, that is an order of magnitude greater with respect to $\dot{\bar{\lambda}}$.

Figure 4.2 displays equilibrium and non equilibrium components of engineering

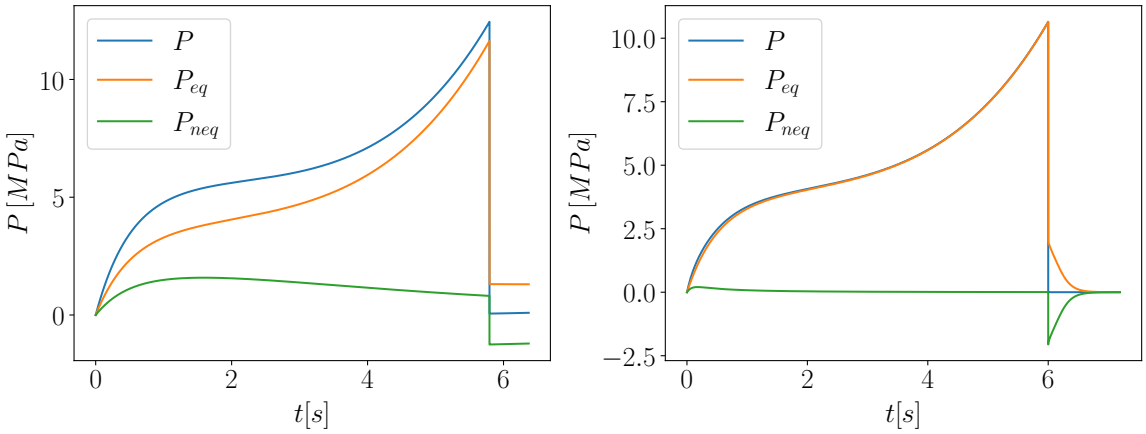

(a) $\eta_K = 10\,MPa\ s$ (b) $\eta_K = 0.1\,MPa\ s$

Figure 4.2: Average along the specimen of engineering stress versus time for uniaxial tensile test. Numerical results for a material with parameters in tab. 4.1, average of stretch ratio $\dot{\bar{\lambda}} = 1\,s^{-1}$ and $\eta_K = 10\,MPa\ s$ (in fig. 4.2a), $\eta_K = 0.1\,MPa\ s$ (in fig. 4.2b). Here the influence of the viscocity on the post-crack phase is shown. In particular the relaxation phenomena after the rupture have a velocity dependent on the viscous parameter η_K.

stresses as well together with the total stress as functions of time. Immediately after the rupture, the total stress jumps to zero. However, its equilibrium and non equilibrium components maintain equal magnitudes but opposite sign, vanishing in a time interval controlled by the material's characteristic time $\tau_{\approx} = \eta_K / r_{neq}$, where r_{neq} is defined in eqn. (4.36). This phenomenon, also illustrated in fig. 4.3, can be interpreted as a strain relaxation phenomenon: at the instance of the crack formation, the bar is immediately divided into two segments, each approximately $L/2$ in length that immediately tend to come back to the stress free configuration with a duration comparable to τ_m. In the rate-independent case ($\tau_m \to 0$), this phenomenon occurs instantaneously, as depicted in fig. 2.32. Consequently, the displacement field jumps from a linear function to a piecewise constant function. Such an instantaneous relaxation is impeded by the viscous balance eqn. (4.42). When the crack is formed, in fact

$$P = P_{eq} + P_{neq} = 0 \quad \forall\, x \in [0; L], \tag{4.47}$$

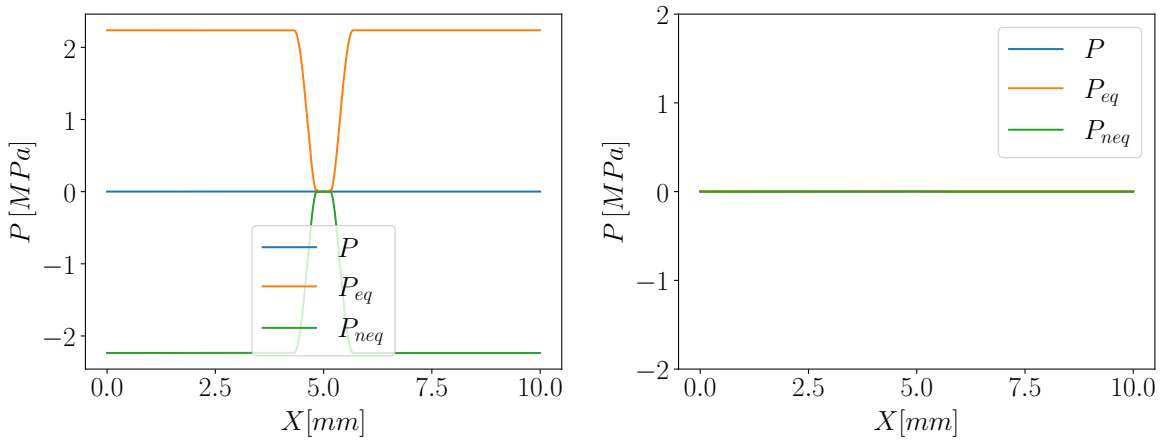

(a) $t = 6\,s$ (b) $t = 7\,s$

Figure 4.3: Specific deformation states from fig. 4.2b showcase P, P_{eq}, P_{neq} along the bar for $\eta_K = 0.1\,MPa\;s$. The time steps analyzed are $t = 6\;s$, just after fracture onset, and $t = 7\;s$, after nearly complete relaxation.

where $P_{eq} = g\,r_{eq}(\lambda - \lambda^{-2})$ and $P_{neq} = g\,r_{neq}(\lambda_v^{-2}\lambda - \lambda_v\lambda^{-2})$. In particular, since the bar is deformed, $\lambda > 1$, thus $P_{eq} > 0$ and $P_{neq} < 0$ due to the balance equation (4.47). This phenomenon becomes crucial in analyzing fracture propagation, especially when studying the stress fields depicted in figures 4.6, 4.8 and 4.10.

4.3 Plane stress loading condition

In this section, the problem is specialized to the case of plane stress. In this situation, $\mathbf{F}$; $\mathbf{F}_v$, $\mathbf{C}$ and $\mathbf{C}_v$ become:

$$\mathbf{F} = \begin{bmatrix} \overline{\mathbf{F}} & \underline{0} \\ \underline{0}^T & \overline{J}^{-1} \end{bmatrix}, \quad \mathbf{F}_v = \begin{bmatrix} \overline{\mathbf{F}}_v & \underline{0} \\ \underline{0}^T & \overline{J}_v^{-1} \end{bmatrix}, \quad \mathbf{C} = \begin{bmatrix} \overline{\mathbf{C}} & \underline{0} \\ \underline{0}^T & \overline{J}^{-2} \end{bmatrix}, \quad \mathbf{C}_v = \begin{bmatrix} \overline{\mathbf{C}}_v & \underline{0} \\ \underline{0}^T & \overline{J}_v^{-2} \end{bmatrix}, \tag{4.48}$$

where the over line stands for the 2x2 sub-matrix and $\overline{J} = \det(\overline{\mathbf{F}})$ and $\overline{J}_v = \det(\overline{\mathbf{F}}_v)$. The first invariants become:

$$\overline{I}_1(\overline{\mathbf{C}}) = \overline{\mathbf{C}} \cdot \mathbf{I} + \overline{J}^{-2}; \qquad \overline{I}_{1e}(\overline{\mathbf{C}}, \overline{\mathbf{C}}_v) = \overline{\mathbf{C}} \cdot \overline{\mathbf{C}}_v^{-1} + (\overline{J}_v/\overline{J})^2; \tag{4.49}$$

and, as in eqn. (4.39) and in sect. 2.4.1 or chp. 3, the following strain energy density will be considered:

$$\psi^{2D}(\overline{\mathbf{C}}, \overline{\mathbf{C}}_v, d) = g(d)\psi^D_{eq}(\overline{I}_1(\overline{\mathbf{C}})) + g(d)\psi^D_{neq}(\overline{I}_1(\overline{\mathbf{C}}, \overline{\mathbf{C}}_v)). \tag{4.50}$$

In this case, the second Piola stress tensor can be evaluated as:

$$\overline{\mathbf{S}} = \frac{\partial \psi^{2D}(\overline{\mathbf{C}}, \overline{\mathbf{C}}_v, d)}{\partial \overline{\mathbf{C}}}, \qquad \overline{\mathbf{P}} = \overline{\mathbf{F}}\overline{\mathbf{S}} \tag{4.51}$$

thus, the macro force balance in eqn. (4.5) (as for eqn. (4.41)) becomes:

$$\mathrm{Div}_2(\overline{\mathbf{P}}) + \underline{b}_{0\,2} = \underline{0}_2 \qquad \text{on } \Omega_0, \qquad + \text{b. c.} \tag{4.52}$$

were the subscript 2 stands for the sub-vector 2x1.

For what concerns the viscous deformation, the evolution equation for $\dot{\overline{\mathbf{C}}}_v$ specializes into

$$\dot{\overline{\mathbf{C}}}_v = \frac{r_{neq}}{\eta_K}(\overline{\mathbf{C}} - \frac{1}{3}\overline{I}_{e1}\overline{\mathbf{C}}_v), \tag{4.53}$$

where $r_{neq} = \partial\psi^{2D}_{neq}(\overline{I}_{1e}(\overline{\mathbf{C}}, \overline{\mathbf{C}}_v))/\partial\overline{I}_{1e}$ as in eqn. (4.36). The damage can still be found by minimizing the scalar eqn. (4.19).

4.3.1 Crack propagation simulation

In this section the experiments of Corre et al. [2020] are reproduced to investigate the influence of viscous parameters on crack tip propagation speed. In these experiments a thin sheet of material is pre-stretched until a certain deformation and, thereafter, a cut is made by a blade in a way that the crack immediately starts to propagate.

According to the experimental set up depicted in fig. 1.3, the numerical analysis is divided into three phases:

- ⊗ A quasi-static loading phase in which the sample undergoes stretching until reaching a specific stretch λ_{cut}. Under these conditions, the viscous deformation equals the total deformation $\mathbf{C}_v = \mathbf{C}$ ($\mathbf{C}_e = \mathbf{I}$) and the dash-pot in the rheological equivalent model in fig. 2.22 is unloaded, leaving the non-equilibrium spring undeformed (as observed in fig. 4.1). In the numerical procedure outlined in sect. 4.1.5, the solution routine skips the viscous iterations (marked by "→" in the procedure in sect. 4.1.5) by setting $\mathbf{C}_v = \mathbf{C}$. For this reason, the value of $\mathbf{C}_v$ is set to $\mathbf{C}^p$, where $\mathbf{C}^p$ is the value of the total deformation $\mathbf{C}$ at the end of this phase.

- ⊗ The second phase occurs at the instant at which the cut is introduced. Since this event is extremely fast, we presume that the deformation is completely elastic and the viscous component $\mathbf{C}_v$ maintains the value at the conclusion of the first phase ($\mathbf{C}_v = \mathbf{C}^p$). Instantaneous changes in the displacement field would occur in this phase, make it challenging to solve equation (4.7). Therefore, an incremental procedure is used to increase the damage in the cut region from 0 to 1 and to update the displacement field by eqn. (4.7).

- ⊗ The final phase consists in the crack propagation, in which both the characteristic times τ_m and τ_d come into play.

Numerical results are described in the next section, and a parametric analysis is performed to investigate the effects of the different model parameters on the crack propagation.

4.3.2 Numerical study

These numerical simulations are carried out with the mesh in fig. 4.4a where half of a $8\,\mathrm{x}\,6$ mm^2 sample is considered due to the symmetry of the experimental set up. This sample is clamped over the left-end side and pre-stretched over the right-end side during the first phase of the simulation (see sect. 4.3.1). In the upper side vertical displacements are blocked to simulate the symmetry condition. This boundary conditions indeed affects the crack propagation rate close to the boundary region and, for this reason, the results of the last part of the simulations, when the crack is close to the boundary, could not be considered reliable. The damage will be imposed in the bottom-right part of the sample

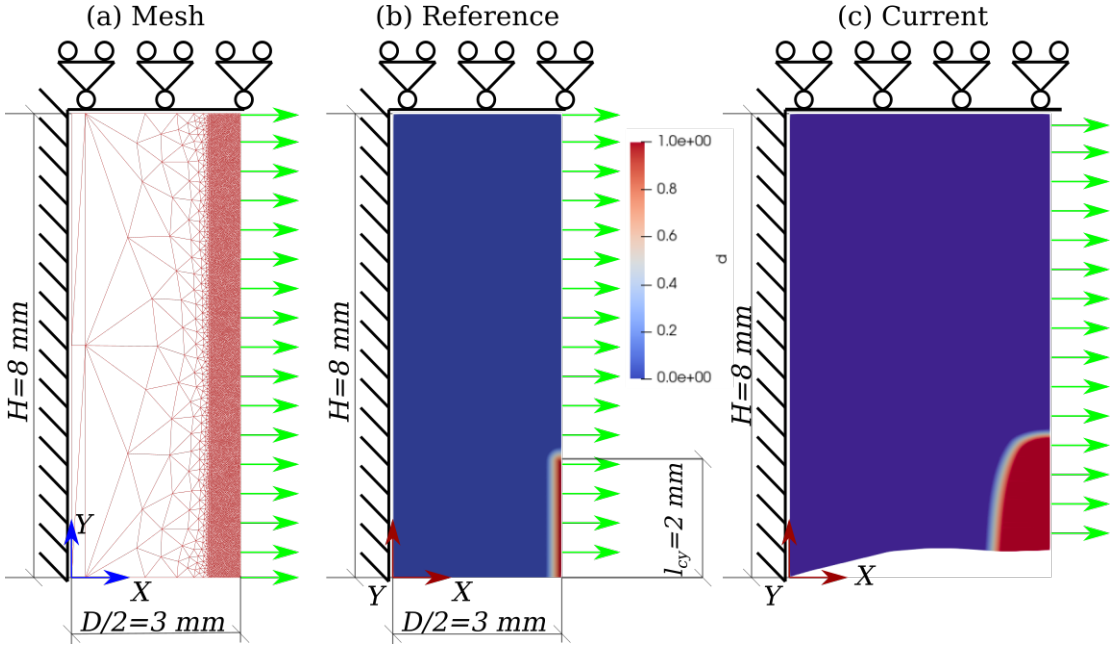

Figure 4.4: (a) boundary conditions and mesh. The mesh size in the refined zone is $l_f/20$. The contour plot in (b) and (c) displays the imposed damage field at the begin of the third phase. The damage is approximated by a quadratic function, according to the solution of the optimal profile (see Pham et al. [2011]).

as in figs. 4.4b and 4.4c as explained in sect. 4.3.1.

All of the simulations are carried out referring to the material in tab. 4.2 for which the elastic energies in eqns. (4.27) are of neo-Hooke type.

The initial series of simulations aim at investigating the impact of τ_m/τ_d (and hence η_K) on crack propagation speed. Specifically, in fig. 4.5, crack tip position versus time (a) and crack tip velocity versus crack tip position (b) are plotted using dimensionless quantities. The simulations show that the maximum and minimum propagation velocities are achieved when $\tau_m/\tau_d \approx 0$ and $\tau_m/\tau_d \to \infty$ respectively. In the former case, the viscous strain develops instantaneously, with zero elastic strain for the entire duration of the experiment. On the contrary, in the latter case, i.e. $\tau_m/\tau_d \to \infty$, the viscous strain remains fixed at the value reached at the end of the pre-stretch phase. These two limit cases are practically reached for ratios of $\tau_m/\tau_d \approx 10^{-4}$ and $\tau_m/\tau_d \approx 1$.

As shown by eqns. (4.15) and (4.29), the damage evolution (and, thus the frac-

Springs			
$\mu = \quad 1\,MPa$	$\alpha = \quad 1$	$m = \quad 0.75\,MPa$	$a = \quad 1$
Damage parameters			
$\lambda_c = \quad 2$	$l_f = \quad 0.5\,mm$	$G_f = \quad 0.667\,MPa/mm$	
Viscous parameters			
$\tau_d = \quad 4 \cdot 10^{-4}\,s$	$\eta_K = \quad 4 \cdot 10^{-5}\,MPa\ s$		

Table 4.2: Parameters used in the plane stress state simulations.

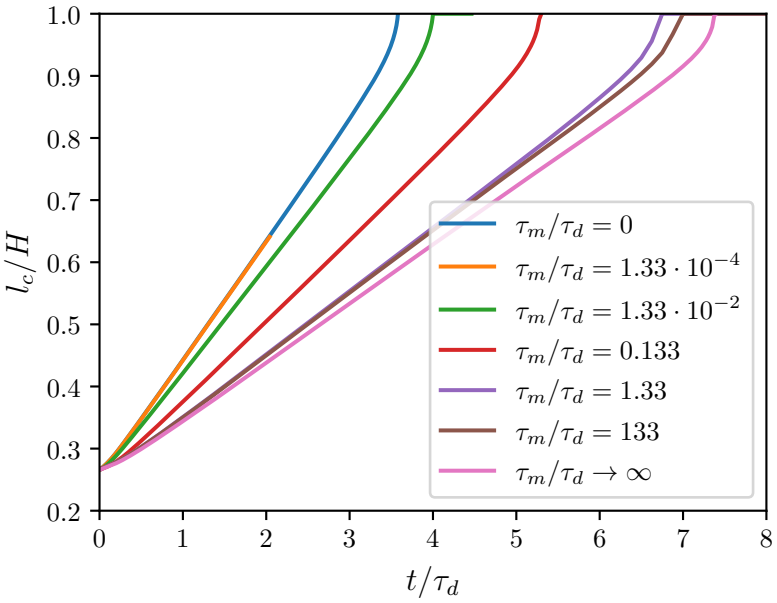

(a) Dimensionless crack length vs dimensionless time.

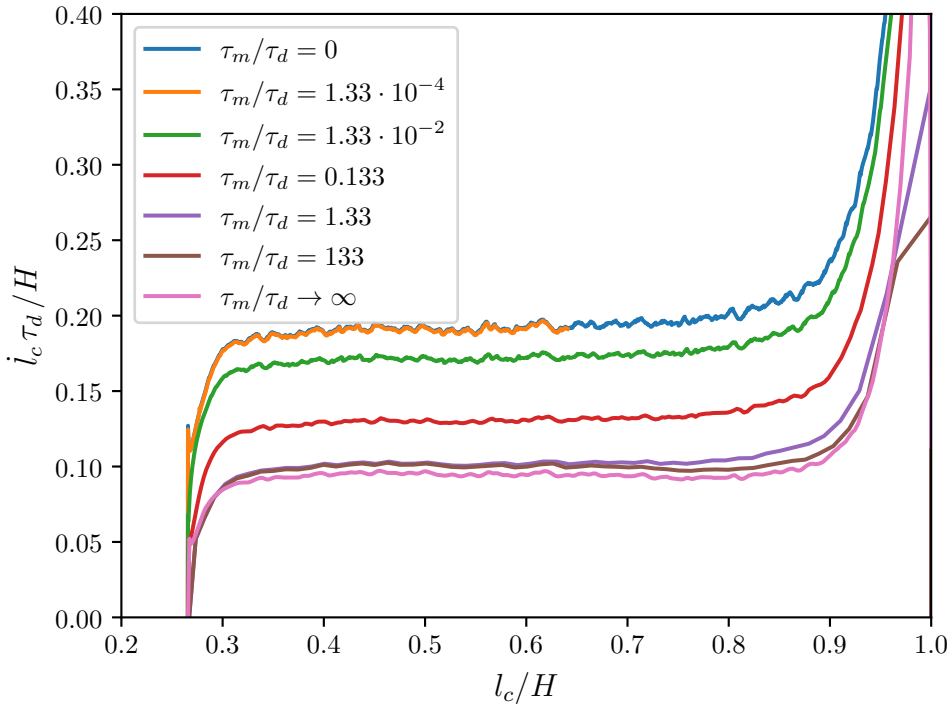

(b) Dimensionless crack speed vs dimensionless crack length.

Figure 4.5: Crack propagation velocity for different values of the ratio between the two characteristic times (τ_m/τ_d), by varying τ_m and keeping fixed $\tau_d = 4 \cdot 10^{-4}\, s$. The pre-stretch is assigned to $\lambda_{cut} = 1.5$. In particular (b) shows a constant crack rate in the central part of the simulation.

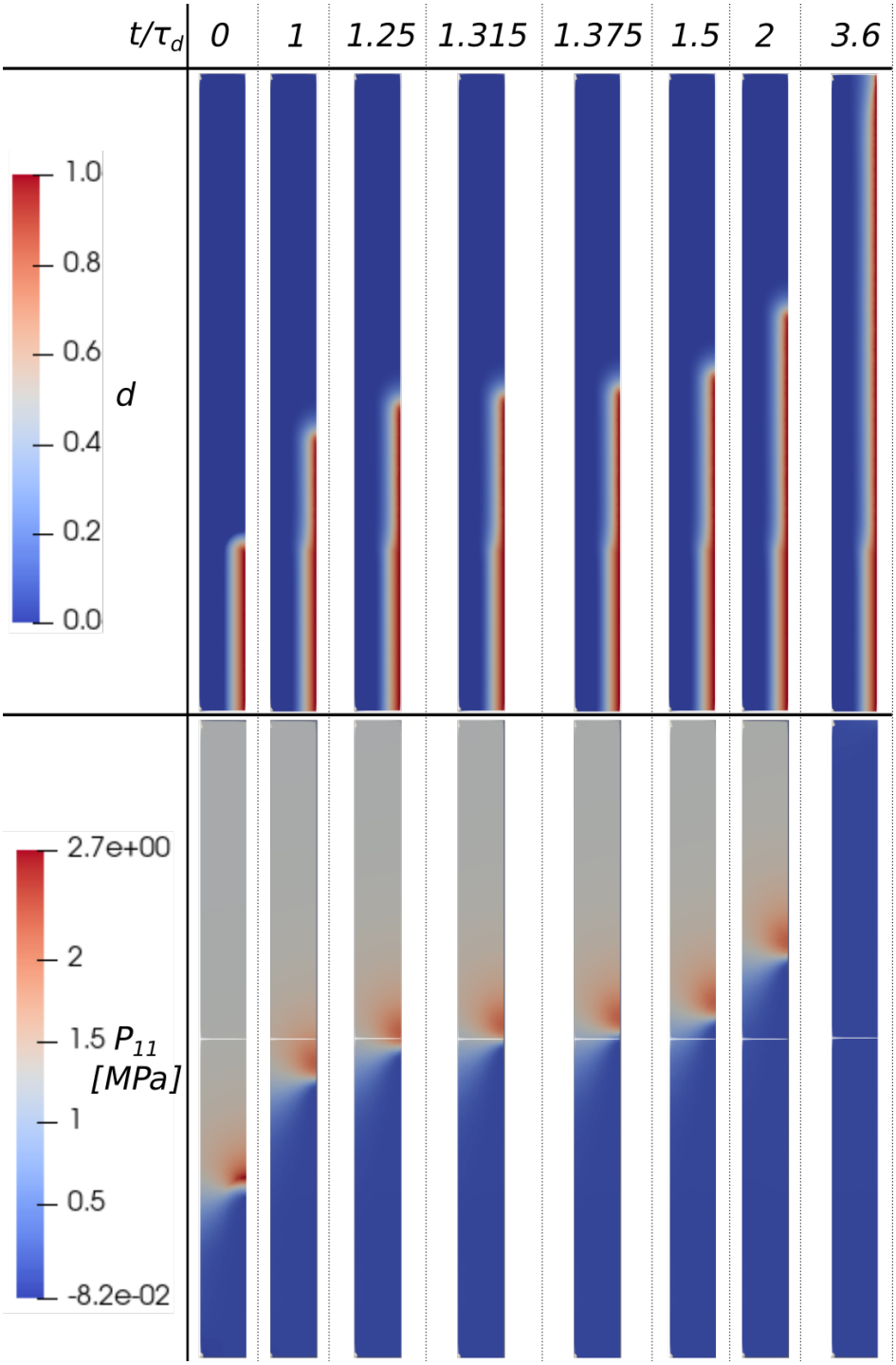

Figure 4.6: Upper figure: damage fiel; lower figure: first component of the first Piola stress tensor (P_{11}). Only the portion of the domain close to the crack tip is displayed. The simulation corresponds to the blue curve in fig. 4.5 in which the non equilibrium component of the stress vanishes.

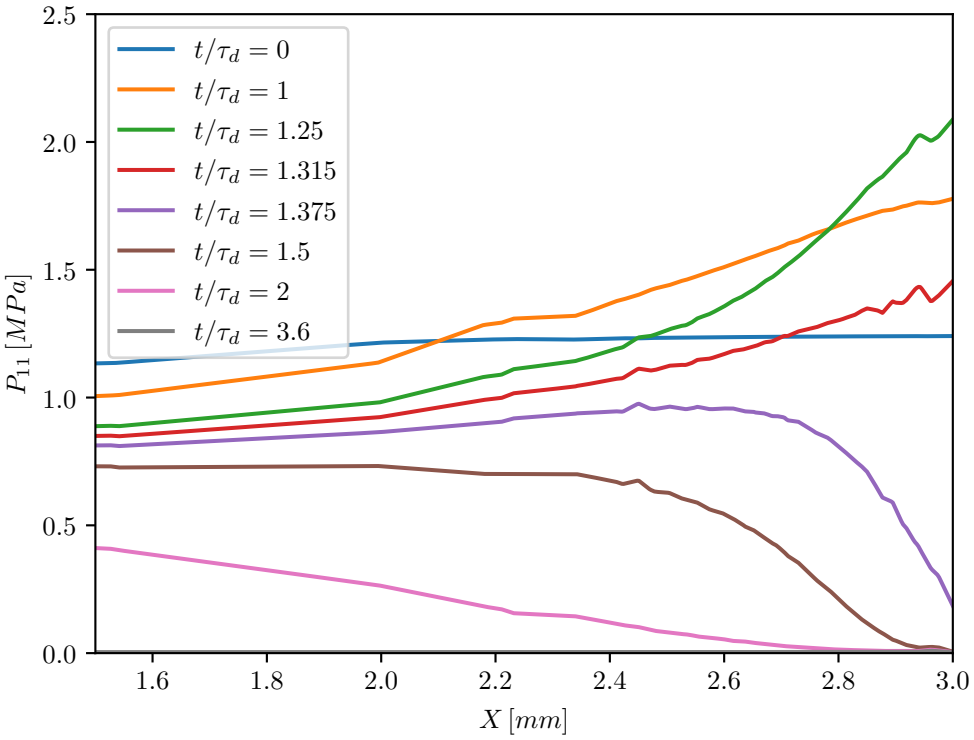

Figure 4.7: Component 11 of the first Piola stress tensor in an horizontal line of coordinates $Y = 4\,mm = H/2$ at different time instants, in case of $\tau_m/\tau_d = 0$ and $\tau_d = 4{\cdot}10^{-4}\,s$ (as in fig. 4.6). This figure shows the stress trend along the specimen during the crack tip passage.

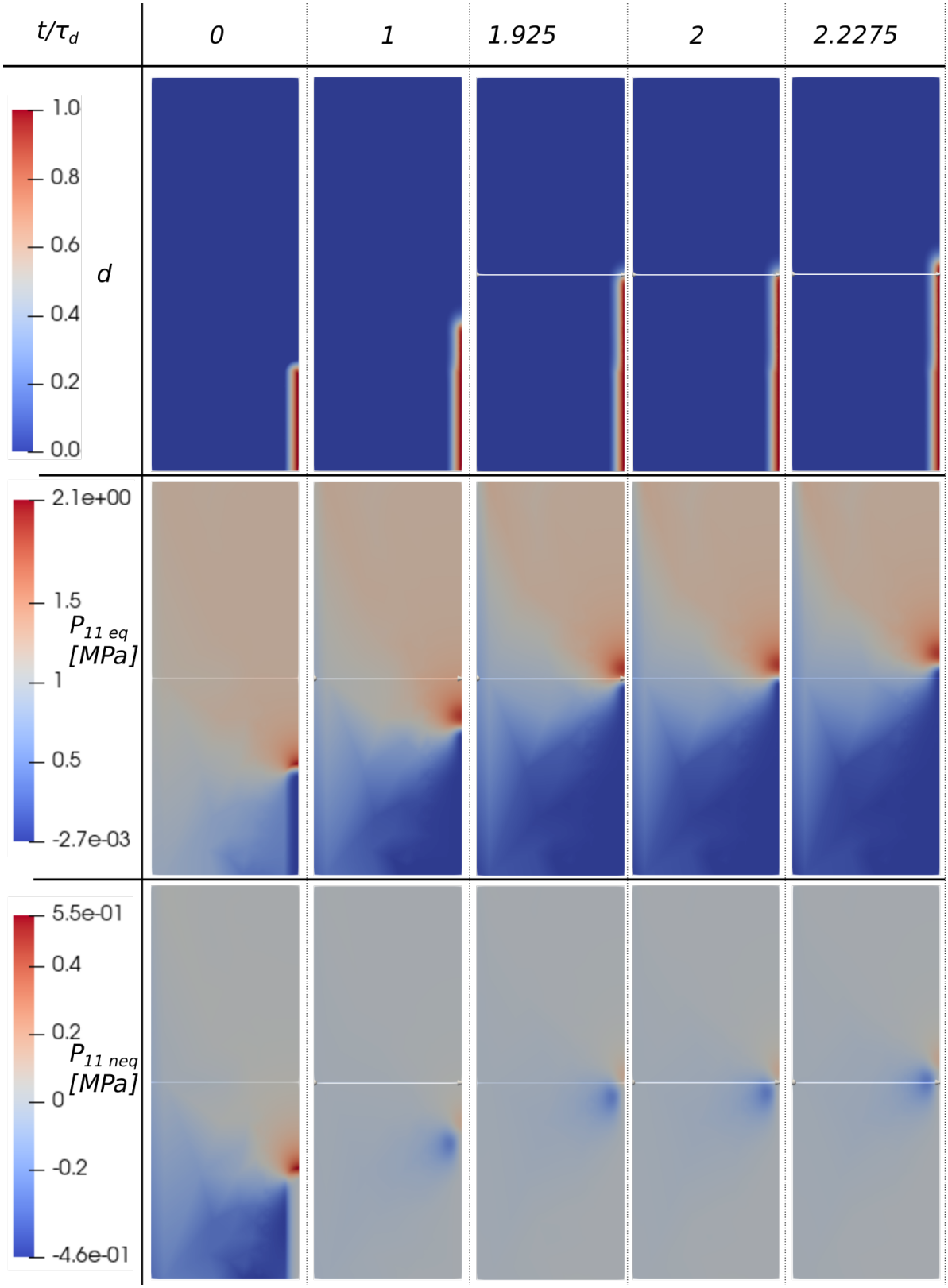

Figure 4.8: Damage field, $P_{11\,eq}$ and $P_{11\,neq}$ in the case of $\tau_m/\tau_d = 0.133$ and $\tau_d = 4 \cdot 10^{-4}\,s$, corresponding to the red curve in fig. 4.5.

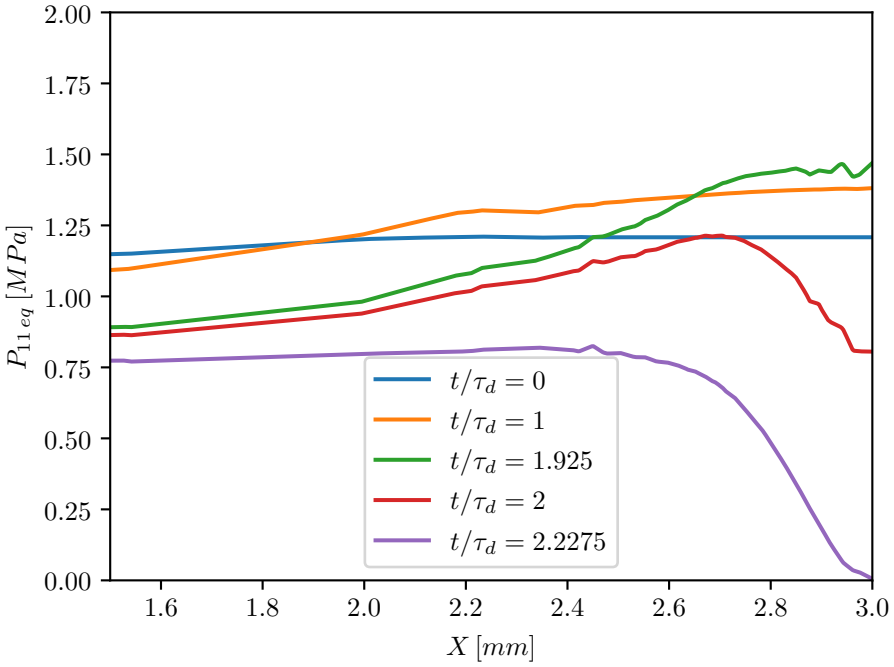

(a) equilibrium

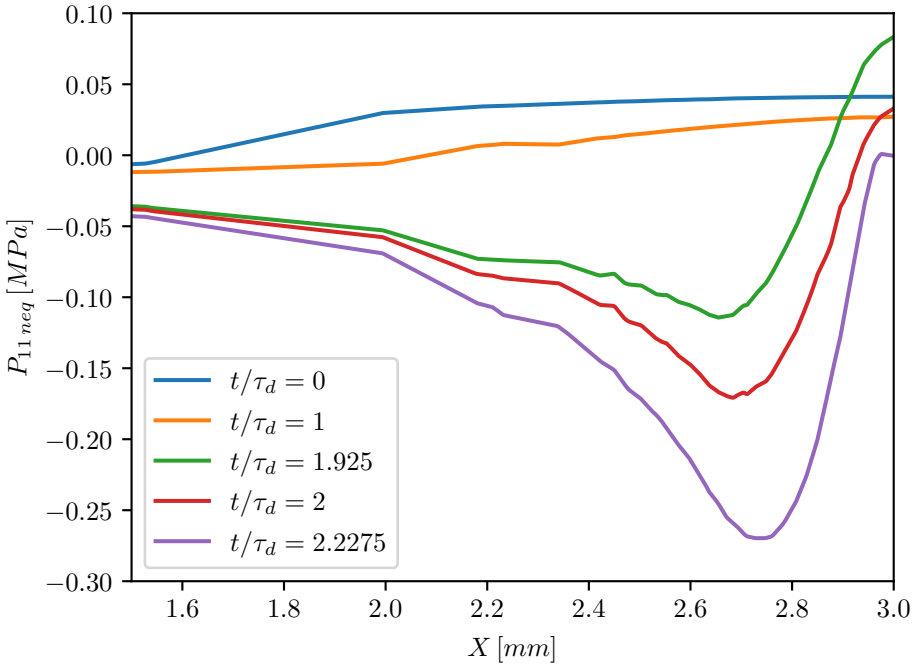

(b) non equilibrium

Figure 4.9: Component 11 of equilibrium and non equilibrium first Piola stress tensor in an horizontal line of coordinates $Y = 4\,mm = H/2$, in the case of $\tau_m/\tau_d = 0.133$ and $\tau_d = 4 \cdot 10^{-4}\,s$ (as in fig. 4.8).

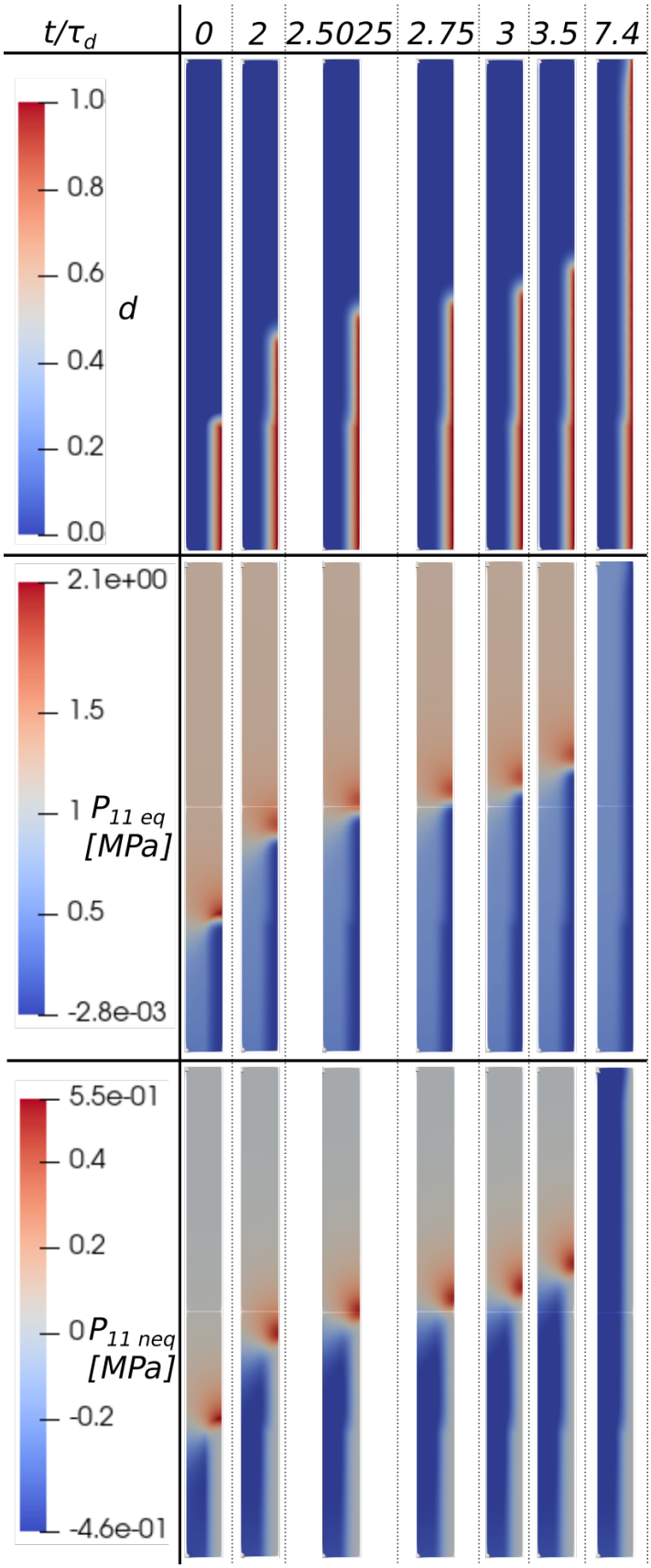

Damage field, components 11 of first Piola stress tensor (equilibrium and non equilibrium parts) in case of $\tau_m/\tau_d \to \infty$ and $\tau_d = 4 \cdot 10^{-4}\, s$, corresponding to the violet curve in fig. 4.5. In this case, the viscous strain does not evolve during the crack propagation, thus, after the crack tip passage, $\mathbf{P}_{11\,neq}$ remains negative, as shown in figs. 4.11.

Figure 4.10

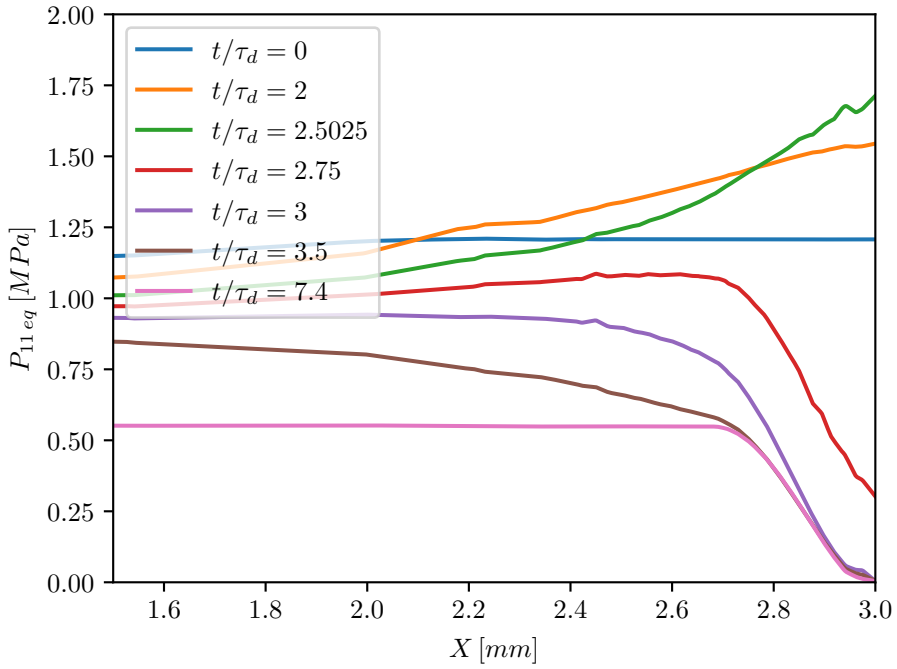

(a) equilibrium

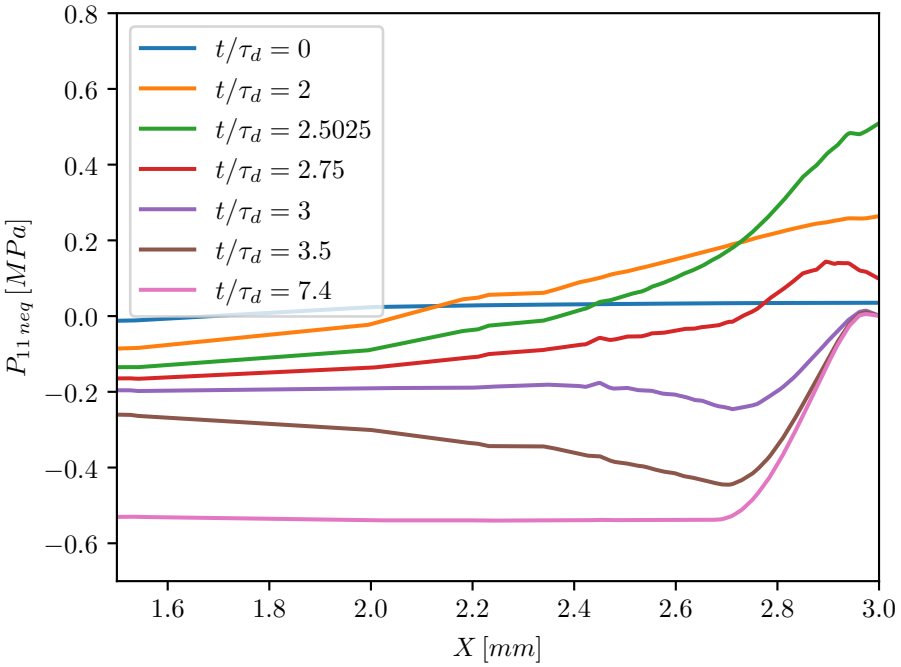

(b) non equilibrium

Figure 4.11: Component 11 of equilibrium and non equilibrium first Piola stress tensor in an horizontal line of coordinates $Y = 4\,mm = H/2$ in case of $\tau_m \to \infty$ and $\tau_d = 4 \cdot 10^{-4}\,s$ (as in fig. 4.10). The region under strain relaxation does not relax because $\tau_m \to \infty$, thus, after the passage of the crack tip, in this region $P_{11\,neq} < 0$.

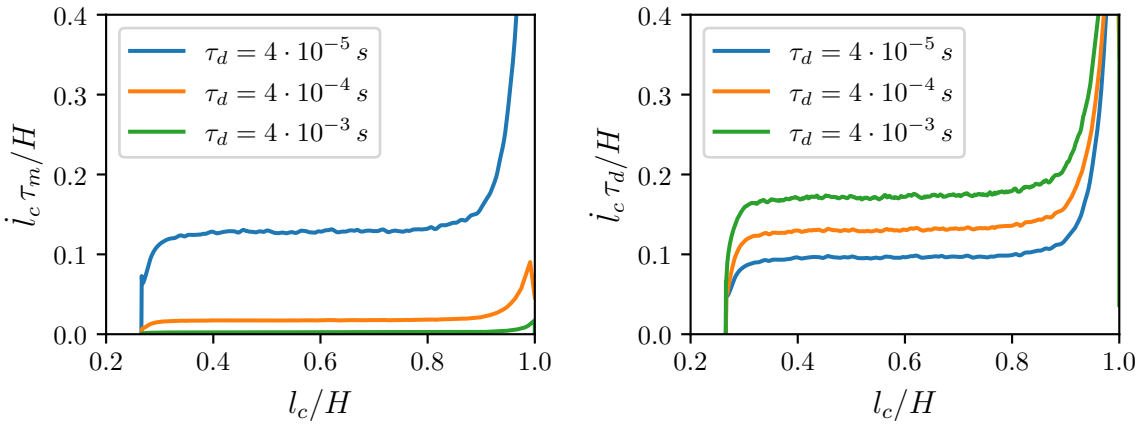

(a) Material characteristic time

(b) Damage characteristic time

Figure 4.12: Crack propagation velocity for different values of τ_d. The material characteristic time is $\tau_m = 5.33 \cdot 10^{-5}\,s$ and the pre-stretch is $\lambda_{cut} = 1.5$. Crack tip velocity is made dimensionless by τ_m in (a) and by τ_d in (b) to show that the crack speed is a decreasing function of τ_d in (a), but not in an inverse proportional manner. Indeed if it was, the graphs in (b) would coincide.

ture propagation), is driven by the increment in the elastic energies, due to the sudden increase of deformation ahead of the crack tip. To further analyze this phenomenon, three simulations are carried out: the two limit cases with $\tau_m/\tau_d \to 0$ and $\tau_m/\tau_d \to \infty$, and the intermediate case with $\tau_m/\tau_d = 0.133$. The state of the sample in these three cases is studied using the damage field and the component $P_{11\,eq} = \mathbf{P}_{eq} \cdot (\hat{e}_1 \otimes \hat{e}_1)$ and $P_{11\,neq} = \mathbf{P}_{neq} \cdot (\hat{e}_1 \otimes \hat{e}_1)$).

The results of this analysis are shown in figs. 4.6-4.11. When $\tau_m/\tau_d = 0$ (figs. 4.6 and 4.7), $\mathbf{P}_{neq} = \mathbf{0}$ and the stress at crack tip is larger then the other two cases in figs. 4.9 and 4.11 which correspond to $\tau_m/\tau_d = 0.133$ and $\tau_m/\tau_d \to \infty$ respectively. This justify the larger velocity of crack propagation achieved for $\tau_m/\tau_d = 0$.

Once the crack tip has passed, there is a strain relaxation phenomenon that increases the strain in the crack tip zone. This effect increases as the ratio τ_m/τ_d decreases. In the limit case of $\tau_m/\tau_d = 0$ (elastic material), the strain relaxation is instantaneous, thus the related crack tip strains are significantly larger than the other two cases. In the other limit case of $\tau_m/\tau_d \to \infty$, the non equilibrium stress $P_{11\,neq}$ behind the crack tip remains negative and, since $\dot{\mathbf{C}}_v = \mathbf{0}$, there is a residual viscous strain $\mathbf{C}_v$ that does not allow the complete relaxation of the broken part of the sample, with significant slower crack propagation velocity. These results show the significant effects of viscoelasticity on the fracture propagation.

In the intermediate scenario, i.e. $\tau_m/\tau_d = 0.133$, a distinct portion of the material just behind the crack tip exhibits negative non equilibrium stress (the blue little regions near the crack tip in the bottom line of fig. 4.8). This means that in that specific region, the material is still undergoing the relaxation phase, thereby resulting in a lower total strain compared to the $\tau_m/\tau_d = 0$ case, but larger than the $\tau_m/\tau_d \to \infty$ one. This phenomenon of strain relaxation occurs, therefore, *during* the passage of the crack tip, and so both of the characteristic times play a role in determining crack velocity.

The influence of τ_d is shown in fig. 4.12, where three simulation are conducted with the parameters of tab. 4.2 for different values of τ_d. The results show that, while the

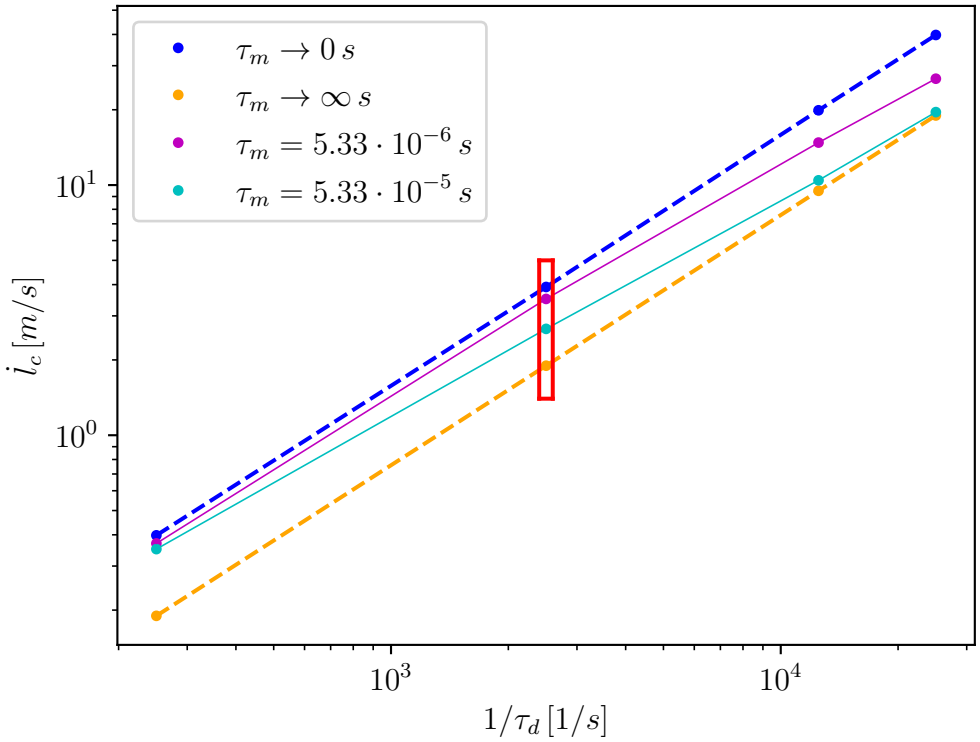

(a) Steady state crack speed vs inverse of τ_d for different values of τ_m in logarithmic scale. Crack speed results linear with respect to $1/\tau_d$ only in the limit cases. In the intermediate cases (e.g. light blue and violet points), the resultant crack speed depends almost on τ_d, and secondly on τ_m, which collocates the crack tip velocity between the two limit values.

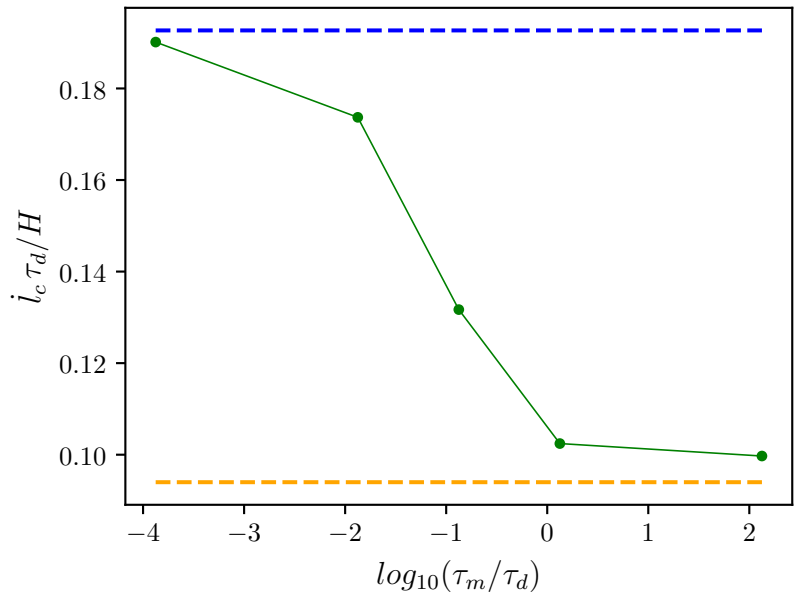

(b) Steady state crack tip velocity versus logarithm of the ratio τ_m/τ_d, for fixed $\tau_d = 4 \cdot 10^{-4}\ s$. The upper ($\tau_m/\tau_d \to 0$) and lower ($\tau_m/\tau_d \to \infty$) bounds are shown in dashed lines. The zone of graph (a) where these simulations can be collocated is highlighted by a red rectangle and they can be found in fig. 4.5.

Figure 4.13: Steady state crack tip velocity for different values of τ_m and τ_d.

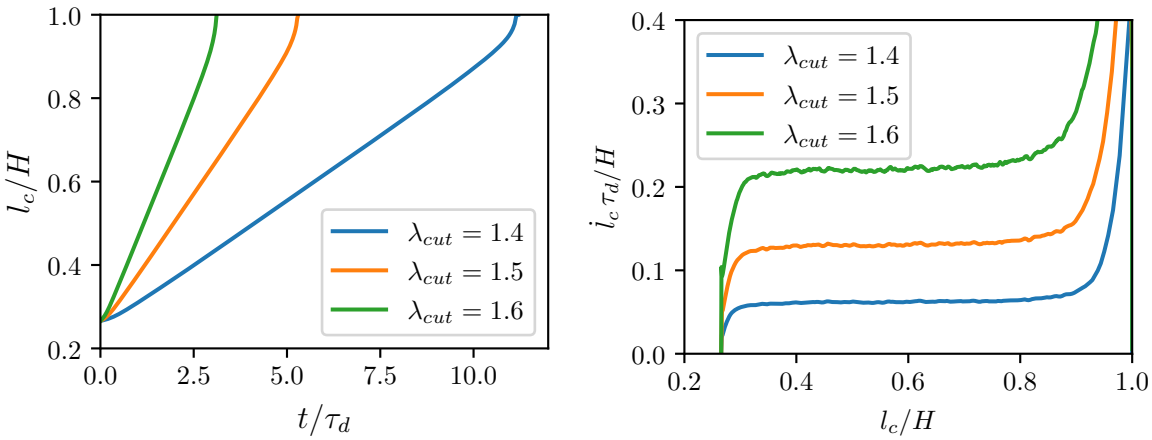

(a) Dimensionless crack length vs time. (b) Dimensionless crack speed vs crack length.

Figure 4.14: Influence of pre-stretch over the crack propagation.

order of magnitude of $\dot{l}_c$ depends on $1/\tau_d$, τ_m plays a secondary role in determining the rate of fracture propagation. In addition, the steady state crack propagation velocity is shown in fig. 4.13 for different set of simulations in which both τ_m and τ_d are varied and, so their ratio. The figure 4.13a shows that in the limit cases represented with dashed lines in the figures, crack propagation speed is inversely proportional to τ_d. In all of the other cases, the steady state crack propagation speed stands between the two limit values. This is confirmed in fig. 4.13b, where the crack propagation velocities are plotted for fixed $\tau_d = 4 \cdot 10^{-4}\, s$ versus the logarithm of the ratio τ_m/τ_d in order to show the migration of $\dot{l}_c$ form the two limit cases.

Another parameter affecting the simulation results is the pre-stretch $\lambda_c ut$ as shown in fig. 4.14 where it is confirmed that the crack speed grows with thelevel of pre-stretch. From a numerical point of view, in figs. 4.15 and 4.16, the values $\Delta t = \tau_d/100$ and $h_{mesh} = l_f/20$ assure a good accuracy of the numerical results. Note that for the finite τ_m case (fig. 4.15a) the convergence is not achieved for $\Delta t = \tau_d/10$ and in the limit case (fig. 4.15b) it gives a different value of crack propagation rate. This means that an appropriate choice of time step is crucial in order to achieve reliable numerical results.

The influence of the dimension of the sample is investigated in fig. 4.17. In these graphs it is clear that while the change of the orthogonal dimension (D in fig. 4.4) has an important influence on the propagation speed, the change of the parallel dimension (H in fig. 4.4) does not affect the simulation as much. This due to the fact that, the area influenced by the crack tip shifts along the specimen during the propagation phase at a constant velocity, without significant changing its dimension; therefore any change in H keeps the speed of the crack propagation almost unchanged.

On the other hand, by varying D, under the same pre-stretch level, the displacement of the left edge of the specimen varies. This alteration influences the crack propagation phase, leading to increase in the strain at the crack tip and, therefore, in the propagation velocity. This trend can be observed through the stresses at the crack tip P_{11}^{tip}, shown in fig. 4.18, where it is seen that their values increase with increasing D. To draw this graph, the edge of the fracture tip where P_{11} is measured, is identified as the point along the coordinate axis $X = D/2$ where the maximum value of P_{11} is reached. This value is located at the end of the damage regularization zone, ahead of the crack tip. The graphs in fig. 4.18 show an the initial stress peak induced by the imposition of damage

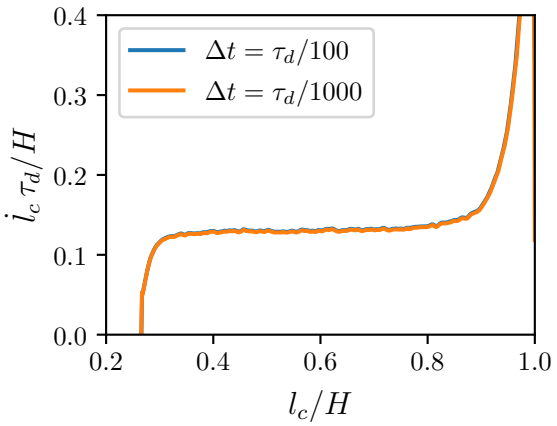

(a) $\tau_m = 5.33 \cdot 10^{-5}\, MPa \cdot s$; $\tau_d = 4 \cdot 10^{-4}\, s$

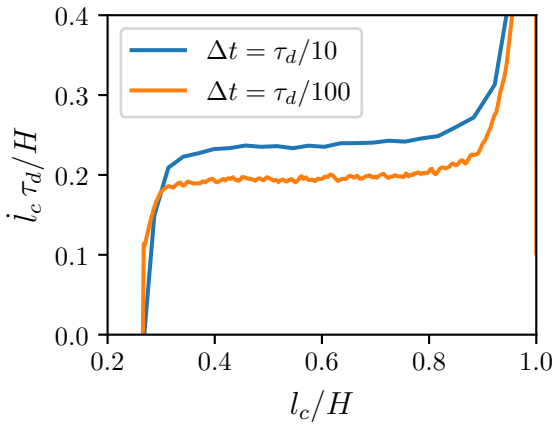

(b) $\tau_m \to 0$; $\tau_d = 4 \cdot 10^{-5}\, s$

Figure 4.15: Dimensionless crack speed vs crack length for different values of Δt, τ_m and τ_d to study the impact of Δt on model convergence. In the simulation shown in (a), employing $\Delta t = \tau_d/10$, convergence wasn't achieved. However, the other two simulations are perfectly coincident ($\Delta t = \tau_d/100$ and $\Delta t = \tau_d/1000$).

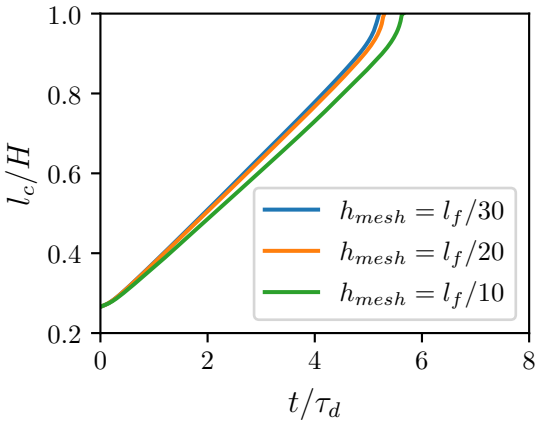

(a) Crack length vs time

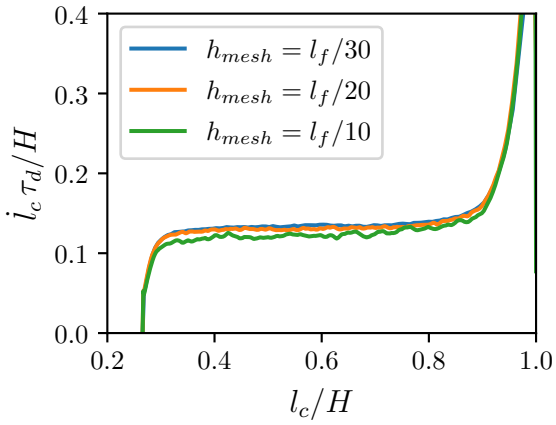

(b) Crack speed vs crack length

Figure 4.16: Influence of mesh size in the crack region about the convergence of the model. From these graphs is clear that a mesh size of $l_f/20$ is a good approximation for the problem.

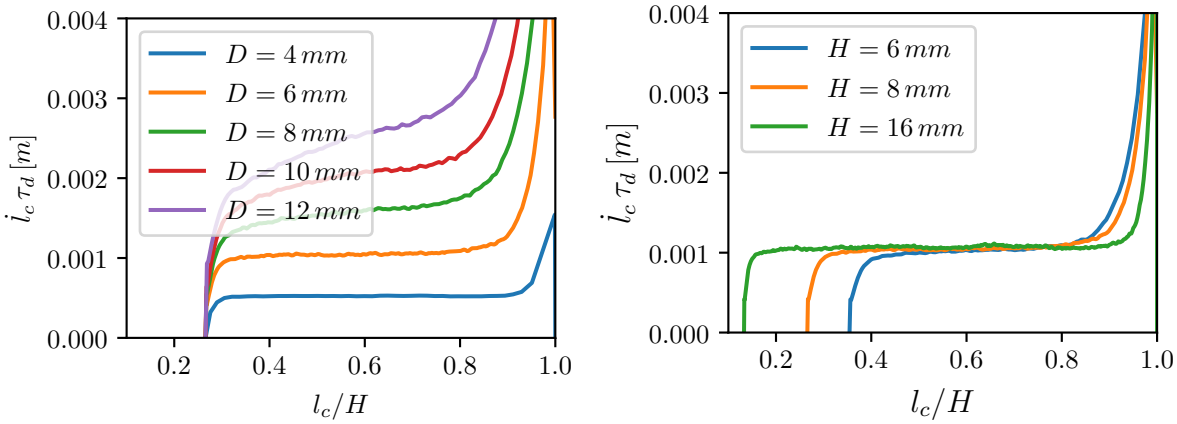

(a) orthogonal dimension influence (D)

(b) parallel dimension influence (H)

Figure 4.17: Dimensionless crack speed vs crack length for different sample's shapes. While the change of the orthogonal dimension respect the crack (a) has an important influence on the propagation speed, the change of the parallel dimension (b) does not.

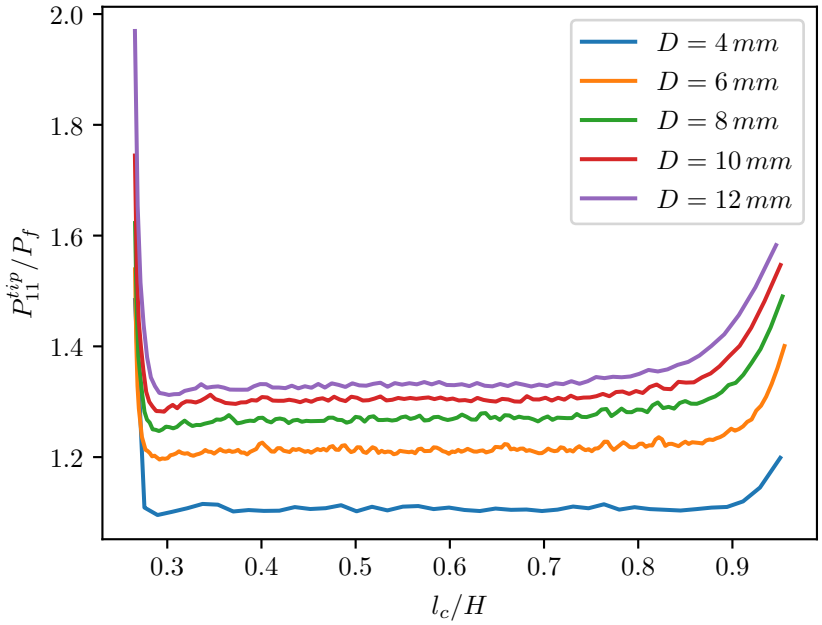

Figure 4.18: Dimensionless P_{11} at the tip of the fracture (respect the fracture engineering stress in eqn. (4.45)) versus dimensionless crack length for different values of D (see fig. 4.17a). When D increases, the deformations around the crack tip also increase, thereby intensifying the stresses.

in the second phase of the procedure outlined in sect. 4.3.1. After this peak, the stress maintains constant values until the rupture, where another peak in stress is observed due to the boundary conditions.

In fig. 4.19a the influence of the internal length l_f on crack propagation velocity is studied and it is shown that as l_f increases, the crack speed decreases, eventually compromising the initiation of crack propagation as in case of $l_f = 1.5\,mm$. Indeed, in this case, crack propagation fails to initiate, and after the initial phase (attributed to the perturbation caused by the instantaneous imposition of the damage), $\dot{l}_c \tau_d / H = 0$.

This interruption is confirmed by the value of P_{11}^{tip} in fig. 4.19b, where the first component of the engineering stress is plotted versus the crack length in dimensionless form. In this graph, for $l_f = 1.5\,mm$, the stress falls below the yield stress of fracture in eqn. (4.45) and, thus, the crack does not propagate.

Considering that, for $l_f \to 0$, the stress in the crack tip diverges to infinity as in the classical fracture mechanics solution, the presence of a regularization zone due to the non local term in the internal energy (4.1), disperses damage across a broader region, thereby regularizing deformations, and consequently, stresses. This process reduces or even nullifies the speed of fracture propagation, as predicted in equation (4.15).

The regularization zone for different values of l_f is shown in fig. 4.20, where the damage field is plotted along a vertical line of coordinates $X = D/2$ and for $Y \in [\,4.2\,mm\,,\,5.6\,mm]$ for the time instants in which $l_c/H \approx 0.6$, when the crack tip passes through these points.

The damage field grows towards 1, dissipating energy during its development. Therefore the internal length can be treated as the zone in which the phenomena related to rupture appear (as cavitation and re-crystallization) and l_f can be related to the crack tip bond breaking (Persson et al. [2005]) or the fracture process zone (Yin et al. [2021]), shown in fig. 2.8.

In any case, given that $h_{mesh} < l_f/20$, the internal length may significantly impact the simulation duration. Consequently, its calibration necessitates a balance between the reliability and the computational effort.

Apart from increasing l_f, reduction of D or λ_{cut} can inhibit the initiation of crack. Hence, it is proposed that the experimental determination of the internal length l_f (and consequently of the FPZ) which is an open problem from an experimental point of view, is achieved through experiments where variations in λ_{cut} or D are implemented until the identification of the limit values that prevent crack propagation. At this point, l_f can be estimated as the minimum length that precludes crack propagation in the numerical simulations.

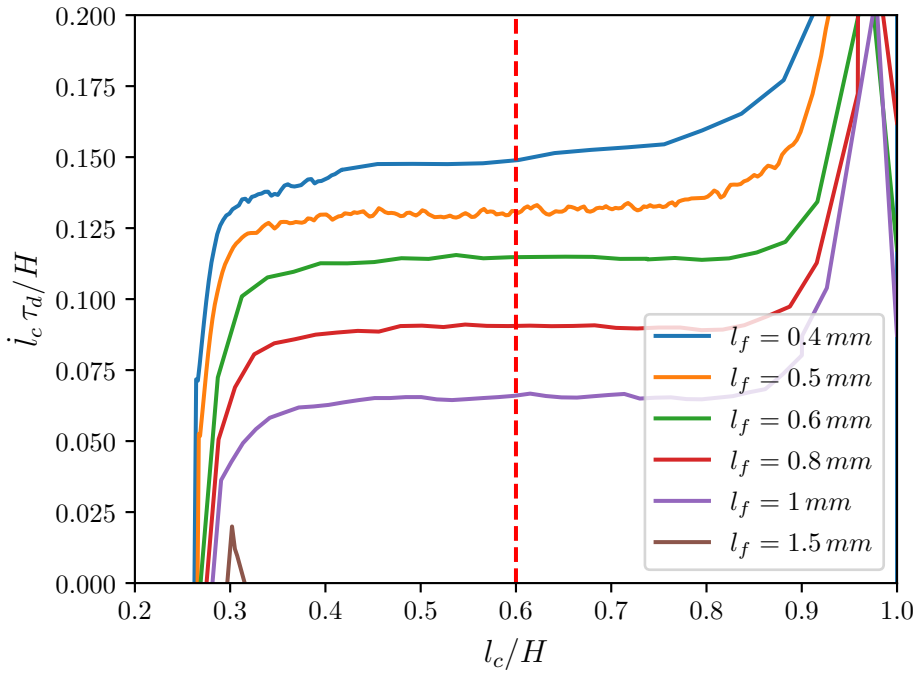

(a) Crack speed vs crack length

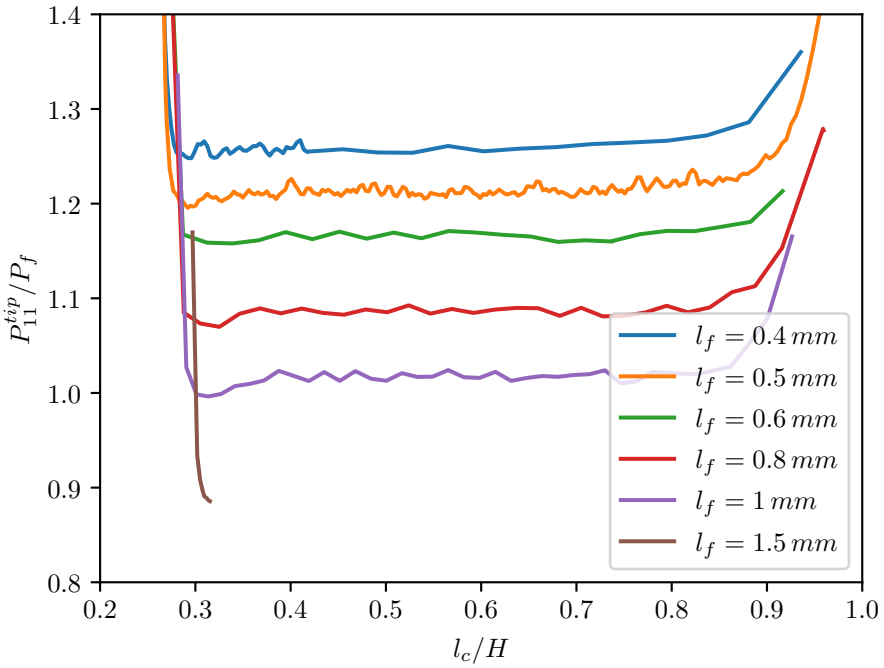

(b) P_{11}^{tip}/P_f versus crack length

Figure 4.19: In these graphs, we investigate the influence of the internal length on crack propagation. Graph (a) shows that an increase in l_f results in a decrease in crack speed, until hindering the initiation of propagation altogether as in case of $l_f = 1.5\,mm$. This trend is corroborated by observations in (b), which displays stress patterns at the fracture tip for various values of l_f. For $l_f = 1.5\,mm$ the stress falls below the yield stress of fracture in eqn. (4.45), for this reason the crack does not propagate.

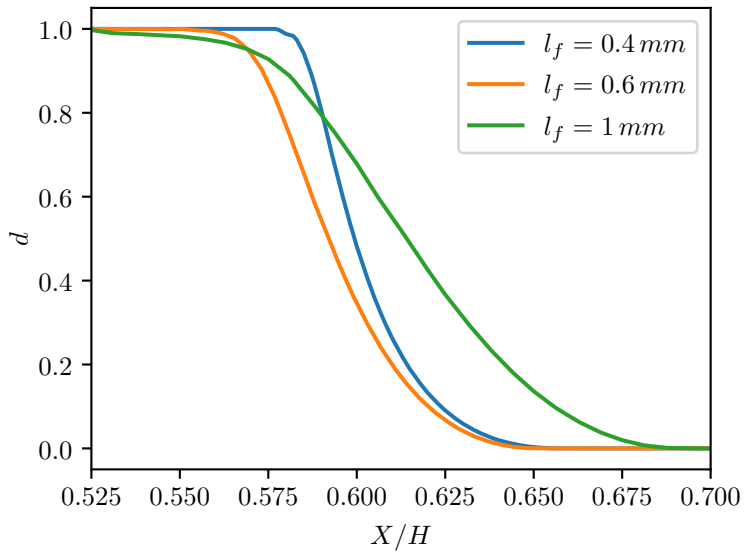

Figure 4.20: Regularization zone in the crack propagation direction for the coordinates $X = D/2$ and $Y \in [4.2\,mm, 5.6\,mm]$ for the time instants in which $l_c/H \approx 0.6$ (red dashed line of fig. 4.19a).

Chapter 5

Conclusion

The thesis was organised in four chapters, each serving a distinct purpose. Chapter 2 provided a comprehensive literature review, offering insights into the phenomenological, theoretical, and numerical modeling aspects relevant to elastomers' behavior and failure mechanisms. While laying the groundwork for the subsequent chapters, particularly 3 and 4, which present the original contributions of the thesis, Chapter 2 also serves as a valuable introduction to the broader context.

In the third chapter of this thesis, we delve into the formulation of a rate independent model, as published in Ciambella et al. [2022]. This particular model presents a damage rate-independent phase-field framework with the remarkable capability to simulate pseudo ductile failure mechanisms. Its primary objective is to accurately reproduces not only brittle failure phenomena of SBR rubber in Hocine et al. [2002] (see sect. 2.3.1), but also the intricate behavior observed in the newly introduced double network elastomers, expounded upon in Millereau et al. [2018] (see sect. 2.3.2).

To comprehend these different failure behaviors, the elastic model in Ogden [2003] is combined with the phase-field damage model in Wu [2017], in order to obtain the necessary adaptability of the resulting model with respect to the considered failure mechanisms. Indeed the model in Ciambella et al. [2022], results capable to replicate both brittle and pseudo ductile behaviors. In addition to the model formulation and the experiments fitting, the chapter includes an in-dept analysis of the numerous parameters that are necessary to include from brittle to pseudo ductile behaviors. This analysis arrives to the definition of the cohesives curves in fig. 3.4, where the longitudinal component of first Piola stress tensor versus the damage related part of the displacement is plotted, using a semi-numerical iterative procedure outlined in sect. 3.2.4. This original contribution is important due to the role played by the cohesive curve into the calibration of the parameters and in their physical interpretation.

However, it's crucial to note that this model relies on numerous experimentally derived parameters and is only applicable under pseudo-static conditions due to its lack of viscosity, that represent an important part of the rubber behavior as explained in sects. 2.1 and 2.2. This limitation impedes its application under dynamic or time-dependent scenarios.

For these reasons, in the fourth chapter, a rate-dependent model is proposed. This newly devised model integrates the formulation of Kumar and Lopez-Pamies [2016] with a phase-field model representing brittle fracture damage as in Pham et al. [2011]. The most relevant characteristic of this model is the ability to effectively capture and replicate the intricate phenomena observed during fracture propagation, that implies a dynamic deformation conditions, also introducing a new damage characteristic time τ_d. This pa-

rameter assumes the role of accounting for the duration of all those phenomena that occurring within the FPZ (see fig. 2.8 and sect. 2.2) at the micro-scale level, such as recrystallization, cavitation, or chain's rupture. The delays related to these phenomena cannot be captured by the viscous deformation alone, that rather represents a macroscopic parameter. The damage characteristic time plays the main role during the fracture propagation, determining the order of magnitude of the crack propagation velocity, as shown in the initial part of sect. 4.3.2.

In the 1D specialization of the rate dependent model (sect. 4.2) the influence of the material viscosity into the fracture initiation (see fig. 4.1) and the phenomenon of the strain relaxation after the rupture of the sample are discussed. The important role played by this phenomenon in the 2D simulations of sect. 4.3.2, is investigated through figs. 4.6-4.11, where also the interaction between the damage and the material characteristic times is discussed. Other important analyses concern the pre-stretch, the dimension of the sample and the internal length, resulting in the proposition of an experimental and numerical routine able to measure the internal length, that represents the zone in which the phenomena related to rupture appear (as cavitation and re-crystallization, described in sect. 2.2). The measure of the internal length represents an open problem.

While both models achieve their goals, many improvements and developments can be made to increase their possible uses:

- The rate dependent model can be integrated with the numerical simulations of the experiments in literature with DENT or SENT specimen (e.g. Loew et al. [2019], Yin and Kaliske [2020], Dammaß et al. [2023]), to improve the adaptation of the viscoelastic parameters.

- The modeling (in 1D and 2D) can be extended to 3D to simulate more complex failure processes (like tires, vibration absorber...).

- Models of finite viscoelasticity can be applied to the description of failure in different materials capable of substantial large deformation, such as biological tissues, hydrogels, among others. Exploring this possibility within the context of the models outlined in this thesis is also worth investigating.

- In Yin et al. [2021] and in Persson et al. [2005], two different zone around the crack tip are highlighted: the fracture process zone (where the damage is growing) and an inelastic zone around the FPZ. While the last internal length is identified in sect. 4.3.2, the length of the inelastic zone does not. A possible investigation can begin taking into account the zone where the magnitude of $\mathbf{S}_{neq}$ increases around the crack tip as measure of the inelastic zone.

- The viscosity could be considered as a not constant function as in Kumar and Lopez-Pamies [2016] (see sect. 2.4.2), in order to accurately reproduce the velocity fields, as shown in Kamasamudram et al. [2023].

- As shown in sects. 2.1 and 2.2, the temperature plays an important role in viscoelastic and fracture behavior of these materials. In the presented models, the effects of temperature are not taken into account, and this restrict the the applicability of the model to the situations in which the temperature remains almost

constant. In addition, changes of temperature due to dissipative phenomena are not explicitly considered. For this reason the inclusion of the temperature effects in the formulations is a possible development for the fields of the models applicability.

- The rate dependent model can be enriched by incorporating the cohesive damage formulation of the rate independent model to reproduce also the rate dependent behavior of that presents a pseudo-ductile fracture behavior in dynamic deformation regime.

- From a numerical perspective, the objective can be to examine the solution method with the aim of enhancing convergence and reducing computation time. One of the possible improvement is the formulation of the problem (or of a part of it) in updated Lagrangian (e.g. Del Piero et al. [2007]) or in an Eulerian formulation (e.g. Rubin [2020]).

- The model's applicability can be applied to problems of interest for industry, such as pneumatic systems, seals, seismic isolators, and other areas where elastomers find application.

- In the formulation of the internal energy described by eqn. (4.1), the degradation functions for the equilibrium and non-equilibrium components of energy are treated as unequal. This implies that even if the damage field is identical for both components (because the material is homogeneous), the impact of damage on the two systems of the Maxwell's rheological model (refer to fig. 2.22) may differ. It is noteworthy that if τ_m is assumed to be independent of damage, the degradation functions for η_K and ψ_{neq} must be identical.

Bibliography

R Alessi, J-J Marigo, and S Vidoli. Gradient damage models coupled with plasticity: variational formulation and main properties. *Mechanics of Materials*, jan 2014. ISSN 01676636. URL `http://www.sciencedirect.com/science/article/pii/S0167663614000039`.

Luigi Ambrosio and Vincenzo Maria Tortorelli. Approximation of functional depending on jumps by elliptic functional via t-convergence. *Communications on Pure and Applied Mathematics*, 1990. ISSN 10970312. doi: 10.1002/cpa.3160430805.

Thomas Louis Marie Baumard. *Investigation on fatigue failure in tyres.* PhD thesis, Queen Mary University of London, 2017.

J. S. Bergström and M. C. Boyce. Constitutive modeling of the large strain time-dependent behavior of elastomers. *Journal of the Mechanics and Physics of Solids*, 1998. ISSN 00225096. doi: 10.1016/S0022-5096(97)00075-6.

VL Biderman. Calculations of rubber parts (en russe). *Rascheti na Prochnost*, 40, 1958.

B. Bourdin, G. A. Francfort, and J. J. Marigo. Numerical experiments in revisited brittle fracture. *Journal of the Mechanics and Physics of Solids*, 48(4):797–826, 2000. ISSN 00225096. doi: 10.1016/S0022-5096(99)00028-9.

Blaise Bourdin, Gilles A. Francfort, and Jean Jacques Marigo. *The variational approach to fracture.* 2008a. ISBN 9781402063947. doi: 10.1007/978-1-4020-6395-4.

Blaise Bourdin, Gilles A Francfort, and Jean-Jacques Marigo. The variational approach to fracture. *Journal of elasticity*, 91:5–148, 2008b.

G. Carbone and B. N.J. Persson. Crack motion in viscoelastic solids: The role of the flash temperature. *European Physical Journal E*, 2005. ISSN 12928941. doi: 10.1140/epje/i2005-10013-y.

Jacopo Ciambella, Giovanni Lancioni, and Nico Stortini. An Ogden-like formulation incorporating phase-field fracture in elastomers: From brittle to pseudo-ductile failures. *Philosophical Transactions of the Royal Society A: Mathematical, Physical and Engineering Sciences*, 2022. ISSN 1364503X. doi: 10.1098/rsta.2021.0323.

T. Corre, M. Coret, E. Verron, B. Leblé, and F. Le Lay. Experimental full field analysis for dynamic fracture of elastomer membranes. *International Journal of Fracture*, 2020. ISSN 15732673. doi: 10.1007/s10704-020-00447-1.

Costantino Creton and Matteo Ciccotti. Fracture and adhesion of soft materials: A review. 2016. ISSN 00344885. doi: 10.1088/0034-4885/79/4/046601.

C.A. Nonato Da Silva, J. Ciambella, J.A.O. Barros, T.D. dos Santos Valente, and I.G. Costa. A multiscale model for optimizing the flexural capacity of FRC structural elements. *Composites Part B: Engineering*, 200:108325, aug 2020. ISSN 13598368. doi: 10.1016/j.compositesb.2020.108325.

Hüsnü Dal, Açıkgöz Kemal, and Yashar Badienia. On the Performance of Isotropic Hyperelastic Constitutive Models for Rubber-Like Materials: A State of the Art Review. 2021. ISSN 00036900. doi: 10.1115/1.4050978.

Franz Dammaß, Marreddy Ambati, and Markus Kästner. A unified phase-field model of fracture in viscoelastic materials. *Continuum Mechanics and Thermodynamics*, 2021. ISSN 14320959. doi: 10.1007/s00161-021-01013-3.

Franz Dammaß, Karl A. Kalina, Marreddy Ambati, and Markus Kästner. Phase-field modelling and analysis of rate-dependent fracture phenomena at finite deformation. *Computational Mechanics*, 2023. ISSN 14320924. doi: 10.1007/s00466-023-02310-1.

D. De Tommasi, G. Puglisi, and G. Saccomandi. Localized versus diffuse damage in amorphous materials. *Physical Review Letters*, 100(8):1–4, 2008. ISSN 00319007. doi: 10.1103/PhysRevLett.100.085502.

Gianpietro Del Piero, Giovanni Lancioni, and Riccardo March. A variational model for fracture mechanics: Numerical experiments. *Journal of the Mechanics and Physics of Solids*, 55(12):2513–2537, 2007. ISSN 00225096. doi: 10.1016/j.jmps.2007.04.011.

Gianpietro Del Piero, Giovanni Lancioni, and Riccardo March. A variational model for fracture mechanics: numerical experiments. *Journal of the Mechanics and Physics of Solids*, 55(12):2513–2537, 2007.

Julie Diani, Bruno Fayolle, and Pierre Gilormini. A review on the Mullins effect. 2009. ISSN 00143057. doi: 10.1016/j.eurpolymj.2008.11.017.

Daniel Charles Drucker. A more fundamental approach to plastic stressstrain relations. In *Proc. 1st US Natl. Congr. Appl. Mech.*, pages 487–491, 1952.

Gholam Hossein Farrahi, Mahdi Javanbakht, and Hossein Jafarzadeh. On the phase field modeling of crack growth and analytical treatment on the parameters. *Continuum Mechanics and Thermodynamics*, 2020. ISSN 14320959. doi: 10.1007/s00161-018-0685-z.

Patrick Farrell and Corrado Maurini. Linear and nonlinear solvers for variational phase-field models of brittle fracture. *International Journal for Numerical Methods in Engineering*, 109(5):648–667, 2017. ISSN 10970207. doi: 10.1002/nme.5300.

G. A. Francfort and J. J. Marigo. Revisiting brittle fracture as an energy minimization problem. *Journal of the Mechanics and Physics of Solids*, 46(8):1319–1342, 1998. ISSN 00225096. doi: 10.1016/S0022-5096(98)00034-9.

Alan N Gent. A new constitutive relation for rubber. *Rubber chemistry and technology*, 69(1):59–61, 1996.

Alan N Gent and AG Thomas. Forms for the stored (strain) energy function for vulcanized rubber. *Journal of Polymer Science*, 28(118):625–628, 1958.

Alan Neville Gent and Joseph D Walter. Pneumatic tire. 2006.

AA Griffith. The phenomena of flow and rupture in solids: Phil. *Trans. Roy. Soc. Lond. Ser. A*, 221:163–98, 1920.

Morton E Gurtin. *An introduction to continuum mechanics*. Academic press, 1982.

Vincent Hakim and Alain Karma. Laws of crack motion and phase-field models of fracture. *Journal of the Mechanics and Physics of Solids*, 2009. ISSN 00225096. doi: 10.1016/j.jmps.2008.10.012.

N. Aït Hocine, M. Naït Abdelaziz, and A. Imad. Fracture problems of rubbers: J-integral estimation based upon η factors and an investigation on the strain energy density distribution as a local criterion. *International Journal of Fracture*, 2002. ISSN 03769429. doi: 10.1023/A:1020967429222.

Gerhard A. Holzapfel. On large strain viscoelasticity: Continuum formulation and finite element applications to elastomeric structures. *International Journal for Numerical Methods in Engineering*, 1996. ISSN 00295981. doi: 10.1002/(SICI)1097-0207(19961130)39:22<3903::AID-NME34>3.0.CO;2-C.

Roy M. Howard. Analytical approximations for the inverse Langevin function via linearization, error approximation, and iteration. *Rheologica Acta*, 2020. ISSN 14351528. doi: 10.1007/s00397-020-01195-8.

Alexei A Ilyushin. On the postulate of plasticity. 1961.

Akira Isihara, Natsuki Hashitsume, and Masao Tatibana. Statistical theory of rubber-like elasticity. IV. (Two-dimensional stretching). *The Journal of Chemical Physics*, 1951. ISSN 00219606. doi: 10.1063/1.1748111.

Vasudevan Kamasamudram, Michel Coret, and Nicolas Moës. Computation of energy evolution during the dynamic fracture of elastomers using the finite viscoelastic model: Its implementation in Abaqus. *Mechanics of Materials*, 2023. ISSN 01676636. doi: 10.1016/j.mechmat.2023.104638.

Wolfgang G. Knauss. A review of fracture in viscoelastic materials. *International Journal of Fracture*, 2015. ISSN 15732673. doi: 10.1007/s10704-015-0058-6.

Werner Kuhn and Felix Grün. Beziehungen zwischen elastischen konstanten und dehnungsdoppelbrechung hochelastischer stoffe. *Kolloid-Zeitschrift*, 101:248–271, 1942.

Aditya Kumar and Oscar Lopez-Pamies. On the two-potential constitutive modeling of rubber viscoelastic materials. *Comptes Rendus - Mecanique*, 2016. ISSN 18737234. doi: 10.1016/j.crme.2015.11.004.

N. Lahellec, F. Mazerolle, and J. C. Michel. Second-order estimate of the macroscopic behavior of periodic hyperelastic composites: Theory and experimental validation. *Journal of the Mechanics and Physics of Solids*, 2004. ISSN 00225096. doi: 10.1016/S0022-5096(03)00104-2.

G. Lancioni and R. Alessi. Modeling micro-cracking and failure in short fiber-reinforced composites. *Journal of the Mechanics and Physics of Solids*, 137: 103854, 2020. ISSN 00225096. doi: 10.1016/j.jmps.2019.103854. URL `https://doi.org/10.1016/j.jmps.2019.103854`.

Giovanni Lancioni. Modeling the Response of Tensile Steel Bars by Means of Incremental Energy Minimization. *Journal of Elasticity*, 2015. ISSN 15732681. doi: 10.1007/s10659-015-9515-8.

Giovanni Lancioni and Valeria Corinaldesi. Variational modelling of diffused and localized damage with applications to fiber-reinforced concretes. *Meccanica*, 2018. ISSN 15729648. doi: 10.1007/s11012-017-0709-y.

Giovanni Lancioni and Tuncay Yalçinkaya. Strain gradient plasticity: Deformation patterning, localization, and fracture. 2019. doi: 10.1007/978-3-319-58729-$5_4$3.

Shawn R. Lavoie, Pierre Millereau, Costantino Creton, Rong Long, and Tian Tang. A continuum model for progressive damage in tough multinetwork elastomers. *Journal of the Mechanics and Physics of Solids*, 125:523–549, 2019. ISSN 00225096. doi: 10.1016/j.jmps.2019.01.001. URL `https://doi.org/10.1016/j.jmps.2019.01.001`.

J Douglas Lawson. An order five runge-kutta process with extended region of stability. *SIAM Journal on Numerical Analysis*, 3(4):593–597, 1966.

Patrick Le Tallec, Christophe Rahier, and Ahmed Kaiss. Three-dimensional incompressible viscoelasticity in large strains: Formulation and numerical approximation. *Computer Methods in Applied Mechanics and Engineering*, 1993. ISSN 00457825. doi: 10.1016/0045-7825(93)90080-H.

E. H. Lee. Elastic-plastic deformation at finite strains. *Journal of Applied Mechanics, Transactions ASME*, 1964. ISSN 15289036. doi: 10.1115/1.3564580.

Valery I. Levitas, Dong Wook Lee, and Dean L. Preston. Interface propagation and microstructure evolution in phase field models of stress-induced martensitic phase transformations. *International Journal of Plasticity*, 2010. ISSN 07496419. doi: 10.1016/j.ijplas.2009.08.003.

Tianyi Li, Jean Jacques Marigo, Daniel Guilbaud, and Serguei Potapov. Gradient damage modeling of brittle fracture in an explicit dynamics context. *International Journal for Numerical Methods in Engineering*, 2016. ISSN 10970207. doi: 10.1002/nme.5262.

P.B. Lindley. Engineering Design With Natural Rubber. *The Malaysian Rubber Producers Research Association.*, 1974.

Pascal J. Loew, Bernhard Peters, and Lars A.A. Beex. Rate-dependent phase-field damage modeling of rubber and its experimental parameter identification. *Journal of the Mechanics and Physics of Solids*, 2019. ISSN 00225096. doi: 10.1016/j.jmps.2019.03.022.

Anders Logg and Garth N. Wells. DOLFIN: Automated finite element computing. *ACM Transactions on Mathematical Software*, 2010. ISSN 00983500. doi: 10.1145/1731022.1731030.

Anders Logg, Kent-Andre Mardal, and Garth Wells, editors. *Automated Solution of Differential Equations by the Finite Element Method*, volume 84 of *Lecture Notes in Computational Science and Engineering*. Springer Berlin Heidelberg, Berlin, Heidelberg, 2012. ISBN 978-3-642-23098-1. doi: 10.1007/978-3-642-23099-8. URL `http://link.springer.com/10.1007/978-3-642-23099-8`.

Oscar Lopez-Pamies. A new I1-based hyperelastic model for rubber elastic materials. *Comptes Rendus - Mecanique*, 2010. ISSN 16310721. doi: 10.1016/j.crme.2009.12.007.

Eric Lorentz and V Godard. Gradient damage models: Toward full-scale computations. *Computer Methods in Applied Mechanics and Engineering*, 200(21-22):1927–1944, 2011.

J. J. Marigo. Constitutive relations in plasticity, damage and fracture mechanics based on a work property. *Nuclear Engineering and Design*, 114(3):249–272, 1989. ISSN 00295493. doi: 10.1016/0029-5493(89)90105-2.

Jean-Jacques Marigo. From Clausius-Duhem and Drucker-Ilyushin inequalities to standard materials. 2006. doi: 10.1007/0-306-46946-$4_2$2.

Jean Jacques Marigo, Corrado Maurini, and Kim Pham. An overview of the modelling of fracture by gradient damage models. *Meccanica*, 51(12):3107–3128, 2016. ISSN 15729648. doi: 10.1007/s11012-016-0538-4.

JE Mark, B Erman, and FR Eirich. Science end technology of rubber, 1994.

C. Miehe, F. Welschinger, and M. Hofacker. Thermodynamically consistent phase-field models of fracture: Variational principles and multi-field FE implementations. *International Journal for Numerical Methods in Engineering*, 2010a. ISSN 00295981. doi: 10.1002/nme.2861.

Christian Miehe and Lisa Marie Schänzel. Phase field modeling of fracture in rubbery polymers. Part I: Finite elasticity coupled with brittle failure. *Journal of the Mechanics and Physics of Solids*, 2014. ISSN 00225096. doi: 10.1016/j.jmps.2013.06.007.

Christian Miehe, Martina Hofacker, and Fabian Welschinger. A phase field model for rate-independent crack propagation: Robust algorithmic implementation based on operator splits. *Computer Methods in Applied Mechanics and Engineering*, 2010b. ISSN 00457825. doi: 10.1016/j.cma.2010.04.011.

Christian Miehe, Fadi Aldakheel, and Arun Raina. Phase field modeling of ductile fracture at finite strains: A variational gradient-extended plasticity-damage theory. *International Journal of Plasticity*, 2016. ISSN 07496419. doi: 10.1016/j.ijplas.2016.04.011.

A Mielke and T Roubíček. *Rate-independent systems*. 2015. ISBN 9781493927050.

Pierre Millereau, Etienne Ducrot, Jess M. Clough, Meredith E. Wiseman, Hugh R. Brown, Rint P. Sijbesma, and Costantino Creton. Mechanics of elastomeric molecular composites. *Proceedings of the National Academy of Sciences of the United States of America*, 2018. ISSN 10916490. doi: 10.1073/pnas.1807750115.

M. Mooney. A theory of large elastic deformation. *Journal of Applied Physics*, 1940. ISSN 00218979. doi: 10.1063/1.1712836.

C.A. Nonato Da Silva, J. Ciambella, J.A.O. Barros, and I.G. Costa. Analytical bond model for general type of reinforcements of finite embedment length in cracked cement based materials. *International Journal of Solids and Structures*, 167:36–47, aug 2019. ISSN 00207683. doi: 10.1016/j.ijsolstr.2019.02.018. URL `https://doi.org/10.1016/j.ijsolstr.2019.02.018` `https://linkinghub.elsevier.com/retrieve/pii/S002076831930099X`.

Ray W Ogden. Nonlinear elasticity with application to material modelling. *Lecture Notes-AMAS*, 2003.

B. N.J. Persson, O. Albohr, G. Heinrich, and H. Ueba. Crack propagation in rubber-like materials. *Journal of Physics Condensed Matter*, 2005. ISSN 09538984. doi: 10.1088/0953-8984/17/44/R01.

Kim Pham, Hanen Amor, Jean Jacques Marigo, and Corrado Maurini. Gradient damage models and their use to approximate brittle fracture. 2011. ISSN 10567895. doi: 10.1177/1056789510386852.

Edvige Pucci and Giuseppe Saccomandi. A note on the gent model for rubber-like materials. *Rubber Chemistry and Technology*, 2002. ISSN 00359475. doi: 10.5254/1.3547687.

G. Puglisi and G. Saccomandi. Multi-scale modelling of rubber-like materials and soft tissues: An appraisal. 2016. ISSN 14712946. doi: 10.1098/rspa.2016.0060.

J. Ramier, C. Gauthier, L. Chazeau, L. Stelandre, and L. Guy. Payne effect in silica-filled styrene-butadiene rubber: Influence of surface treatment. *Journal of Polymer Science, Part B: Polymer Physics*, 2007. ISSN 08876266. doi: 10.1002/polb.21033.

Stefanie Reese and Sanjay Govindjee. A theory of finite viscoelasticity and numerical aspects. *International Journal of Solids and Structures*, 1998. ISSN 00207683. doi: 10.1016/s0020-7683(97)00217-5.

J. R. Rice. A path independent integral and the approximate analysis of strain concentration by notches and cracks. *Journal of Applied Mechanics, Transactions ASME*, 1968. ISSN 15289036. doi: 10.1115/1.3601206.

Ronald S Rivlin. Large elastic deformations of isotropic materials iv. further developments of the general theory. *Philosophical transactions of the royal society of London. Series A, Mathematical and physical sciences*, 241(835):379–397, 1948.

Miles B Rubin. *Continuum mechanics with Eulerian formulations of constitutive equations*, volume 265. Springer Nature, 2020.

François Sidoroff. Un modèle viscoélastique non linéaire avec configuration intermédiaire. 1974.

J. C. Simo and J. W. Ju. Strain- and stress-based continuum damage models-I. Formulation. *International Journal of Solids and Structures*, 1987. ISSN 00207683. doi: 10.1016/0020-7683(87)90083-7.

Brandon Talamini, Yunwei Mao, and Lallit Anand. Progressive damage and rupture in polymers. *Journal of the Mechanics and Physics of Solids*, 2018. ISSN 00225096. doi: 10.1016/j.jmps.2017.11.013.

L. R.G. Treloar. Stress-strain data for vulcanised rubber under various types of deformation. *Transactions of the Faraday Society*, 1944. ISSN 00147672. doi: 10.1039/tf9444000059.

LR G Treloar. The physics of rubber elasticity. 1975.

Kirk C. Valanis. The Valanis–Landel strain energy function Elasticity of incompressible and compressible rubber-like materials. *International Journal of Solids and Structures*, 2022. ISSN 00207683. doi: 10.1016/j.ijsolstr.2021.111271.

Malcolm L. Williams, Robert F. Landel, and John D. Ferry. The Temperature Dependence of Relaxation Mechanisms in Amorphous Polymers and Other Glass-forming Liquids. *Journal of the American Chemical Society*, 1955. ISSN 15205126. doi: 10.1021/ja01619a008.

Jian Ying Wu. A unified phase-field theory for the mechanics of damage and quasi-brittle failure. *Journal of the Mechanics and Physics of Solids*, 2017. ISSN 00225096. doi: 10.1016/j.jmps.2017.03.015.

Jian Ying Wu. Robust numerical implementation of non-standard phase-field damage models for failure in solids. *Computer Methods in Applied Mechanics and Engineering*, 340:767–797, 2018. ISSN 00457825. doi: 10.1016/j.cma.2018.06.007. URL `https://doi.org/10.1016/j.cma.2018.06.007`.

Jian Ying Wu and Vinh Phu Nguyen. A length scale insensitive phase-field damage model for brittle fracture. *Journal of the Mechanics and Physics of Solids*, 119:20–42, 2018. ISSN 00225096. doi: 10.1016/j.jmps.2018.06.006. URL `https://doi.org/10.1016/j.jmps.2018.06.006`.

O. H. Yeoh. Characterization of Elastic Properties of Carbon-Black-Filled Rubber Vulcanizates. *Rubber Chemistry and Technology*, 1990. ISSN 0035-9475. doi: 10.5254/1.3538289.

O. H. Yeoh. Some forms of the strain energy function for rubber. *Rubber Chemistry and Technology*, 1993. ISSN 00359475. doi: 10.5254/1.3538343.

OH Yeoh. Analysis of deformation and fracture of 'pure shear'rubber testpiece. *Plastics, rubber and composites*, 30(8):389–397, 2001.

Bo Yin and Michael Kaliske. Fracture simulation of viscoelastic polymers by the phase-field method. *Computational Mechanics*, 65:293–309, 2020.

Tenghao Yin, Tonghao Wu, Junjie Liu, Shaoxing Qu, and Wei Yang. Essential work of fracture of soft elastomers. *Journal of the Mechanics and Physics of Solids*, 156 (March):104616, 2021. ISSN 00225096. doi: 10.1016/j.jmps.2021.104616. URL `https://doi.org/10.1016/j.jmps.2021.104616`.